

Inclusive and differential cross section measurement of $t\bar{t}b\bar{b}$ production and studies of $t\bar{t}$ production with additional jet radiation

Zur Erlangung des akademischen Grades eines
DOKTORS DER NATURWISSENSCHAFTEN (Dr. rer. nat.)

von der KIT-Fakultät für Physik des
Karlsruher Instituts für Technologie (KIT)
angenommene

DISSERTATION

von M.Sc. Jan van der Linden
aus Backnang

Tag der mündlichen Prüfung: 07. July 2023

Referent:	Prof. Dr. Ulrich Husemann	Institute of Experimental Particle Physics
Korreferent:	PD Dr. Roger Wolf	Institute of Experimental Particle Physics



This document is licensed under a Creative Commons Attribution-Non Commercial 4.0 International License (CC BY-NC 4.0): <https://creativecommons.org/licenses/by-nc/4.0/deed.en>

Erklärung der selbstständigen Anfertigung der Dissertationsschrift

Hiermit erkläre ich, dass ich die Dissertation mit dem Titel

Inclusive and differential cross section measurement of $t\bar{t}b\bar{b}$ production and studies of $t\bar{t}$ production with additional jet radiation.

selbstständig angefertigt, alle benutzten Hilfsmittel vollständig und genau angegeben und alles kenntlich gemacht habe, was aus Arbeiten anderer unverändert oder mit Abänderungen entnommen wurde.

Ich versichere außerdem, dass ich die Dissertation nur in diesem und keinem anderen Promotionsverfahren eingereicht habe und dass diesem Promotionsverfahren keine endgültig gescheiterten Promotionsverfahren vorausgegangen sind.

Karlsruhe, 01. June 2023

.....
(Jan van der Linden)

Contents

Introduction	1
I Foundations	5
1 The standard model of particle physics	7
1.1 The particles of the standard model	7
1.2 The standard model as a gauge theory	11
1.3 Spontaneous symmetry breaking and the origin of masses	14
1.4 Quantum chromodynamics	18
1.5 Cross sections and Feynman diagrams	19
1.6 The physics of top quarks	22
2 Experimental setup	25
2.1 The Large Hadron Collider	25
2.2 The Compact Muon Solenoid	27
2.3 Definition of the data set	32
3 Object reconstruction	35
3.1 Tracks and vertices	35
3.2 The Particle Flow algorithm	36
3.3 Jet reconstruction	39
3.4 Missing transverse momentum	45
4 Cross section measurements	47
4.1 Maximum likelihood fits	47
4.2 Normalized differential cross section measurements	50
5 Event simulation	53
5.1 Parton distribution functions	53
5.2 Hard scattering	54
5.3 Parton showers	56
5.4 Hadronization	56
5.5 Underlying event description	57
5.6 Pileup	57
5.7 Detector simulation	57
5.8 Tools	57
6 Corrections to simulated events	61
6.1 Pileup reweighting	61
6.2 L1 pre-firing	62
6.3 Trigger efficiencies	63
6.4 Electron reconstruction efficiencies	64
6.5 Muon reconstruction efficiencies	64
6.6 Jet energy corrections	64
6.7 Jet flavor tagging efficiency	65

II Measurement of the $t\bar{t}b\bar{b}$ process	69
7 Introduction	71
7.1 Motivation	71
7.2 Topology of the $t\bar{t}b\bar{b}$ process	73
7.3 Strategy of the $t\bar{t}b\bar{b}$ measurement	76
7.4 Related work	77
8 Ingredients for the $t\bar{t}b\bar{b}$ measurement	83
8.1 Event simulation	83
8.2 Fiducial phase space definition	88
8.3 Event selection	91
8.4 Validation of simulation	94
8.5 Ancillary variables	101
8.6 Out-of-acceptance process definitions	101
8.7 Systematic uncertainties	103
9 Measurement of the $t\bar{t}b\bar{b}$ process	111
9.1 Extraction of fiducial and normalized differential cross sections	111
9.2 Inclusive cross section results	116
9.3 Differential cross section results	123
9.4 Scale choices of the nominal signal model	134
III Additional studies on $t\bar{t}$+jets production	141
10 Introduction	143
10.1 Modeling of $t\bar{t}$ +jets events	143
10.2 Setup of the $t\bar{t}$ +jets measurement	145
10.3 Definition of observables	147
11 Measurement of the $t\bar{t}$+jets process	149
11.1 Inclusive cross section results	149
11.2 Differential cross section results	152
Summary and Outlook	159
Appendix	163
A Supplemental material for the $t\bar{t}b\bar{b}$ measurement	163
B Supplemental material for the $t\bar{t}$ +jets measurement	191
Acronyms	207
Bibliography	209
Final words	219

Introduction

Since the discovery of the Higgs boson in 2012, many of the other open questions in elementary particle physics remain unanswered. While the standard model (SM) of particle physics describes many aspects of elementary particles and their interactions precisely, it fails to describe, for example, the origin of Dark Matter (DM), the gravitational force, the matter-antimatter asymmetry in the universe, or the non-zero mass of the neutrino. With the discovery of the Higgs boson, an important puzzle piece has been added to the SM, explaining the origin of particle masses, but leaving the other questions unanswered.

Many attempts are made at finding hints towards new particles, signatures, or interactions; none of them have been successful as of yet. Measurements can be performed, that, for example, attempt to find candidates for dark matter particles, or attempt to find evidence for new types of interactions. A wide range of such searches are performed, ruling out many possibilities that could explain the unexplained. In the last decade, more and more possibilities are ruled out, making the discovery of something new more and more difficult. At the collider experiments at the Large Hadron Collider (LHC) at the European Organization for Nuclear Research (CERN) many such measurements are performed but are only able to access a certain energy range, such that for example potentially undiscovered heavier particles might not be identified in a direct search such as has been performed for the Higgs boson. A large number of searches for new particles and interactions are performed, and any new hints towards the unexplained are absent. This raises the question, are the things that explain the missing pieces within reach or still very far away? This lack of new discoveries also revives this field of research, making the development of new measurement strategies or new theories that can be tested even more important. In that context, this area of particle physics accelerates towards indirect search methods, for example using the concept of effective field theories, where hints for new particles or interactions are searched for in the low-energetic limit of the actual high-energetic process. For example, an undiscovered heavy particle could alter the momentum distribution of the Higgs boson or a top quark due to interactions of that particle that are not resolved at the energies at the LHC.

On the other side of particle physics research, the focus lies on the precise measurement of the properties of the already established particles of the SM. To date, the interactions and properties of the particles that are predicted by the SM are not yet all confirmed by measurements, hence this field of SM physics is still very active. The predictions of the SM have to be confirmed, and parameters that are not inherently predicted by the

Introduction

SM have to be measured, such as the interaction strengths of the Higgs boson to itself or other particles. At the same time, precise measurements of the SM properties might also reveal hints towards particles or interactions that are not described by the SM, if, for example, a measurement result shows a significant discrepancy to the SM prediction. Among the precision measurements of SM predictions, the determination of the coupling of the Higgs boson to quarks is an important aspect. During Run 2 of the LHC between 2015 and 2018, the coupling of the Higgs boson to bottom quarks has been established and measured with high precision. The coupling of the Higgs boson to lighter quarks, such as the charm quark, is predicted to be rarer and has hence not been discovered as of yet, but is expected to be one of the highlights of the physics program at the LHC in the coming years. Important for the measurement of both of these Higgs boson interactions is the Higgs boson production process in association with a top quark-antiquark pair ($t\bar{t}$), together, $t\bar{t}H$. This production process gives a unique opportunity to, simultaneously, probe the coupling of the Higgs boson to the top quark, as well as to the decay particle of the Higgs boson, for example, the bottom or charm quark ($H \rightarrow b\bar{b}$, $H \rightarrow c\bar{c}$). At the same time, the signature of two top quarks makes this Higgs boson production process distinguishable from most processes.

Important for a precise measurement of the $t\bar{t}H$ production process is the precise knowledge of the remaining processes that are indistinguishable from the $t\bar{t}H$ production process. In cases where the Higgs boson decays into a pair of bottom or charm quarks ($t\bar{t}H(b\bar{b})$, $t\bar{t}H(c\bar{c})$), the signature that is recorded in collider experiments such as the Compact Muon Solenoid (CMS) experiment of the LHC, is indistinguishable from $t\bar{t}$ production in association with additional quarks ($t\bar{t}q\bar{q}$), where the additional quarks are produced via the strong interaction. Specifically, if these additional quarks are bottom quarks ($t\bar{t}b\bar{b}$), this yields the same final state of particles as the $t\bar{t}H(b\bar{b})$ process. The quarks that are produced in the highly-energetic collisions hadronize into sprays of particles, called jets, which can be reconstructed in the detectors. Previous measurements of the $t\bar{t}H(b\bar{b})$ process showed that the major limitation in such measurements is the limited knowledge of the $t\bar{t}b\bar{b}$ process due to its challenging description. For future measurements of $t\bar{t}H(c\bar{c})$ production, the expectation is similar; the measurements will be limited by the $t\bar{t}b\bar{b}$ and $t\bar{t}C$ backgrounds, the latter being the case where charm jets are produced in addition to the $t\bar{t}$ system.

Besides the importance of $t\bar{t}b\bar{b}$ for a precise measurement of $t\bar{t}H(b\bar{b})$, the modeling of this process is also an interesting probe of perturbative quantum chromodynamics (QCD) calculations. The precise description of the $t\bar{t}b\bar{b}$ process is difficult, as it combines bottom quarks with non-negligible mass, and top quarks with, in comparison, very large mass. Hence, the interactions of these particles exist at very different energy scales and have to be combined in one common calculation. Such calculations of inclusive or differential production probabilities of processes are performed in perturbation theory, which has to combine the two energy scales to yield valid predictions. The experimental precision with the amount of data collected in the recent years is large, which requires higher-order corrections to be included in the calculations and simulations in order to provide a suitable estimation for the $t\bar{t}b\bar{b}$ process. The simulation of the process contains tunable parameters, which have to be adjusted to match the observations from data. The description of the $t\bar{t}b\bar{b}$ process, whether it be the inclusive or differential production probabilities, differ significantly, depending on the choices made in the modeling of that process in Monte-Carlo (MC) event generators. The measurements presented in this thesis will provide important input to the development of new and improved $t\bar{t}b\bar{b}$ models which will be a crucial ingredient for future $t\bar{t}H$ measurements.

In this thesis, inclusive and normalized differential cross sections measurements of the $t\bar{t}b\bar{b}$ process are presented. This aims at providing more insight into the $t\bar{t}b\bar{b}$ process and allows for the comparison of the measurements with different modeling approaches and calculations. This can give insight into the weaknesses and strengths of the modeling approaches and the choices made for the modeling approaches for an accurate description of the $t\bar{t}b\bar{b}$ process in data. In this measurement, observables of the $t\bar{t}b\bar{b}$ process are probed, targeting the global event description, such as jet or b jet multiplicities, and observables related to the b jets not from $t\bar{t}$ decay. The latter are especially sensitive to the description of the $t\bar{t}b\bar{b}$ process, as the origin of the b jets differs between the modeling approaches that are studied in this thesis.

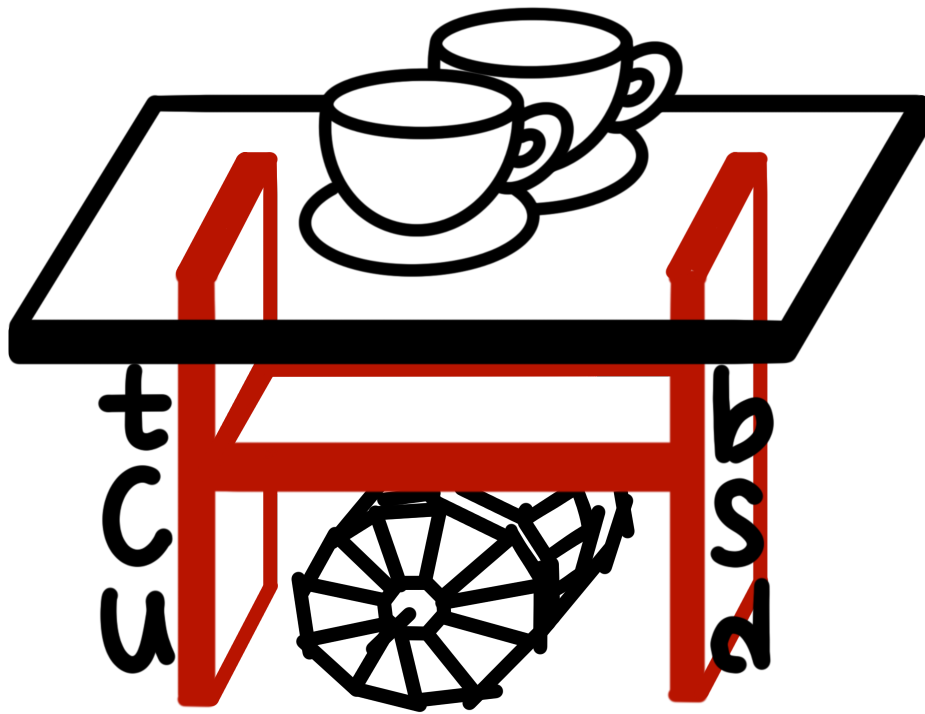
This thesis also contains an extension of the $t\bar{t}b\bar{b}$ measurements to the production of $t\bar{t}$ in association with quarks of any flavor, $t\bar{t}+\text{jets}$, aiming to also provide insight into the quality of the modeling of this process, and the possible origin of the apparent mismodeling of certain quantities. For example, observables are probed which are sensitive to the modeling of the top quark momentum and the angular distribution of the jets produced in addition to the $t\bar{t}$ system.

The measurements of this thesis are performed with events collected between 2016 and 2018 at the CMS experiment at the LHC in proton-proton (pp) collisions at a center-of-mass energy of $\sqrt{s} = 13$ TeV. Collision events are selected for data analysis if they contain exactly one electron or muon, targeting the decay channel of the $t\bar{t}$ system in which one top quark decay includes an electron or muon, and the other does not. Events further are required to have a certain number of jets and b-tagged jets in order to be selected, thereby targeting the high jet multiplicity final state of $t\bar{t}b\bar{b}$ production.

This thesis is structured as follows. First, in Part **I**, the foundations necessary for the interpretation of the measurements of this thesis are introduced. This includes a brief review of the SM of particle physics, the experimental environment at the LHC, the reconstruction of events recorded at the CMS experiment, the concept of cross section measurements, a review of event simulations, and lastly an overview over corrections applied to simulated events. Afterward, the measurements of the $t\bar{t}b\bar{b}$ process are discussed in Part **II**. This includes a review of related measurements and the current state of the modeling of the $t\bar{t}b\bar{b}$ process, a detailed description of the measurement strategy and the associated selections, object definitions and uncertainties considered in the measurement. Then, in Part **III**, the measurements of the $t\bar{t}+\text{jets}$ process are discussed, including a brief review of the modeling of $t\bar{t}+\text{jets}$ production. Finally, a conclusion is drawn, summarizing the results and giving an outlook on the future.

Part I

Foundations



1 The standard model of particle physics

The standard model (SM) of particle physics describes the theoretical framework in which the work of this thesis is interpreted. The SM encompasses a description of all particles and interactions on an elementary level, except for gravitational interactions. Some open questions in high energy physics, like the non-zero mass of neutrinos, the origin of Dark Matter (DM), or the incorporation of gravitation into the SM motivate a precise and redundant measurement of all parameters of the SM. This either validates the theory or enables the uncovering of discrepancies with the theory prediction that might be explained with some of the aforementioned open questions. The work in this thesis focuses on one aspect of SM physics, namely the precise measurement of the production of a pair of top quark and antiquark ($t\bar{t}$) in association with jets. These processes are well established in the SM, such that the measurements performed here are considered precision measurements to improve the understanding of this area of top quark physics. In the following, the theory of the SM will be introduced in short to set the framework in which the results of this thesis are interpreted. In Section 1.1, first a brief overview of the particles of the SM is given. The interactions and properties of these particles are described by gauge theories which are discussed in Section 1.2. As an example, the derivation of the Lagrangian density of quantum electrodynamics (QED) will be sketched in this section. The electroweak unification is an important aspect of the SM and will be discussed briefly in Section 1.2.1. Based on these discussions, an open question of the SM is the origin of particle masses, which will be discussed in Section 1.3. In Section 1.4, quantum chromodynamics (QCD) and running masses will be discussed. In Section 1.5, the concepts of cross sections and Feynman rules are introduced. Finally, as the measurements of this thesis all involve a $t\bar{t}$ pair, in Section 1.6, the physics of the top quark will be emphasized. The explanations in this chapter are loosely based on Refs. [1–4], where also additional details to the (only briefly) reviewed topics can be found.

All discussions and results in this thesis are presented using natural units, following the convention $c = \hbar = 1$. To this effect, energies, momenta, and masses all have units of energy, commonly expressed in electronvolt, $1 \text{ eV} = 1.6 \cdot 10^{-19} \text{ J}$. Similarly, electric charge is given in elementary units, $1e = 1.6 \cdot 10^{-19} \text{ C}$.

1.1 The particles of the standard model

In this section, a short review of all fundamental particles and interactions contained in the SM of particle physics is given. Generally, all particles can be classified either

Table 1.1: **Bosons and forces of the standard model.** Gauge bosons are listed separately from the Higgs boson. All Gauge bosons have spin 1, while the Higgs boson has spin 0. The charge is given in units of elementary charge e . All values are taken from Ref. [1].

Force	Gauge boson	Multiplicity	Charge	Mass (GeV)
Electromagnetic	Photon (γ)	1	0	0
Weak (charged)	W bosons (W^\pm)	2	± 1	80.377 ± 0.012
Weak (neutral)	Z boson (Z)	1	0	91.188 ± 0.002
Strong	Gluons (g)	8	0	0
Higgs boson		1	0	125.25 ± 0.17

as fermions or bosons, depending on their spin. Fermions carry half-integer spin and adhere to Fermi-Dirac statistics [5, 6], which does not allow two particles to occupy the same quantum state (Pauli exclusion principle) [7]. This principle allows fermions to build complex structures such as atoms or nuclei, which are organized in varying energy levels governed by the quantum state of the particles. Bosons carry integer spin and adhere to Bose-Einstein statistics [8, 9], which allows multiple bosons to occupy the same quantum state. Bosons are the force carriers of the SM and as such are responsible for the interactions of fundamental particles like electromagnetic (EM) interactions.

1.1.1 Bosons and interactions

In the SM, three of the four fundamental forces are described, the EM force, the weak force, and the strong force. The gravitational force cannot be described by the SM. In Table 1.1 the bosons of the SM and some of their properties are summarized.

The EM force is mediated by photons γ . Photons are massless spin-1 particles without any charge. Their interactions are described in quantum electrodynamics (QED) as will be introduced in Section 1.2. The weak interaction is responsible for the decay of particles and is mediated by W^\pm and Z bosons. The W^\pm bosons have a charge of ± 1 and are the only known particles to change the flavor of fermions. Both, the W and Z bosons are massive, which is explained via the Higgs mechanism, introduced in Section 1.3.1. The W boson was introduced to describe the β -decay, which first was postulated by E. Fermi as a four-point contact interaction, but was not able to describe divergences in the cross section of the process [10]. The divergences were resolved by R. Feynman and M. Gell-Mann [11], introducing a Vector-Axialvector (V-A) theory [12], postulating the existence of massive, charged W bosons. The term V-A theory refers to the coupling structure of the theory, which encompasses a superposition of vector-like and axialvector-like interactions¹, which is a result of the electroweak unification. The EM and weak forces can be unified to the electroweak force via the Glashow-Salam-Weinberg model [13–15]. This unification describes all three bosons (W boson, Z boson, photon) and both forces, as will be explained in Section 1.2.1. The unified theory could not explain the origin of the mass of W and Z bosons, which was resolved by introducing the Higgs mechanism² as detailed

¹A vector-like coupling is invariant under parity transformation which changes the space-time coordinates x to $-x$, contrary to axial vector fields which change sign under parity transformation.

²The name of this mechanism is sometimes extended to give credit to further contributions to the concept. For example, Ref. [2] refers to the mechanism as NGAEBHGHKMP mechanism (Nambu-Goldstone-Anderson-Englert-Brout-Higgs-Gilbert-Hagen-Kibble-Migdal-Polyakov mechanism) [16–28]. While many publications contributed to the mechanism as it is described today, it will be referred to as Higgs mechanism in this thesis for readability purposes.

Table 1.2: **Leptons of the standard model.** The charge is given in units of elementary charge e . The third component of the weak isospin I_3 is indicated for the left-handed leptons. Right-handed leptons are isospin singlets with $I_3 = 0$. For each of the listed leptons, a corresponding antilepton exists with opposite charge. For antileptons, the right-handed component carries the indicated isospin while the left-handed component has $I_3 = 0$. All values are taken from Ref. [1].

Gen.	Particle	Charge	I_3	Mass (MeV)
1	Electron (e)	-1	-1/2	0.511
	Electron neutrino (ν_e)	0	1/2	$< 1.1 \cdot 10^{-6}$
2	Muon (μ)	-1	-1/2	105.7
	Muon neutrino (ν_μ)	0	1/2	< 0.19
3	Tau lepton (τ)	-1	-1/2	1776.86 ± 0.12
	Tau neutrino (ν_τ)	0	1/2	< 18.2

in Section 1.3.1 [16–28]. With the Higgs mechanism, the Higgs boson is introduced to the SM, which is a neutral scalar (spin-0) boson. By construction, the W and Z bosons obtained their masses through interactions with the Higgs field. From the same mechanism also the Higgs boson itself obtained its mass, which was first successfully measured at the LHC experiments ATLAS and CMS in 2012 [29, 30], thereby proving the existence of the Higgs mechanism. Finally, the SM also describes the strong interaction, which is responsible for the hadronization of particles and the formation of atomic nuclei. The force carrier of the strong force are gluons, which are massless particles carrying color charge and anticharge. The strong force is described via quantum chromodynamics (QCD), which is introduced in Section 1.4.

1.1.2 Fermions

The fermions of the SM can be classified into two groups, leptons and quarks. These groups are distinguishable via their interactions. For both groups three generations of particles are known, each consisting of two particles and two corresponding antiparticles. The distinction between particle and antiparticle is via the electric charge, which have opposite signs but the same absolute values. An overview of leptons (quarks) is given in Table 1.2 (Table 1.3).

Leptons are fermions that interact via the electroweak force, but not the strong force as they do not carry color charge. A generation of leptons consists of a charged lepton (electron, muon, tau), and a corresponding neutrino. The charged leptons all carry a charge of -1 , while the neutrinos are all neutral. Furthermore, all charged leptons have non-zero mass, while in the SM, the neutrinos are considered massless. The lepton of the first generation, the electron, is the lightest of the charged leptons, and is the only charged lepton that is stable. The other, heavier, leptons (muon and tau) decay into electrons via the charged current of the electroweak interaction (e.g. $\mu^- \rightarrow \nu_\mu (W^- \rightarrow e^- \bar{\nu}_e)$)³. Hence, electrons are one of the fundamental particles in atomic physics, responsible for the generation of atoms.

³This notation indicates the decay of a muon (μ^-) into a muon neutrino (ν_μ) and a W boson (W^-). The W boson then decays into an electron e^- and an electron antineutrino ($\bar{\nu}_e$).

Table 1.3: **Quarks of the standard model.** The charge is given in units of elementary charge e . The third component of the weak isospin I_3 is indicated for the left-handed fermions. Right-handed fermions are isospin singlets with $I_3 = 0$. For each of the listed quarks, a corresponding antiquark exists with opposite charge. For antiquarks, the right-handed component carries the indicated isospin while the left-handed component has $I_3 = 0$. All values are taken from Ref. [1].

Gen.	Particle	Charge	I_3	Mass (GeV)
1	Up quark (u)	2/3	1/2	$(2.16_{-0.26}^{+0.49}) \cdot 10^{-3}$
	Down quark (d)	-1/3	-1/2	$(4.67_{-0.17}^{+0.48}) \cdot 10^{-3}$
2	Charm quark (c)	2/3	-1/2	1.27 ± 0.02
	Strange quark (s)	-1/3	1/2	$(93.4_{-3.4}^{+8.6}) \cdot 10^{-3}$
3	Top quark (t)	2/3	-1/2	172.69 ± 0.30
	Bottom quark (b)	-1/3	1/2	$4.18_{-0.02}^{+0.03}$

Quarks are fermions that interact both with the electroweak and the strong force and are the only known fundamental particles that carry color charge. A generation of quarks consists of an up-type and down-type quark, where the up-type quarks have charge $+2/3$ and the down-type quarks charge $-1/3$. The first generation of quarks consists of the up quark and the down quark, which can be considered as ground states of the quark sector and primarily make up the nucleons (protons and neutrons), the building blocks of atomic nuclei. The second generation of quarks consists of charm and strange quarks, and the third generation consists of top and bottom quarks. The quarks of each generation are increasingly heavier, with the top quark being the heaviest fundamental particle of the SM carrying around the same weight as a gold atom. Quarks hadronize into hadrons, which are color-neutral combinations of quarks and antiquarks. At least two types of fundamental hadrons exist, mesons, which are a combination of a quark and antiquark (such as pions), and (anti)baryons, which are combinations of three (anti)quarks (such as protons and neutrons). This hadronization is explained through the color confinement property of QCD, discussed in Section 1.4. The top quark is special in this regard, as its large mass results in a short lifetime, shorter than the time scale of hadronization ($\sim 10^{-24}$ s). Hence, the top quark never hadronizes and decays as a free particle. Up-type quarks can be converted into down-type quarks (and vice-versa) via the electroweak interaction (e.g. $t \rightarrow b(W^+ \rightarrow q\bar{q}')$). With the introduction of the Higgs mechanism, the flavor and mass eigenstates of quarks are distinct, resulting in a mixing of quark flavors. This also allows for transitions of one generation into another generation, governed by the Cabibbo-Kobayashi-Maskawa matrix (CKM) [31, 32]. This matrix is a unitary 3×3 matrix and describes the transition probabilities of quarks to quarks of any of the three generations. This mechanism exhibits an intrinsic hierarchy, where transitions in the same generation are by far dominant relative to transitions into other generations. As a consequence, the top quark almost exclusively decays into a bottom quark, as especially the transition probabilities of the third generation (top and bottom quark) to the other generations are seen to be strongly suppressed. Due to the large mass difference, the bottom quark cannot decay into a top quark, and hence exhibits a (relatively speaking) long lifetime. This feature can be exploited for b tagging as described in Section 3.3.2. Some more aspects of the top quark will be discussed in Section 1.6.

1.2 The standard model as a gauge theory

Mathematically, the SM of particle physics is formulated as a relativistic quantum theory in which the elementary particles are described as quantum fields (quantum field theory). The quantum fields are described by Lagrangian densities

$$\mathcal{L} = \mathcal{L}[\psi, \partial_\mu \psi]. \quad (1.1)$$

These Lagrangian densities include the dynamics of the quantum fields and their interactions. Particles in the SM are described as excitations of the quantum fields, represented by quantum field operators $\psi[x]$, where x are four-dimensional space-time coordinates⁴. The Lagrangian density is also a function of the gradient of the field $\partial_\mu \psi[x]$, where $\partial_\mu = \partial/\partial x_\mu$ is the four-dimensional partial derivative w.r.t. x with $\mu = 0, 1, 2, 3$. The principle of stationary action, a fundamental principle in physics, describes the idea that nature always chooses the path which requires the least amount of energy. Mathematically, this is the path that minimizes the action \mathcal{S} , i.e. yields $\delta\mathcal{S} = 0$. The action of a Lagrangian density is defined as its integral,

$$\mathcal{S} = \int d^4x \mathcal{L}[\psi, \partial_\mu \psi]. \quad (1.2)$$

This is equivalent to the requirement that the Lagrangian density satisfies the Euler–Lagrange equation,

$$\frac{\partial \mathcal{L}}{\partial \psi} - \partial_\mu \frac{\partial \mathcal{L}}{\partial (\partial_\mu \psi)} = 0. \quad (1.3)$$

The components and features of the Lagrangian density can be illustrated based on the example of quantum electrodynamics (QED).

QED describes the dynamics and EM interactions of electrically charged particles and the photon. The description of QED was first formulated in works of S. Tomonaga [33], J. Schwinger [34, 35], R. Feynman [36–38], and F. Dyson [39, 40]. The Lagrangian density of a free fermion field (which can for example be an electron or a quark) with particle mass m can be postulated as [41]

$$\mathcal{L}_{\text{Dirac}} = \bar{\psi}(i\gamma^\mu \partial_\mu)\psi - m\bar{\psi}\psi. \quad (1.4)$$

Here, γ^μ is the four-dimensional vector of Dirac matrices and $\bar{\psi} = \psi^\dagger \gamma^0$ is the adjoint field. Essentially, the first term of the Lagrangian density describes the kinematic behavior of the field ψ , while the second term describes the particle at rest, quantified via its mass m . Using the Euler–Lagrange equation (1.3), this yields the Dirac equation [41] for a free fermion with mass m ,

$$(i\gamma^\mu \partial_\mu - m)\psi[x] = 0. \quad (1.5)$$

This description does not yet include any interaction of the field ψ . Such an interaction can be introduced by using Noether’s theorem [42], which postulates that every symmetry in nature corresponds to a conserved quantity, and vice versa⁵. The introduction of such symmetries transforms the quantum field theory of the SM into a gauge theory, acknowledging that the laws of physics should be invariant under certain transformations

⁴In some of the equations the functional dependence of $\psi[x]$ is omitted for the purpose of readability. Generally, it is assumed that each field, operator or phase is a localized quantity and hence a function of space-time coordinates x .

⁵A simple example of Noether’s theorem is for example the conservation of energy in nature, which originates in the symmetry of time translation, implying that the laws of nature are the same at every point in time.

1 The standard model of particle physics

(gauge transformations). In QED, a local phase $\theta[x]$ can be introduced [43], transforming the fermion field $\psi[x]$ as

$$\psi[x] \rightarrow e^{i\theta[x]} \psi[x], \quad (1.6)$$

$$\bar{\psi}[x] \rightarrow e^{-i\theta[x]} \bar{\psi}[x]. \quad (1.7)$$

This local phase $\theta[x]$ describes rotations of $\psi[x]$ at the space-time coordinate x . Following the principle of gauge transformations and symmetries, this phase should not change the underlying laws of physics. For QED, the simplest transformation fulfilling this requirement is the U(1) symmetry group, i.e. a one-dimensional unitary group consisting of all complex numbers with absolute value of one. All elements of the group can be expressed via its generator, here $e^{i\theta[x]}$. Inserting the transformation of $\psi[x]$ into eq. (1.4) shows that the Lagrangian density is at first not invariant against this transformation, as an additional term $-\bar{\psi}\gamma^\mu\psi\partial_\mu\theta[x]$ is obtained. This can be resolved by adding the interaction with an additional field $A_\mu[x]$ to the Lagrangian density,

$$\mathcal{L}_{\text{QED}} = \bar{\psi}(i\gamma^\mu\partial_\mu)\psi - m\bar{\psi}\psi - qA_\mu\bar{\psi}\gamma^\mu\psi. \quad (1.8)$$

The introduced field A_μ is a vector field and can be associated with the EM photon field. The electric charge q is introduced as a conserved quantity, following the postulate in Noether's theorem [42], and describes the strength of the interaction of the fermion field ψ with the vector field A_μ . Generally, terms such as $X_\mu\bar{\psi}\Gamma^\mu\psi$ can be identified as the interaction of a particle ψ with a field X_μ , this will be illustrated later in Section 1.5. Here, Γ^μ indicates a generic combination of γ matrices. In the specific case of A_μ and the fermion fields ψ , this interaction is a vector-like interaction, indicated by the γ^μ matrix in the coupling term. In order to retain the gauge invariance, the photon field has to transform as

$$A_\mu[x] \rightarrow A_\mu[x] - \frac{1}{q}\partial_\mu\theta[x]. \quad (1.9)$$

With both these gauge transformations, the Lagrangian density in eq. (1.8) is invariant. Alternatively, the partial derivative ∂_μ can also be replaced with the gauge covariant derivative

$$\mathcal{D}_\mu = \partial_\mu + iqA_\mu[x], \quad (1.10)$$

yielding the same invariance behavior. The additional term in eq. (1.8) describes the interaction of photons and fermions proportional to the electric charge q of the fermion. What is not yet included in this equation is the description of the propagation (i.e. kinematics) of the photon field. By construction, the field $A_\mu(x)$ is a boson field with spin-1, whose equation of motion is described by the Proca equation,

$$(\partial_\mu\partial^\mu - m_A^2)A^\nu = 0, \quad (1.11)$$

corresponding to the Lagrangian density

$$\mathcal{L}_{\text{Proca}} = -\frac{1}{4}F^{\mu\nu}F_{\mu\nu} + \frac{1}{2}m_A^2A^\nu A_\nu. \quad (1.12)$$

Here, $F^{\mu\nu} = (\partial^\mu A^\nu - \partial^\nu A^\mu)$ is the field strength tensor, which describes the EM field components at space-time point x and their derivatives w.r.t. space and time. In eq. (1.12), again, the first term can be associated with the kinetics of the vector field and the second term with the particle of the field at rest, quantified by its mass m_A .⁶ This is a generalized

⁶Note the difference in the mass term for bosons, $m^2X_\mu X^\mu$, and fermions, $m\bar{\psi}\psi$. These terms have quadratic mass dependence for bosons and linear mass dependence for fermions.

description of a vector field. Adding eq. (1.12) to the QED Lagrangian in eq. (1.8) shows that the first term (the kinetic term) is indeed invariant under the U(1) transformation while the second one (the mass term) is not. This implies for QED that the particle associated with the photon field (i.e. the photon) has to be massless such that the second term vanishes and the gauge invariance is retained. In summary, this yields the full QED Lagrangian density

$$\mathcal{L}_{\text{QED}} = \bar{\psi}(i\gamma^\mu \partial_\mu)\psi - m\bar{\psi}\psi - qA_\mu\bar{\psi}\gamma^\mu\psi - \frac{1}{4}F^{\mu\nu}F_{\mu\nu}. \quad (1.13)$$

In a similar manner the Lagrangian densities of the electroweak unification and quantum chromodynamics (QCD) can be described, which is included in the remainder of this chapter.

1.2.1 Electroweak unification

The weak interaction can in principle be introduced to the SM similar to the EM interaction. Measurements such as the Wu experiment [44], however, showed that the weak force, mediated by W and Z bosons, behaves somewhat differently than the EM force. It was observed that the charged current of the weak interaction, i.e. the force mediated by W bosons, only interacts with left-handed fermions and right-handed antifermions (i.e. the chirality states). The chiral symmetry is described via the $\gamma^5 = i\gamma^0\gamma^1\gamma^2\gamma^3$ operator. It can be used to project the left- and right-handed parts of the fermion field ψ , as

$$\psi_{\text{L}} = \frac{1}{2}(1 - \gamma^5)\psi, \quad (1.14)$$

$$\psi_{\text{R}} = \frac{1}{2}(1 + \gamma^5)\psi. \quad (1.15)$$

Following the results of the Wu experiment [44] the charged current of the weak interaction is shown to only act on the left-handed parts of ψ , i.e. only on ψ_{L} . At the same time, the EM interaction still acts indistinguishably on left- and right-handed fermion fields. Therefore, this requires a modification of the previously introduced QED Lagrangian density and transformation behavior in order to encompass both features. This is referred to as the electroweak unification and was first described via the Glashow-Salam-Weinberg theory [13–15].

The gauge transformation that can describe the required behavior is the $\text{SU}(2)_{\text{L}} \times \text{U}(1)_{\text{Y}}$ group. The U(1) group is already known from Section 1.2, but has a different conserved quantity here, namely the hypercharge $Y = 2(q - I_3)$, where I_3 is the third component of the weak isospin⁷. The $\text{SU}(2)_{\text{L}}$ group is the special unitary group consisting of complex 2×2 matrices that have a determinant of one. These matrices describe rotations in three-dimensional space, e.g. via the three Pauli matrices σ^i . The index L indicates that this group only acts on the left-handed spinor ψ_{L} . The conserved quantity of the $\text{SU}(2)_{\text{L}}$ group is the weak isospin I . Following the explanations of gauge transformations in Section 1.2, two gauge transformations can now be introduced for the electroweak Lagrangian density via covariant derivatives

$$\mathcal{D}_\mu\psi_{\text{L}} = \partial_\mu\psi_{\text{L}} - \frac{i}{2}\left(g'YB_\mu + g\sigma^iW_\mu^i\right)\psi_{\text{L}}, \quad (1.16)$$

$$\mathcal{D}_\mu\psi_{\text{R}} = \partial_\mu\psi_{\text{R}} - \frac{i}{2}\left(g'YB_\mu\right)\psi_{\text{R}}. \quad (1.17)$$

⁷Note that this conserved quantity is still related to the electric charge which was introduced previously as the conserved quantity of QED. The weak isospin itself is a more abstract concept, it is an additional quantum number to classify the behavior of different particles.

1 The standard model of particle physics

Here, g' is the coupling strength of the U(1) group and g the coupling strength of the SU(2) group. This construction results in three vector fields W_{μ}^i , only acting on the left-handed spinor, and another vector field B_{μ} acting homogeneously on both spinor projections. The Lagrangian density can be constructed for this gauge group as

$$\mathcal{L}_{\text{EW}} = \bar{\psi}_{\text{L}}(i\gamma^{\mu}\mathcal{D}_{\mu})\psi_{\text{L}} + \bar{\psi}_{\text{R}}(i\gamma^{\mu}\mathcal{D}_{\mu})\psi_{\text{R}} - \frac{1}{4}W_{\mu\nu}^i W^{i,\mu\nu} - \frac{1}{4}B_{\mu\nu}B^{\mu\nu}, \quad (1.18)$$

where $W^{i,\mu\nu}$ ($i = 1, 2, 3$) are the field strength tensors of the weak isospin following

$$W^{i,\mu\nu} = \partial^{\mu}W^{i,\nu} - \partial^{\nu}W^{i,\mu} + g\epsilon_{ijk}W^{j,\mu}W^{k,\nu}, \quad (1.19)$$

and $B^{\mu\nu}$ the field strength tensor of the hypercharge defined analog to $F^{\mu\nu}$ in Section 1.2. The last term in eq. (1.19) implies that a contraction of $W_{\mu\nu}^i W^{i,\mu\nu}$ in the Lagrangian density of eq. (1.18) would yield cubic and quartic terms of W_{μ}^i which are interpreted as cubic or quartic self-interactions of the gauge bosons. Such a term is not present for $F^{\mu\nu}$ or $B^{\mu\nu}$, as the U(1) group is an abelian (commutative) gauge group, while the SU(2) group is non-abelian (non-commutative). In non-abelian groups, the order of operations is relevant and the operators do not commute.

Altogether, this transformation behavior fulfills the requirements set towards the theory, i.e. is maximally parity violating. In other words, the interaction of a particle changes depending on the parity of the coordinate system. If one would perform a parity operation, i.e. changing the space-time coordinates x to $-x$, the interactions of particles would change as this parity operation is equivalent to changing the chirality of particles. The theory yields four gauge fields, from which the physical gauge bosons of the electroweak interaction can be obtained from linear combinations,

$$W_{\mu}^{\pm} = \frac{1}{2}(W_{\mu}^1 \mp iW_{\mu}^2), \quad (1.20)$$

and

$$Z_{\mu} = \cos\theta_{\text{W}}W_{\mu}^3 - \sin\theta_{\text{W}}B_{\mu}, \quad (1.21)$$

$$A_{\mu} = \sin\theta_{\text{W}}W_{\mu}^3 + \cos\theta_{\text{W}}B_{\mu}. \quad (1.22)$$

The first equation describes the W boson fields responsible for charged current interactions. From the other equations, two neutral current mediators are obtained, one being the photon field A_{μ} and the other the Z boson field Z_{μ} . These neutral fields are mixed states of the W_{μ}^3 and B_{μ} fields rotated via the Weinberg angle θ_{W} , related to the coupling strengths g and g' via

$$\cos\theta_{\text{W}} = \frac{g}{\sqrt{g^2 + g'^2}}, \quad \text{and} \quad \sin\theta_{\text{W}} = \frac{g'}{\sqrt{g^2 + g'^2}}. \quad (1.23)$$

Experimentally, the force carriers of the weak interaction, the W and Z bosons, are proven to be massive, but the construction in eq. (1.18) does not allow for mass terms of the gauge fields W_{μ}^i and B_{μ} . This problem will be addressed in the following section.

1.3 Spontaneous symmetry breaking and the origin of masses

The theory of electroweak unification predicts massless gauge bosons by construction in order to retain its gauge invariance (see discussions of the QED gauge invariance in

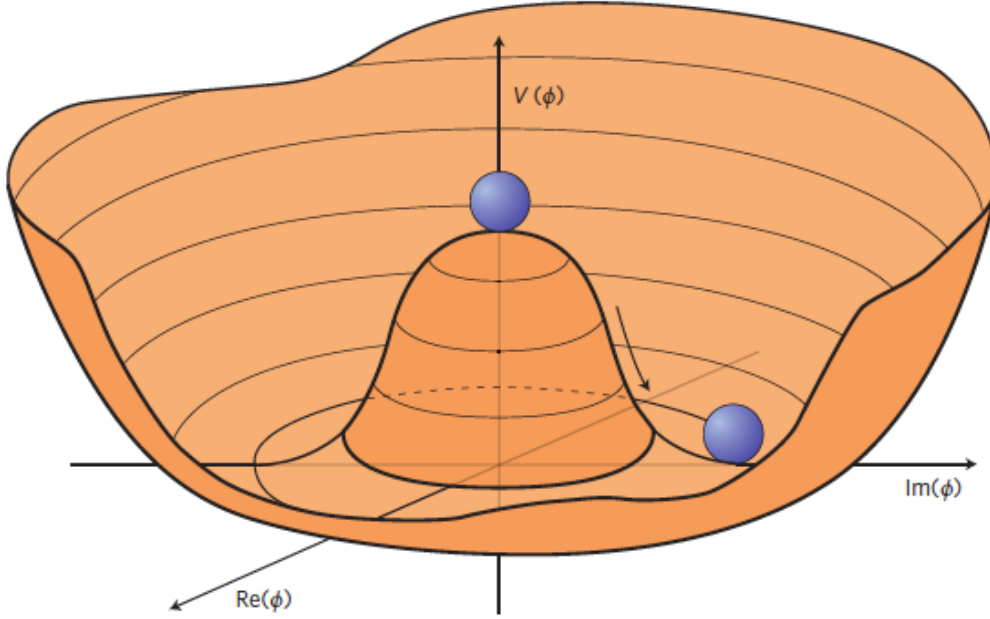


Figure 1.1: **Illustration of the Higgs potential.** The Higgs potential of eq. (1.25) is shown for $\mu^2 < 0$. The minimum of the potential is at $|\phi|^2 = -\mu^2/(2\lambda)$. From Ref [2].

Section 1.2). This is unproblematic for the massless photon, but poses an issue for the W and Z bosons. Furthermore, massive fermions would break the gauge invariance of SU(2) in the formulation of the previous section due to the maximal parity violating nature of the charged current of the weak force. The first problem is solved by introducing a spontaneous symmetry breaking mechanism in which the electroweak gauge symmetries are retained but are not present in the energetic ground state of the system, allowing for the introduction of non-zero boson masses. This spontaneous symmetry breaking is described via the Higgs mechanism [16–28]. The second problem is addressed by introducing the coupling of the Higgs field to the fermions which generate the fermion masses.

1.3.1 The Higgs mechanism

The concept of spontaneous symmetry breaking describes the process in which a physical system is symmetrical in its initial state, but by introducing small perturbations this symmetry is broken. This can be illustrated with the example of a ball lying on the apex of a perfectly symmetrical hill (see illustration in Figure 1.1). In its equilibrium this system is symmetrical. As the system is unstable (i.e. small perturbations will break the system) the ball will at some point roll down the hill in any random direction, until the ball (i.e. in this analogy the physical system) reaches its stable ground state. This (random) process defines the initially degenerate ground state, as the ball did roll down the hill in a specific direction, and thus the symmetry of the system is broken. Such a process can be introduced to the electroweak Lagrangian density in eq. (1.18) by adding a spin-0 field, which will be identified with the Higgs field ϕ . Such a field obeys the equation of motion given by the Klein-Gordon equation, yielding a Lagrangian density of

$$\mathcal{L}_{\text{Higgs}} = (\mathcal{D}_\mu \phi)^\dagger (\mathcal{D}^\mu \phi) - V[|\phi|^2]. \quad (1.24)$$

Here, V is the potential of the Higgs field ϕ . In order to retain the invariance of the SU(2)_L × U(1)_Y gauge group, this scalar field has to be an isospin doublet with $Y = 1$,

1 The standard model of particle physics

$\phi = (\phi^+, \phi^0)^T$. From this construction, one component of the doublet is charged (ϕ^+) and the other is neutral (ϕ^0). The potential of the Higgs field has to take the form

$$V[|\phi|^2] = \mu^2|\phi|^2 + \lambda|\phi|^4, \quad (1.25)$$

constructed such that the degenerate ground states are non-zero. This is illustrated in Figure 1.1. As the possible ground states are degenerate, the ground state can be chosen such that it matches the requirements of the gauge symmetry⁸. For this case, a ground state ϕ_0 and corresponding vacuum expectation value (VEV) v are chosen to be

$$\phi_0[x] = \frac{1}{\sqrt{2}} (0, v + H[x])^T, \quad \text{with } v = \sqrt{-\mu^2/\lambda} \quad \text{and } \mu^2 < 0. \quad (1.26)$$

In this ground state, the charged component of the field ϕ is zero, which matches the observation that the Higgs boson field is neutral. In this construction, the field is described via its ground state v and small excitations around the ground state, $H[x]$, which can be identified as the Higgs boson. Introducing ϕ_0 to eq. (1.24) yields a range of interesting terms which can be associated with different interactions and particles. From the potential V , for example, a term $\lambda v^2 H^2$ arises, which is a mass term for the Higgs boson, yielding its mass $m_H = \sqrt{\lambda v^2}$. From the potential V also terms cubic and quartic in $H(x)$ arise, which correspond to the cubic and quartic self-coupling of the Higgs boson. From the kinetic terms in eq. (1.24), interactions of the Higgs field and the gauge bosons arise, also containing the mass terms of the gauge bosons, leading to $m_W = gv/2$ and $m_Z = m_W/\cos\theta_W$. From the explicit choice of the ground state of the Higgs field (by construction) no mass terms for the photon field A_μ are obtained. The masses of the bosons are degrees of freedom of the SM, cannot be determined from first principles and require explicit measurements. The degrees of freedom from Higgs, W, and Z boson masses can alternatively be expressed through the coupling strengths λ , g , and g' .

1.3.2 Fermion masses

With the introduction of the spontaneous symmetry breaking mechanism and the Higgs field, fermion masses would still break gauge invariance under SU(2), hence an additional mechanism has to be introduced in order to explain the massive fermions. As the Higgs field is responsible for the generation of boson masses, a mechanism is introduced that explains the origin of the fermion masses also via the interaction with the Higgs field. This interaction is called Yukawa interaction [47], constituting a linear coupling of the Higgs field ϕ with the fermion fields ψ ,

$$\mathcal{L}_{\text{Yukawa}} = -y_f (\bar{\psi}_L \phi \psi_R + \bar{\psi}_R \phi^\dagger \psi_L). \quad (1.27)$$

Here, y_f is the coupling constant for fermion f . The fermion spinors are introduced with their left-handed (isospin doublet) and right-handed (isospin singlet) projections as this retains the SU(2) symmetry⁹. As an example, the mass generation can be shown for the electron. By introducing the explicit form of the fermion fields and the Higgs field ϕ , one obtains

$$\mathcal{L}_{\text{Yukawa},e} = -\frac{1}{\sqrt{2}} y_e (\bar{\nu}_e, \bar{e}_L) (0, v + H)^T e_R + \text{h.c.} \quad (1.28)$$

This results in one term $-\frac{y_e}{\sqrt{2}} \bar{e}_L e_R$, from which the mass of fermions can be inferred as $m_e = y_e v/\sqrt{2}$. From this mechanism, the mass of the fermions is determined by the

⁸By choosing a different ground state one could for example also construct a theory that predicts a non-zero mass of the photon, or a charged Higgs boson.

⁹Note that this interaction changes the chirality eigenstate of the particle which is unique to this interaction.

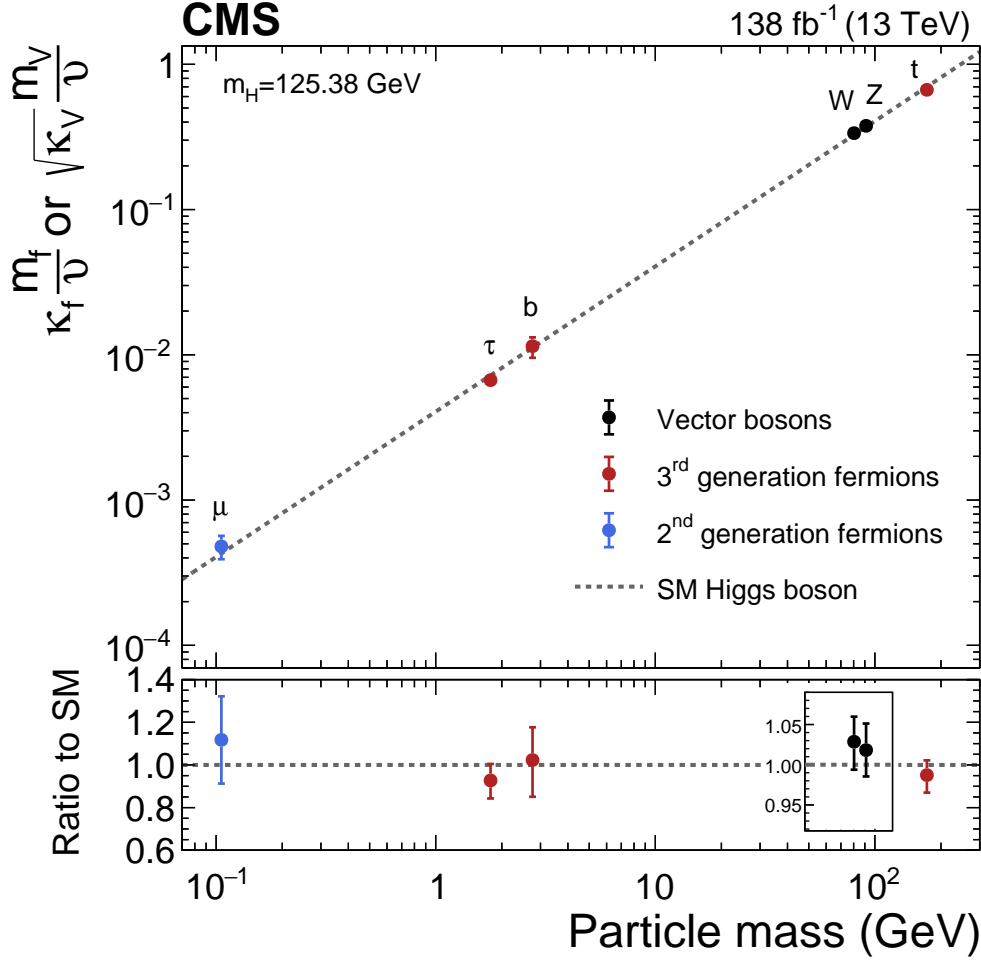


Figure 1.2: **Coupling of fermions and bosons to the Higgs field.** Shown are the measurements by the CMS Collaboration. The horizontal axis shows the mass of the particles. The vertical axis shows a value proportional to the coupling modifier κ_f for fermions and the square root of the coupling modifier κ_V for the gauge bosons. The coupling modifiers are defined via the κ -framework [45], in which all SM predictions are scaled via κ^2 values to quantify deviations from the SM expectations of $\kappa = 1$. The SM expectation is indicated as a diagonal dashed line. From Ref [46].

Yukawa coupling constant y_f and the VEV v . Again, the masses (or alternatively y_f) are not determined by the theory but have to be measured experimentally.

A second term in eq. (1.28), which is proportional to $m_e \bar{e}_L H e_R$ constitutes the coupling of the fermion (here electron) to the Higgs boson. No other interactions of fermions and the Higgs bosons or Higgs field are predicted by this formalism unlike for the bosons where also quartic interactions (e.g. $WWHH$) are predicted. The measurement of the coupling of the fermions (and bosons) to the Higgs boson is an active field of study. While the coupling of the heaviest fermions to the Higgs boson has been established already, the couplings to lighter fermions still have to be measured. Due to the linear dependence of the Yukawa coupling strength to the mass of the fermion, the coupling measurements of lighter fermions are more difficult, as the small coupling strength is translated to lower rates of the process of interest. In Figure 1.2, the current state of coupling measurements of fermions and bosons to the Higgs boson is shown.

1.4 Quantum chromodynamics

Quantum chromodynamics is another aspect of the SM, describing the strong force which acts exclusively on color-charged particles, i.e. quarks. The concepts of QCD were first introduced by M. Gell-Mann [48, 49] and G. Zweig [50]. Similar to the other symmetries, the color symmetry is obtained from a gauge group, here SU(3). This symmetry group is, analog to SU(2), a special unitary group, here consisting of complex 3×3 matrices that have a determinant of one. The group can be expressed via the eight Gell-Mann matrices λ^a . The gauge transformation of QCD is introduced via the covariant derivative

$$\mathcal{D}_\mu = \partial_\mu - i\sqrt{4\pi\alpha_s} \lambda^a G_\mu^a, \quad (1.29)$$

where α_s is the strong coupling constant and G_μ^a the gauge fields of QCD. The associated field strength tensor of the gauge fields is

$$F_{\mu\nu}^a = \partial^\mu G_\nu^a - \partial_\nu G_\mu^a + \sqrt{4\pi\alpha_s} f_{abc} G_\mu^b G_\nu^c. \quad (1.30)$$

Similar to the field strength tensor of SU(2) in eq. (1.19), $F_{\mu\nu}^a$ contains self-interactions, indicated by the non-vanishing term $\sqrt{4\pi\alpha_s} f_{abc} G_\mu^b G_\nu^c$. The fields G_μ^a can be identified as eight gluon fields. From eq. (1.30), cubic and quartic self-interactions of gluons are expected. This self-interaction leads to the confinement property of QCD [51–53]. Due to the gluon self-interactions, strings of gluons are formed between quarks. As two quarks are pulled apart, a flux tube of gluons is formed between the quarks. With increasing distance between the quarks the energy stored in these flux tubes increases until the energy becomes large enough to create a new pair of quarks which form bound states with the already existing quarks. This essentially prevents single quarks from existing as they rather form color-neutral hadrons.

The Lagrangian density of QCD, following the introductions above, is given as

$$\mathcal{L}_{\text{QCD}} = \bar{\psi}(i\gamma^\mu \partial_\mu)\psi - m\bar{\psi}\psi + \sqrt{4\pi\alpha_s} \bar{\psi}\gamma^\mu \lambda^a \psi G_\mu^a - \frac{1}{4} F^{a,\mu\nu} F_{\mu\nu}^a. \quad (1.31)$$

Here, ψ is a vector of quark spinors where each entry has one of the colors red, green and blue, and all entries have the same quark flavor (one of up, down, strange, charm, bottom, top). In QCD, the mass term $m\bar{\psi}\psi$ does not break the gauge invariance under SU(3) transformations. However, quarks also participate in the electroweak interactions introduced in Section 1.2.1 where the mass terms are not gauge invariant under SU(2) transformations. Hence, the quark masses are also obtained from interactions with the Higgs field via the Yukawa-type interactions introduced in Section 1.3.2. It is worth noting, however, that the SU(3) symmetry remains intact and hence no mass terms for gluons are obtained.

With QCD, this completes the gauge theoretical description of the SM as it is known today. In summary, the SM is described via the $U(1)_Y \times SU(2)_L \times SU(3)_c$ gauge group.

1.4.1 Running couplings

The coupling constants introduced in the previous sections are misnomered as the coupling strengths are not constant. The coupling strengths depend on the energy scale Q^2 at which the interaction takes place. This effect is most pronounced in the strong coupling, governed by the coupling strength α_s . Due to the self-interaction of the gluon fields, and vacuum fluctuations, each color-charged particle is always surrounded by a cloud of gluons, which effectively screen or enhance the color charge of the particle. The

self-interactions of gluons manifest by spontaneously creating gluon pairs from the vacuum. At the same time, the coupling of gluons to quarks spontaneously creates quark-antiquark pairs from the vacuum¹⁰. To account for this effect, couplings depending on α_s can be perturbatively expanded in α_s if $\alpha_s \ll 1$. Divergences at large momenta Q can appear in these expansions as higher orders in α_s are neglected. To counter this, cut-off scales μ are introduced, called renormalization scales. The term renormalization refers to one of the principles of quantum field theory, which states that each theory has to be renormalizable, i.e. has to yield finite values (sometimes after introducing additional, non-physical scales for that purpose), as otherwise, the theory becomes meaningless in the limits where it diverges. After introducing the renormalization scale, the observables calculated at finite orders of perturbation theory (such as the cross section) become dependent on μ . This dependency is non-physical as a calculation of the observable under scrutiny to all orders of perturbation theory would remove the dependency on μ . The running of the coupling can be expressed via renormalization group equations. The solutions of these differential equations relate the observable at one energy scale Q to a reference scale Λ . Hence, once an observable is known at one scale Λ , it can be related to an arbitrary scale Q . For the strong coupling constant this yields (at the precision of subleading order in α_s)

$$\alpha_s[Q^2] = \frac{\alpha_s[\Lambda^2]}{1 + \beta_0 \alpha_s[\Lambda^2] \ln(Q^2/\Lambda^2)}. \quad (1.32)$$

The so-called one-loop beta function β_0 is calculated as [51, 54]

$$\beta_0 = \frac{11N_c - 2N_q}{12\pi}, \quad (1.33)$$

with N_q the number of active quark flavors at a given energy scale¹¹, and N_c the number of colors. For the SM, where $N_c = 3$ and $N_f \leq 6$, it follows $\beta_0 > 0$, i.e. indicating that α_s decreases at higher energy scales Q (or smaller distances) with $\propto 1/(1 + \ln(Q^2/\Lambda^2))$. The two terms of β_0 can be associated with the two aforementioned screening effects of color charge from vacuum fluctuations. The first term corresponds to the gluon pairs and the second term corresponds to quark-antiquark pairs. Due to the relative sign between these contributions, this can be interpreted such that the gluons increase, i.e. enhance, the effective color charge with increasing distances (or decreasing energies) and the quark-antiquark vacuum fluctuations decrease, i.e. screen, the effective color charge. Altogether, in the limit of high energy, this leads to the asymptotically free behavior of color-charged particles. In this limit, the coupling strength $\alpha_s[Q^2]$ is very small, and thus color charged particles behave as if they were free particles. On the other side of the spectrum, at lower energy scales Q this leads to the confinement property of QCD as discussed before. In cases where the coupling strength α_s becomes too large, a perturbative expansion in α_s is no longer possible. This regime is referred to as the non-perturbative regime of QCD where for example the hadronization of color-charged particles is calculated (see Section 5.4). In Figure 1.3 a summary of recent measurements of α_s at different energy scales Q is shown.

1.5 Cross sections and Feynman diagrams

As detailed in the previous sections, interactions of particles in the SM can be identified in the Lagrangian density as terms with a product of at least three fields. The cross section

¹⁰In QED, such a screening also exists, but due to the missing self-interaction of photons, only a screening of the EM charge via vacuum fluctuations of particle-antiparticle pairs is present.

¹¹For example below the energetic threshold of bottom quarks, only four active flavors are present, namely up, down, strange, and charm.

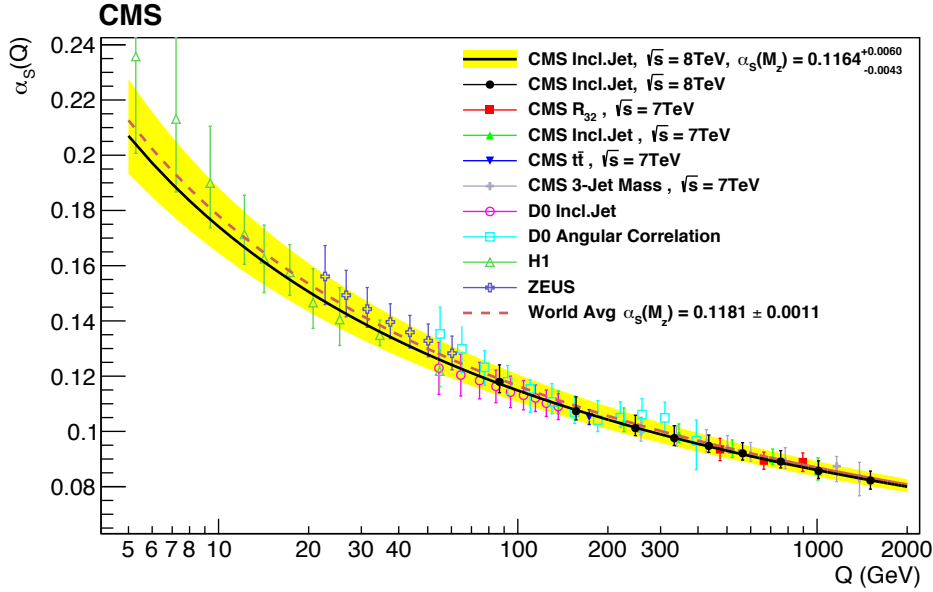


Figure 1.3: **Running of strong coupling.** Measurements of the strong coupling constant as a function of energy scale Q by different experiments. From Ref [55].

(i.e. the probability) of a certain process or interaction depends on the matrix element $|\mathcal{M}_{i \rightarrow f}|^2$, which encompasses the transition probability of an initial state i to a final state f . The transition probability $\Gamma_{i \rightarrow f}$ is defined via Fermi's golden rule [56]

$$\Gamma_{i \rightarrow f} = 2\pi\rho|\mathcal{M}_{i \rightarrow f}|^2, \quad (1.34)$$

where ρ is the available phase space of the final state f . This can be related to the cross section $\hat{\sigma}$ via integration over the available phase space. In essence, Fermi's golden rule states that the probability of a process is proportional to the coupling strengths of the (multiple) interactions, encoded in the matrix element, as well as the energy difference between initial and final states, encoded in the phase space. To calculate a cross section, all possible transition amplitudes (i.e. matrix elements) between initial state and final state have to be taken into account. Feynman diagrams can be used as an illustration of the processes on the level of particles and interactions, but primarily act as visualization of mathematical expressions for the calculation of scattering amplitudes. When the coupling constants are small, i.e. in the regime of asymptotic freedom at high energies, the cross section or the matrix element can be expressed as a perturbative series expanded in the coupling constant α . In terms of the Feynman diagrams that contribute to \mathcal{M} , this corresponds to sorting all possible diagrams by the number of vertices. In that ordering, the diagrams with the smallest number of interaction vertices are referred to as leading order (LO). This order of perturbation already gives a first approximation of the exact value of \mathcal{M} , as the following contributions are subdominant due to the suppression in higher orders of α . The subleading order of perturbation is referred to as next-to-leading order (NLO). For a better approximation of the cross section, higher orders of the perturbative series have to be calculated. The precision of LO cross section calculation is mostly insufficient considering the level of precision of cross section measurements at the LHC. Calculation of higher orders in the perturbative expansion becomes more complicated as both the number of possible diagrams increases exponentially, and the difficulty to calculate each single diagram increases.

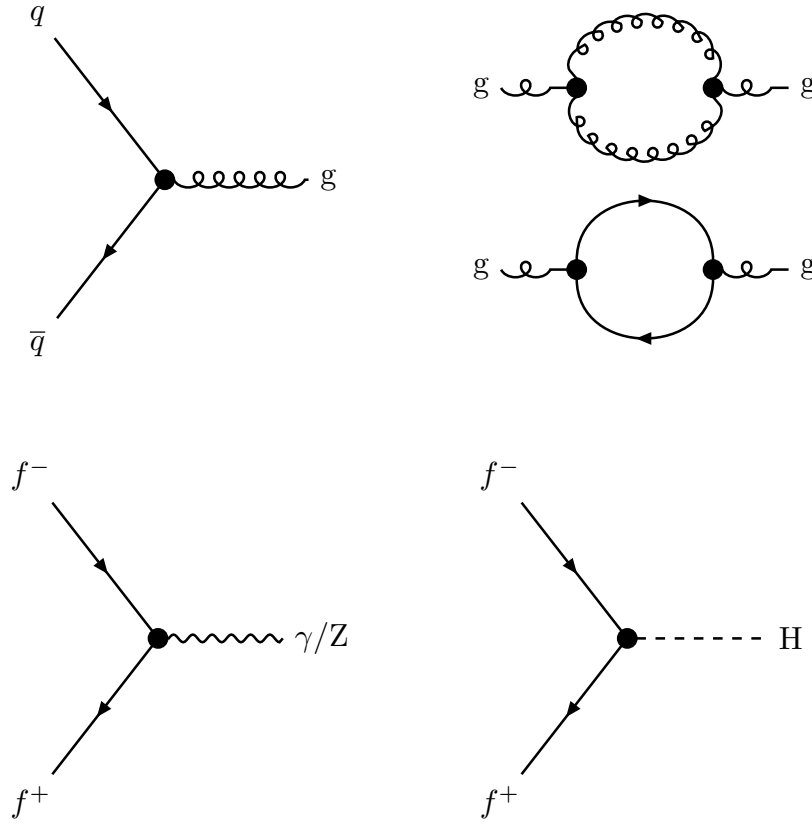


Figure 1.4: Illustration of some interactions and couplings of the standard model.

A few examples of SM interactions are illustrated in Figure 1.4 as schematic Feynman diagrams. In the first row, the first diagram shows the interaction of a quark-antiquark pair and a gluon, which is obtained from eq. (1.31) and is proportional to $\sqrt{\alpha_s}$.¹² Such an interaction is important for the description of the $t\bar{t}b\bar{b}$ process which will be discussed in more detail in this thesis (e.g. Section 7.2). If inverted, i.e. with a gluon in the initial state decaying to a pair of quarks ($g \rightarrow q\bar{q}$), this process describes the dominant mechanism for a production of a bottom quark-antiquark pair ($b\bar{b}$), which in association with a top quark-antiquark pair ($t\bar{t}$) yields the $t\bar{t}b\bar{b}$ process. The two diagrams on the top right are the two processes discussed in Section 1.4.1, where either a pair of gluons (top) or a quark-antiquark pair (bottom) is created from vacuum fluctuations and therewith induces the running of the coupling strength α_s . In the second row, the first diagram depicts a coupling of a charged fermion (such as an electron or a top quark) with a neutral gauge boson (γ or Z), as is for example present in eq. (1.13) for the photon field ($qA_\mu\bar{\psi}\gamma^\mu\psi$). The last diagram shows the coupling of fermions to the Higgs boson which is the Yukawa interaction introduced in eq. (1.27), proportional to the fermion masses ($m\bar{\psi}\psi$). These two diagrams are for example part of the background processes present in the measurements of this thesis. The first diagram can describe the production of a Z boson with a top quark, and the second diagram the production of a Higgs boson with a top quark. Adding this to the production of $t\bar{t}$ can yield the $t\bar{t}H$ and $t\bar{t}Z$ background processes.

¹²Note that the cross sections $\hat{\sigma}$ are proportional to $|\mathcal{M}|^2$, and therefore scale with α_s .

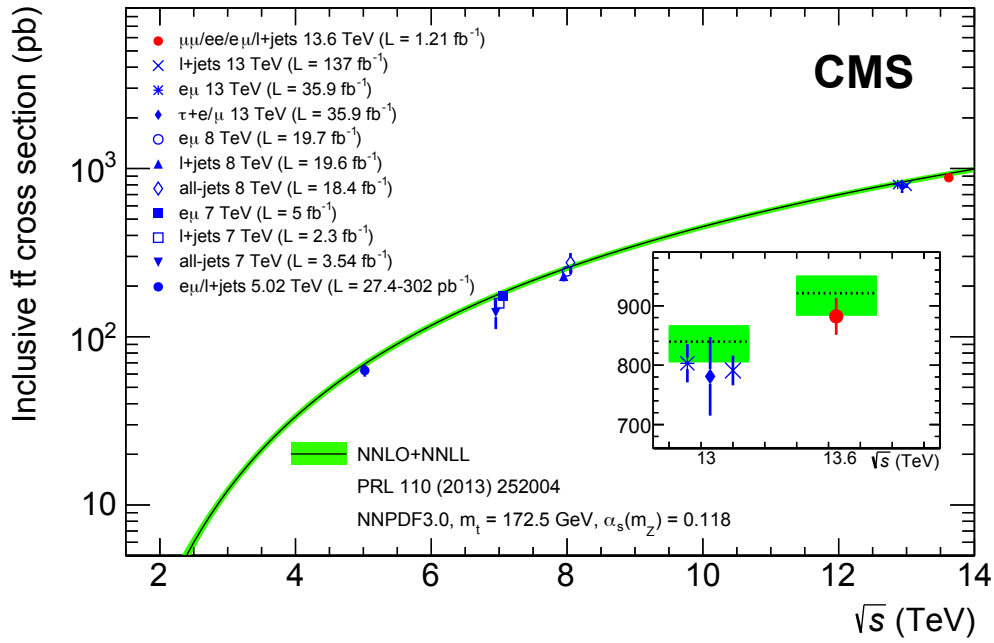


Figure 1.5: Cross section of $t\bar{t}$ production as a function of the center-of-mass energy at the CMS experiment. The blue and red points each constitute an independent measurement and the green band indicates the SM predictions calculated in Ref. [59]. From Ref. [60].

1.6 The physics of top quarks

For the measurements presented in this thesis, the top quark plays a special role. The processes that are analyzed consist of a top quark antiquark pair ($t\bar{t}$) in association with additional hadronic radiation. The top quark is with a mass of $m_t = 172.69 \pm 0.30$ GeV [1] the heaviest known particle of the SM. The top quark was discovered by the CDF and D0 Collaborations at the Tevatron collider [57, 58] (both targeting $t\bar{t}$ events), and its properties such as mass and spin correlations have since been measured extensively. The top quark is also well suited for some measurements of Higgs boson properties and couplings, as the high mass of the top quark results in a large coupling strength between Higgs boson and the top quark. The value of the Yukawa coupling y_t is of the order of one, following $y_t = \sqrt{2}m_t/v \approx 1$, where the VEV is $v \approx 246$ GeV [1]¹³.

1.6.1 Top quark pair production

The dominant production mechanism for top quarks at hadron colliders is top quark pair production ($t\bar{t}$). Figure 1.5 shows measurements of the inclusive $t\bar{t}$ cross section as a function of the center-of-mass energy \sqrt{s} at the CMS experiment. With increasing \sqrt{s} , the production cross section of $t\bar{t}$ also increases, as the available phase space for $t\bar{t}$ production increases¹⁴. Example Feynman diagrams for the production of a $t\bar{t}$ pair are shown in Figure 1.6. The diagram on the top left shows an example of $t\bar{t}$ production at LO via $g g \rightarrow t\bar{t}$, which contains two QCD coupling vertices $\sim \sqrt{\alpha_s} \bar{\psi} \gamma^\mu \lambda^a \psi G_\mu^a$ (from eq. (1.31)). Based on

¹³The value of the VEV can be obtained from measurements of the muon lifetime, in which the Fermi constant G_F is determined. This constant is related to the VEV as $v = \sqrt{2/G_F}$.

¹⁴The top quarks are heavy, so the constituents of the proton-proton collision have to carry a significant fraction of the proton momentum in order to yield enough energy to produce a pair of top quarks.

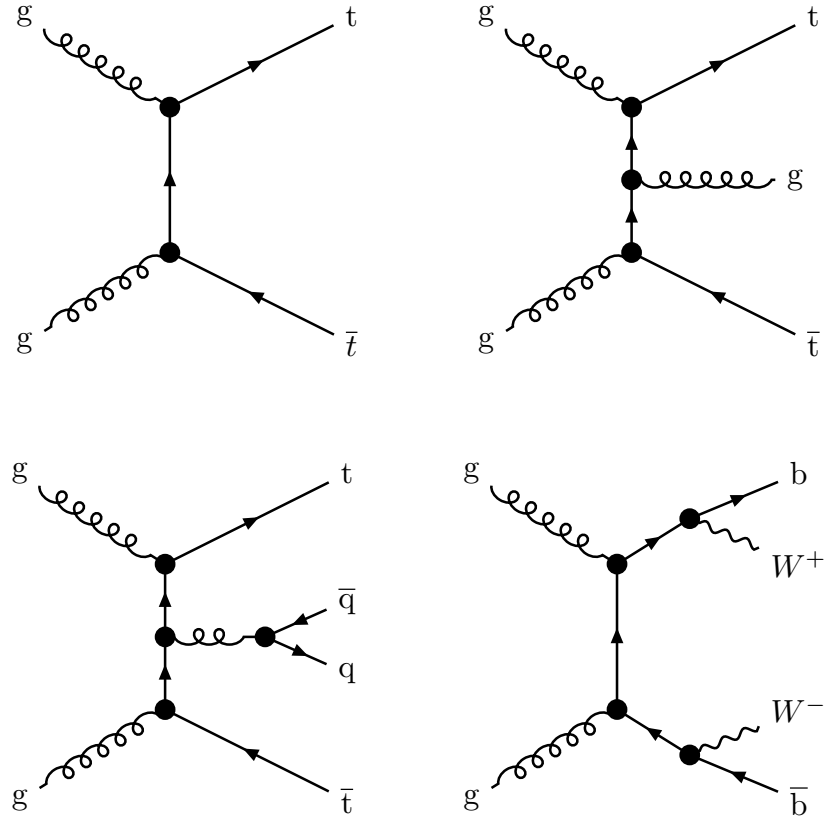


Figure 1.6: **Illustration of $t\bar{t}$ production and decay.** The diagram on the top left is an example of an LO $t\bar{t}$ production diagram. The diagram on the top right shows a possible NLO contribution. The diagram on the bottom left shows a possible diagram for $t\bar{t}q\bar{q}$ production. The diagram on the bottom right shows the decay of the $t\bar{t}$ system.

the calculation of the cross section from eq. (1.34) this yields $\hat{\sigma}_{\text{LO}} \propto \alpha_s^2$. Higher orders in perturbation theory are indicated as an example in the top right of Figure 1.6, where an additional gluon is produced ($gg \rightarrow t\bar{t}g$). Such additional radiation, or diagrams with loops contribute to the NLO of the $t\bar{t}$ cross section and scale via $\hat{\sigma}_{\text{NLO}}(t\bar{t}) \propto \alpha_s^3$. The $t\bar{t}$ cross section has been calculated up to next-to-next-to-leading order (NNLO), e.g. in Ref. [59]. As indicated in the example diagrams in Figure 1.6, the dominant production mechanism for $t\bar{t}$ at the LHC is from gluon initial states, but $t\bar{t}$ can also be produced via $q\bar{q} \rightarrow t\bar{t}$ at the same order of α_s^2 . The relative fraction of these initial states depends on the type and energy of the primary particles in the collider environment. At high energies, such as the LHC, the parton distribution function (pdf) of protons (see Section 5.1) is dominated by gluons, which enhances the production mode from gluon initial states. At colliders that use proton-antiproton collisions, the probability for $q\bar{q}$ initial state increases, as both initial quarks can be obtained from valence quarks of the (anti)protons, which is not possible in proton-proton collisions.

Figure 1.6 also depicts an example production of $gg \rightarrow t\bar{t}q\bar{q}$ at LO (bottom left), i.e. the associated production of $t\bar{t}$ and a pair of quarks. The cross section of this process scales with $\hat{\sigma}_{\text{LO}}(t\bar{t}q\bar{q}) \propto \alpha_s^4$. This $t\bar{t}q\bar{q}$ process is an overarching representation of all processes that are analyzed in this thesis. Part II focusses on the associated production of a pair of b quarks ($t\bar{t}b\bar{b}$), while in Part III, additional studies of $t\bar{t}$ +jets are presented, where one of

the possible production process is the depicted process. In Section 7.2, this will be further discussed in the context of $t\bar{t}b\bar{b}$.

1.6.2 Top quark decay

The quarks of the SM decay into other quarks via the charged current of the weak interaction, for the top quark $t \rightarrow d'W$, where d' indicates any down-type quark (bottom, strange, down). This was already discussed briefly in Section 1.1. The CKM matrix describes the behavior of electroweak quark decays, predicting large transition amplitudes of quarks in the same generation relative to transitions to quarks of other generations. Taking this into account, and also the large difference between the top quark mass and all other quarks, this results in top quark decays almost exclusively into bottom quarks, $\Gamma(t \rightarrow bW)/\Gamma(t \rightarrow d'W) > 0.955$ (at 95% confidence level) [61]. For the $t\bar{t}$ process the decay of top quarks is shown in the diagram on the bottom right of Figure 1.6.

This opens up a range of possibilities for the measurement of top quark processes. For example, top quarks can be indirectly identified via a b quark (and its b jet) and the W boson (and its decay products in the detector). In addition, due to the rapid decay of the top quark, the spin and spin correlations of top quarks are preserved and inherited by the decay particles, which makes measurements of spin or polarization of top quarks easier than for other particles. Furthermore, as a top quark decay always yields a W boson, the top quark decays can be classified via the W boson decay. In around 66% of cases a W boson decays hadronically into a pair of quarks [1], i.e. $W \rightarrow q\bar{q}'$. In the other 33% of cases, a W boson decays leptonically into a charged lepton and a neutrino [1], i.e. $W \rightarrow \ell\nu$. For $t\bar{t}$ this means that three final states are possible, classified via the number of charged leptons. The fully-hadronic $t\bar{t}$ final state, in which both top quarks decay hadronically, has no charged leptons in its final state and encompasses around 45% of cases. The dileptonic $t\bar{t}$ final state, in which both top quarks decay leptonically, has two charged leptons in its final state and encompasses around 11% of cases. The remaining cases, in which one of the top quarks decays hadronically and the other decays leptonically, are referred to as the semileptonic $t\bar{t}$ decay channel and encompass around 44% of cases. In the measurements of this thesis, exclusively the latter final state, the semileptonic $t\bar{t}$ final state, is analyzed. Each of the final state has its advantages and disadvantages from the perspective of data analysis. The dileptonic final state has very clear signatures (charged leptons are easier to identify than hadronic decays), but have only low rates (11%). The fully hadronic final state has a high rate (45%) but no leptons in its final state, which makes the distinction between $t\bar{t}$ processes and other QCD processes without top quarks more difficult. The semileptonic final state encompasses both advantages, as the one charged lepton makes the signature of $t\bar{t}$ distinctive enough while also having a high rate (44%).

2 Experimental setup

The theories of the SM, and also all theories that attempt to describe the unanswered phenomena have to be tested in experiments. The close collaboration of understanding the processes in particle physics and their experimental tests is an important aspect of this field of science. In this chapter, the experimental setup used for the results of this thesis is introduced briefly. The measurements are performed with data recorded at the Compact Muon Solenoid (CMS) experiment, which will be introduced in Section 2.2. The CMS experiment is located at the Large Hadron Collider (LHC), which will be introduced in Section 2.1.

2.1 The Large Hadron Collider

The Large Hadron Collider (LHC) is a synchrotron accelerator, designed to accelerate and collide hadrons. At the European Organization for Nuclear Research (CERN)¹, many decades of developments in accelerator technology have resulted in the design and realization of the LHC. It is the largest human-made particle collider to date, measuring 27 km in circumference². The goal of such an accelerator is to accelerate charged particles to the highest possible energies in a controlled environment, which allows for the production of new or rare particles in the high-energy collision. Some particles, such as the Higgs boson or the top quark, are very heavy in comparison to other elementary particles and hence require high energy collisions in order to be produced and studied. The study of the Higgs boson has not been possible with any other collider before the LHC. The machine is designed to collide protons and heavy ions such as lead or gold ions³. An accelerator complex consisting of multiple pre-acceleration steps is used to accelerate the protons to increasing energies, ending with the LHC, where protons are accelerated up to an energy of 7 TeV. The full accelerator complex at CERN is shown in Figure 2.1. For the LHC, the acceleration chain starts with the creation of protons from hydrogen atoms by removing the electrons in the hydrogen atoms via strong electric fields. Then, the protons are accelerated to an energy of 50 MeV in the LINAC4 linear accelerator. In the BOOSTER,

¹Conseil européen pour la recherche nucléaire.

²Unimportantly, the LHC is built in a tunnel which lies 45–170 m under the surface in the Swiss-French border region in Geneva with an excellent view of the Jura mountains.

³As the results in this thesis exclusively use the pp collisions, only those will be discussed in the remainder of the thesis.

2 Experimental setup

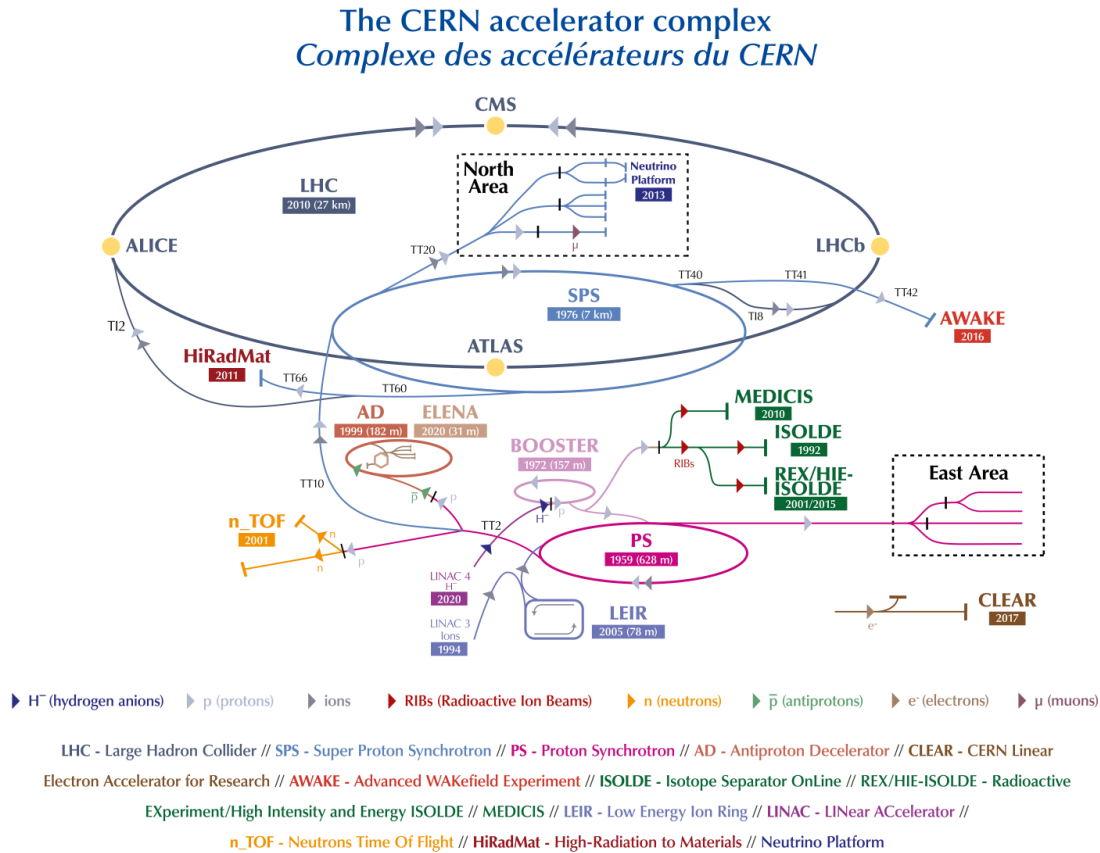


Figure 2.1: The CERN accelerator complex. From Ref. [66].

a synchrotron accelerator, the protons are further accelerated to 1.4 GeV. Compared to linear accelerators, synchrotron accelerators are circular and can use the same acceleration setup for multiple consecutive acceleration steps. In the BOOSTER, the constant stream of protons is split into packages, called bunches, which consist of $\sim 10^{11}$ protons each. Next, the protons are accelerated to 25 GeV in the Proton Synchrotron and subsequently to 450 GeV in the Super Proton Synchrotron. Today, these synchrotron accelerators are repurposed as pre-accelerators for the LHC, while in their original design these machines were state-of-the-art accelerators and reached the, at the time, highest possible energies. For example, the existence of W and Z bosons was experimentally verified at detectors located at the Super Proton Synchrotron [62–65] extended to a proton-antiproton collider. Finally, the protons are injected into the LHC.

The LHC uses superconducting dipole magnets to force the particles on the circular trajectory of the accelerator. Quadrupole and higher-order magnets are used to focus the protons. The particles can be accelerated to 7 TeV using a superconducting radio frequency cavity. The LHC consists of two spatially separated beam pipes where protons are circulated and accelerated in opposite directions. The proton bunches are brought into collision at four points in the collider where the four detectors for the measurement of the collisions are placed. The four experiments are the LHCb experiment [67], the ALICE experiment [68], the ATLAS experiment [69], and the CMS experiment [70]. The LHCb experiment specializes in the measurement of B hadrons and CP violation, the ALICE experiment specializes in the measurement of heavy ion collisions, and the ATLAS and CMS experiments are general-purpose detectors, designed to perform precision mea-

measurements of the SM and the search for new particles and interactions. While the design center-of-mass energy of the proton-proton (pp) collisions is $\sqrt{s} = 14$ TeV, this has as of yet never been reached. In the first running period (Run 1) of the LHC, the machine was operated at $\sqrt{s} = 7$ TeV and $\sqrt{s} = 8$ TeV, which was sufficient to discover the Higgs boson at the ATLAS and CMS experiments [29, 30]. In the second running period (Run 2) between 2015–2018, the machine reached $\sqrt{s} = 13$ TeV, corresponding to 6.5 TeV per proton. The data collected during the 2016–2018 running period is used in this thesis for data analysis. Since 2022 (Run 3), the LHC is operated at $\sqrt{s} = 13.6$ TeV. More details on the LHC can be found in Ref. [71].

2.1.1 Luminosity

In the pp collisions, processes of interest are often rare and hence require a large number of collisions to be analyzed with high precision. For that purpose, protons are brought to collision every 25 ns in proton bunches consisting of around 10^{11} protons each. The rate dN/dt of pp collisions depends on the total pp cross section (i.e. production probability) σ_{pp} , and the instantaneous luminosity L of the particle collider,

$$\sigma_{pp} \cdot L = \frac{dN}{dt}. \quad (2.1)$$

The instantaneous luminosity L is defined via the parameters of the proton beams,

$$L = \frac{N_b^2 n_b f_{\text{rev}}}{4\pi\sigma_x\sigma_y}, \quad (2.2)$$

with N_b the number of particles per bunch, n_b the number of bunches per beam, f_{rev} the revolution frequency of the collider, and σ_x and σ_y the size of the proton bunches in the (x, y) -plane, orthogonal to the beam direction.

For the measurement of cross sections, the precise knowledge of the integrated luminosity L_{int} is very important,

$$L_{\text{int}} = \int dt L. \quad (2.3)$$

This parameter quantifies the amount of data collected and is commonly measured in units of inverse femtobarn, $1 \text{ fb}^{-1} = 10^{-39} \text{ cm}^{-2}$. With the precise knowledge of the integrated luminosity, the cross section of a process can be measured based on counting experiments, as will be introduced in Chapter 4. During Run 2, the instantaneous luminosity in pp collisions at the LHC reached values of up to $2 \cdot 10^{-5} \text{ fb}^{-1} \text{ s}^{-1}$, translating to around 10^9 pp interactions per second.

2.2 The Compact Muon Solenoid

The Compact Muon Solenoid (CMS) experiment is built around one of the four interaction points of the LHC⁴. It is designed to record all (stable) particles produced in the pp collisions, except for neutrinos. As most particles produced in the pp collisions have lifetimes that are too short to be directly recorded in such a detector, mostly only the particles from the decay of primary particles are recorded in the detector itself. The origin of these particles, i.e. the process in the pp collision, has to be inferred via reconstruction algorithms (see Chapter 3) and data analysis. The CMS detector consists of multiple detector elements placed around the interaction point, where each of the detector elements

⁴Irrelevantly, the CMS detector is 28.7 m long, has a diameter of 15 m and a total weight of 14 000 t.

2 Experimental setup

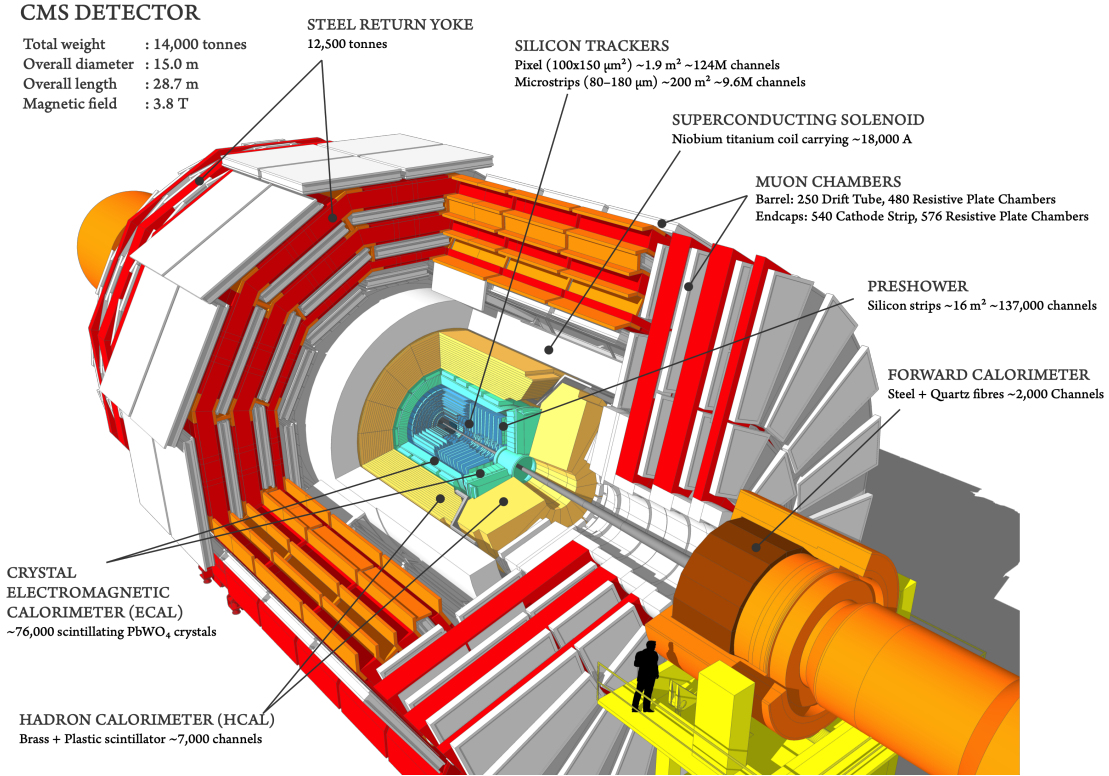


Figure 2.2: Visualization of the CMS detector. From Ref. [72].

is responsible for the detection, reconstruction, or identification of a subset of particles that are expected in the pp collisions. The innermost detector component is a tracking system, followed by an electromagnetic and a hadronic calorimeter system. This is surrounded by a solenoid magnet and muon detectors on the outer layers. These detector components will be discussed briefly in Section 2.2.2. In Section 2.2.1, first, relevant kinematic quantities and the coordinate system of the CMS detector are introduced. Details on the CMS detector can be found in Ref. [70].

2.2.1 Coordinate system and collider quantities

At the CMS experiment, a right-handed coordinate system is used, where the x axis is defined towards the center of the LHC and the y axis points upwards. The z axis is defined in the direction of the beam. The CMS detector is cylindrical with the center being the pp interaction point. Correspondingly, an azimuthal angle ϕ is defined in the (x, y) -plane, and a polar angle θ relative to the beam direction. The collisions and resulting processes are symmetrical in ϕ .

The protons in both colliding beams have the same energy, i.e. equal but opposite momentum in the z direction, and negligible momentum in the (x, y) -plane. As the protons are composite particles, the protons themselves do not collide, but rather their partons, which can be treated as free particles at this energy due to the asymptotic freedom of QCD (see Section 1.4). The fraction of momentum of the partons in a single pp collision is not known, hence the total momentum of the collision in the z direction is unknown. Therefore, it is convenient to define a quantity that is invariant against (unknown) boosts in z direction, such as the transverse momentum

$$p_{\text{T}} = \sqrt{p_x^2 + p_y^2}. \quad (2.4)$$

The transverse momentum quantifies the momentum in the (x, y) -plane.

Another common quantity is the rapidity y , which is defined as

$$y = \frac{1}{2} \left(\frac{E + p_z}{E - p_z} \right). \quad (2.5)$$

Differences in the rapidity Δy are invariant against Lorentz boosts along the z direction, resulting in a suitable quantity to measure the angular separation of two particles. Commonly, the pseudorapidity η is used instead, defined as

$$\eta = -\ln(\tan(\theta/2)), \quad (2.6)$$

This quantity only depends on the polar angle θ instead of the energy and momentum of the particles, which is easier to measure. In the relativistic limit where $m \ll p$, the rapidity and pseudorapidity are equal, which makes the pseudorapidity the preferred quantity. The pseudorapidity is defined such that $\eta = 0$ is perpendicular to the beam axis and $\eta \rightarrow \pm\infty$ is parallel to the beam axis. Angular distances in the (θ, ϕ) -plane are usually quantified with ΔR ,

$$\Delta R = \sqrt{(\Delta\phi)^2 + (\Delta\eta)^2}, \quad (2.7)$$

using the pseudorapidity η instead of the polar angle θ .

2.2.2 Detector components

The CMS detector and its component are separated into a barrel region and two endcap regions. The barrel region is cylindrically built around the interaction point and extends to around $|\eta| < 1.5$. The endcaps are two symmetrical parts (disks) placed at both ends of the barrel regions to also cover the areas closer to the beam pipe.

The solenoid magnet

The CMS experiment makes use of a superconducting solenoid magnet that surrounds the tracking and calorimeter systems. This solenoid magnet is designed to reach a field strength of 4 T, but is operated at 3.8 T. The purpose of the magnet is to bend electrically charged particles onto helix-like trajectories, which allows for the measurement of the momentum of the particles. The return yoke of the solenoid magnet is interleaved with the muon detectors.

The tracking system

The tracking detectors [73–75] are the innermost detector components of the CMS experiment. With these detector components, the trajectory of charged particles originating from the collision point are reconstructed. For a reconstruction of the particle trajectories, multiple points of the trajectory have to be recorded (see Section 3.1). For that purpose, the tracking system consists of multiple concentric detector layers, guaranteeing the detection of a single particle at multiple points. The detector consists of silicon semiconductors, used as diodes in reverse bias voltage direction. Charged particles passing through a silicon detector ionize in the depletion zone of the diode, resulting in an electric current that can be measured. The inner part of the tracking system consists of pixel detectors, where each silicon pixel has a size of $100 \times 150 \mu\text{m}^2$, allowing for spatial resolution of up to $15 \mu\text{m}$. Due to the proximity of this detector element to the interaction point, a high flux of particles is expected, requiring a highly-performant read-out of

2 Experimental setup

signals. The pixel detector is designed to read out each pixel independently, allowing a precise detection of the interaction point and trajectory of particles in three dimensions. Until 2016 (Phase-0), the pixel detector consisted of three pixel detector layers situated between 44 mm and 102 mm away from the pp interaction point. After 2016 (Phase-1), the pixel detector was replaced with an upgraded detector, consisting of four pixel detector layers between 29 mm and 160 mm away from the pp interaction point [75]. This improved detector is able to identify the origin of particles more accurately as its inner layer is closer to the interaction point, allowing for a more accurate resolution of decay vertices e.g. of B hadrons, important for the identification of b jets (see Section 3.3.2) [76]. The pixel detector covers a range of $|\eta| < 2.5$ (2.4 until 2016). A silicon strip detector surrounds the pixel detector. As the occupancy decreases further away from the interaction point, this detector component is coarser than the pixel detector and consists of a lower number of read-out channels, and only provides a spatial measurement in two dimensions. The strip detector consists of ten cylindrical layers in the barrel region and twelve layers in the endcap regions.

The electromagnetic calorimeter

The electromagnetic calorimeter (ECAL) [77–79] surrounds the tracking system and is supposed to measure the energy of electromagnetically charged particles. Electrons and photons entering the calorimeter material produce a cascade of particles (electromagnetic (EM) shower) via photon emission (bremsstrahlung) and $\gamma \rightarrow e^+e^-$ pair production processes. This cascade continues until the energy of the shower particles is too low for further electron-positron pair-production processes. These low-energetic particles are then absorbed in the detector material. The energy (or number) of photons in these showers can be measured via scintillation and transformed into electrical signals with photodiodes. As the shower evolution is quite homogeneous, the energy of the initial particle can be determined from the amount of scintillation light detected. The active material of the ECAL, where the particles are absorbed, is lead tungstate (PbWO_4), which at the same time acts as the scintillation material. The lead tungstate crystals have a size of $2.2 \times 2.2 \times 23$ cm ($2.9 \times 2.9 \times 22$ cm) in the barrel (endcap) regions at $|\eta| < 1.48$ ($1.48 < |\eta| < 3.0$), large enough to encompass ~ 25 radiation lengths. The radiation length is the mean distance after which $1/e$ of the energy of the shower particles remains. The high density of lead tungstate allows for a compact design of this ECAL, guaranteeing that in most cases the full EM shower is contained in a single crystal, enabling a precise energy measurement. Shorter calorimeter crystals would decrease the resolution of the particle momentum especially at high particle energies, as the full shower would not be able to be contained in the calorimeter. In front of the ECAL in the endcaps, pre-shower detectors are installed for the purpose of already inducing EM showers before entering the lead tungstate crystals. This detector consists of lead absorbers and a silicon strip detector element, and allows to resolve EM showers initiated from either one or two photons, the latter e.g. originating from a decay of a neutral pion.

The hadronic calorimeter

The hadronic calorimeter (HCAL) [80, 81] is a sampling calorimeter, responsible for the energy measurement of charged and neutral hadrons. Incoming particles interact with the absorber material via scattering processes, producing new, lower energetic particles, also leading to a cascade of particles. Such hadronic showers are less homogeneous than the EM counterparts, as multiple different particles are created, also including EM sub-showers. The detection principle of the HCAL is similar to the ECAL, however instead of using a homogeneous calorimeter material, alternating layers of absorber and scintillator

material are used (sampling). Typically, the mean interaction length of nuclear interactions is significantly longer than that of EM interactions, which requires the size of this detector to be larger. In the barrel and endcap regions, the HCAL consists of brass absorber layers and plastic scintillators, extending to $|\eta| < 3.0$. In the central region, the size of the HCAL is limited by the ECAL on the inside and the solenoid magnet on the outside, allowing only for ~ 6 – 10 nuclear interaction lengths between $|\eta| = 0$ and $|\eta| = 1.3$. This does not guarantee a full absorption of the hadronic shower in the HCAL. Hence, additional HCAL layers are installed outside the solenoid magnet at $|\eta| < 1.26$ to improve the energy measurement in the barrel region. The solenoid magnet also acts as additional absorber material. In the forward region at large $|\eta|$ close to the beam direction an additional calorimeter system is installed, covering a range of $2.85 < |\eta| < 5.2$, consisting of steel and quartz fiber layers. Due to the inhomogeneity of the hadronic showers, the sampling of the shower in alternating detector layers, and the lower number of interaction lengths of the detector, the HCAL generally has a lower energy resolution than the ECAL.

The muon system

The muon system [82, 83] is located outside the solenoid magnet, embedded in the return yoke of the solenoid magnet, and comprises the outermost layer of the CMS detector. Muons are minimum ionizing particles in the energy range relevant for the interactions at the CMS experiment and are not absorbed in the calorimeter systems. Hence, the muon system is installed for the explicit purpose of identification of muons and the measurement of their momenta as these would otherwise leave the detector undetected. The detection principle of the muon systems relies on gaseous detectors. Such gas detectors commonly have lower resolution than solid state detectors such as the silicon tracking detector but can cover a larger detector area more easily due to the comparably cheaper design. These types of detectors are filled with a gas that gets ionized when a charged particle passes through the gas. A high voltage is applied between a cathode and an anode in the gas detector, which makes the electrons and ions drift and accelerate in the gas. The acceleration of electrons creates additional free electrons, leading to a cascade that can be measured as a current. In the barrel region at $|\eta| < 1.2$, the muon system consists of drift tube chambers, which have good time and spatial resolution. At $0.9 < |\eta| < 2.4$ cathode strip chambers are used which have better spatial resolution, but worse time resolution. The full range $|\eta| < 2.4$ is also interleaved with resistive plate chambers which have very good time resolution but comparably low spatial resolution. After 2018, additional gas electron multiplier chambers were installed in the endcap regions, which have very good time resolution and can be used to trigger muons also in the forward regions of the detector.

2.2.3 The trigger system

Proton bunches collide in the center of the CMS detector with a frequency of 40 MHz, where each of these bunch crossings has the probability of one or more pp collisions. With the instantaneous luminosities recorded e.g. in 2018, an average of around 40 pp collisions are expected per bunch crossing, assuming a total inelastic pp cross section of 80 mb as predicted by PYTHIA [84]. The data rate associated with this is in the order of multiple TB/s, which is unfeasible to be recorded. Therefore, a two-tiered trigger system is applied at the CMS experiment to reduce the data rate and to record only events with interesting signatures. What constitutes interesting is defined by the trigger requirements.

2 Experimental setup

Table 2.1: **Integrated luminosity.** The luminosity values correspond to the luminosity recorded at the CMS experiment between 2016 and 2018 and are certified for data analysis. Data taken in 2016 is separated into a 2016preVFP and 2016postVFP era due to significant differences in detector conditions.

Era	Integrated luminosity
2016preVFP	19.5 fb ⁻¹
2016postVFP	16.8 fb ⁻¹
2017	41.5 fb ⁻¹
2018	59.8 fb ⁻¹
Total	138 fb ⁻¹

The first trigger level, the Level-1 (L1) trigger, is a hardware-based trigger that is partly installed inside the CMS detector, described in detail in Ref. [85]. This installation reduces the latency of the trigger modules, and enables to make trigger decisions within 4 μ s. This trigger uses two, at first, independent trigger systems in the muon system and the calorimeter systems, based on a coarse read-out of the detector components, called trigger primitives. In the muon systems neighboring hits are compared and if possible combined to identify possible tracks. In the calorimeters, energy deposits are clustered in neighboring calorimeter cells. From combinations of clusters, global observables to identify jets, charged leptons, and photon candidates are calculated. The information of both systems is then combined and compared to a list of predetermined simple selection criteria based on these simple objects. Only if the event fulfills one of these selection criteria, is the event read out in full. With the L1 trigger system, the event rates are reduced by a factor of 400 to about 100 kHz.

The second trigger level, the high-level trigger (HLT), is a software-based trigger system using a computer farm situated next to the CMS detector, described in detail in Ref. [86]. For this triggering step an event reconstruction is performed with loose requirements on the reconstructed objects. This procedure is similar to the object reconstruction defined in Chapter 3. In the HLT step also a jet clustering algorithm (see Section 3.3) is employed, as well as identification criteria for charged leptons and photons. HLT paths are defined which contain sequences of reconstruction steps. These paths are generated in a way to minimize unnecessary calculations and redundancies, e.g. by ordering the reconstruction steps by increasing complexity. This facilitates a fast performance needed to make HLT trigger decisions during runtime. HLT decisions are made within around 300 ms. An HLT menu is employed at the CMS detector, which encompasses HLT trigger paths for a wide range of purposes. If at least one of the predefined HLT trigger paths is fulfilled the event is stored. All other events are discarded. With the HLT trigger system the data rate can be decreased to levels of 100 Hz to 1 kHz. For some of the HLT paths prescales are applied. A prescale n is applied to store only each n -th event passing a certain HLT path. This procedure is employed in order to reduce the rate of stored events for triggers that have high expected rates but are nevertheless interesting enough to be stored.

2.3 Definition of the data set

Data amounting to around 160 fb⁻¹ of integrated luminosity was delivered by the LHC between 2016 and 2018. The measurements in this thesis use 138 fb⁻¹ of high-quality data recorded by the CMS experiment in that period. In total, 147 fb⁻¹ of data was recorded by the CMS detector in that period, but not all was certified for data analysis, due to inefficiencies or failures in subsets of detector elements. Due to changes in the detector, e.g. the

pixel detector upgrade after 2016, changes in the HLT configurations, or small detector inefficiencies, events are analyzed separately per year. This also holds for the simulation of events, where separate detector simulations and trigger menus are employed, reflecting as precisely as possible the actual setup during data taking.

In addition, data from 2016 is separated into two parts, 2016preVFP and 2016postVFP, due to significant differences in detector conditions. In the first part (2016preVFP) the silicon strip detector showed inefficiencies, especially when running at high luminosities. This was caused by low signal-to-noise ratios in the strip detector, resulting in fewer hits being identified in the detector due to saturation effects in the readout chips [87]. This issue was resolved during the 2016 data-taking period by changing the preamplifier feedback voltage bias (VFP). Hence, data analyzed in this thesis is separated into four parts, henceforth referred to as eras. The integrated luminosities associated with each era are summarized in Table 2.1.

3 Object reconstruction

In Section 2.2, the CMS detector and its components have been introduced. In order to facilitate analysis of the recorded data, the read-out signals have to be combined and reconstructed to physics objects. The data analysis described in the latter chapters will rely solely on the objects defined in this chapter. Hence, in the following the algorithms and configurations to reconstruct all relevant objects will be introduced. The first step is the reconstruction of tracks and interaction vertices (Section 3.1). Then, the Particle Flow (PF) algorithm is applied to identify final-state particles (Section 3.2). Based on these PF candidates, jet algorithms are applied to cluster sprays of hadrons into jet objects (Section 3.3). Jet flavor identification algorithms are employed in order to identify the flavor of the initial particle of a jet (Section 3.3.2). Finally, the energy of particles not interacting with the detector is identified as missing energy (Section 3.4).

3.1 Tracks and vertices

Charged particles traversing the pixel and strip tracking detectors form helix-shaped trajectories in the magnetic field of the solenoid magnet. Their electromagnetic interaction with the detector layers can be identified and read out as signals, or hits, determining the point where the particle passed through the detector. These hits can be combined to reconstruct trajectories, called tracks. The track reconstruction uses a combinatorial track finding algorithm [88], which is based on Kálmán filters [89, 90], consisting of three steps. First, possible seeds are generated by combining neighboring hits to track candidates. These seeds use hits in three neighboring layers of the pixel detector. Then, trajectories are built by identifying hits from all detector layers that are compatible with the track candidate extrapolated from the initial seed. This step uses a Kálmán filter technique, where the track segments are extended to neighboring detector layers or components to identify suitable hit candidates. Tracks require at least eight hits assigned to them after this procedure. Finally, a track-fitting algorithm is applied to the track candidate to determine the properties of the track based on the combination of hits. This takes into account deviations from trajectories like uncertainties in the hit position determination, bremsstrahlung effects, or energy loss in the detector material. In this step, the track is also extrapolated to its origin, which is later used to identify vertices. Tracks are discarded if their transverse momentum and extrapolated origin do not fulfill certain criteria. The tracking algorithm is applied iteratively after all hits assigned to successfully reconstructed tracks are removed from the collection of hits. In the iterative procedure, the

3 Object reconstruction

same track reconstruction algorithm is applied to the remaining hits with relaxed seeding and reconstruction quality criteria. Similarly, tracks are reconstructed in the muon system based on the hits recorded in the muon detector components.

Identifying vertices of primary interactions is important to distinguish particles originating from one pp interaction of interest, and other interactions in the same bunch crossing. The tracks extrapolated to the center of the detector are uniquely assigned to vertices using a deterministic annealing algorithm [91]. The vertex finding algorithm clusters tracks into candidates of vertices based on the z position of their extrapolated origin. The position of the vertex candidate is then determined using an adaptive vertex fitter algorithm [92]. Hard interactions of interest often include highly energetic particles. Therefore a primary vertex is defined as the vertex with the highest sum of the squared transverse momenta p_T^2 of the tracks assigned to this vertex. All remaining vertices are categorized as pileup interactions for the purpose of data analysis. In order to be considered in the measurements of this thesis, quality criteria have to be fulfilled by the designated primary vertex. The position of the primary vertex has to be located within $|z| \leq 24$ cm and a radius of $r \leq 2$ cm relative to the geometrical center of the detector (see definition of CMS coordinate system in Section 2.2). Furthermore, the number of degrees of freedom in the vertex fit has to exceed five, implying that at least four tracks are associated with this vertex. Events whose primary vertex does not fulfill these criteria are not further considered in this thesis.

3.2 The Particle Flow algorithm

The PF algorithm [93] is an algorithm employed by CMS to reconstruct physics objects from the read-out signals of the different detector components. The PF algorithm uses an optimal combination of all detector components to reconstruct the different expected types of particles. The reconstruction is performed with an inherent order. This way, particles that are relatively easy to reconstruct will be reconstructed first, with the best resolution of energy, direction, and momentum, combined from all relevant detector components. Then, particles that are harder to identify are reconstructed from the remaining signals. This guarantees an optimal reconstruction of all possible particles. For example, measurements of the tracker and the calorimeters are combined to yield the best resolution for the energy and momentum of reconstructed particles. The PF algorithm starts from the tracks and vertices whose reconstruction is described in Section 3.1, and links these elements together with a link algorithm, following a set of requirements, e.g. close distance or successful extrapolation of tracks to calorimeter clusters. A group of PF elements that are linked together with this algorithm is referred to as a PF block. For each of these blocks, a reconstruction sequence is applied, starting with the reconstruction and identification of muon candidates (Section 3.2.1). This is followed by electron (Section 3.2.2) and photon (Section 3.2.3) candidates. The remaining PF elements are then associated with charged or neutral hadrons (Section 3.2.4).

3.2.1 Muons

Muons are, with a mass of 106 MeV, minimum ionizing particles in the energy range relevant for detection at the CMS detector. Hence, muons only deposit minimum amounts of energy in the calorimeters and traverse the detector to the muon system situated outside the calorimeter systems and the solenoid magnet. Due to their high mass, in comparison to electrons, muons also produce only small amounts of bremsstrahlung, leading to clean track signatures. Therefore, muons have a unique signature in the detector, consisting of a bent track in the silicon tracker and a (reversely) bent track in the muon systems.

Previously defined track candidates in the silicon tracker and muon systems are used to define three types of muon candidates [83]. Standalone muon candidates are identified using only tracks from the muon system. Tracker muon candidates are identified from tracks in the silicon tracker by extrapolating and matching them to hits in the muon systems. Global muons are built from standalone muon candidates that are matched to tracker muon candidates. Most muon candidates are both identified as tracker and global muons. The tracker muon reconstruction shows higher efficiency at low momenta where the tracker is most accurate. Global muons rely more on the muon system and are therefore more efficient at higher muon momenta when multiple hits in the muon system are present.

Object requirements for data analysis

Muons considered in this thesis follow additional quality requirements, e.g. in order to separate muons originating from hard scattering processes from cosmic muons or muons from meson decays. Identification criteria are defined by the CMS Collaboration to commonly define high-quality muons [83]. In this measurement two types of muons are used, one passing a set of tight and one passing a set of loose identification criteria. The criteria are listed in Table 3.1. In addition, a relative muon isolation I_μ is used, defined as

$$I_\mu = \frac{1}{p_{T,\mu}} \left[\sum_{\Delta R < 0.4} p_{T,\text{CH}} + \max \left(0, \sum_{\Delta R < 0.4} p_{T,\text{NH}} + \sum_{\Delta R < 0.4} p_{T,\gamma} - \frac{1}{2} \sum_{\Delta R < 0.4} p_{T,\text{PU}} \right) \right]. \quad (3.1)$$

This quantifies the relative energy content in the vicinity of the muon. A cone with a radius of $R = 0.4$ in the (η, ϕ) -plane is defined around the muon. Particles inside the cone are considered for the calculation of the isolation. The transverse momenta of charged hadrons (CH), neutral hadrons (NH), and photons (γ) are considered. The transverse momentum of charged hadrons identified as coming from pileup interactions (PU) is subtracted with a factor of $\frac{1}{2}$. This factor was determined from simulation as a good approximation of the relative energy fraction of neutral hadrons coming from pileup, which is necessary as the origin of neutral hadrons cannot be identified and hence the NH contribution unavoidably contains neutral hadrons from pileup which need to be subtracted [83]. The requirements on I_μ for the data analysis selections are also summarized in Table 3.1. This requirement discards muons originating from semileptonic hadron decays in jets. These so-called non-prompt muons are not of interest in the measurements of this thesis.

Furthermore, a requirement of $|\eta| \leq 2.4$ is set for the pseudorapidity of muons to be considered in this thesis, covering the full range of the muon system. Muons reconstructed outside this pseudorapidity range are reconstructed with lower efficiencies and accuracies and are hence not regarded further.

3.2.2 Electrons

Electrons are light in comparison to muons and produce large amounts of bremsstrahlung in magnetic fields. This results in track candidates dressed with many bremsstrahlung photons along the track curvature. Electrons reaching the ECAL produce electromagnetic showers. The signature of an electron, therefore, consists of a bent track in the silicon tracker dressed with bremsstrahlung photons and an electromagnetic shower in the ECAL. Shower-shape analysis of ECAL showers enables the identification of showers originating from electrons. ECAL deposits of bremsstrahlung photons are clustered together in a (so-called) supercluster (SC). The SC is connected to track candidates to

3 Object reconstruction

Table 3.1: **Muon identification requirements.** Loose and tight identification criteria are defined for muons [83]. The criteria for I_μ are also included in the table but do not directly belong to the CMS-provided IDs.

Criteria	tight ID	loose ID
Global muon	✓	—
PF muon	✓	✓
Global or tracker muon	—	✓
χ^2/ndof of global-muon track fit	< 10	—
# hits in muon chambers	> 0	—
# segments in muon stations	> 1	—
$ d_{xy} $	< 2 mm	—
$ d_z $	< 5 mm	—
# pixel hits	> 0	—
# tracker layer hits	> 5	—
I_μ	< 0.15	< 0.25

form an electron [94]. As electrons lose a significant fraction of their energy from interactions in the silicon tracker detector material, the tracks of electrons are re-reconstructed using a Gaussian sum filter (GSF), which models the energy loss [95, 96].

Object requirements for data analysis

Similar to muons, electrons undergo additional identification criteria in order to be considered for measurements in this thesis. Identification flags for electrons, defined by the CMS Collaboration [94], are used at the veto and tight thresholds summarized in Table 3.2. Separate sets of requirements are set for electrons in the barrel ($|\eta_{\text{SC}}| \leq 1.48$) and endcap ($|\eta_{\text{SC}}| > 1.48$) regions. A relative isolation observable I_e is defined, similar to the muon isolation I_μ , as

$$I_e = \frac{1}{p_{T,e}} \left[\sum_{\Delta R < 0.3} p_{T,\text{CH}} + \max \left(0, \sum_{\Delta R < 0.3} p_{T,\text{NH}} + \sum_{\Delta R < 0.3} p_{T,\gamma} - \rho A_{\text{eff}} \right) \right]. \quad (3.2)$$

Charged hadrons (CH), neutral hadrons (NH), and photons (γ) in a cone of radius $R = 0.3$ around the electron, contribute to the calculation of the isolation. In addition, an effective term ρA_{eff} is subtracted, which removes contributions from pileup to the NH contribution [94]. This contribution is parametrized via the average NH energy density ρ and the effective area of the electron A_{eff} . Unlike for muons, the relative isolation is part of the CMS-provided identification thresholds, as these are crucial for successful electron identification.

Additional requirements are set on the impact parameters of electrons, i.e. their distance to the interaction vertex. This impact parameter is defined separately for the longitudinal direction, $|d_z|$, and the radial directions, $|d_{xy}|$. The thresholds for these values are also included in Table 3.2 and differ between barrel and endcap regions. Finally, electron candidates are only considered for measurements in this thesis with $|\eta| < 2.5$ due to the limited silicon tracker coverage.

3.2.3 Photons

Isolated photons are reconstructed similar to electrons from ECAL showers but without a track in the silicon tracker associated with them [94]. A distinction is made between isolated photons which originate from the hard scattering process and non-isolated photons

Table 3.2: **Electron identification requirements.** Veto and tight identification criteria are defined for electrons [94]. The set of requirements differs for electrons in the barrel region ($|\eta_{\text{SC}}| \leq 1.48$) and the endcap region ($|\eta_{\text{SC}}| > 1.48$). The first table summarizes the identification criteria for the barrel region and the second table for the endcap region. The criteria for $|d_{xy}|$ and $|d_z|$ are included in the tables but do not directly belong to the definition of the IDs.

Criteria ($ \eta_{\text{SC}} \leq 1.48$)	tight ID	veto ID
$\sigma_{i\eta i\eta}$ (shower shape)	< 0.0104	< 0.0126
$ \Delta\eta(\text{SC, track}) $	< 0.00255	< 0.00463
$ \Delta\phi(\text{SC, track}) $	< 0.022	< 0.148
Hadronic energy / EM energy	$< 0.026 + 1.15/E_{\text{SC}} + 0.0324\rho/E_{\text{SC}}$	$< 0.05 + 1.16/E_{\text{sc}} + 0.0324\rho/E_{\text{SC}}$
I_e	$< 0.0287 + 0.506/p_T$	$< 0.198 + 0.506/p_T$
$ E_{\text{SC}}^{-1} - p_{\text{track}}^{-1} $	< 0.159	< 0.209
# missing inner hits	≤ 1	≤ 2
Pass conversion veto	\checkmark	\checkmark
$ d_{xy} $	$< 0.5 \text{ mm}$	—
$ d_z $	$< 1 \text{ mm}$	—

Criteria ($ \eta_{\text{SC}} > 1.48$)	tight ID	veto ID
$\sigma_{i\eta i\eta}$ (shower shape)	< 0.0353	< 0.0457
$ \Delta\eta(\text{SC, track}) $	< 0.00501	< 0.00814
$ \Delta\phi(\text{SC, track}) $	< 0.0236	< 0.19
Hadronic energy / EM energy	$< 0.0188 + 2.06/E_{\text{SC}} + 0.183\rho/E_{\text{SC}}$	$< 0.05 + 2.54/E_{\text{sc}} + 0.183\rho/E_{\text{SC}}$
I_e	$< 0.0445 + 0.963/p_T$	$< 0.203 + 0.963/p_T$
$ E_{\text{SC}}^{-1} - p_{\text{track}}^{-1} $	< 0.0197	< 0.132
# missing inner hits	≤ 1	≤ 3
Pass conversion veto	\checkmark	\checkmark
$ d_{xy} $	$< 1 \text{ mm}$	—
$ d_z $	$< 2 \text{ mm}$	—

which originate from hadronization processes. Isolated photons are not further described here. Non-isolated photons are identified from remaining ECAL clusters with $|\eta| \leq 2.5$ that do not fulfill the requirements of isolated photons. In the region of $|\eta| > 2.5$, non-isolated photons are identified only from remaining ECAL clusters without HCAL clusters linked to them. This is because, outside the silicon tracker acceptance of $|\eta| \leq 2.5$, no tracks can be reconstructed. Therefore a distinction between charged and neutral hadrons is not possible.

3.2.4 Hadrons

Clusters in the ECAL and HCAL associated with tracks in the silicon tracker are classified as charged hadrons. The remaining clusters in the HCAL without associated ECAL clusters are classified as neutral hadrons for $|\eta| \leq 2.5$. Outside the acceptance of the tracker, remaining clusters in the HCAL and ECAL are assigned to neutral and charged hadron showers as no distinction can be made.

A charged hadron subtraction (CHS) procedure is employed, where the tracks of charged hadrons are matched to pileup vertices [93]. Charged hadrons identified as likely coming from a pileup vertex are removed from the collection of PF candidates and are not considered for jet clustering in the following.

3.3 Jet reconstruction

Particles produced in the initial hard scattering are to a large degree not color neutral but are assumed to be free, as at the high energy of the collision the strong coupling con-

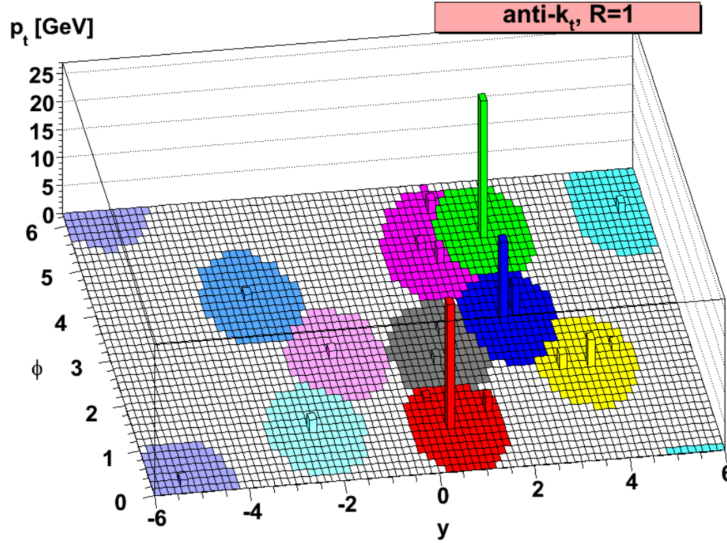


Figure 3.1: **Example of simulated event clustered with the anti- k_T algorithm.** In this example a clustering radius of $R = 1$ is used. Jets, clustered separately with the anti- k_T algorithm are shown in different colors. Taken from Ref. [97].

stant is small (asymptotic freedom). When the particles reach lower energy scales the strong coupling constant becomes large and no free color charges can exist anymore (confinement). Hence, particles hadronize, i.e. form color-neutral hadrons. In this process, cascades, or showers, of hadrons and leptons are produced with increasing particle multiplicity. The particles detected and reconstructed with the PF algorithm are considered stable but are mostly not interesting in themselves for data analysis. The interest for most data analysis lies in the particles from the hard scattering process, like Higgs bosons, top or bottom quarks. Hence, jet algorithms are employed after the PF particle identification and reconstruction to cluster particles together in jet objects. A jet here represents a cascade of hadrons with a common ancestor particle from before hadronization. The properties of the ancestor particle can then be inferred from the properties of the jet. As hadrons also decay into leptons via weak or EM decays, non-isolated leptons can also be part of hadron showers and are also considered in the jet clustering algorithm.

3.3.1 Jet clustering

The most common type of jet clustering algorithms employed are sequential recombination algorithms. This type of clustering algorithm has the advantage of being infrared and collinear safe. Infrared safety implies that gluons radiated off color-charged particles at very low momentum fractions x do not produce additional jets. In the limit of $x \rightarrow 0$, this low-energy QCD radiation does not affect the underlying physics of the process in the hard scattering and should therefore not alter the interpretation on the level of jets. Similarly, collinear safety implies that a splitting of a single particle into two particles with very small angular separation θ does not produce an additional jet.

The sequential reconstruction algorithm used for jet definitions in this thesis is the anti- k_T algorithm [97]. As a first step a distance measure d_{ij} is defined between all pairs of PF candidates i and j as

$$d_{ij} = \min \left(p_{T,i}^{-2}, p_{T,j}^{-2} \right) \frac{\Delta R_{ij}^2}{R^2}. \quad (3.3)$$

This distance metric relies on the spatial distance ΔR_{ij} of the two particles in the (η, ϕ) -plane and their transverse momenta p_T . A threshold parameter R is defined which is

set to $R = 0.4$ for the default jets at the CMS Collaboration, referred to as AK4 jets. An additional value d_i is calculated for each particle as

$$d_i = p_{T,i}^{-2}. \quad (3.4)$$

In the second step of the algorithm the smallest value d_{ij} or d_i is identified among all values. If the smallest value is a distance measure d_{ij} , the two particles i and j are combined to a pseudo-particle k . The particles i and j are removed from the collection of particles and the new pseudo-particle is added. All new distance measures d_{kl} and d_k are calculated and the process is iterated. If the smallest value is a d_i value the particle (or pseudo-particle) i is removed from the collection and declared a jet. The process is repeated with the remaining particles and repeated until all PF candidates are clustered into jets. An example event clustered with the anti- k_T algorithm is shown in Figure 3.1. The resulting jets are circular when further than $2R$ away from the next jet. Jets that are closer to each other share a boundary which is straight if jet momenta are equal.

This algorithm is designed such that particles close to other particles with high p_T are clustered together first, representing axes of major energy flow. Soft particles with similar ΔR distances will be clustered with each other only later. The cut-off values d_i force the algorithm to stop clustering new particles into the jet e.g. if the ΔR of the hardest (pseudo-)particle to other particles is larger than the threshold parameter R . This leads to jet shapes that are cone-like with approximate radii of $R = 0.4$. The collinear and infrared safety of these algorithms is apparent, as particles with small energies from infrared splittings and particles with small angular distances from collinear splittings are clustered together into new pseudo-particles early in the algorithm.

Data analysis at CMS also uses anti- k_T jets with clustering radii of $R = 0.8$ (AK8 jets) and $R = 1.5$ (AK15 jets). These jets are designed to cluster heavier objects at high momenta into a single jet, e.g. all decay products of a top quark or Higgs boson decay. The same signature would most likely lead to three or two AK4 jets, respectively. The measurements in this thesis exclusively make use of AK4 jets.

The jet clustering algorithm is implemented in the FASTJET package using a nearest-neighbor approach in order to avoid unnecessary calculations of d_{ij} [98].

Object requirements for data analysis

Jets have to fulfill a set of quality criteria to be considered for further data analysis. These criteria are employed to, e.g., remove jets clustered from background noise or pileup. Requirements are set on the number of constituents clustered into a jet and their neutral and charged energy fractions. The criteria for the CMS-provided tight identification criteria are summarized in Table 3.3 [99]. These criteria also include limits on energy fractions from charged leptons in order to reduce the number of prompt leptons to be misidentified as being jets. For that purpose, an additional jet-lepton cleaning procedure is applied where jets in the vicinity of electrons or muons (as previously defined) are discarded. The threshold for this cleaning is $\Delta R(\ell, \text{jet}) \leq 0.4$ and is applied to all jets in this thesis. Additionally, only jets with $|\eta| \leq 2.4$ are considered in the following. This restriction is due to the acceptance of the silicon tracker, outside of which the quality of jet reconstruction suffers due to missing tracking information of charged hadrons and leptons. Jets with $p_T \leq 50$ GeV additionally have to pass a loose pileup removal criterion based on a boosted decision tree (BDT) to reject jets likely originating from pileup interactions.

Table 3.3: **Jet identification requirements.** The tight identification criteria are defined for jets [99]. These criteria include limits on energy fractions of charged leptons.

Criteria	tight ID
Neutral hadron energy fraction	< 0.9
Neutral EM energy fraction	< 0.9
# constituents	> 1
Muon energy fraction	< 0.8
Charged hadron energy fraction	> 0
# charged hadrons	> 0
Charged EM energy fraction	< 0.8
# neutral particles	—

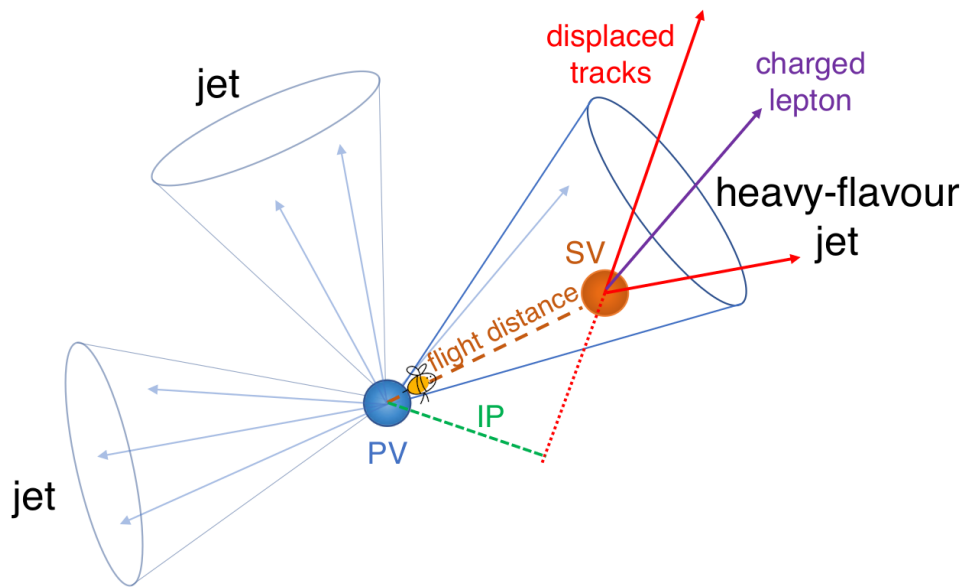


Figure 3.2: **Representation of a secondary vertex inside a jet.** Shown is a hard-scattering interaction, resulting in the reconstruction of a primary vertex (PV). A B hadron is visualized with a resolvable flight distance. The decay of the B hadron takes place in the secondary vertex (SV). Decay products of the B hadron are indicated, originating from the SV. These tracks are clustered together into a jet. Adapted from Ref. [100].

3.3.2 b jets

An important part of the measurements presented in this thesis is the identification of jets originating from the hadronization of b quarks, b jets. Hence, jets are classified as b jets using jet tagging algorithms. Jet tagging algorithms utilize the kinematic features of a jet to determine the flavor of the initial particle. Historically, jet tagging was enabled by using the information of secondary vertices (SV) found inside jets. A b jet evolves e.g. via hadronization of the initial b quark into a B hadron. Due to the CKM-suppression of b quark decays (see Section 1.1), B mesons have long lifetimes of about $\tau = 10^{-12}$ s. Hence, B hadrons will travel around a few hundred micrometers before decaying in their rest frame. This decay of the hadron generates secondary vertices inside the jet where the decay particles from the hadron decay originate. This is visualized in Figure 3.2. The tracks associated with the hadron decay will leave signatures of displaced tracks inside the jet with impact parameters relative to the primary vertex, i.e. the jet origin.

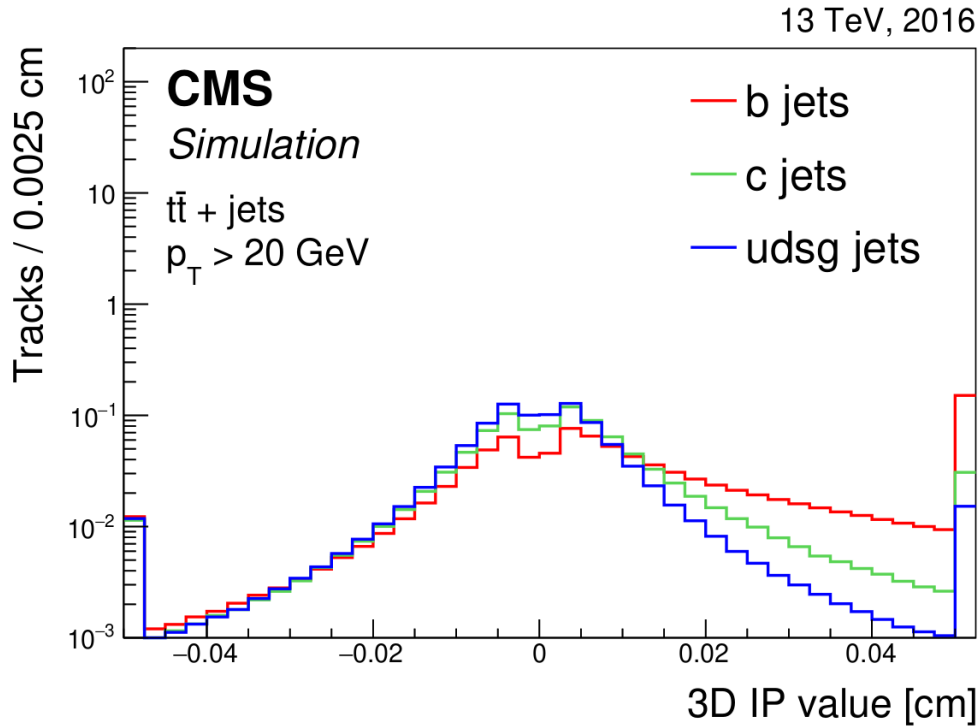


Figure 3.3: **Impact parameters of tracks associated to simulated jets of different flavors.** The three dimensional impact parameter value (3D IP) is histogrammed for jets from b, c and light (udsg) quarks in simulated $t\bar{t}$ events. Tracks from b jets show an excess of 3D IPs at high values, while tracks from light jets have 3D IPs symmetrically distributed around zero. Taken from Ref. [100].

In Figure 3.3, the impact parameters of tracks are shown for jets of different flavors in simulated events. This demonstrates how the impact parameters of tracks are on average larger for b jets than for other jets.

Secondary vertices can be reconstructed with the same vertex finding algorithms introduced in Section 3.1. In order to resolve secondary vertices and the track origin on a sub-millimeter level, good performance of the silicon tracker, especially the pixel detector is necessary. Using these track features a basic b jet algorithm can be designed. In modern jet tagging algorithms, in addition, the full jet kinematics and the constellation of PF constituents of the jets are considered when attempting to identify the jet flavor. The jet tagging algorithm used throughout this thesis is the DEEPJET algorithm [101], which is based on a neural network (NN) architecture as illustrated in Figure 3.4. The algorithm uses features of the 25 leading neutral and charged PF candidates and of the four leading secondary vertices as inputs. These features are processed in separate feature-engineering steps, where convolutional neural network (CNN) layers [102] with a kernel size of 1×1 are used to process the input features. The 1×1 convolutional elements act independently on each input candidate and derive secondary features taking into account the information of all features of the PF candidate or secondary vertex under scrutiny. The features generated after three to four iterations of this procedure are used as input to recurrent NN elements (specifically long short term memory (LSTM) elements [103]). These treat the input PF candidates and secondary vertices as a sequence, here ordered by p_T . The results of this step are concatenated for the, so far, independent processing steps for charged and neutral PF candidates and secondary vertices. Additionally, six global

3 Object reconstruction

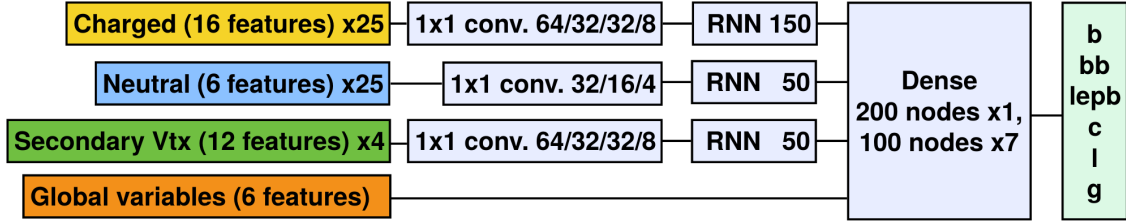


Figure 3.4: Illustration of neural network architecture of the DEEPJET b tagging algorithm. Taken from Ref. [101].

Table 3.4: b jet tagging WPs. The tight and medium b tagging WPs are used, corresponding to around 0.1% and 1% light-jet misidentification rates.

Data-taking era	medium WP	tight WP
2016preVFP	0.2598	0.6502
2016postVFP	0.2489	0.6377
2017	0.3040	0.7476
2018	0.2783	0.7100

jet features are added to the concatenation of this step. The combination is processed in a fully-connected (dense) NN and yields six output values associated to different jet flavors. Three of these output nodes are dedicated to b jets, one for c jets, one for light jets from other quarks (uds), and the last for gluons. The three b jet identification nodes differentiate between jets with one or two B hadrons and B -hadron decays involving charged leptons. These three output values are added together to yield the b jet tagging values used throughout this thesis.

The working points (WPs) are defined for the DEEPJET algorithm, based on its performance on a set of simulated events. WPs are defined at constant light-jet misidentification rates on that data set. The term light jets refers to jets originating from up, down and strange quarks, as well as gluons unless stated otherwise. Two WPs used throughout this thesis are defined as 0.1% (tight) and 1% (medium) light-jet misidentification rates. The DEEPJET b jet discriminator values corresponding to these WPs are summarized in Table 3.4. At the medium (tight) WP, b jets are correctly identified with efficiencies of around 75–80% (60%), evaluated on $t\bar{t}$ events used in the $t\bar{t}b\bar{b}$ measurement described in Part II. At the same WPs, c jets are seen to be misidentified as b jets in around 15% (3%) of cases.

The impact of the aforementioned secondary vertex reconstruction is emphasized in Figure 3.5, which shows the b jet identification efficiency versus the light jet misidentification rate of the DEEPJET algorithm for data taking eras in LHC Run 2. A clear improvement between the b jet identification efficiencies in 2016 and 2017/2018 can be observed. This is correlated to the improved pixel detector for Phase-1 of the CMS detector. As mentioned in Section 2.2.2, the innermost layer of the pixel detector had a distance of 44 mm to the interaction point in 2016, which was decreased to 29 mm starting from 2017 with the commissioning of the new pixel detector. An improvement of about 5% in the b jet identification rate at the same misidentification rate for light jets was achieved due to this improvement.

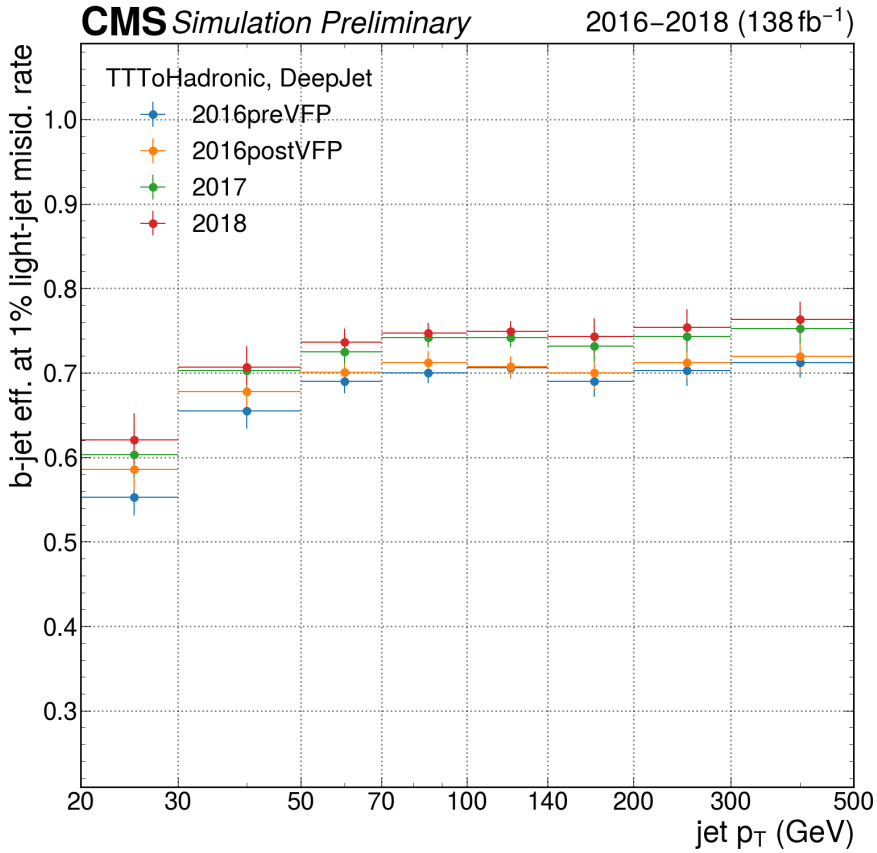


Figure 3.5: **Performance of the DEEPIET algorithm for data-taking eras during LHC Run 2.** The b jet identification efficiency on the vertical axis is shown relative to the p_T of jets on the horizontal axis at a constant light jet misidentification rate of 1%. Higher b jet efficiencies are registered in 2017 and 2018 relative to 2016 across the full p_T range. Taken from Ref. [76].

3.4 Missing transverse momentum

Some particles produced in the pp interaction cannot be reconstructed with the CMS detector, as these particles do not interact with the detector material, and are hence invisible for the purpose of detection. Examples are neutrinos, which interact only via weak interaction, or hypothetical DM candidate particles, which have not yet been observed to interact except for gravitational interactions on cosmological scales. In order to gain information on these missing particles the vectorial sum of the transverse momenta of all visible particles is calculated to yield

$$\vec{p}_T^{\text{miss}} = - \sum_{\text{vis. particles}} \vec{p}_{T,i}. \quad (3.5)$$

This uses the fact that in the initial pp collision, no (or rather negligible) momenta are present in the transverse (η, ϕ)-plane, hence the transverse momentum sum of all final-state particles should account for zero. In the longitudinal plane, this argument is not valid anymore, as the longitudinal momentum fraction of the partons inside the protons is unknown, and hence the sum of all longitudinal momenta is also unknown. The vector \vec{p}_T^{miss} thus gives an estimation of the amount of momentum in the transverse plane carried by invisible particles.

4 Cross section measurements

In this chapter, the formalism of cross section measurements will be introduced. The cross section measurements in this thesis rely heavily on the simulation of collision events, as described in detail in Chapter 5. This requires knowledge about which physics processes to expect in that phase space, at which rates, and how they are kinematically distributed. Only then, the quantities of interest can be extracted. Simplified this means, if one attempts to measure the cross section σ of a certain process, one needs to define a selection of events that match the expected signature of said process, determine the number of events from other processes that contribute to the same selection of events ($N_{\text{background}}$), and extract the difference between the number of data events (N_{data}) and $N_{\text{background}}$. The difference then corresponds to the contribution of the process of interest. To access the cross section also the integrated luminosity L_{int} , i.e. a measure of the amount of data (see Section 2.1.1), and the efficiency ϵ of the selection of the process of interest are needed, in summary yielding

$$\sigma = \frac{(N_{\text{data}} - N_{\text{backgrounds}})}{\epsilon \cdot L_{\text{int}}}. \quad (4.1)$$

The efficiency ϵ can be obtained from the simulation of the process of interest.

Realistically this procedure is more complicated as uncertainties on the knowledge of the backgrounds, the simulation, the difference between simulation and data, and the data itself have to be accounted for. To improve the sensitivity of the process of interest, i.e. to distinguish it better from the backgrounds usually also differential distributions are used for the extraction of the cross section (or any other parameter of interest). This requires, in addition to the knowledge of the expected rate of background events also information on their kinematic distributions. For example, one could use the distribution of the jet multiplicity to gain more sensitivity on a process that usually has more jets than its background processes. Cross sections are commonly measured via maximum likelihood fits, which will be introduced in Section 4.1. Specific to this thesis, normalized differential cross sections are measured, which will be introduced thereafter in Section 4.2. More details on the statistical foundations discussed here can be found in Ref. [104].

4.1 Maximum likelihood fits

In high energy physics, the determination of cross sections is commonly performed via maximum likelihood fits, where the systematic and statistical uncertainties of signal and

4 Cross section measurements

background processes are incorporated as so-called nuisance parameters α . The cross section σ can be parameterized via the signal-strength parameter μ , defined as

$$\mu = \frac{\sigma_{\text{obs.}}}{\sigma_{\text{exp.}}}, \quad (4.2)$$

where $\sigma_{\text{obs.}}$ is the cross section to be measured, and $\sigma_{\text{exp.}}$ is the expected cross section, e.g. from SM calculations, or from the simulation of the process of interest. This construction enables a measurement of the parameter μ , which is expected to be equal to one if the measured cross section $\sigma_{\text{obs.}}$ corresponds to the expected cross section $\sigma_{\text{exp.}}$. Parameters $\vec{\mu}$ are referred to as parameter of interest (POI) and can also take different forms than the signal strength. These parameters of interest are determined in the maximum likelihood fits. For this purpose, first, a basic likelihood \mathcal{L} is constructed as

$$\mathcal{L}[\mu] = \mathcal{P}(n|y[\mu; s, b]) = \frac{y[\mu; s, b]^n}{n!} e^{-y[\mu; s, b]}. \quad (4.3)$$

Here, \mathcal{P} is the Poisson distribution as the experiment is a simple counting experiment. It is a function of the number of observed data events n , and the expected number of events y , defined as

$$y[\mu; s, b] = \mu \cdot s + b, \quad (4.4)$$

with s being the number of expected signal events, and b the number of expected background events. The likelihood \mathcal{L} here follows a Poissonian distribution which is maximized when the expected number of events y matches the observed number of events in data n . In other words, the maximization of the likelihood finds the optimal parameter μ for the given system of n , s and b .

This is extended to a binned (i.e. discretized) likelihood, by accounting for data, signal and background events in multiple bins i , as well as the possibility for multiple parameters μ and multiple backgrounds j , yielding

$$\mathcal{L}[\vec{\mu}] = \prod_i \mathcal{P} \left(n_i \left| S_i[\vec{\mu}] + \sum_j b_{ji} \right. \right). \quad (4.5)$$

Here, the signal contribution S_i is parameterized as an arbitrary function of the parameters $\vec{\mu}$, where in the simplest form this expression could take the form of eq. (4.4), $\mu \cdot s$. The parameters $\vec{\mu}$ correspond to the pre-defined signal-strength parameters. In Section 4.2, S_i will be defined differently, in order to allow for normalized differential cross section measurements.

4.1.1 Nuisance parameters

This construction does not yet account for systematic uncertainties in the determination of the signal contributions s and background contributions b . This dependence is introduced as nuisance parameters $\vec{\alpha}$, which incorporate the variation of signal and background components based on the estimation of systematic uncertainties, i.e. yielding

$$\mathcal{L}[\vec{\mu}, \vec{\alpha}] = \prod_i \mathcal{P} \left(n_i \left| S_i[\vec{\mu}, \vec{\alpha}] + \sum_j b_{ji}[\vec{\alpha}] \right. \right) \cdot \mathcal{N}[\vec{\alpha}]. \quad (4.6)$$

The term $\mathcal{N}[\vec{\alpha}]$ is an auxiliary likelihood of the nuisance parameters, introduced as a constraint term to take into account the value of the nuisance parameters. This term is often approximated as the probability density of a multivariate Gaussian distribution with

mean values $\tilde{\alpha}$, or as log-normal distributions for rate-changing effects (see below). Variations of the nuisance parameters away from its priors, therefore, decrease the likelihood function \mathcal{L} . The values of the nuisance parameters are predetermined, either from theory or auxiliary measurements, such as the measurement or calibration of efficiencies (see Chapter 6).

Explicitly, a distinction is made between uncertainties having an effect only on the overall rate of a process, or having an effect on the distribution of a process in the bins i , referred to as shape-changing effects.

Rate-changing uncertainties

The rate-changing effects are modeled via log-normal distributions

$$\mathcal{N}[\alpha; \tilde{\alpha}] \propto \frac{1}{\alpha \ln(K)} \cdot \exp\left(-\frac{\ln(\alpha/\tilde{\alpha})^2}{2 \ln(K)^2}\right), \quad (4.7)$$

where $\tilde{\alpha}$ is the best estimate of the nuisance parameter α , e.g. from auxiliary measurements. The parameter K is defined as $K = e^\epsilon \simeq 1 + \epsilon$, where ϵ is the rate of variation from this uncertainty. For example, an uncertainty of 5% would be encoded via $\epsilon = 0.05$ and therefore $K = 1.05$. This also allows for asymmetric variations, by specifying K_{up} and K_{down} for independent variations in both directions. The probability density function \mathcal{N} is maximized where $\alpha = \tilde{\alpha}$. Variations of the nuisance parameter α by $K^{\pm n}$ are identical and follow the Gaussian probabilities, i.e. contain n standard deviations of the integrated probability.

The contributions of processes in eq. (4.6), e.g. b , are functions of the nuisance parameters α , and are multiplied by $K[\alpha]^\alpha$ with an interpolation of K , following

$$K[\alpha] = \begin{cases} K_{\text{up}} & \text{if } \alpha > 1, \\ \frac{\alpha}{4}(3 - \alpha^2)(K_{\text{up}} - K_{\text{down}}) + \frac{1}{2}(K_{\text{up}} + K_{\text{down}}) & \text{if } |\alpha| \leq 1, \\ K_{\text{down}} & \text{if } \alpha < -1 \end{cases} \quad (4.8)$$

Here, α follows a Gaussian distribution with central value $\alpha = 0$ and standard deviation ± 1 . This interpolation yields $K(1) = K_{\text{up}}$ and $K(-1) = K_{\text{down}}$, i.e. scales the process by K if the nuisance parameter α is varied by one standard deviation.

Shape-changing uncertainties

Systematic uncertainties for which an individual effect on each bin i is expected are implemented via varied templates which describe the estimated variation by one standard deviation relative to the nominal distribution, obtained from the auxiliary measurements of α . The templates are interpolated by factorizing the event yields e.g. of b as $b_i[\alpha] = I[\alpha] \cdot N_i[\alpha]$, such that I is the integral of b . The difference between the nominal event yields and the event yields in the variations are considered as separate rate-changing uncertainties using $K^{\text{up/down}} = I^{\text{up/down}}/I^{\text{nom}}$, following the implementation described above. The morphing of the templates for the remaining shape variation is defined based on the normalized variations $N[\alpha]$ as

$$N[\alpha] = \begin{cases} N^{\text{up}} + (\alpha - 1) \cdot \Delta^{\text{up}} & \text{if } \alpha < 1, \\ N^{\text{nom}} + \frac{\alpha}{2}(N^{\text{up}} - N^{\text{down}}) + \frac{\alpha^2}{16}(3\alpha^4 - 10\alpha^2 + 15) \cdot (\Delta^{\text{up}} + \Delta^{\text{down}}) & \text{if } |\alpha| \leq 1, \\ N^{\text{down}} - (\alpha + 1) \cdot \Delta^{\text{down}} & \text{if } \alpha > 1 \end{cases} \quad (4.9)$$

4 Cross section measurements

Here, $\Delta^{\text{up/down}}$ correspond to the difference of the varied and nominal contributions after the aforementioned removal of the rate contribution I to the nuisance parameter, $\Delta^{\text{up/down}} = N^{\text{up/down}} - N^{\text{nom}}$.

4.1.2 Construction of the likelihood ratio

Following the Neyman-Pearson lemma [105], the optimal test of a simple statistical hypothesis is the likelihood ratio. Hence, a negative log-likelihood ratio is constructed from the likelihood defined above as

$$q_{\vec{\mu}} = -2 \ln \frac{\mathcal{L}[\vec{\mu}, \hat{\vec{\alpha}}_{\vec{\mu}}]}{\mathcal{L}[\hat{\vec{\mu}}, \hat{\vec{\alpha}}_{\hat{\vec{\mu}}}]}, \quad (4.10)$$

referred to as the test statistic. The ratio is defined from the likelihood at two different points, the first using the set of parameters $\{\vec{\mu}, \hat{\vec{\alpha}}_{\vec{\mu}}\}$ which maximize the likelihood \mathcal{L} at fixed values of $\vec{\mu}$, and the set of parameters $\{\hat{\vec{\mu}}, \hat{\vec{\alpha}}_{\hat{\vec{\mu}}}\}$ which globally maximize \mathcal{L} . In this construction, the nuisance parameters $\vec{\alpha}$ are determined as functions of $\vec{\mu}$, referred to as the profile likelihood estimation. By constructing this negative log-likelihood ratio, the parameters $\vec{\mu}$, given the nuisance parameters $\vec{\alpha}$, can be estimated by minimizing $q_{\vec{\mu}}$.

Confidence intervals

Confidence intervals of the estimated parameters can be constructed using Wilks' theorem [106] to approximate the test statistic as parabolic in the limit of large enough samples where an approximation of the Poissonian likelihoods as Gaussian distributions is valid. The confidence interval of z Gaussian standard deviations for a certain $\theta \in \{\vec{\mu}, \vec{\alpha}\}$ can be obtained by profiling the other parameters $\vec{\theta}$ and finding θ^{\pm} such that

$$q_{\vec{\mu}^{\pm}}(\theta^{\pm}) = q_{\vec{\mu}}^{\min} + z^2. \quad (4.11)$$

In the large sample limit, the confidence intervals can also be obtained from the covariance matrix C , which is estimated using the inverse of the Hessian (inverse of the second derivative) of the likelihood at its maximum [107],

$$C_{ij}^{-1} = \left. \frac{\partial^2 \mathcal{L}}{\partial \theta_i \partial \theta_j} \right|_{\hat{\vec{\theta}}}. \quad (4.12)$$

Confidence intervals are then obtained from

$$\theta_k^{\pm} = \hat{\theta}_k \pm \sqrt{C_{kk}}. \quad (4.13)$$

The covariance matrix C can also be used to estimate the correlations of parameters $\vec{\theta} \in \{\vec{\mu}, \vec{\alpha}\}$ in the likelihood estimation.

4.2 Normalized differential cross section measurements

The results of this thesis are parameterized as normalized differential cross section measurements. In Part II, the cross section of the $t\bar{t}b\bar{b}$ process is independently measured as a function of a range of observables. For each observable the following parameterization is used. The fiducial cross section σ_{fid} is separated into pre-defined generator-level bins j of the observable X (see introduction in Section 7.3), σ_j , such that

$$\sum_j \sigma_j = \sigma_{\text{fid}}. \quad (4.14)$$

4.2 Normalized differential cross section measurements

For the construction of the likelihood, signal-strength modifiers are defined for the fiducial cross section, μ_{fid} , to scale σ_{fid} , and $N - 1$ parameters μ_j to scale the fractions f_j of events in the first $N - 1$ generator-level bins j of the observable X . The fractions f_j are defined as

$$f_j = \frac{\sigma_j}{\sigma_{\text{fid}}} = \frac{\sigma_j}{\sum_i \sigma_i}. \quad (4.15)$$

Accordingly, the signal-strength modifiers are defined as

$$\mu_{\text{fid}} = \frac{\sigma_{\text{fid}}^{\text{obs.}}}{\sigma_{\text{fid}}^{\text{exp.}}}, \text{ and } \mu_j = \frac{f_j^{\text{obs.}}}{f_j^{\text{exp.}}}, \quad (4.16)$$

where $\sigma_{\text{fid}}^{\text{exp.}}$ and $f_j^{\text{exp.}}$ are the fiducial cross section and the fractions obtained from simulation, and $\sigma_{\text{fid}}^{\text{obs.}}$ and $f_j^{\text{obs.}}$ are the fiducial cross section and fractions from the measurement. Following the parameterization of the likelihood in eq. (4.6), the event yields S_{ij} of the first $N - 1$ generator-level bins j are scaled as

$$S_{ij} = \mu_{\text{fid}} \mu_j s_{ij}, \quad (4.17)$$

where s_{ij} are the expected yield of signal events of generator-level bin j and bin i of the distribution used in the fit (see Section 4.1). The last generator-level bin N is scaled as a function of all other POIs in order to retain the appropriate number of degrees of freedom, by defining μ_N as

$$\mu_N = \frac{1}{f_N^{\text{exp.}}} \left(1 - \sum_{k=1}^{N-1} \mu_k f_k^{\text{exp.}} \right). \quad (4.18)$$

Following this construction, the fiducial cross section can be obtained directly from eq. (4.16), and the normalized differential cross sections are defined as

$$\frac{1}{\sigma_{\text{fid}}^{\text{obs.}}} \frac{d\sigma_j^{\text{obs.}}}{dX} = \mu_j f_j^{\text{exp.}} / w_j, \quad (4.19)$$

where w_j is the width of generator-level bin j . This also allows for obtaining the confidence intervals of the fiducial and normalized differential cross sections directly from profiling the corresponding parameters μ_{fid} and μ_j (for $j < N$) and from the covariance matrix C (for $j = N$).

The calculations of the likelihoods and their minimization are performed using the `smoofit` software package [108]. This package uses the JAX software package [109] for automated differentiation of the negative log-likelihood function.

5 Event simulation

The simulation of collision events is an important part of LHC data analysis. The physics processes happening in a single pp collision are usually unknown, and only the final state, consisting of stable particles registered in the detector, is known. Hence, simulations of various processes are performed in order to get an estimate of what to expect for a certain process in terms of the number of events and their kinematic distributions. The simulation of events is performed in multiple stages, designed to reflect as well as possible the particle physics processes taking place in the detector environment. The central part of the event simulation is the simulation of the hard scattering process, described in Section 5.2. This is interfaced with parton distribution functions describing the substructure of the protons, discussed in Section 5.1. The final-state partons of the hard scattering undergo parton showering and hadronization, summarized in Section 5.3. To mimic the processes recorded in the detector, the underlying event and pileup have to be accounted for as well, described in Section 5.5 and Section 5.6. As a last step, in Section 5.7 the simulation of the detector response is introduced. An illustration of these processes is shown in Figure 5.1. A summary of simulation tools relevant for this thesis is given in Section 5.8. This also includes a description of jet flavor identification for simulated jets and a description of the flavor schemes (FSs) used in simulation.

5.1 Parton distribution functions

At pp colliders like the LHC protons are brought to collision at high energies. At such high energies the particles effectively interacting are not the protons themselves, but their constituents, referred to as partons. The probability to find a certain parton at momentum fraction x in a proton is described by the parton distribution function (pdf). The pdfs depend on the type of parton, which are mostly quarks and gluons, and the energy scale μ^2 at which they are probed. It is not currently possible to obtain pdfs from first principles. However, the description of the evolution of pdfs is possible with the Dokshitzer-Gribov-Lipatov-Altarelli-Parisi (DGLAP) evolution equations [111–114]. These equations relate a pdf at two different scales μ^2 . Hence, pdfs can be measured at some energy scale and evolved to other energy scales. As the universal behaviour of the proton also does not change depending on the experimental environment, these pdf measurements are globally valid independent of the experimental setup.

As an approximation at low energies, a proton consists of three valence quarks; two up quarks and one down quark. These valence quarks carry large momentum fractions of

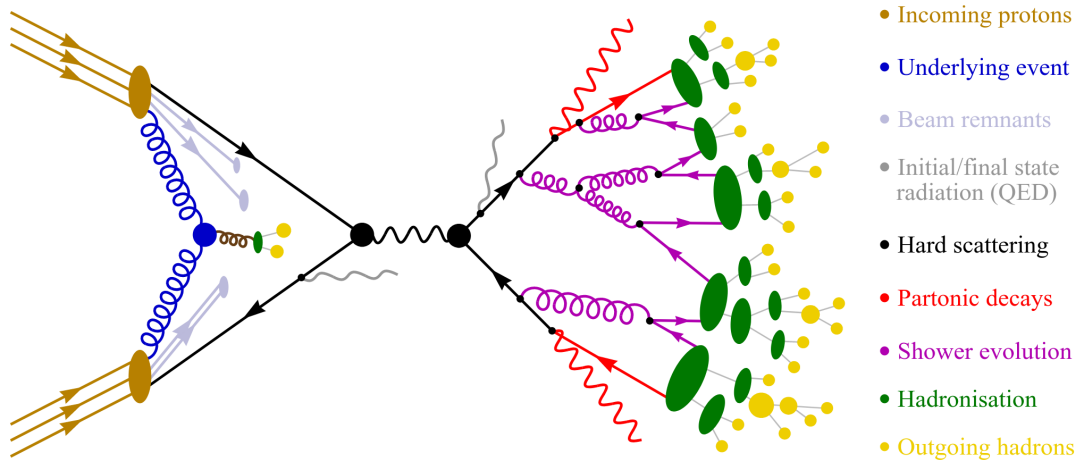


Figure 5.1: **Illustration of a pp collision.** The hard scattering process (black) occurs between partons of the incoming protons. The final-state partons after the hard interactions decay (red) and radiate gluons, forming parton showers (violet). Partons form hadrons (green) during hadronization and decay into lighter hadrons (yellow). Additional parton interactions (blue) and the beam remnant (grey) are considered as underlying event contributions. Taken from Ref. [110].

the proton, yielding two pdfs with similar momentum distributions, but twice the probability density for up quarks. Gluons are exchanged by the valence quarks and can additionally form quark-antiquark pairs, called sea quarks. These sea quarks and gluons also carry a fraction of the proton momentum. As they originate in low-energy gluon exchanges their pdfs are dominant at low x . With increasing energy of the proton, the number and momentum fraction of sea quarks and gluons increases, as QCD interactions between the partons become more frequent, leading to an increase of their pdfs. This is illustrated in Figure 5.2 for the NNPDF3.1 pdf set at two different energy scales [115]. The NNPDF3.1 pdf set is a NNLO pdf set obtained from a global fit of a wide range of measurements at the D0, LHCb, ATLAS, and CMS experiments. This pdf set is the first that includes $t\bar{t}$ and Z boson p_T measurements by the ATLAS and CMS Collaborations. Unless stated otherwise, this pdf set is employed for all event simulations used in this thesis.

5.2 Hard scattering

The hard scattering describes the partonic subprocess, where the partons of the colliding protons interact and form new particles. Cross sections (i.e. probabilities) $\hat{\sigma}$ can be calculated for this partonic subprocess using the Feynman diagrams and rules introduced in Section 1.5. For an exact calculation of the scattering matrix element (ME), in principle, all possible Feynman diagrams that yield the desired final state have to be considered. As adding, for example, more additional radiation is in principle unlimited, this is not possible. However, the ME and its calculation can be parameterized as a perturbation theory, evolved in orders of a small parameter. The parameter suitable for this evolution is the strong coupling constant α_s which is small at the high energies where the hard scattering takes place (see Section 1.4.1). Hence, the cross section is determined as a perturbative series

$$\hat{\sigma} = \sigma_{\text{LO}} \cdot \left(1 + \alpha_s \sigma_{\text{NLO}} + \alpha_s^2 \sigma_{\text{NNLO}} + \dots \right). \quad (5.1)$$

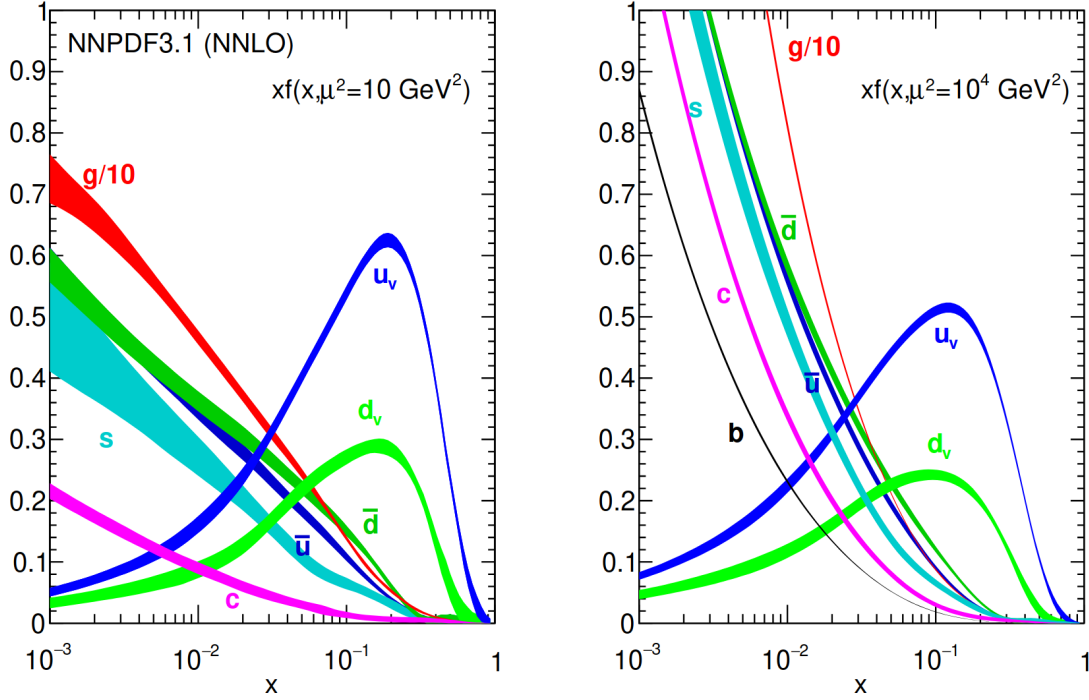


Figure 5.2: NNPDF3.1 NNLO pdf as a function of the momentum fraction X of partons in a proton. The NNPDF3.1 NNLO pdf set is evaluated at two different scales μ^2 , on the left at lower energy scale $\mu^2 = 10 \text{ GeV}^2$ and on the right at higher energy scale $\mu^2 = 10^4 \text{ GeV}^2$. The gluon pdfs (red) are scaled by a factor of $1/10$ as their contribution is by far dominant at low momentum fraction x . Taken from Ref. [115].

The LO cross section σ_{LO} contains only Feynman diagrams with the lowest order in α_s , i.e. with the lowest number of vertices in the diagram. Additional corrections σ_{NLO} and σ_{NNLO} can be calculated, corresponding to NLO and NNLO corrections, respectively. These are suppressed with increasing orders of α_s , and hence contribute less and less. Therefore, a good approximation of $\hat{\sigma}$ is often already achieved at a few orders of the perturbation series. Corrections at NLO include, for example, virtual corrections to the LO amplitude, i.e. a loop in the Feynman diagram, or one real emission of an additional particle, increasing the number of final-state partons. Corrections at NNLO include diagrams with two loops, two additional real emissions, or one emission and one loop.

To obtain the total cross section σ of a process, the partonic cross section $\hat{\sigma}$ can be convoluted with the pdfs of Section 5.1. This factorized approach is possible due to the factorization theorem which states that the physics processes at low energies and high energies can be treated independently. This also allows for the universal use of the proton pdfs determined in one experiment at other experiments. The total cross section describes the probability of producing the desired final state X , here with a pp initial state. Hence, all possible initial partons a, b of the hard scattering with respective momentum fractions x inside the proton have to be considered. This yields the QCD factorization theorem

$$\sigma(\text{pp} \rightarrow X) = \sum_{a,b} \iint dx_1 dx_2 p_a[x_1, \mu_F^2] p_b[x_2, \mu_F^2] \hat{\sigma}_X[x_1, x_2, \mu_F^2, \mu_R^2]. \quad (5.2)$$

The hard scattering cross section $\hat{\sigma}_X$ is a function of two energy scales, the factorization scale μ_F at which the pdfs p are evaluated, and the renormalization scale μ_R , which describes the scale dependence of the strong coupling constant α_s . For the event simulation,

5 Event simulation

these two scales have to be explicitly chosen as these are not physical parameters that can be determined. These energy scales determine the transition from pdfs to hard scattering MEs (μ_F), and the scale at which the perturbative calculation of hard scattering MEs is performed (μ_R).

When matching the ME calculation to a parton shower (PS), a matching scale has to be specified. For that purpose, the h_{damp} parameter is used in ME simulations with the POWHEG generator [116, 117]. This h_{damp} parameter is a threshold that separates emissions with larger momentum and smaller momentum. A damping procedure is applied that reduces the emissions with smaller momentum from the ME simulation which is then left to be described with the PS.

5.3 Parton showers

The final-state particles produced in the hard scattering have to be evolved to lower energy scales, where a realistic comparison with data is possible. This process accounts for higher-order corrections that have as of yet not been accounted for due to the fixed-order calculation of the scattering ME. Hence, PS models are employed to approximate the higher-order contributions. The PSs add additional electromagnetic (EM) and QCD radiation to the initial state before the scattering, initial-state radiation (ISR), and after the scattering, final-state radiation (FSR). Photons or gluons generated in this process can then split into quark-antiquark or lepton pairs, producing a shower of partons with iteratively lowering energies. The splitting into two partons is described by the Sudakov form factor [118] which describes the probability of a parton at energy scale q_1 to evolve to energy scale q_2 without splitting. The PSs are evolved to the energy scale of hadronization, at around 1 GeV. In the initial state, additional adjustments have to be taken into account, as a splitting of initial-state partons changes the energy scale at which the partons enter the scattering ME calculations. Hence, a backward evolution is employed for the initial-state showers, which makes the Sudakov factors dependent on the ratio of pdfs at both energy scales q_1 and q_2 .

In most cases, the PS calculations are complementary to the perturbative ME calculations, as they describe processes at lower energy scales. However, when using higher-order ME calculations (i.e. NLO and above), additional initial-state and final-state partons can be described by both the PS and the ME simulation, and can hence be double counted if they occupy the same phase space. As the PSs are evolved in the soft and collinear limits, they do not often produce well-separated radiation, while the additional radiation from higher-order calculations do. This enables matching and merging algorithms for the ME calculation and PS simulation, where overlaps are removed, in such a way that the strengths of the ME calculation and PS simulation are exploited.

5.4 Hadronization

The PS process evolves the partons of the ME calculations to energy scales where the partons hadronize and form hadrons. At these energy scales, the partons are no longer free (asymptotic freedom), as the running strong coupling constant is large, i.e. particles are in the regime of confinement (see Section 1.4). As this energy regime does not allow for perturbative calculations any longer, phenomenological models have to be employed to describe the evolution of hadronization. For this purpose, for example, the Lund string model is used [119]. In the Lund string model, gluons, as the carriers of the strong interaction, form flux tubes between color-charged particles. As the distance between these particles increases, the energy contained in the flux tubes increases due to their linear

potential. If the potential energy is high enough, a new quark-antiquark pair is created which forms new flux tubes with the other particles. This hadronization model is used for example in the PYTHIA general-purpose event generator [84]. A different model, the cluster hadronization model, is used for example by the HERWIG event generator [120, 121]. In this model quarks and gluons are combined into color-neutral clusters which are iteratively fragmented into smaller clusters until they form stable hadrons.

5.5 Underlying event description

As indicated in Figure 5.1, besides the hard scattering also soft interactions and proton remnants are present in a pp collision and have to be taken into account in a realistic simulation of data. Two factors contribute to the so-called underlying event simulation. The first is multi-parton interactions (MPIs), which are additional soft interactions of other partons in the pp collision. The second is beam remnants, i.e. the parts of the protons that did not partake in the elastic scattering processes. As these processes are low-energetic processes, phenomenological models are needed for their description. Therefore, underlying-event tunes are provided, where the parameters of the underlying-event models are tuned to a certain pdf set for ME and PS calculations at a certain value of the strong coupling constant α_s . The CP5 underlying-event tune [122] is used for almost all simulations at the CMS Collaboration, tuned to the NNPDF3.1 NNLO pdf set and the PYTHIA PS at $\alpha_s = \alpha_s(\mu_R = m_Z) = 0.118$, i.e. the strong coupling constant evaluated using the Z boson mass as the renormalization scale.

5.6 Pileup

The contribution of additional interactions in the same bunch crossing is also taken into account in the simulation, referred to as pileup. Pileup profiles are assumed before the simulation, with a mean expected number of pileup interactions per bunch crossing, modeled via Poisson distributions. Additionally, out-of-time pileup has to be considered, where interactions of one bunch are falsely associated with the next or previous bunch crossing, due to the limited detector response time.

5.7 Detector simulation

As a final step, the response of the particles from the event simulation chain to the CMS detector has to be simulated. For this, the GEANT4 package is used [123], which contains a full model of the CMS detector and simulates the interaction of all particles with the different detector components, as well as the read-out of the signals via sensors inside the detector. This facilitates a good comparison with the data recorded at the CMS experiment.

5.8 Tools

In this section, an overview is given of the tools used for event simulation in the measurements of this thesis.

MadGraph5_aMC@NLO: The MADGRAPH5_aMC@NLO ME generator [124] is the combination of the MADGRAPH [125] and MC@NLO [126] event generators, which are matched with PS simulations. In this event generator, processes at LO are computed with the MADGRAPH generator, while NLO diagrams are calculated with the MC@NLO

generator. The MC@NLO generator avoids overcounting of contributions by subtracting the approximation of the NLO contribution of the PS simulation from the exact NLO calculation independently for each simulated event, i.e. potentially reducing the weight of the event¹. As the approximation of the NLO contribution in the PS (which is subtracted) does not necessarily need to be smaller than the contribution of the NLO calculation itself, negative event weights are possible with this generation approach.

MadSpin: MADSPIN [127] is an algorithm employed in the MADGRAPH event generator to simulate the decay of narrow resonances (i.e. resonances with a small decay width) while preserving spin correlation and finite-width effects in the decay.

POWHEG: The positive weight hardest emission generator (POWHEG) is an ME generator [116, 117]. It provides calculations at LO and NLO precision. The generator is designed such that it yields only events with positive weights even at NLO, by generating the hardest emission first. The POWHEG event generator can hence be interfaced with any p_T -ordered PS simulation with double-logarithmic accuracy in the PS. Implementation of new processes is possible in the POWHEG-BOX [116].

POWHEG-BOX-RES: The POWHEG-BOX-RES [128] is an updated version of the POWHEG-BOX, also supporting radiation in decaying resonances.

OPENLOOPS: With the OPENLOOPS package [129] automatic calculations of tree-level and one-loop scattering amplitudes can be performed.

PYTHIA: PYTHIA is an ME generator that also provides PS simulation and a description of underlying-event processes [84]. The calculation of MEs is only performed at LO, hence, often only the PS and underlying-event simulation are used, while interfaced with another NLO ME generator. PYTHIA uses a p_T -ordered PS implementation and relies on the Lund string model for hadronization [119].

HERWIG: HERWIG is an ME event generator that also provides PS simulation and a description of underlying-event processes [120, 121]. In this thesis, it is only used as a PS simulation for an alternative $t\bar{t}b\bar{b}$ prediction. HERWIG uses the cluster hadronization model. A dedicated underlying-event tune, the CH3 tune [130] is used for HERWIG, matched to the same pdf and α_s settings as described in Section 5.5 for PYTHIA.

SHERPA: SHERPA is a general purpose event generator, supporting ME and PS simulation and underlying-event description [131]. In this thesis, it is only used for the simulation of an alternative $t\bar{t}b\bar{b}$ prediction.

FxFx merging: The FxFx merging scheme [132] is a merging scheme at NLO for ME and PS simulation for final states with a fixed number of additional jet radiation, for example the production of $t\bar{t}$ with zero, one or two additional jets. The processes are merged based on the number of emissions above a certain merging scale Q which orthogonalizes the independent simulations.

MLM merging: The multi-leg merging (MLM) procedure [133] is a merging scheme at NLO for ME and PS simulation, where jet algorithms are used to match jets from the PS to the final state partons. Double counting of contributions is mitigated by discarding events in which unique matches of final-state and partons are not possible. This effectively discards events where two partons are so close that no unique separate jets are found for both, or one parton has too low energy to generate its own jet.

¹Generally, simulated events are weighted according to the sampling density of the event generators in order to match the distribution of events expected in data. For example, more events could be simulated in a sparse phase space region in order to get a good estimate of the processes in that region.

5.8.1 Jet flavor identification in simulation

In order to identify the flavor of a jet on truth level, i.e. in simulation, a ghost-clustering algorithm is applied [134]. This algorithm adds the hadrons from hadronization to the clustering of stable final-state particles, with momenta scaled to a negligible value but keeping their direction. Following this method, the hadrons are clustered in the particle-level jets without affecting the clustering procedure itself. Hence, the flavor of the hadron can be used to identify the origin of the jet, and by extension its flavor. Different classes are defined, based on the number and flavor of the hadrons clustered inside a jet. A particle-level jet containing one or more ghost-clustered B hadrons is referred to as b jet. Particle-level jets without any ghost-clustered B hadrons, but at least one C hadron are classified as c jets. All other jets, i.e. without any B or C hadron are classified as light jets².

In addition, the origin of these particle-level jets can be of interest, i.e. when identifying whether a jet originated from the decay of top (anti)quarks or not. For that purpose, the MC history of the top quarks is used to define what constitutes an additional jet. A particle-level jet in which any of the ghost-clustered hadrons have a top (anti)quark in their MC decay-chain ancestry is classified as a $t\bar{t}$ jet, and all other jets are classified as additional jets. This procedure only takes into account particle-level jets with $p_T \geq 20$ GeV and $|\eta| \leq 2.4$.

5.8.2 Flavor schemes

Pairs of b quarks and antiquarks can also be present inside a proton if the proton energy is high enough. This is reflected in Figure 5.2, where at the lower energy scale (left) of $\mu^2 = 10$ GeV² no b pdf is present yet, but appears at the higher energy scale (right) of $\mu^2 = 10^4$ GeV², which is well above the $b\bar{b}$ production threshold of $2m_b$, at the order of 10 GeV.

The pdfs are evaluated at energy scales μ_F where the mass of the b quark is negligible compared to the energy scale. This justifies ME calculations in which the mass of the b quark is set to zero. This approach is called the five flavor scheme (5FS) as it assumes five active flavors in the proton pdf. Calculations of hard scattering processes involving heavy quarks involve terms with logarithms in μ^2/m_Q^2 and evolutions in powers of m_Q^2/μ^2 , where μ^2 is the energy scale of the hard scattering and m_Q is the mass of the heavy quark, e.g. the b quark. By setting the b quark mass to zero, the terms m_Q^2/μ^2 vanish and simplify the ME calculations. The origin of the logarithmic terms is collinear gluon splitting processes into massive quarks, e.g. $g \rightarrow b\bar{b}$. As these would lead to divergences when assuming $m_Q = 0$, these processes are absorbed into the pdf for initial state $g \rightarrow b\bar{b}$ splitting and into the PS for final state $g \rightarrow b\bar{b}$ splitting.

An alternative approach is to consider the b quarks as massive, which is justified relative to the mass of the proton. In this case, the calculation of the MEs cannot be simplified. This approach is called the four flavor scheme (4FS) as it assumes four active flavors in the proton pdf. In this flavor scheme, initial states with b quarks do not have to be considered, i.e. the b quark pdf of the proton are neglected and initial b quarks are obtained from initial-state $g \rightarrow b\bar{b}$ splitting in the ME. As this FS provides a more accurate description of $g \rightarrow b\bar{b}$ splittings in the ME, this FS is often preferred for processes with b quarks in the initial- or final-state, for example the $t\bar{t}b\bar{b}$ process.

²Note that the definition of light jets in Part II includes c jets, as for that measurement only a distinction between b jets and other jets is necessary.

6 Corrections to simulated events

After the simulation steps introduced in Chapter 5, residual differences between simulated events and data events are still present. For example, efficiencies of triggers or lepton identification algorithms can differ between simulation and data. These residual differences are corrected via scale factors (SFs) derived in auxiliary measurements. Most of the necessary SFs are determined in a combined effort by the CMS Collaboration. They are applied as weights to simulated events, reweighting the kinematic distributions of simulated events to match the distributions observed in data. In the following, all corrections to simulated events necessary for the measurements in this thesis are introduced. The uncertainties of the resulting corrections are considered as part of the measured uncertainties and are further described in Section 8.7 for the $t\bar{t}b\bar{b}$ measurement.

6.1 Pileup reweighting

In the central production of simulated events by the CMS Collaboration, an average number of pileup interactions, and a pileup profile are included (see Section 5.6). A Poisson-distributed pileup profile is used in simulation with the mean value of pileup interactions set to an estimated value for the data taking. As the production of simulated events is time-consuming, this process is already started before the actual data taking. Hence, the assumed pileup profile in the simulation does not necessarily match the observed distribution. For example, changes in the instantaneous luminosity during the run affect the number of pileup interactions. In order to correct for this effect, SFs between data and simulation are derived and applied to simulated samples to match the pileup profile observed in data. The corrections are derived with an inclusive data set, assuming a total inelastic proton-proton cross section of 69.2 mb [135]. As the assumed and measured pileup profiles vary per data-taking era, independent corrections are derived for each data-taking era. In Figure 6.1, the distribution of the number of primary vertices is shown after applying the pileup-reweighting factors. The agreement between data and simulation is abhorrent, even after correction. As this reweighting is orthogonal to other kinematic observables in the high- p_T regime relevant for measurements in this thesis, a further correction of this mismodeling is not applied. Possible variations of the assumed inelastic proton-proton cross section would, however, improve the agreement, as can be inferred from the shaded bands in Figure 6.1.

6 Corrections to simulated events

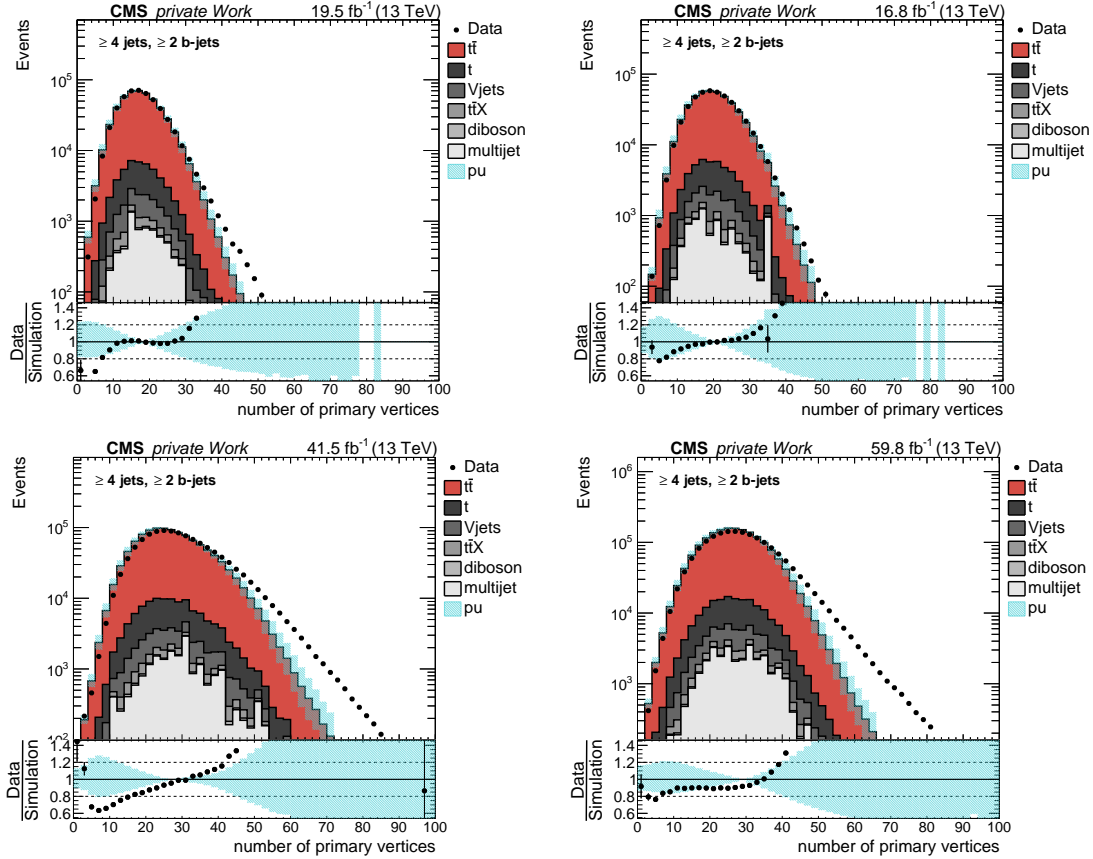


Figure 6.1: **Number of primary vertices per event.** The primary vertex distribution is shown for the selection of events described in Section 8.4. The distributions of simulated events are shown after pileup-reweighting factors are applied. Each era is shown separately, 2016preVFP (top left), 2016postVFP (top right), 2017 (lower left), and 2018 (lower right). The shaded band indicates a variation of $\pm 4.6\%$ of the assumed inelastic pp cross section.

6.2 L1 pre-firing

As explained in Section 2.2.3, the L1 trigger uses trigger primitives to make trigger decisions. During the 2016 and 2017 data-taking, it was observed that a significant fraction of trigger primitives of the ECAL were associated with the wrong bunch crossing due to a timing shift in the ECAL read-out electronics (pre-firing). Two consecutive bunch crossings are not allowed to be triggered by the same L1 trigger primitives. Hence, an association of the trigger primitive to the previous bunch crossing can veto a trigger on the actual bunch crossing, effectively leading to a self-veto of the event. This issue was most pronounced in the ECAL in a range of $2 \leq |\eta| \leq 3$. A similar issue was observed for muons in the muon system due to the limited time resolution of the muon system, which is most pronounced in 2016 but also impacts 2017 and 2018 data.

As this feature is not reflected in the simulation, dedicated correction factors are applied to simulated events in the respective years to account for this difference. The SFs are derived by calculating pre-firing probabilities for all photons, jets, and muons as

$$w_{\text{L1 pref.}} = \prod_{\gamma, \mu, \text{jets}} \left(1 - \epsilon_{\text{pref.}}[\eta, p_{\text{T}}] \right), \quad (6.1)$$

where $\epsilon_{\text{pref.}}$ are the observed pre-fire efficiencies, parameterized as functions of p_{T} and η .

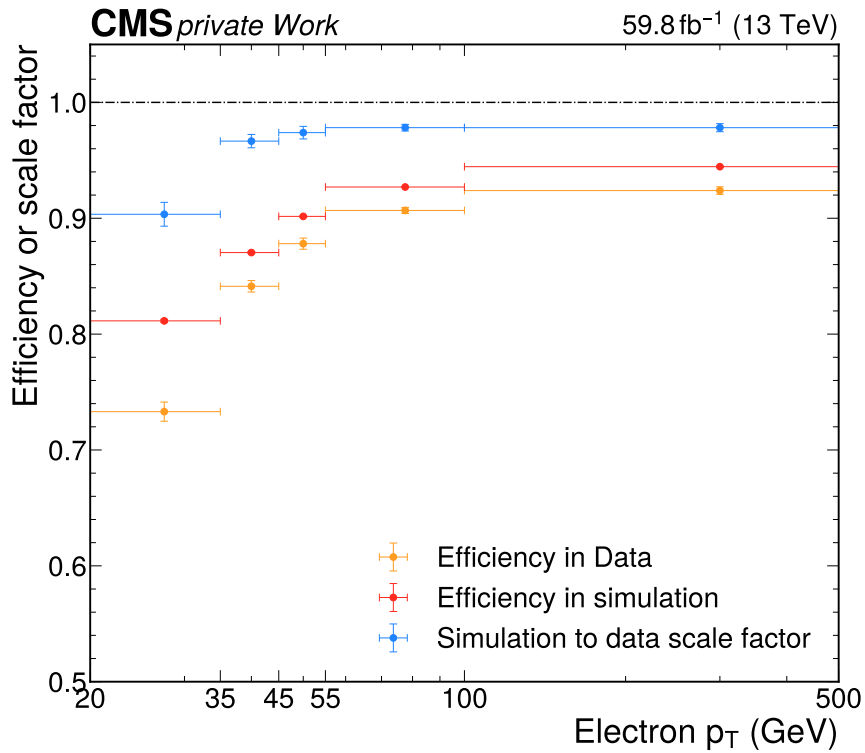


Figure 6.2: **Efficiency of electron HLT configuration used in 2018.** The trigger efficiency is shown for simulated events (red) and data (orange). The ratio of both, the SF, is shown in blue.

6.3 Trigger efficiencies

The HLTs applied for data taking are also included in the simulation of events. Residual differences in the trigger performance between simulation and data are corrected with trigger SFs. SFs have to be derived for each combination of HLT paths used in the measurements. The trigger efficiencies are derived by using an uncorrelated reference trigger from the ratio of events passing the reference trigger and the trigger under scrutiny, and the events passing the reference trigger (tag-and-probe method). By using events that pass an uncorrelated reference trigger, the efficiency of the trigger under scrutiny can be determined in an unbiased way and translated from the trigger SF derivation region to the analysis phase space. In the measurements of this thesis, separate HLT path combinations are used for triggering electrons and muons. The trigger configurations are introduced in Section 8.3. SFs for the muon channels are derived from a selection of events enriched in $Z \rightarrow \ell\ell$ and are provided by CMS [83]. The electron HLT SFs are derived specifically for these measurements and use a $t\bar{t}$ -enriched phase space with one electron and one muon. The same HLT muon triggers are used as a reference trigger for this trigger efficiency measurement. The correlation between the muon and electron triggers was calculated to be less than 1%. In Figure 6.2, the trigger efficiency for the electron HLT combination is shown, as an example, for data and simulation in 2018, as a function of the electron p_T . The trigger efficiency in both simulation and data is around 90% after an initial turn-on at $p_T \leq 50$ GeV. Due to the similarity of trigger efficiencies in data and simulation, a resulting SF close to one is obtained. The SF is derived as a function of electron p_T and η .

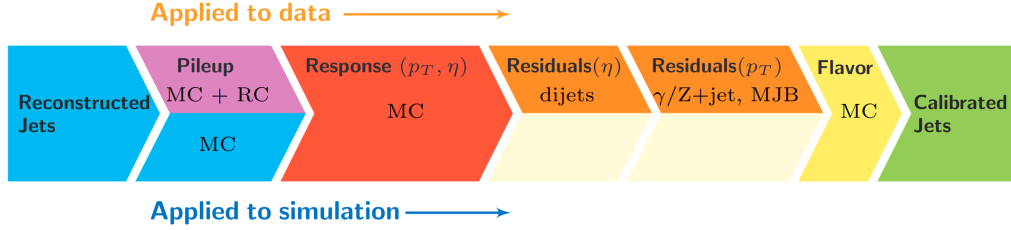


Figure 6.3: Visualization of jet energy correction levels. Taken from Ref. [99].

6.4 Electron reconstruction efficiencies

Differences in electron identification and reconstruction efficiencies between simulation and data are corrected with dedicated SFs provided centrally by CMS [94]. The electron efficiency is calculated as

$$\epsilon_e = \epsilon_{\text{ID}} \cdot \epsilon_{\text{reco}|\text{ID}} \cdot \epsilon_{\text{trig}|\text{reco}}, \quad (6.2)$$

consisting of identification (ID), reconstruction (reco), and the aforementioned trigger (trig) SFs. The efficiencies are dependent on each other, e.g. the reconstruction efficiency calculation already uses muons corrected for identification efficiency differences, and so forth, indicated by subscripts, e.g. reco|ID. Identification and reconstruction efficiencies and associated SFs are determined in auxiliary measurements in phase space regions enriched in $Z \rightarrow e^+e^-$ events.

6.5 Muon reconstruction efficiencies

Similar to the electron efficiencies, identification (ID), isolation (iso), and reconstruction (reco) efficiencies are calculated for muons in addition to the aforementioned trigger efficiencies, as

$$\epsilon_\mu = \epsilon_{\text{ID}} \cdot \epsilon_{\text{iso}|\text{ID}} \cdot \epsilon_{\text{reco}|\text{iso}} \cdot \epsilon_{\text{trig}|\text{reco}}. \quad (6.3)$$

Similarly, the difference between data and simulation efficiencies is corrected via SFs provided centrally by the CMS Collaboration [83]. These SFs are derived from phase space regions enriched in $Z \rightarrow \mu^+\mu^-$ events. Muons, unlike electrons, require separate SFs for isolation efficiencies, as the isolation criteria introduced in Section 3.2.1 are separated from muon identification criteria.

6.6 Jet energy corrections

The measurement of jet energies in the detector environment is not trivial and requires a good calibration of all detector components. The jet energy response, i.e. the measured jet energy relative to the true jet energy, has to be corrected for differences between simulation and data, same as for the other objects (e.g. muons or electrons). As jets are supposed to be an estimate of the initial particle, the measured energy requires additional corrections, e.g. due to energy loss of the detected particles, or missing particles in the detector. Hence, a set of jet energy corrections are applied to simulation and data in order to correct these effects. A factorized approach is employed, where different effects are treated sequentially in a fixed order. The levels of correction are visualized in Figure 6.3 and are introduced in the following. More details can be found in Ref. [99].

Pileup corrections: The first level of corrections removes energy from pileup interactions from the jets. The corrections are determined from simulated dijet events which are simulated once with additional pileup interactions and once without. This correction is derived as a function of jet p_T , η , area, and ρ . The offset energy density ρ is defined as the

median of all jet p_T over jet areas in an event. Residual differences between data and simulation are determined using a random cone method in zero-bias events. This zero-bias dataset is collected using a random trigger and therefore contains mostly events without hard scattering processes of interest. With the random cone method, several jets are reconstructed from randomly placed cones in these zero-bias events. The average momentum of these random jets is measured to determine an average energy offset due to random interactions, i.e. pileup. This correction is determined as a function of jet η .

MC-truth corrections: The jet response in simulation and data is corrected by comparing the reconstructed p_T of jets to the jet on generator level in a sample of dijet events. These corrections are derived as a function of jet p_T and η .

Residual corrections: Small remaining differences in the jet response for simulation and data are applied to jets in data. One correction accounts for the relative jet energy scale as a function of η , derived from dijet events in which both jets have similar momenta and one of these jets is in the barrel region. Another correction accounts for differences in the absolute jet energy scale as a function of p_T , derived from jets in the barrel region in Z+jet, γ +jet and multijet events.

In addition, the difference in jet energy resolution between simulation and data is corrected in simulated events to match the jet energy resolution in data. The correction is applied depending on whether or not a reconstructed jet is in the vicinity ($\Delta R < 0.2$) of a particle-level jet. If the reconstructed jet is associated with a particle-level jet, the jet momentum is scaled based on the difference in p_T between the simulated and reconstructed jet and an SF to account for the resolution difference between simulation and data. If no particle-level jet can be associated with the reconstructed jet, the jet momentum is scaled via the resolution SF smeared via a random value drawn from a standard Gaussian distribution.

6.7 Jet flavor tagging efficiency

SFs for b jet efficiency calibrations can be derived for two different purposes. A simple correction, designed to correct the efficiencies of b jet identification for the WPs introduced in Section 3.3.2 will yield distributions of b tagged jet multiplicities in data and simulation that are corrected for efficiency differences. If besides the information whether certain jets pass the predefined WPs, also the full discriminant distribution of the b tagger is used, the full discriminant distribution has to be corrected with SFs as a function of the discriminant value, which is not used in the measurements of this thesis.

The correction of b jet tagging efficiencies for the predefined WPs is referred to as fixed working point (fixedWP) SFs. SFs are derived independently for b jets and light jets. The SFs for b jets are derived from five different methods and are combined afterward to yield smaller uncertainties. These methods use phase space regions enriched in multijet events where at least one jet contains a muon, or phase space regions enriched in $t\bar{t}$ events with one or two charged leptons. The selection of jets with muons enriches the multijet events in jets originating from the hadronization of b quarks, as a muon clustered inside a jet is a good indicator for the decay of a B meson into a muon and other hadronic particles (semi-leptonic decay). The different SF derivation methods are described in detail in Ref. [100]. An example of the resulting SFs is shown in Figure 6.4 (top) for data and simulation in 2018. The SFs obtained from the different derivation methods are all compatible with each other within the uncertainties of the derivation procedures, and yield combined SFs with significantly smaller uncertainties. The SFs are derived as a function of the jet transverse momenta, p_T .

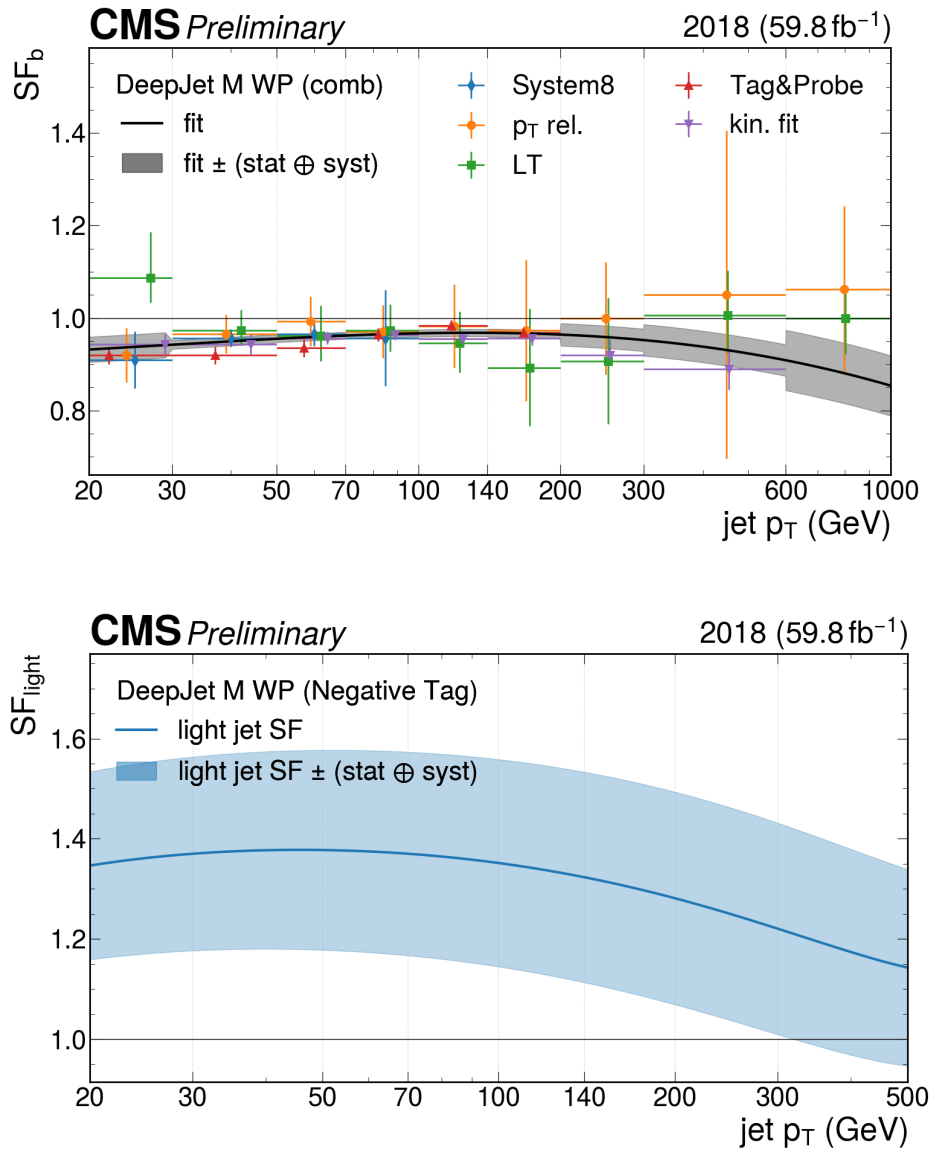


Figure 6.4: **b jet (top) and light jet (bottom) SFs for b tagging at fixed WPs in 2018.** The figure on the top shows the SFs for b jets obtained from the five different SF derivation methods as a function of jet p_T for the medium WP. Included is a combination of the SFs (indicated as fit) and the associated uncertainties. The figure on the bottom shows the SFs for light jets for the medium WP. Taken from Ref. [76].

The SFs for light jets are derived in a multijet enriched phase space and make use of a negative tagger to obtain the simulation-to-data SFs. The negative tagger uses the same b tagging algorithm as employed for b jet tagging, but only considers tracks with negative impact parameters. As impact parameters of light jets are symmetrically distributed around zero, and tracks of b and c jets have non-negligible impact parameters (see Figure 3.3), this separates light jets from other jets. In Figure 6.4 (bottom) the SFs obtained in 2018 are shown. In contrast to the b jet tagging SFs, the light jet SFs are commonly around values of 1.0 – 1.5, implying that the light jet content is underestimated in simulation. These SFs have larger uncertainties compared to the b jet SFs as only one method is used for SF derivation. SFs for light jets are also derived as a function of jet p_T .

6.7 Jet flavor tagging efficiency

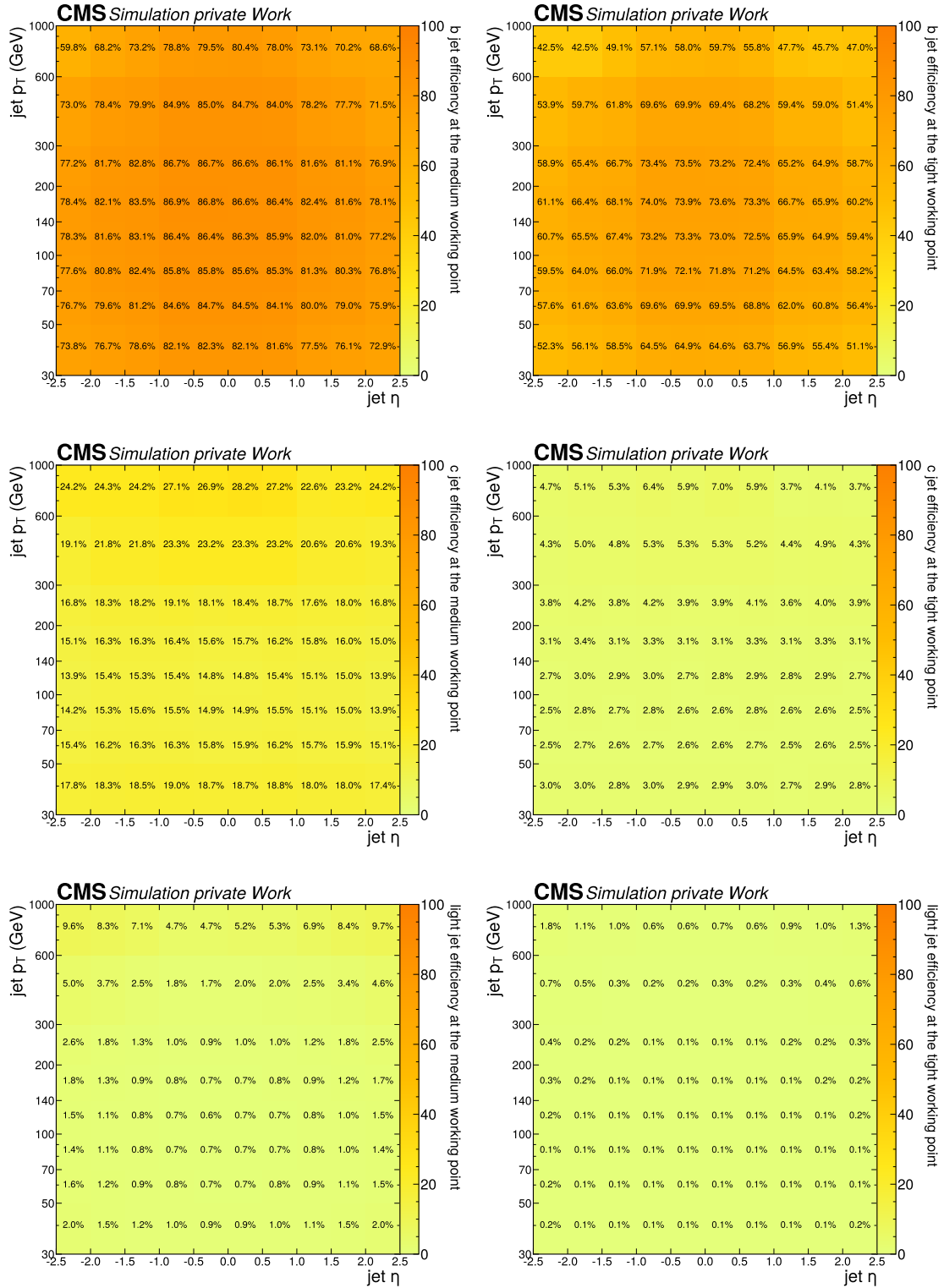


Figure 6.5: **b tagging efficiencies for simulated events in 2018.** Efficiencies for b (upper row), c (middle row), and light jets (lower row) for the medium (left) and tight (right) WPs of the DEEPJET tagger. Efficiencies are parameterized as functions of jet p_T and η .

No dedicated SFs for c jets are derived. To still account for this uncorrected contribution, c jets are scaled with the SFs derived for b jets and receive uncertainties inflated by a factor of two [100].

6 Corrections to simulated events

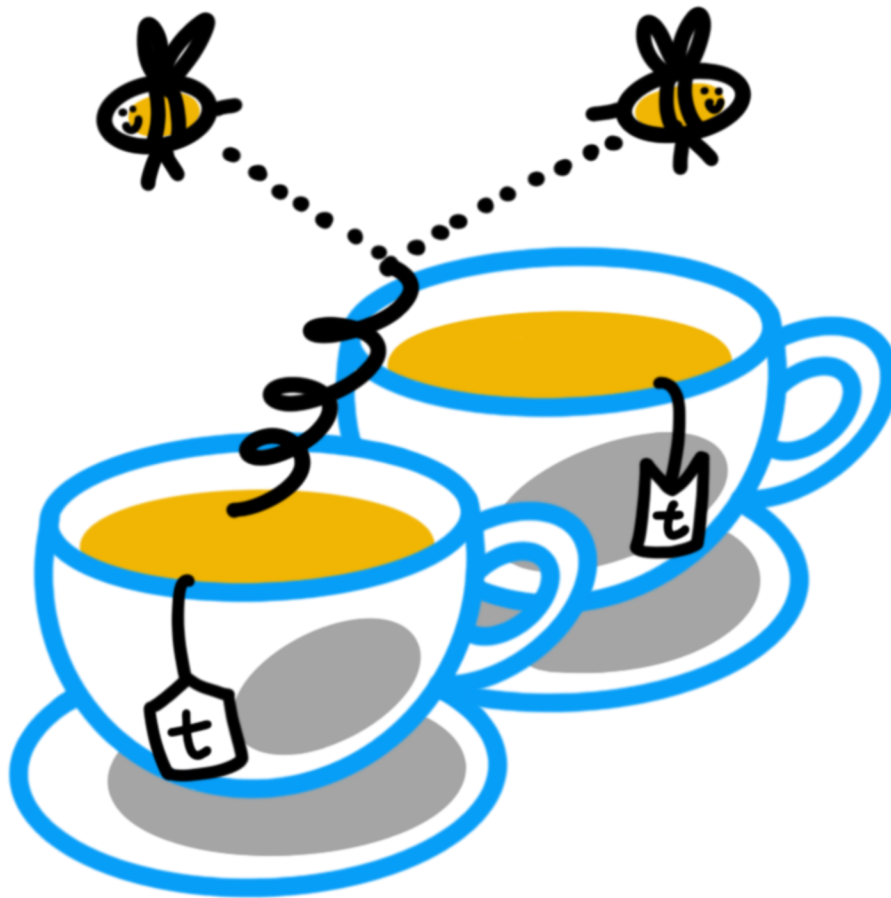
SFs are applied to simulated events via event weights taking into account all selected jets in the event as

$$w_{\text{fixedWP}} = \prod_{i=\text{tagged jets}} \text{SF}_i[\text{flav}, p_T] \prod_{j=\text{not tagged jets}} \frac{1 - \text{SF}_j[\text{flav}, p_T] \cdot \epsilon_j[\text{flav}, p_T, \eta]}{1 - \epsilon_j[\text{flav}, p_T, \eta]}. \quad (6.4)$$

Here, $\text{SF}_{i,j}$ are the b and light jet SFs derived previously, and $\epsilon_{i,j}$ are tagging efficiencies in simulation, commonly derived as a function of jet flavor, p_T , and η . These tagging efficiencies are calculated for each measurement in order to account for differences in the tagging efficiencies of the SF derivation regions and the phase space of the measurement. An example of efficiencies calculated for the measurements in this thesis are shown in Figure 6.5 for the medium and tight b tagging WPs obtained from simulated events under 2018 conditions.

Part II

Measurement of the $t\bar{t}b\bar{b}$ process



7 Introduction

This part of the thesis encompasses a measurement of the $t\bar{t}b\bar{b}$ process. This measurement was performed within the CMS Collaboration and is, at the time of writing, in the process of publication in a journal. A preliminary publication of the measurement exists at Ref. [136]. The measurement is described in this thesis in detail. In this chapter, first, a motivation for the measurement is given in Section 7.1, followed by a description of the $t\bar{t}b\bar{b}$ topology in Section 7.2. An outline of the measurement strategy is then given in Section 7.3. Finally, in Section 7.4, related measurements will be discussed to set this measurement into context. Afterward, Chapter 8 introduces the necessary tools for the measurement, e.g. event selections, simulation approaches, and the systematic model. The discussion of the measurement itself will take place in Chapter 9.

7.1 Motivation

Many measurements performed at pp collider experiments rely on accurate simulation to estimate background processes with similar signatures in the detectors compared to the process of interest (signal process). In such measurements, a subset of events is selected that contain a large fraction of events stemming from the signal process. In order to determine the contribution of the signal process to the set of selected events, an estimation of known SM-like processes can be performed via simulation of the known processes. In some measurements, one of these background processes is the $t\bar{t}b\bar{b}$ process. The understanding of the $t\bar{t}b\bar{b}$ process is important in those measurements, as an accurate and reliable description of the $t\bar{t}b\bar{b}$ process will allow for a measurement of the signal process under scrutiny with high accuracy. Two examples are the measurement of a pair of top quarks in association with a Higgs boson ($t\bar{t}H$), where the Higgs boson decays into a pair of bottom quarks ($H \rightarrow b\bar{b}$), and the production of four top quarks ($t\bar{t}t\bar{t}$) in channels in which most of the top quarks decay hadronically. Both these measurements give access to the Yukawa coupling of the top quark to Higgs bosons and thereby constitute important tests of the SM. In Section 7.4 these two measurements and their limitations due to the $t\bar{t}b\bar{b}$ modeling will be discussed briefly. One goal of the $t\bar{t}b\bar{b}$ measurement in this thesis is to gain improved understanding of this important and irreducible background process for the two aforementioned measurements and thereby improve the sensitivity of the measurements of these processes.

A detailed study of the $t\bar{t}b\bar{b}$ process is also of interest due to the challenging modeling of the process. In Section 7.2 this aspect will be further emphasized. In summary, the $t\bar{t}b\bar{b}$

process is difficult to model accurately as it contains b quarks with low but non-negligible masses, and, by comparison, heavy top quarks. Hence, finding appropriate energy scales for the calculation of $t\bar{t}b\bar{b}$ MEs and interfacing the MEs with PS and pdf calculations is a difficulty. Uncertainties related to the choice of renormalization and factorization scales can, in ME calculations at NLO in QCD, lead to uncertainties of up to 50% in fiducial and differential cross section predictions of $t\bar{t}b\bar{b}$ [137]. Improved knowledge in this process via fiducial and differential measurements of $t\bar{t}b\bar{b}$ is therefore of prime interest in order to validate or discard scale choices made for state-of-the-art simulations. A more accurate modeling of the process can then improve the central prediction in the modeling of this background process, e.g. in the measurements of the $t\bar{t}H(b\bar{b})$ and $t\bar{t}t\bar{t}$ processes, and give a better estimate of the uncertainties associated with the modeling of the $t\bar{t}b\bar{b}$ process.

The modeling and simulation of the $t\bar{t}b\bar{b}$ process have been studied extensively. In Refs. [138–141], NLO corrections in QCD at fixed order are presented for inclusive and differential calculations of the $t\bar{t}b\bar{b}$ process. Furthermore, calculations of $t\bar{t}b\bar{b}$ with additional radiation ($t\bar{t}b\bar{b}j$) are performed in Ref. [142]. Alternatively, full NLO QCD off-shell calculations of $t\bar{t}b\bar{b}$ are available in Refs. [143, 144]. These calculations are performed at fixed order on parton level, i.e. they consider the full phase space of $t\bar{t}b\bar{b}$ production but without decay of the final-state b and top quarks. Experimentally, this level of information is not accessible easily and would require extrapolation of the data measured at the CMS experiment to the parton-level phase space. A more suitable level of prediction for a comparison between experimental data and theory calculations lies in the combination of matrix element (ME) event generators (making fixed-order predictions) interfaced with parton shower (PS) models. This level of prediction also facilitates the interpretation of results for other measurements like the aforementioned measurements of $t\bar{t}H$ and $t\bar{t}t\bar{t}$ where $t\bar{t}b\bar{b}$ constitutes a major limiting factor. In this context, the state-of-the-art predictions of $t\bar{t}b\bar{b}$ production are obtained from ME-level generators at NLO in QCD matched to PSs. In calculations in which the b quarks are treated as massive, the b quark is not part of the proton pdf but is integrated out (see Section 5.8.2). Therefore, pdf sets with only four active flavors, without b quarks, are used, called 4FS pdfs. Contributions of b quarks arise e.g. through gluon-splitting into a pair of b quarks ($g \rightarrow b\bar{b}$). As these ME calculations treat the b quarks as massive, the description of $g \rightarrow b\bar{b}$ splittings is more accurate than in the zero-mass approximation of the pdf and covers the full phase space of $g \rightarrow b\bar{b}$ splittings.

The measurements presented in this thesis aim at verifying the $t\bar{t}b\bar{b}$ simulation models and how these describe the process as a function of selected observables. This measurement consists of fiducial cross section measurements and normalized differential cross section measurements. A set of fiducial phase space regions and observables has been chosen to be measured and will be detailed in Section 8.2. Previous measurements by the ATLAS and CMS Collaborations showed that the cross section of $t\bar{t}b\bar{b}$ is under-predicted by all simulation approaches tested in these measurements. Differential distributions probed in these measurements generally show good agreement but are measured with large uncertainties which do not allow for ruling out any of the tested simulation approaches and their modeling choices (such as the renormalization or factorization scales). A review of the relevant results of these previous measurements will be summarized in Section 7.4. The measurement described in Chapter 9 improves upon these previous results and provides measurements of fiducial and differential cross sections with smaller uncertainties, which facilitates a more meaningful comparison to different simulation approaches and modeling choices. The results of this measurement, which will be discussed in Section 9.2 and Section 9.3, show varying levels of compatibility of the simulation approaches that were probed with data.

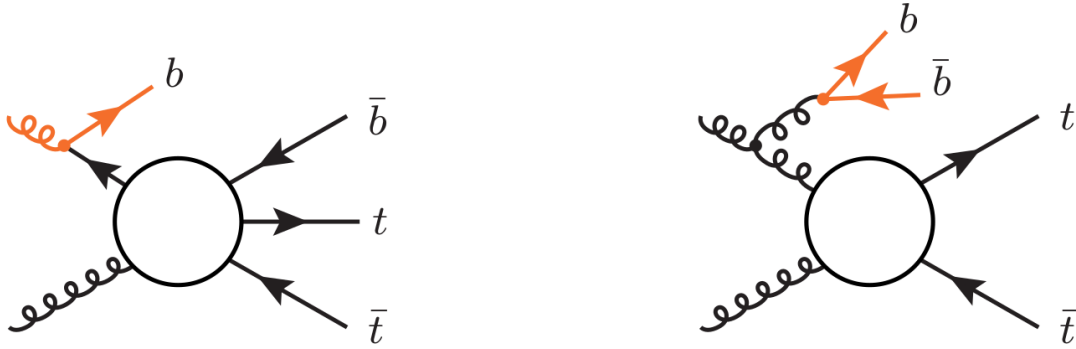


Figure 7.1: **Illustration of $t\bar{t}b\bar{b}$ diagrams using an NLO $t\bar{t}$ ME simulation interfaced with a PS.** The diagram on the left shows $g \rightarrow b\bar{b}$ splitting in the initial state, the diagram on the right shows $g \rightarrow b\bar{b}$ splitting in the final state. The colored parts of the diagrams are simulated by the PS, while the remaining parts are included in the ME simulation. From Ref. [137].

7.2 Topology of the $t\bar{t}b\bar{b}$ process

The $t\bar{t}b\bar{b}$ process is a process of multiple scales, incorporating heavy top quarks and in comparison light b quarks in the final state. This makes the $t\bar{t}b\bar{b}$ process an interesting probe of quantum chromodynamics (QCD) in presence of heavy quarks and a complicated multi-scale environment [137]. In comparison to simple $t\bar{t}$ production, where the process takes place at the energy scale of the top quarks, the $t\bar{t}b\bar{b}$ process is a more complicated environment. This is also reflected in the options of simulating this process, discussed in the following. The discussions are based on Ref. [137].

Simulation of $t\bar{t}b\bar{b}$ with NLO $t\bar{t}$ matrix elements

The $t\bar{t}b\bar{b}$ process can be described using NLO $t\bar{t}$ ME simulations, interfaced with a PS, and a 5FS pdf. In this setup, $2 \rightarrow 3$ processes in the ME such as $gb \rightarrow t\bar{t}b$ or $gg/q\bar{q} \rightarrow t\bar{t}g$ can yield a description of $t\bar{t}b\bar{b}$ together with the PS. This is illustrated in Figure 7.1. In the $gb \rightarrow t\bar{t}b$ process, one b quark is obtained from the ME, but requires an initial b quark from the pdf, which is described via backward evolution of the PS to the initial state as described in Section 5.3. In the $gg/q\bar{q} \rightarrow t\bar{t}g$ process, the gluon is described at the ME level, while the $g \rightarrow b\bar{b}$ splitting has to be described by the PS. This contribution dominates the topology of $t\bar{t}b\bar{b}$ in this simulation approach. The simulation approach has the disadvantage of describing the $t\bar{t}g$ process at LO accuracy in the ME, and relying on the PS for the $g \rightarrow b\bar{b}$ splitting description.

Simulation of $t\bar{t}b\bar{b}$ with $t\bar{t}$ +jets multi-jet merging

An alternative description of $t\bar{t}b\bar{b}$ can be obtained via $t\bar{t}$ +jets simulation approaches, where multiple simulations of $t\bar{t}+0,1,2$ jets are merged into an inclusive sample (see Section 5.8). This requires the definition of a merging scale Q , based on which the number of resolved additional partons is determined for each simulated event, and subsequently merged. In this simulation approach, if the $b\bar{b}$ pair and gluon are produced below the merging scale, this effectively yields a $t\bar{t}$ ME, and the description of the gluon and the $g \rightarrow b\bar{b}$ splitting by the PS. If the gluon becomes harder, i.e. larger momentum, the $t\bar{t}g$ process is described at the ME-level, and only the $g \rightarrow b\bar{b}$ splitting is described by the PS. If the $g \rightarrow b\bar{b}$ splitting is above the merging scale Q , the $g \rightarrow b\bar{b}$ splitting can be described by the ME, but only if it belongs to the hardest emissions, as all other emissions will be

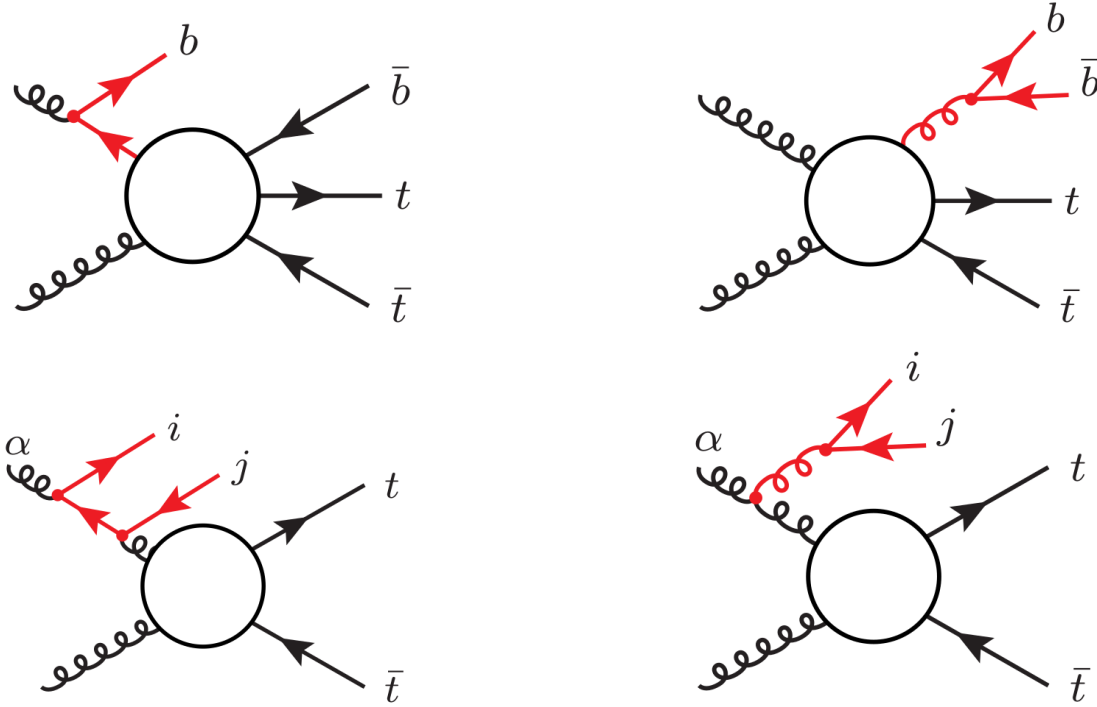


Figure 7.2: **Illustration of $t\bar{t}b\bar{b}$ diagrams using an NLO $t\bar{t}b\bar{b}$ ME simulation.** The diagrams on the left show $g \rightarrow b\bar{b}$ splitting in the initial state, and the diagrams on the right show $g \rightarrow b\bar{b}$ splitting in the final state. The full diagrams are simulated at ME level. The colored parts of the diagrams indicate the $g \rightarrow b\bar{b}$ splitting processes. From Ref. [137].

described by the PS. Hence, in this $t\bar{t} + \text{jets}$ simulation approach, contributions from $t\bar{t}b\bar{b}$ MEs are included, but only at large momenta in the $g \rightarrow b\bar{b}$ splitting, as otherwise other, harder, emissions will take precedence in the merging scheme. This solves the issue of divergences in $g \rightarrow b\bar{b}$ splitting at lower momenta (assuming a b quark mass of zero), as these will not be described by the ME. In this simulation approach, the contribution of the full ME description of $t\bar{t}b\bar{b}$ is shown to be small, even at low merging scales of $Q = 20 \text{ GeV}$, as the hardest emissions in the events are usually either gluon emission or additional light jet radiation, which (at the level of $t\bar{t} + 2 \text{ jets}$) predominantly yields a description of $g \rightarrow b\bar{b}$ splitting by the PS. Hence, this modeling approach also mostly relies on the PS description of $g \rightarrow b\bar{b}$ splitting.

Simulation of $t\bar{t}b\bar{b}$ with NLO $t\bar{t}b\bar{b}$ matrix elements

More recently, descriptions of $t\bar{t}b\bar{b}$ at the ME level have become available at NLO accuracy for the full b quark phase space. This simulation approach minimizes the dependence on the PS and its description of the $g \rightarrow b\bar{b}$ splitting. The ME simulation is interfaced with a 4FS pdf set, i.e. it uses massive b quarks (see Section 5.8.2). The b quarks for the description of $t\bar{t}b\bar{b}$ can be obtained in initial-state and final-state processes, as is illustrated in Figure 7.2. This simulation approach provides a description of $t\bar{t}$ with ≥ 1 b in the full phase space of b quarks, modeled by different aspects of the MEs. For final-state gluon radiation, the ME is able to describe also the collinear $g \rightarrow b\bar{b}$ splitting regime due to the non-zero mass of the b quarks. This also enables a homogeneous description of events in which the b quarks are not resolvable, and hence are merged into a single jet containing both b quarks ($t\bar{t}b$ signature). In initial-state $g \rightarrow b\bar{b}$ splittings the spectator b quark (diagram in Figure 7.2 top left) can be emitted in the direction of the beam axis, and can therefore remain undetected, also yielding a description of $t\bar{t}b$ signatures.

In Ref. [137], the contributions of the final-state gluon radiation and $g \rightarrow b\bar{b}$ splitting are shown to dominate the $t\bar{t}b\bar{b}$ phase space (diagrams in Figure 7.2 on the right). In observables such as the invariant mass or the ΔR of the two leading b jets, the tail of the distributions contain also large interference effects with the $t\bar{t}b\bar{b}$ description from initial-state $g \rightarrow b\bar{b}$ splitting (diagrams in Figure 7.2 on the left). This can be explained by how the b jets are correlated with each other in this region of phase space. In the initial-state $g \rightarrow b\bar{b}$ splitting, either, one b jet comes from the initial $g \rightarrow b\bar{b}$ splitting and the other one from the subsequent $gb \rightarrow t\bar{t}b$ process, or the b jets come from individual $g \rightarrow b\bar{b}$ splitting processes in the initial state (diagram in Figure 7.2 bottom left). As these contributions are no longer governed by the collinear $g \rightarrow b\bar{b}$ splitting regime, the angle ΔR between the b jets can be larger and the invariant mass no longer traces back to the intermediate gluon and therefore allows for larger values on average.

Scale choices in the matrix-element $t\bar{t}b\bar{b}$ simulation

Due to its QCD coupling nature, the $t\bar{t}b\bar{b}$ cross section scales with α_s^4 , and is therefore highly sensitive to the choice of renormalization scale μ_R (see Section 5.2). As the $t\bar{t}b\bar{b}$ process incorporates a top quark and a b quark, in Ref. [137] choices of the renormalization scale for an ME-level simulation are recommended as

$$\mu_R = \xi_R \sqrt{\mu_{t\bar{t}} \mu_{b\bar{b}}}, \quad (7.1)$$

where ξ_R are scale-variation factors and $\mu_{t\bar{t}}$ and $\mu_{b\bar{b}}$ are defined as the geometric average of the transverse masses of the $t\bar{t}$ and $b\bar{b}$ systems,

$$\mu_{t\bar{t}} = \sqrt{m_{T,t} m_{T,\bar{t}}}, \quad \text{and} \quad \mu_{b\bar{b}} = \sqrt{m_{T,b} m_{T,\bar{b}}}. \quad (7.2)$$

Here, the transverse mass is defined as $m_{T,i} = \sqrt{m_i^2 + p_{T,i}^2}$. For the factorization scale μ_F , recommended choices are

$$\mu_F = \frac{\xi_F}{2} \sum_{i=t,\bar{t},b,\bar{b},j} m_{T,i}, \quad (7.3)$$

where ξ_F is again a scale-variation factor. The scale-variation factors ξ_F and ξ_R are dimensionless and are commonly chosen to be in the range [0.5, 2].

Predictions in Ref. [137], using stable top quarks and $\xi_R = \xi_F = 1$, show that variations in the μ_R and μ_F scales at NLO (LO) yield cross section variations of around 25–35% (40–70%). These scale variations are estimated from envelopes of μ_R and μ_F variations by a factor of two in both directions. The uncertainties are dominated by μ_R variations as expected from the strong $\alpha_s^4(\mu_R)$ dependence of the $t\bar{t}b\bar{b}$ ME calculations. The relative fraction of $t\bar{t}b$ over $t\bar{t}b\bar{b}$ events is shown to be around five, originating from the large contributions of collinear or soft b quarks in final state $g \rightarrow b\bar{b}$ splitting due to the non-negligible b quark mass (see Section 5.8.2). Including also the PS, Ref. [137] finds only a small change in the $t\bar{t}b$ cross section at the combined ME+PS-level compared to ME-level alone (2%), but a larger correction in the $t\bar{t}b\bar{b}$ cross section (12%). This originates from double $g \rightarrow b\bar{b}$ splitting processes, where one $g \rightarrow b\bar{b}$ splitting takes place in the ME, yielding one b quark, and another $g \rightarrow b\bar{b}$ splitting takes place in the PS, yielding a second b quark. Additionally, the impact of the μ_R and μ_F variation increases in the ME-PS-matched predictions by around 10%. Investigations of differential distribution in Ref. [137] also show that observables related to the b jets show negligible shape-dependence of the scale variations, while observables e.g. related to additional light jet radiation show a stronger shape-dependence on these scale uncertainties. This is due

to the difference in origin in the description of b jets, which are fully described with the $\alpha_s^4(\mu_R)$ NLO ME while the additional light jets are described at LO in the ME and therefore depend on $\alpha_s^5(\mu_R)$. Furthermore, contributions from the PS are shown to be relatively homogeneous for b jets in $t\bar{t}b$ events (i.e. they do not significantly depend on the kinematics of the b jets), but are sensitive to the kinematics of b jets in $t\bar{t}b\bar{b}$ events, again motivated by the aforementioned double $g \rightarrow b\bar{b}$ splitting. For example in the ΔR observable, the cross section at large ΔR is enhanced when considering also the PS compared to the raw NLO $t\bar{t}b\bar{b}$ ME calculations, as contributions from double $g \rightarrow b\bar{b}$ splitting processes are mostly not collinear and hence have larger opening angles. This will be picked up again in the interpretation of results in Section 9.4.

Finally, Ref. [137] also provides a study of the $t\bar{t}b\bar{b}$ process including top quark decays, taking into account also spin-correlations. The results show that the effect of the top quark hadronization is almost negligible, and hence the results obtained at parton level and particle level after top decays are expected to be compatible.

7.3 Strategy of the $t\bar{t}b\bar{b}$ measurement

The goal of this measurement is the extraction of fiducial and differential cross sections of the $t\bar{t}b\bar{b}$ process in the $t\bar{t}$ decay channel with exactly one charged lepton. In order to enrich the data events in the $t\bar{t}b\bar{b}$ process a base selection of five jets and three b tagged jets is applied together with a selection of exactly one charged lepton. These event selections are detailed in Section 8.3 and lead to a signal fraction of around 25%. Four fiducial phase space regions are explored, targeting different aspects of the $t\bar{t}b\bar{b}$ process. The most inclusive of these signal definitions requires signal events with at least five jets, of which at least three are b jets, referred to as 5j3b, targeting most inclusively the additional radiation of b jets outside the $t\bar{t}$ system. A more stringent signal definition requires at least six jets, of which at least four are b jets, instead, referred to as 6j4b, which constitutes the signature expected from a fully resolved $t\bar{t}b\bar{b}$ process at leading order. Two additional phase space regions are defined which require at least three light jets in addition to the b jets required in the 5j3b and 6j4b phase space regions, leading to one phase space with at least six jets, of which at least three are b jets and three are light jets (6j3b3l), and at least seven jets, of which at least four are b jets and three are light jets (7j4b3l). These two additional phase space regions are defined in order to measure the description of additional light jet radiation in $t\bar{t}b\bar{b}$ events. All of these definitions require exactly one charged lepton (electron or muon), to match the single-lepton $t\bar{t}$ decay channel. All these fiducial signal definitions are defined without reference to the origin of b jets. With this, comparisons to different simulation approaches are simplified, as the signal definition does not depend on the simulated history of the top quark decays. In Ref. [136], also an alternative approach is explored, where a fiducial signal is defined, explicitly requiring two b jets not to originate from top (anti)quark decay. This additional study is not repeated in this thesis.

Fiducial cross sections are measured in all of these phase space regions, as well as normalized differential cross sections of observables tailored to each of the phase space regions. These fiducial definitions and observables are discussed in Section 8.2.

For each observable independently, the differential cross section is obtained via unfolding to particle level. The unfolding is performed (via a likelihood-based unfolding procedure) using a maximum likelihood fit. The foundations of maximum likelihood fits are discussed in Chapter 4 while the explicit configuration of the fits for this measurement

is discussed in Section 9.1. In each of these fits the fiducial cross section for the respective phase space is extracted as a parameter of interest (POI), yielding the inclusive cross sections discussed in Section 9.2.

7.4 Related work

In this section work related to the $t\bar{t}b\bar{b}$ measurement of this thesis is discussed. This is limited to measurements using LHC Run 2 data collected at a center-of-mass energy of $\sqrt{s} = 13$ TeV. First, a short overview of past $t\bar{t}b\bar{b}$ measurements is given in Section 7.4.1, followed by a brief discussion of $t\bar{t}H(b\bar{b})$ and $t\bar{t}t\bar{t}$ measurements in Section 7.4.2 which estimate $t\bar{t}b\bar{b}$ background from simulation.

7.4.1 Related $t\bar{t}b\bar{b}$ measurements

During LHC Run 2 multiple cross section measurements of the $t\bar{t}b\bar{b}$ process have been performed with partial data sets, i.e. data sets not containing the full 2016–2018 data set.

The ATLAS Collaboration has published a measurement of $t\bar{t}b\bar{b}$ in final states with one or two charged leptons, using 36.1 fb^{-1} of data [145]. In Figure 7.3, the fiducial cross sections obtained in that measurement are shown. The lepton+jet $\geq 3b$ and $\geq 4b$ values correspond to fiducial definitions similar to those explored in this thesis. A comparison of the results will be made in Section 9.2.2. The fiducial cross sections are determined with uncertainties ranging between 14% and 30%, where the most precise measurements are from the measurements with two leptons. The measured fiducial cross sections are compared to a set of simulation approaches which mostly predict lower cross section values than observed in data. The measurement is limited by uncertainties of the $t\bar{t}$ modeling, b tagging, and jet energy calibrations. In Ref [145], also a range of normalized differential cross section measurements is performed, probing the b jet multiplicity, H_T , p_T of b jets and the system of the two leading b jets in p_T , and the system of the two b jets closest in ΔR . The normalized differential cross sections are determined with uncertainties ranging between 10% and 30% and are found to be well-described by most of the simulation approaches, considering the large measurement uncertainties. In the measurement of the b jet multiplicity, the models using a $t\bar{t}$ ME simulation at NLO were found to not describe that observable well, all predicting lower fractions of high b jet multiplicities.

The CMS Collaboration published two $t\bar{t}b\bar{b}$ measurements using 35.9 fb^{-1} of data, one using final-states with zero charged leptons [146], and the other using final states with one or two charged leptons [148]. In Ref. [146], the $t\bar{t}b\bar{b}$ cross section is measured for a full phase space and two fiducial phase space definitions. One of these fiducial phase space definitions is particle-level based and does not reference the simulated history of the $t\bar{t}$ pair. The cross sections are determined with uncertainties of around 30%. Also here, the cross sections predicted by various signal models are lower than the measured cross sections in data. The challenge of that measurement is the dominating background from events containing only jets produced through the strong interaction (multijet events), which cannot be estimated well from simulation and require data-driven background estimations. In Ref. [148] the cross sections of $t\bar{t}b\bar{b}$ and $t\bar{t}jj$ ($t\bar{t}$ production in association with any pair of jets) are measured, as well as their ratio. Results are obtained as fiducial cross sections defined on stable-particle level, and are extrapolated to the full phase space referencing the simulated history of the $t\bar{t}$ pair to identify jets not originating from the decay of top quarks. The fiducial cross sections are determined with uncertainties between 11% and 18% and are higher than the values predicted by various simulation approaches.

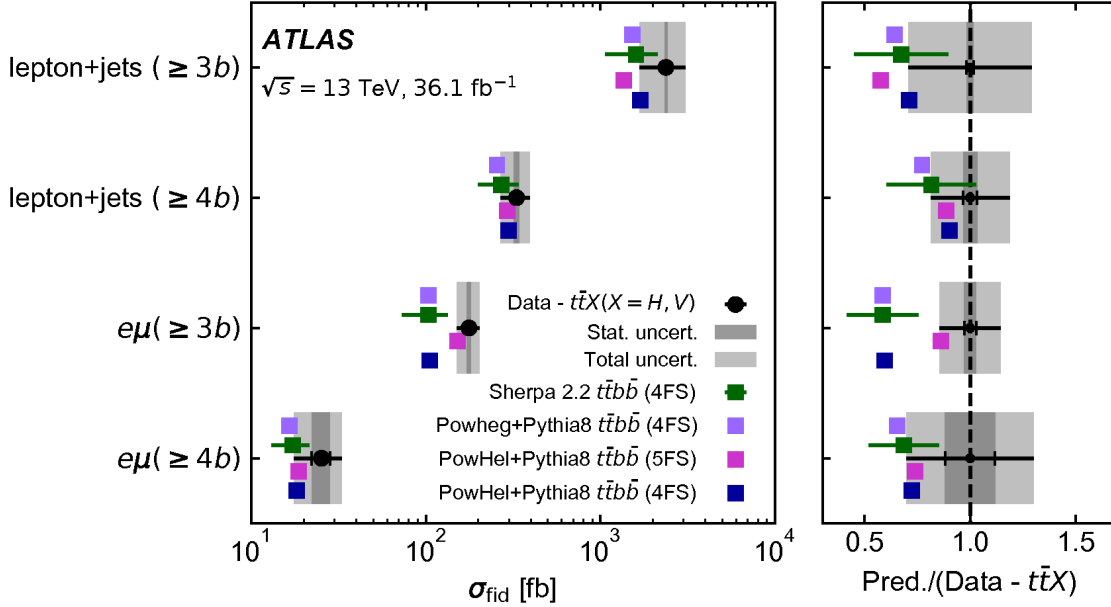


Figure 7.3: **Measured fiducial cross section values of $t\bar{t}b\bar{b}$ by the ATLAS Collaboration.** The measured cross sections in data are indicated with black dots, with horizontal bars and shaded bands representing the measurement uncertainties. Cross section predictions from different modeling approaches are shown as colored squares. The panel on the right shows the ratio between the predicted and measured cross sections. From Ref. [145].

The definitions of fiducial phase space regions differ in some aspects from the ones used in this thesis (see Section 8.2).

Additionally, a measurement was performed by the CMS Collaboration targeting the production of $t\bar{t}C$ events in final states with two charged leptons, using 41.5 fb^{-1} of data [147]. Even though mainly the $t\bar{t}C$ process is targeted in that measurement, the $t\bar{t}b\bar{b}$ cross section is also determined, as the phase space region defined for that measurement is enriched in both these processes. In Ref. [147], cross sections are only measured on parton level, i.e. with reference to the simulated history of the top quarks. Jets outside the $t\bar{t}$ system are classified based on their flavor, enabling the simultaneous measurement of the $t\bar{t}C$, $t\bar{t}b\bar{b}$, and $t\bar{t}j\bar{j}$ processes. The $t\bar{t}b\bar{b}$ cross section is measured with a precision of 11%. Also in this measurement, the cross sections predicted by the simulation of $t\bar{t}b\bar{b}$ are lower than the measurement. The measurements presented in this thesis are the first differential measurements of the $t\bar{t}b\bar{b}$ process by the CMS Collaboration.

In Figure 7.4, the results for the $t\bar{t}b\bar{b}$ cross section measurements in the full phase space by the CMS Collaboration are summarized, all showing the aforementioned underprediction of $t\bar{t}b\bar{b}$ cross sections by the probed modeling approaches.

7.4.2 Related $t\bar{t}H(b\bar{b})$ and $t\bar{t}t\bar{t}$ measurements

The ATLAS Collaboration performed a measurement of the $t\bar{t}H$ process in $H \rightarrow b\bar{b}$ final states with one or two charged leptons, using the full 139 fb^{-1} data set of LHC Run 2 [149]. In this inclusive measurement of the $t\bar{t}H$ cross section, the dominant background in the regions enriched in the signal process is $t\bar{t}b\bar{b}$ production, as it exhibits the same final state after the top quark and Higgs boson decays. In the measurement regions with the largest relative contribution of $t\bar{t}H$, the $t\bar{t}b\bar{b}$ background exceeds the $t\bar{t}H$ contribution by factors of around 50. The $t\bar{t}b\bar{b}$ background is estimated using a ME simulation of $t\bar{t}b\bar{b}$ at

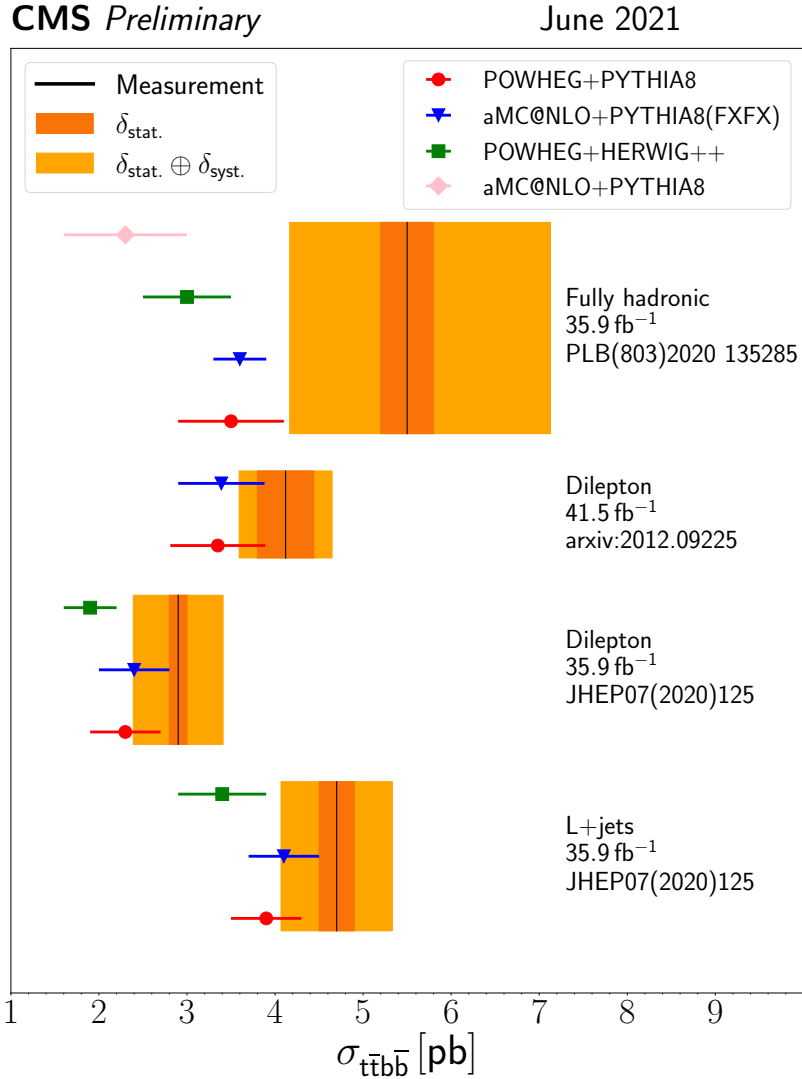


Figure 7.4: **Measured fiducial cross section values of $t\bar{t}b\bar{b}$ by the CMS Collaboration.** The measured cross sections in data are indicated with black lines and orange bands representing the measurement uncertainties. From top to bottom, the measurements correspond to the results of Ref. [146], Ref. [147], and Ref. [148]. Cross section predictions from different modeling approaches are shown as colored symbols.

NLO, and corresponds closely to the PP8 $t\bar{t}b\bar{b}$ 4FS simulation approach discussed in the following chapters, e.g. Section 8.1. The μ_R and μ_F scale choices in this $t\bar{t}b\bar{b}$ background estimation correspond to $\xi_R = 1$ and $\xi_F = 1$ (see eq. (7.1) and eq. (7.3)) and are both chosen to be larger than in the PP8 $t\bar{t}b\bar{b}$ 4FS model used in this thesis by a factor of two. In Section 9.4, the impact of different scale choices will be discussed, also comparing to this ATLAS measurement. The normalization of the $t\bar{t}b\bar{b}$ background in this measurement is found to be 28% higher than expected from the background model. The $t\bar{t}H$ cross section is measured with 35% uncertainty, while the $t\bar{t}b\bar{b}$ background modeling contributes more than half to that uncertainty.

7 Introduction

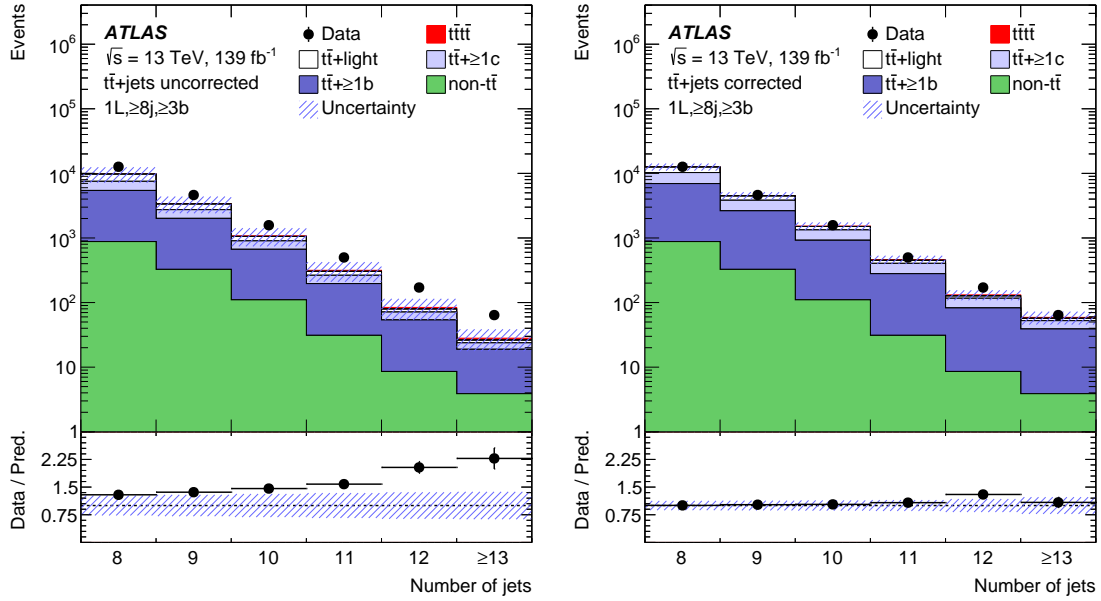


Figure 7.5: Jet multiplicity distribution in one measurement region of the $t\bar{t}t\bar{t}$ measurement performed by the ATLAS Collaboration. The distribution on the left shows the simulation without a reweighting of $t\bar{t}$ +jets processes, and the distribution on the right shows the simulation with a reweighting of $t\bar{t}$ +jets processes. The lower panels show the ratio between simulation and data. From Ref. [152].

The CMS Collaboration performed a measurement of the $t\bar{t}H$ process in $H \rightarrow b\bar{b}$ final states with zero, one or two charged leptons, using 41.5 fb^{-1} of data [150], combined with a previous measurement using 35.9 fb^{-1} of data [151]. With this combined data set, the $t\bar{t}H$ cross section is determined with an uncertainty of 30%, where about half of this uncertainty is associated with the background modeling of the $t\bar{t}b\bar{b}$ process. For the estimation of the $t\bar{t}b\bar{b}$ process in this measurement an inclusive $t\bar{t}$ simulation at NLO accuracy is used, indicating that the estimation of b jets in association with the $t\bar{t}$ system is predominantly modeled with the PS (see Section 7.2). In this measurement, the $t\bar{t}b\bar{b}$ background estimation is also shown to under-predict the contribution in data.

The ATLAS Collaboration performed a measurement of the $t\bar{t}t\bar{t}$ process in final states with one or two charged leptons using the full 139 fb^{-1} data set of LHC Run 2 [152]. In the most signal-enriched measurement regions, the $t\bar{t}b\bar{b}$ background exceeds 80% of all events. The background estimation of $t\bar{t}b\bar{b}$ for this measurement uses the same configuration as introduced above for the $t\bar{t}H(b\bar{b})$ measurement in Ref. [149]. In this measurement, a separate fit is performed in phase space regions where the $t\bar{t}t\bar{t}$ signal contribution is low in order to determine scaling factors for the $t\bar{t}b\bar{b}$ and other $t\bar{t}$ +jets backgrounds. For the $t\bar{t}b\bar{b}$ contribution a scaling factor of 1.33 is determined, again showing the under-prediction of $t\bar{t}b\bar{b}$ in simulation relative to the measurements in data. In addition, the $t\bar{t}b\bar{b}$ and $t\bar{t}$ +jets backgrounds are rescaled differentially in observables such as the jet multiplicity and H_T to better describe the data. This is shown in Figure 7.5 for the jet multiplicity as one representative example. On the left side of the figure, this shows a significant mis-modeling of the jet multiplicity distribution in simulation relative to data, suggesting a shortcoming of the $t\bar{t}b\bar{b}$ simulation approach. This is later also confirmed in the measurements of this thesis, e.g. in Section 9.3. The $t\bar{t}t\bar{t}$ cross section is determined in that measurement with a precision of 35%, with around half of the uncertainty associated with the modeling and reweighting of the $t\bar{t}b\bar{b}$ background.

The CMS Collaboration performed a measurement of the $t\bar{t}\bar{\ell}\bar{\ell}$ process in final states with zero, one, or two charged leptons using the full 138 fb^{-1} data set of LHC Run 2 [153]. The contributions from $t\bar{t}b\bar{b}$ to the measurement regions are modeled using a $t\bar{t}$ simulation at NLO and hence rely on the description of $t\bar{t}b\bar{b}$ on the PS modeling. The $t\bar{t}\bar{\ell}\bar{\ell}$ cross section is measured with a precision of around 30%, where the modeling of the $t\bar{t}b\bar{b}$ background contributes around 4% relative to the measured cross section value. Compared to other $t\bar{t}\bar{\ell}\bar{\ell}$ and $t\bar{t}H(b\bar{b})$ measurements this measurement is not limited significantly by the $t\bar{t}b\bar{b}$ modeling which hints towards an underestimation of the $t\bar{t}b\bar{b}$ modeling uncertainties in that measurement.

8 Ingredients for the $t\bar{t}b\bar{b}$ measurement

In order to facilitate the measurement of the $t\bar{t}b\bar{b}$ process a range of ingredients are needed, which will be introduced in this chapter. First, the simulation approaches used for signal and background processes are described in Section 8.1. The definitions of fiducial phase space regions and the observables for the differential measurements are summarized in Section 8.2. The corresponding definitions and event selections on detector level are described in Section 8.3. The contributions of simulated events to the event selections are discussed in Section 8.4 using data-to-simulation comparisons. In Section 8.5, the use of an ancillary variable is introduced. In Section 8.6, special attention is drawn to the distinction between $t\bar{t}$ and $t\bar{t}b\bar{b}$ processes, and a definition of out-of-acceptance (OOA) contributions of the $t\bar{t}b\bar{b}$ process is introduced. Finally, sources of uncertainty considered in the $t\bar{t}b\bar{b}$ measurements and their estimation are summarized in Section 8.7.

8.1 Event simulation

As introduced in Chapter 5, simulated events are used to estimate the contributions and kinematic distributions of different processes to data recorded in the CMS detector. In this section, the simulated physics processes used for the $t\bar{t}b\bar{b}$ measurement are introduced. These simulated samples are used in this measurement to estimate the contributions of signal and background processes to the measurement regions, i.e. to model their selection and acceptance efficiencies. In addition, the measurement is designed and validated on simulated events in order not to bias the strategy of the measurement. A short description of the different simulation packages and tools has already been given in Section 5.8. In all of the simulation approaches the detector response is simulated with GEANT4, as introduced in Section 5.7.

Simulation of $t\bar{t}$ events

Events with a pair of top quarks¹ ($t\bar{t}$) are simulated with the POWHEG v2 [116, 117] ME generator at NLO accuracy in QCD. This perturbative order allows for at most one real emission at ME level outside of the $t\bar{t}$ system (e.g. an additional quark or gluon).

¹This does not include $t\bar{t}$ processes with additional heavy boson radiation like $t\bar{t}Z$, $t\bar{t}H$ or $t\bar{t}W$, which are simulated separately.

8 Ingredients for the $t\bar{t}b\bar{b}$ measurement

POWHEG v2 is interfaced with PYTHIA v8.240 [84] for parton showering and hadronization. This simulation setup is henceforth referred to as PP8 $t\bar{t}$ 5FS. As the signal process ($t\bar{t}B$) contains, next to the $t\bar{t}$ system, one or two more b quarks, the ME calculation of the PP8 $t\bar{t}$ 5FS simulation cannot account for this final state. Therefore this simulation relies on the PS to generate additional b quarks, e.g. via splitting of the gluon to a pair of b quarks ($g \rightarrow b\bar{b}$). Details on this have been introduced in Section 7.2. The pdf of the protons is described using the 5FS NNPDF3.1 NNLO pdf set [115] (see Section 5.1). Due to the FS, b quarks are assumed to be massless in this simulation approach (see Section 5.8.2). The factorization and renormalization scales are both dynamically set to

$$\mu_R = \mu_F = \sqrt{\frac{1}{2} \left(m_{T,t}^2 + m_{T,\bar{t}}^2 \right)}, \quad (8.1)$$

with the transverse mass $m_{T,i} = \sqrt{m_i^2 + p_{T,i}^2}$. Here, m_t and $p_{T,t}$ are the mass and transverse momentum of the top quarks, where the top quark mass is set to $m_t = 172.5$ GeV. The scales are referred to as dynamic scales due to their dependence on the transverse momenta of particles in the events, rather than a fixed value. The CP5 tune [122] (see Section 5.5) is used for the description of the underlying event. The POWHEG damping parameter h_{damp} is set to $h_{\text{damp}} = 1.379m_t$ (see Section 5.2). The configuration of the PS (including the CP5 tune), the h_{damp} parameter, the pdf, and the top quark mass are the same for all simulated samples used in this measurement unless stated otherwise.

Simulation of $t\bar{t}B$ events with POWHEG and PYTHIA

Signal-like $t\bar{t}$ events with at least one additional b jet (see Section 5.8.1) can also be simulated separately in order to obtain a description of $t\bar{t}b\bar{b}$ at ME level (see Section 7.2). These events are simulated using POWHEG-BOX-RES [128] and OPENLOOPS [129] for the ME generation, interfaced with PYTHIA. This configuration is referred to as the $t\bar{t}b\bar{b}$ sample or PP8 $t\bar{t}b\bar{b}$ 4FS in the following and is used as the nominal $t\bar{t}b\bar{b}$ model in this measurement. This sample uses a pdf set with massive b quarks, i.e. a 4FS pdf set. The b quark mass is set to $m_b = 4.75$ GeV. As detailed in Section 7.2, the factorization and, especially, renormalization scales have a large impact on the rate and kinematic distributions of events generated by this simulation setup due to the large dependence on α_s in the simulation of $t\bar{t}b\bar{b}$ MEs. The renormalization and factorization scales in this simulation approach use $\xi_R = \xi_F = 0.5$ following eq. (7.1) and eq. (7.3), i.e. explicitly yield

$$\mu_R = \frac{1}{2} \prod_{i=t,\bar{t},b,\bar{b}} \sqrt[4]{m_{T,i}}, \quad \text{and} \quad \mu_F = \frac{1}{4} \sum_{i=t,\bar{t},b,\bar{b},j} m_{T,i}. \quad (8.2)$$

The indices i run over the expected final state quarks of the LO ME calculation, i.e. top (anti)quarks and bottom (anti)quarks, and also all additional partons j in case of μ_F . This simulation approach cannot account for $t\bar{t}$ events without additional b jet radiation, hence the PP8 $t\bar{t}$ 5FS simulation approach has to be used for non- $t\bar{t}b\bar{b}$ events in order to account for the full $t\bar{t}$ phase space. To obtain the full $t\bar{t}$ phase space coverage, all events which contain at least one particle-level jet with a ghost-matched B hadron in addition to the $t\bar{t}$ system (additional b jet) are simulated with the PP8 $t\bar{t}b\bar{b}$ 4FS setup, while the remaining events are taken from the PP8 $t\bar{t}$ 5FS sample. This selection of events with at least one additional b jet is referred to as $t\bar{t}B$, indicating that at least one B hadron is present in addition to the $t\bar{t}$ system. The remaining events from the PP8 $t\bar{t}$ 5FS sample are separated into two classes to treat them as separate processes. Events with at least one particle-level jet with a ghost-matched C hadron (but no B hadron) in addition to the $t\bar{t}$ system are assigned to the $t\bar{t}C$ process, while the rest is assigned to the $t\bar{t}$ +light process. This

separation gives more freedom to the background description for the $t\bar{t}b$ measurements, as, for example, uncertainty sources relevant for radiation of additional jets for the $t\bar{t}c$ process can be treated independently of the $t\bar{t}$ +light process where either no, or only light jet radiation is expected. An example of this are the uncertainties associated with the initial-state and final-state radiation in the PS.

Alternative $t\bar{t}b\bar{b}$ signal models

In order to facilitate a comparison of the nominal $t\bar{t}b\bar{b}$ model (PP8 $t\bar{t}b\bar{b}$ 4FS) with other modeling approaches, five additional signal models are defined here. These signal models are only used for comparisons of the measured data distributions in Sections 9.2 and 9.3, and are not used for the signal or background description.

One of these alternative signal models has already been introduced as the PP8 $t\bar{t}$ 5FS sample. Relative to the nominal signal model, this model obtains additional b quarks mostly from the PS process. Hence, comparisons between this model and the nominal signal model are sensitive to differences in the description of additional b jet radiation between PS and ME.

One alternative model is based on the simulation of $t\bar{t}$ with the POWHEG ME generator at NLO accuracy in QCD, interfaced with HERWIG v.7.13 [120, 121] for parton showering and hadronization. The underlying-event description is tuned with the CH3 tune [130]. This signal model is referred to as PH7 $t\bar{t}$ 5FS. Comparisons of this signal model to the PP8 $t\bar{t}$ 5FS signal model are sensitive to differences in the description of parton showering and hadronization processes, as both simulation approaches use the same settings in the $t\bar{t}$ ME simulation. As explained in Section 5.4, the PYTHIA and HERWIG PSs use significantly different hadronization models.

Another alternative model uses the MADGRAPH5_AMC@NLO v2.6.5 [124] generator for the simulation of $t\bar{t}b\bar{b}$ MEs at NLO accuracy in QCD. This is interfaced with PYTHIA for parton showering and hadronization and uses MADSPIN for the decay of top quarks [127]. This model is referred to as AMCP8 $t\bar{t}b\bar{b}$ 4FS, and uses a 4FS pdf set. The renormalization and factorization scales in this model are set to

$$\mu_R = \mu_F = \sum_i m_{T,i}, \quad (8.3)$$

with i running over all final-state partons. As this model uses the same PS model and pdf set as the nominal signal model, comparisons between both are sensitive to the differences in ME calculations with the corresponding simulation settings of POWHEG-BOX-RES and MADGRAPH5_AMC@NLO.

Another model, also using a 4FS pdf set, is simulated using SHERPA v2.2.4 [131] with OPENLOOPS [129] for a description of $t\bar{t}b\bar{b}$ at NLO accuracy in QCD. The description of parton showering and hadronization also uses the SHERPA event generator. This model is referred to as SHERPA $t\bar{t}b\bar{b}$ 4FS. In this model, the renormalization and factorization scales use $\xi_R = \xi_F = 1$ following eq. (7.1) and eq. (7.3). Comparisons of this model to the other $t\bar{t}b\bar{b}$ simulations using the 4FS pdf give insight into the quality of the SHERPA simulation with these scale choices relative to the POWHEG and MADGRAPH5_AMC@NLO simulation approaches which are used more often in the CMS Collaboration.

Finally, the MADGRAPH5_AMC@NLO event generator is used for a description of $t\bar{t}$ +jets events with up to two additional jets at NLO in QCD, merged using the FxFx scheme [132]. The cut-off scale in the ME is set to 20 GeV and the merging scale is set to 40 GeV. This

8 Ingredients for the $t\bar{t}b\bar{b}$ measurement

simulation approach uses the 5FS pdf set and is interfaced with PYTHIA for the description of the parton shower and hadronization. This model is referred to as AMCP8 $t\bar{t}$ +jets FFX 5FS. The renormalization and factorization scales in this model are set to

$$\mu_R = \mu_F = \sum_i m_{T,i}, \quad (8.4)$$

with i running over all final-state partons. As explained in Section 7.2, this simulation approach can, in principle, describe $t\bar{t}b\bar{b}$ at the ME level if the b jets from $g \rightarrow b\bar{b}$ splitting are hard enough to be among the leading radiations. However, studies in Ref. [137] showed that this ME-level contribution is subdominant and the majority of the phase space utilizes the PS for the $g \rightarrow b\bar{b}$ splitting simulation. Hence, this simulation approach is another probe of the b jet description via the PS.

The generator settings of all generator setups for the modeling and comparison of $t\bar{t}b\bar{b}$ are summarized in Table 8.1.

Simulation of $t\bar{t}X$ events

Besides $t\bar{t}$ production, other, minor, backgrounds contribute to the phase space regions of this measurement. Contributions of $t\bar{t}$ production in association with a Higgs boson ($t\bar{t}H$) are simulated using the POWHEG v2 ME generator at NLO in QCD, assuming a Higgs boson mass of $m_H = 125$ GeV. Contributions of $t\bar{t}$ production and a Z boson ($t\bar{t}Z$) are simulated using MADGRAPH5_amc@NLO v2.6.5 [124] at NLO accuracy in QCD. For this process, the MADSPIN package [127] is used for the decay of heavy particles. The production of a W boson in addition to the $t\bar{t}$ system ($t\bar{t}W$) is simulated using MADGRAPH5_amc@NLO at NLO accuracy in QCD and up to one additional jet, merged using the FFX merging scheme [132]. This also uses the MADSPIN package for the decay of heavy particles. Throughout this measurement, these three $t\bar{t}$ -associated boson production processes are collectively referred to as $t\bar{t}X$, unless a distinction is necessary. The combination of $t\bar{t}W$ and $t\bar{t}Z$ is sometimes also referred to as $t\bar{t}V$, indicating the additional production of a vector boson.

Simulation of single top quark production

The contributions of single top (anti)quark production are simulated with different approaches depending on the production channel of the top (anti)quark. In the s -channel, events are simulated using the MADGRAPH5_amc@NLO generator at NLO accuracy in QCD, while in the t -channel and when produced in association with a W boson (referred to as tW -channel), POWHEG is used at NLO accuracy in QCD.

Simulation of vector boson production in association with jets

Contributions of a vector boson (W or Z) in association with jets (Vjets) are simulated using the MADGRAPH5_amc@NLO event generator at LO accuracy with up to four jets at the ME level, merged using the MLM scheme [133].

Normalization of background contributions

The number of events in all background samples is normalized to state-of-the-art theory calculations of the respective cross sections. The $t\bar{t}$, single top, and Vjets processes are normalized to calculations at NNLO accuracy in QCD, while for the inclusive $t\bar{t}$ simulation, additionally, soft gluons are resummed to next-to-next-to-leading logarithm (NNLL) accuracy [59, 154]. The $t\bar{t}X$ processes are normalized to calculations at NLO accuracy in QCD. The nominal signal model (PP8 $t\bar{t}b\bar{b}$ 4FS) is normalized to the cross section predicted by the generator. The explicit lists of simulated samples and the assumed cross sections [59, 124, 154–158] are summarized in Table 8.2.

Table 8.1: **Generator settings for different modeling approaches of $t\bar{t}b\bar{b}$ production.** The top quark mass value is set to $m_t = 172.5$ GeV for all generator setups, and for the generator setups using massive b quarks, the b quark mass value is set to $m_b = 4.75$ GeV. In the scale settings, $m_{T,i}^2 = m_i^2 + p_{T,i}^2$ is the transverse mass. For the MADGRAPH5_AMC@NLO setup, Q_{cut} corresponds to the merging scale, and Q_{cutME} corresponds to the jet cut-off in the ME calculation.

Generator set up	Process/ME order	Generator/Shower	Tune	PDF set	h_{damp}	Scales
PP8 $t\bar{t}$ 5FS	$t\bar{t}$ / NLO	POWHEG v2/ PYTHIA 8	CP5	5FS NNPDF3.1 NNLO	$1.397m_t$	$\mu_F = \mu_R = \sqrt{\frac{1}{2} (m_{T,t}^2 + m_{T,\bar{t}}^2)}$
PH7 $t\bar{t}$ 5FS	$t\bar{t}$ / NLO	POWHEG v2/ HERWIG 7.13	CH3	5FS NNPDF3.1 NNLO	$1.397m_t$	$\mu_F = \mu_R = \sqrt{\frac{1}{2} (m_{T,t}^2 + m_{T,\bar{t}}^2)}$
PP8 $t\bar{t}b\bar{b}$ 4FS	$t\bar{t}b\bar{b}$ / NLO	POWHEG-BOX/ PYTHIA 8	CP5	4FS NNPDF3.1 NNLO as 0118	$1.397m_t$	$\mu_R = \frac{1}{2} \prod_{i=t,\bar{t},b,\bar{b}} m_{T,i}^{1/4}$ $\mu_F = \frac{1}{4} \sum_{i=t,\bar{t},b,\bar{b},g} m_{T,i}$
SHERPA $t\bar{t}b\bar{b}$ 4FS	$t\bar{t}b\bar{b}$ / NLO	SHERPA 2.2.4	SHERPA	4FS NNPDF3.0 NNLO as 0118	—	$\mu_R = \prod_{i=t,\bar{t},b,\bar{b}} m_{T,i}^{1/4}$ $\mu_F = \frac{1}{2} \sum_{i=t,\bar{t},b,\bar{b},g} m_{T,i}$
AMCP8 $t\bar{t}b\bar{b}$ 4FS	$t\bar{t}b\bar{b}$ / NLO	MADGRAPH5_AMC@NLO/ PYTHIA 8	CP5	4FS NNPDF3.1 NNLO as 0118	—	$\mu_F = \mu_R = \sum m_T$
AMCP8 $t\bar{t}$ +jets FxFx 5FS	$t\bar{t}$ +jets FxFx/ NLO [≤ 2 jets]	MADGRAPH5_AMC@NLO/ PYTHIA 8	CP5	4FS NNPDF3.1 NNLO	—	$\mu_F = \mu_R = \sum m_T$, $Q_{\text{cut}} = 40$ GeV, $Q_{\text{cutME}} = 20$ GeV

Table 8.2: **Processes used for the signal and background estimation in the $t\bar{t}b\bar{b}$ measurement.** Processes are listed together with their cross sections (σ), or cross sections times branching fractions ($\sigma \times \mathcal{B}$), where applicable. The cross sections are obtained either from calculations or the simulation itself, as indicated in the comment column.

Process	σ (pb)	Comment	
$t\bar{t}$ (2ℓ)	$\sigma \times \mathcal{B} = 88.50$	based on Ref. [59, 154]	
$t\bar{t}$ (1ℓ)	$\sigma \times \mathcal{B} = 366.30$	based on Ref. [59, 154]	
$t\bar{t}$ (0ℓ)	$\sigma \times \mathcal{B} = 378.90$	based on Ref. [59, 154]	
$t\bar{t}b\bar{b}$ (2ℓ)	$\sigma \times \mathcal{B} = 4.60$	from simulation	
$t\bar{t}b\bar{b}$ (1ℓ)	$\sigma \times \mathcal{B} = 19.20$	from simulation	
$t\bar{t}b\bar{b}$ (0ℓ)	$\sigma \times \mathcal{B} = 19.90$	from simulation	
$t\bar{t}H$	$\sigma = 0.51$	based on Ref. [155]	
$t\bar{t}Z$	$\sigma = 0.78$	based on Ref. [124]	
$t\bar{t}W$	$\sigma = 0.61$	based on Ref. [124]	
single top	(s -channel)	$\sigma = 3.30$	based on Ref. [156]
	(t -channel, t)	$\sigma = 136.00$	based on Ref. [157]
	(t -channel, \bar{t})	$\sigma = 81.00$	based on Ref. [157]
	(tW -channel, t)	$\sigma = 19.60$	based on Ref. [156]
	(tW -channel, \bar{t})	$\sigma = 19.60$	based on Ref. [156]
W jets ($W \rightarrow \ell\nu$)	($70 \text{ GeV} \leq H_T \leq 100 \text{ GeV}$)	$\sigma \times \mathcal{B} = 1443$	based on Ref. [158]
	($100 \text{ GeV} \leq H_T \leq 200 \text{ GeV}$)	$\sigma \times \mathcal{B} = 1435$	based on Ref. [158]
	($200 \text{ GeV} \leq H_T \leq 400 \text{ GeV}$)	$\sigma \times \mathcal{B} = 383.20$	based on Ref. [158]
	($400 \text{ GeV} \leq H_T \leq 600 \text{ GeV}$)	$\sigma \times \mathcal{B} = 51.70$	based on Ref. [158]
	($600 \text{ GeV} \leq H_T \leq 800 \text{ GeV}$)	$\sigma \times \mathcal{B} = 2.50$	based on Ref. [158]
	($800 \text{ GeV} \leq H_T \leq 1200 \text{ GeV}$)	$\sigma \times \mathcal{B} = 5.60$	based on Ref. [158]
	($1200 \text{ GeV} \leq H_T \leq 2500 \text{ GeV}$)	$\sigma \times \mathcal{B} = 1.30$	based on Ref. [158]
Z jets ($Z \rightarrow \ell\ell$)	($H_T \geq 2500 \text{ GeV}$)	$\sigma \times \mathcal{B} = 0.01$	based on Ref. [158]
	($10 \text{ GeV} \leq m(\ell\ell) \leq 50 \text{ GeV}$)	$\sigma \times \mathcal{B} = 8610$	based on Ref. [158]
	($m(\ell\ell) \geq 50 \text{ GeV}, 70 \text{ GeV} \leq H_T \leq 100 \text{ GeV}$)	$\sigma \times \mathcal{B} = 211.20$	based on Ref. [158]
	($m(\ell\ell) \geq 50 \text{ GeV}, 100 \text{ GeV} \leq H_T \leq 200 \text{ GeV}$)	$\sigma \times \mathcal{B} = 183.20$	based on Ref. [158]
	($m(\ell\ell) \geq 50 \text{ GeV}, 200 \text{ GeV} \leq H_T \leq 400 \text{ GeV}$)	$\sigma \times \mathcal{B} = 55.30$	based on Ref. [158]
	($m(\ell\ell) \geq 50 \text{ GeV}, 400 \text{ GeV} \leq H_T \leq 600 \text{ GeV}$)	$\sigma \times \mathcal{B} = 7.85$	based on Ref. [158]
	($m(\ell\ell) \geq 50 \text{ GeV}, 600 \text{ GeV} \leq H_T \leq 800 \text{ GeV}$)	$\sigma \times \mathcal{B} = 1.93$	based on Ref. [158]
	($m(\ell\ell) \geq 50 \text{ GeV}, 800 \text{ GeV} \leq H_T \leq 1200 \text{ GeV}$)	$\sigma \times \mathcal{B} = 0.83$	based on Ref. [158]
($m(\ell\ell) \geq 50 \text{ GeV}, 1200 \text{ GeV} \leq H_T \leq 2500 \text{ GeV}$)	$\sigma \times \mathcal{B} = 0.18$	based on Ref. [158]	
($m(\ell\ell) \geq 50 \text{ GeV}, H_T \geq 2500 \text{ GeV}$)	$\sigma \times \mathcal{B} = 0.01$	based on Ref. [158]	

8.2 Fiducial phase space definition

The definition of fiducial phase space regions is necessary to define what constitutes a signal process for the purpose of interpreting the results. In the case of the $t\bar{t}b\bar{b}$ process, the differentiation between $t\bar{t}$ production and $t\bar{t}$ production in association with additional jets is intricate and requires a proper method of differentiation. There are multiple options available to define a fiducial region of $t\bar{t}b\bar{b}$ in the inclusive $t\bar{t}$ phase space region. Based on the process categorizations in Section 8.1, the $t\bar{t}B$ definition could be used as a fiducial phase space definition. This definition, however, depends on the identification of the $t\bar{t}$ pair and its decay products, and a definition of what constitutes an additional b jet based on that identification. Therefore, this definition is not purely based on particle level, but references the Monte-Carlo decay chain. A definition like this is difficult to employ for comparisons with a range of event generators and is therefore disfavored. An alternative

method of defining a fiducial phase space is to only use the information of stable final-state particles. Here, this refers to final-state particles with a proper lifetime $\tau \geq 10$ mm and $|\eta| \leq 5$. This definition is accessible for all general-purpose Monte-Carlo generators and facilitates easy comparisons of the results in this measurement. A disadvantage of such a purely particle-level-based definition is the ambiguity in the origin of the particle-level b jets. Some observables that are of general interest in a differential measurement of $t\bar{t}b\bar{b}$ are therefore not accessible. Specifically, these are observables targeting directly the b jets not from top decay (additional b jets), or observables targeting the top (anti)quarks directly, e.g. the p_T of the top (anti)quarks. In this thesis, only the measurements using the particle-level fiducial phase space definitions are discussed. Later, in Part III an additional measurement of the top (anti)quark p_T will be discussed for the $t\bar{t}$ +jets process ($t\bar{t}$ +jets refers to the associated production of a $t\bar{t}$ pair with jets of any flavor), where also a particle-level reconstruction of the top quarks is performed (pseudo-top).

As already introduced in Section 7.3, four different fiducial phase space regions are defined in this measurement. These phase space regions target different aspects of the $t\bar{t}b\bar{b}$ process and the fiducial cross sections of these fiducial phase space definitions are measured alongside a set of differential observables tailored to the respective phase space regions. The fiducial phase space regions all use the same definition of particle-level jets, muons, and electrons, which are introduced in the following. The definitions are chosen to correspond as closely as possible to the selections of objects that will be introduced in Section 8.3 on the detector level. The detector-level selections and object definitions adhere to the constraints of the experimental environment, like trigger thresholds or reconstruction efficiencies. Hence, the particle-level definitions defined here are adjusted to these constraints.

Electrons: Electrons require a transverse momentum of $p_T \geq 29$ GeV and $|\eta| \leq 2.5$. Photons in a cone of $\Delta R \leq 0.1$ around the electron are added to the electron in order to account for bremsstrahlung effects in the final state (“dressing”).

Muons: Muons require a transverse momentum of $p_T \geq 26$ GeV and $|\eta| \leq 2.4$. The same dressing procedure is performed for the electrons but its relevancy is subdominant for muons.

Veto leptons: A group of veto leptons is defined by loosening the previous lepton definitions to $p_T \geq 15$ GeV, and $|\eta| \leq 2.5$ (2.4) for electrons (muons). These veto leptons are used to define the single-lepton final state where exactly one such lepton is allowed to be present in the fiducial region. Events with more or fewer veto leptons are considered as background to this measurement.

Jets: Jets are clustered with the anti- k_T algorithm (see Section 3.3.1) using all stable final-state particles except neutrinos. The clustering radius is $R = 0.4$. Only jets with $p_T \geq 25$ GeV and $|\eta| \leq 2.4$ are considered for this measurement. The p_T threshold is lower than on the reconstruction level (see Section 8.3) to minimize the out-of-acceptance contribution (see Section 8.6) while still keeping both definitions close to each other. Furthermore, any jet within the proximity of a lepton (following the previous definitions) is vetoed. The threshold for this veto is $\Delta R = 0.4$. The flavor of the jets is defined via the ghost-matching procedure described in Section 5.8.1. Jets with a ghost-clustered B hadron are defined as b jets, while the remaining jets are referred to as light jets for the purpose of fiducial phase-space and observable definitions.

Based on these object definitions the four fiducial signal regions are defined. All of these fiducial definitions require exactly one electron or muon following the veto lepton definitions. These fiducial volumes are not mutually exclusive.

8 Ingredients for the $t\bar{t}b\bar{b}$ measurement

The most inclusive fiducial signal definition requires at least five jets, of which at least three have to be b jets (5j3b). This phase space encompasses $\sim 11.1\%$ of events defined as $t\bar{t}B$ and is a subset of that definition. The purpose of the phase space region is to probe the rate and kinematics of $t\bar{t}$ production in association with at least one b jet. This is reflected in the choice of observables for this phase space, which focuses on global event observables and the kinematics of the third hardest (in p_T) b jet. Differential cross sections are measured for the multiplicity of jets (N_{jets}) and b jets (N_b), and the scalar sum of all jets (H_T^{jets}) and b jets (H_T^b). For the third hardest b jet the p_T and $|\eta|$ distributions ($p_T(b_3)$ and $|\eta(b_3)|$) are measured. In this fiducial phase space, the third hardest b jet corresponds to an additional b jet in $\sim 49\%$ of cases. The two leading b jets in p_T originate predominantly from top quark decays, as the high mass of top quarks yields, on average, decay products with higher momenta. This motivates the choice of this observable in order to access the description of additional b jet radiation in $t\bar{t}$ events without any reference to the simulated history of the b jets. The other three fiducial phase space regions are subsets of this 5j3b phase space region.

The 6j4b fiducial phase space region is defined by requiring at least six jets, of which at least four have to be b jets. This fiducial volume encompasses the full signature expected from a single-lepton $t\bar{t}b\bar{b}$ event at LO, where each b quark at ME-level is reconstructed in a separate jet. A large set of differential distributions of interest can be extracted from this phase space. Similar to the 5j3b phase space also the jet multiplicity (N_{jets}) and the H_T^{jets} and H_T^b observables are extracted here to get a quality measure of the description of global event observables in this fiducial volume. Following along the same lines of argumentation as before, the p_T and $|\eta|$ of the third ($p_T(b_3)$, $|\eta(b_3)|$) and fourth hardest ($p_T(b_4)$, $|\eta(b_4)|$) b jets are measured. In this phase space, the third (fourth) hardest b jet corresponds to an additional b jet in $\sim 53\%$ ($\sim 65\%$) of cases. Additionally, two observables are probed by considering all possible pairs of b and \bar{b} jets (bb). The average ΔR over all bb-pairs ($\Delta R_{bb}^{\text{avg}}$) is measured to be sensitive to mis-modelings of angular distributions in bb-pairs. The invariant mass of the bb-pair with the largest invariant mass (m_{bb}^{max}) is probed as this constitutes a background in a measurement of $t\bar{t}H$ production. Due to the high mass of the Higgs boson, the bb-pair in $t\bar{t}b\bar{b}$ events with the highest invariant mass is the most probable candidate to be selected as a fake Higgs boson candidate in $t\bar{t}b\bar{b}$ background events. Therefore, good modeling of this observable is of high importance.

An additional set of observables in the 6j4b phase space region relies on the identification of the two b jets with the smallest spatial separation in ΔR , in the following referred to as bb^{extra} pair. This pair of b jets has a large overlap with the definition of additional b jets (which is inaccessible with the purely particle-level-based definition of the signal fiducial volume). Around 68% of the b jets selected via this method correspond to additional b jets, while in $\sim 49\%$ ($\sim 38\%$) of cases both (exactly one) of the bb^{extra} jets correspond to the additional b jets. By selecting the b jets closest to each other these observables are sensitive to collinear gluon-splitting effects, where a gluon splits into a $b\bar{b}$ -pair ($g \rightarrow b\bar{b}$). This regime is an important aspect of the $t\bar{t}b\bar{b}$ process, as, depending on the method of simulation and calculation, this may yield different differential distributions. As explained in Section 7.2, when comparing, for example, the PP8 $t\bar{t}$ 5FS and PP8 $t\bar{t}b\bar{b}$ 4FS simulation approaches for obtaining a description of the $t\bar{t}b\bar{b}$ process, the $g \rightarrow b\bar{b}$ splitting is predominantly described by the PS in the former and the ME calculation in the latter case. To ascertain if these approaches with the chosen simulation settings model the kinematic distributions of the bb^{extra} pair well, the opening angle ($\Delta R(bb^{\text{extra}})$), the invariant mass ($m(bb^{\text{extra}})$), the p_T and $|\eta|$ of the bb^{extra} pair ($p_T(bb^{\text{extra}})$, $|\eta|(bb^{\text{extra}})$), as well as the p_T and $|\eta|$ of the two b jets of the bb^{extra} pair ($p_T(b_1^{\text{extra}})$, $p_T(b_2^{\text{extra}})$, $|\eta(b_1^{\text{extra}})|$, $|\eta(b_2^{\text{extra}})|$) are probed.

The remaining two fiducial phase space regions are designed to probe the radiation of an additional light jet in $t\bar{t}b\bar{b}$ events. In simulation approaches like PP8 $t\bar{t}$ 5FS at most one real emission in addition to the $t\bar{t}$ system is described by the ME calculation, while for the PP8 $t\bar{t}b\bar{b}$ 4FS simulation, the same is true for one real emission in addition to the $t\bar{t}b\bar{b}$ system. Hence, the quality and possible differences in the description of additional light jet radiation with these modeling approaches are probed. One additional phase space region is defined based on the 5j3b phase space, by requiring at least three light jets in addition to at least three b jets, i.e. requiring at least six jets in total (6j3b3l). This takes into account the two light jets already expected from $t\bar{t}$ decays at LO in the single-lepton final state. The last phase space region is defined similarly based on the 6j4b phase space region, also with at least three light jets (7j4b3l), yielding at least seven jets in total. By requiring at least three light jets in these phase space regions and retaining the requirements to the b jet multiplicity, additional light jet radiation in the fiducial volume is guaranteed. In both phase space regions, the same observables are probed. The scalar sum of p_T of all light jets (H_T^{light}) and the p_T of the leading additional light jet ($p_T(lj_1^{\text{extra}})$) are measured to probe the description of the light jet momenta. Here, additional light jets are defined based on a W boson identification procedure applied to all light jets in the event. For that purpose, the invariant mass of all combinations of two light jets is compared to an assumed W boson mass of $m_W = 79.6$ GeV. The pair closest to that value is determined to be the pair of light jets originating from hadronic W boson decay of the hadronic top quark decay. The remaining light jets in the events are labeled additional light jets. In both the 6j3b3l and 7j4b3l phase space regions the hardest additional light jet corresponds to a jet without a W boson or top (anti)quark in its simulated history in $\sim 94\%$ of cases. Lastly, the angular distance in ϕ of the hardest additional light jet and the softest b jet ($|\Delta\phi(lj_1^{\text{extra}}, b_{\text{soft}})|$) is measured to probe the correlation of the light jet and b jet radiation outside of the $t\bar{t}$ system. The softest b jet corresponds to an additional b jet in $\sim 50\%$ ($\sim 65\%$) of cases in the 6j3b3l (7j4b3l) phase space regions.

In each of these phase space regions, the fiducial cross section is measured alongside these observables. An overview of all measured observables is shown in Table 8.3.

8.3 Event selection

Data at the CMS experiment is collected for a multitude of different measurements. Analyzing all of these data events for the purpose of this measurement is not feasible and also not very useful. The events of interest occupy only a small phase space region of all events recorded. Hence, offline event selections are applied to select a subset of data events that correspond, as closely as possible, to the process(es) of interest, here the $t\bar{t}b\bar{b}$ process. As explained in Section 2.2.3, data is recorded via a two-tiered trigger system that makes decisions during runtime whether to keep or discard a certain event. The data sets of interest for this measurement are recorded with HLTs for charged leptons (electrons or muons). The trigger configurations used here are summarized in Table 8.4 and change depending on the year of data taking. The reason for these differences are changes in the trigger menu set by the CMS Collaboration. As the available bandwidth for recording events is limited, decisions have to be made about which events are to be recorded. So it could happen that, for example, the p_T -threshold of when an event with an electron is recorded, is increased in order to save bandwidth. Similarly, prescales can be applied to record only every n -th event that activates a trigger. The trigger paths in Table 8.4 correspond to the unprescaled trigger paths with the lowest thresholds, thereby maximizing the selection efficiency of events with electrons or muons. For muons, the HLT thresholds are $p_T \geq 24/27/24$ GeV for data taken in 2016/2017/2018. For electrons, the trigger threshold was $p_T \geq 27$ GeV in 2016 and $p_T \geq 32$ GeV in 2017 and 2018. Due

8 Ingredients for the $t\bar{t}b\bar{b}$ measurement

Table 8.3: **Observables measured in the each of the different fiducial phase space regions of the $t\bar{t}b\bar{b}$ measurement.**

Observable		5j3b	6j4b	6j3b3l	7j4b3l
σ_{fid}	Inclusive cross section	✓	✓	✓	✓
Global observables					
N_{jets}	Jet multiplicity	✓	✓		
N_{b}	b jet multiplicity	✓			
$H_{\text{T}}^{\text{jets}}$	Scalar sum of jet p_{T}	✓	✓		
H_{T}^{b}	Scalar sum of b jet p_{T}	✓	✓		
$H_{\text{T}}^{\text{light}}$	Scalar sum of light jet p_{T}			✓	✓
Observables related to b jets					
$p_{\text{T}}(\mathbf{b}_3)$	p_{T} of third hardest b jet	✓	✓		
$ \eta(\mathbf{b}_3) $	$ \eta $ of third hardest b jet	✓	✓		
$p_{\text{T}}(\mathbf{b}_4)$	p_{T} of fourth hardest b jet		✓		
$ \eta(\mathbf{b}_4) $	$ \eta $ of fourth hardest b jet		✓		
Observables considering all pairs of b jets (bb)					
$\Delta R_{\text{bb}}^{\text{avg}}$	Average ΔR of all bb pairs		✓		
$m_{\text{bb}}^{\text{max}}$	Highest invariant mass among all bb pairs		✓		
Observables related to the pair of b jets closest in ΔR (bb^{extra})					
$p_{\text{T}}(\mathbf{b}_1^{\text{extra}})$	p_{T} of leading extra b jet		✓		
$ \eta(\mathbf{b}_1^{\text{extra}}) $	$ \eta $ of leading extra b jet		✓		
$p_{\text{T}}(\mathbf{b}_2^{\text{extra}})$	p_{T} of subleading extra b jet		✓		
$ \eta(\mathbf{b}_2^{\text{extra}}) $	$ \eta $ of subleading extra b jet		✓		
$\Delta R(\text{bb}^{\text{extra}})$	ΔR of bb^{extra} pair		✓		
$ \eta (\text{bb}^{\text{extra}})$	$ \eta $ of bb^{extra} pair		✓		
$m(\text{bb}^{\text{extra}})$	invariant mass of bb^{extra} pair		✓		
$p_{\text{T}}(\text{bb}^{\text{extra}})$	p_{T} of bb^{extra} pair		✓		
Observables related to extra light jets					
$p_{\text{T}}(\mathbf{l}_{\text{J}_1^{\text{extra}}})$	p_{T} of leading extra light jet			✓	✓
$ \Delta\phi(\mathbf{l}_{\text{J}_1^{\text{extra}}}, \mathbf{b}_{\text{soft}}) $	$\Delta\phi$ of leading extra light jet and softest b jet			✓	✓

Table 8.4: **HLT paths for electrons and muons in the different data taking years.**

Year	Electron channel	Muon channel
2016	HLT_E1e27_WPTight_Gsf	HLT_IsoMu24 OR HLT_IsoTkMu24
2017	HLT_E1e28_eta2p1_WPTight_Gsf_HT150 OR HLT_E1e32_WPTight_Gsf_L1DoubleEG	HLT_IsoMu27
2018	HLT_E1e32_WPTight_Gsf OR HLT_E1e28_eta2p1_WPTight_Gsf_HT150	HLT_IsoTkMu24

to the increase of the trigger threshold in 2017 and 2018, the fraction of recorded events is decreased w.r.t. 2016. Hence, a second trigger path is used in these years, requiring an electron with $p_{\text{T}} \geq 28$ GeV and $|\eta| \leq 2.1$ in combination with $H_{\text{T}} \geq 150$ GeV. This allows for still selecting electrons with lower p_{T} while having more stringent requirements on the $|\eta|$ range of the electron and also requiring additional hadronic activity in the form of jets in the event, reflected in large H_{T} .

The offline selection criteria for electrons and muons reflect these trigger thresholds. In general, the p_{T} selection requirements are set to be 2 GeV above the trigger thresholds

to avoid the turn-on region where the triggers have not reached their full efficiency yet. More details about the measurement of trigger efficiencies are summarized in Section 6.3.

Electrons: Electrons have to pass the quality criteria for electrons introduced in Section 3.2.2. Electrons passing the tight identification threshold criteria are selected. Furthermore, only electrons are selected with $p_T \geq 29$ GeV and $|\eta| \leq 2.5$ in 2016, and either $p_T \geq 34$ GeV and $|\eta| \leq 2.5$ or $p_T \geq 30$ GeV and $|\eta| \leq 2.1$ in 2017 and 2018, based on the thresholds of the HLT paths used in the respective years. Additionally, electrons whose supercluster (SC) is in the region of $1.44 \leq |\eta_{SC}| \leq 1.57$, i.e. in the transition region between the barrel and endcap region of the detector, are discarded due to the insufficient coverage of the detector in this region.

Muons: Muons have to pass the quality criteria for muons introduced in Section 3.2.1 and pass the criteria defined for the tight identification threshold. Due to the HLT thresholds, muons are selected with $p_T \geq 26$ GeV in 2016 and 2018, and with $p_T \geq 29$ GeV in 2017 and have to be in a region with $|\eta| \leq 2.4$.

Veto leptons: A separate group of electrons and muons is defined in order to veto events with more than one electron or muon. This lepton definition is a loosened definition of the electrons and muons described above. The veto identification criteria for electrons (see Section 3.2.2) and loose criteria for muons (see Section 3.2.1) are applied. Additionally, a common threshold of $p_T \geq 15$ GeV is applied for electron and muon definitions. Events are only selected if they have exactly one electron or muon following this veto definition.

Jets: Jets have to pass the set of identification requirements defined in Section 3.3. The remaining jets are selected with $p_T \geq 30$ GeV. The p_T threshold of 30 GeV is higher than the threshold of 25 GeV for jets in the fiducial definitions on particle-level. The p_T threshold is not lowered to 25 GeV here due to the decreased b jet tagging efficiency below 30 GeV, as shown in Figure 3.5.

b tagged jets: Jets passing the medium working point of the DEEPIET b tagging algorithm are defined as b jets for the purpose of event selections and definition of observables. The algorithm, its efficiencies, and working points have been introduced in detail in Section 3.3.2. In addition, a subset of jets is identified as tight b tagged jets, which have stronger requirements on the b jet identification. These tight b tagged jets are used in Section 8.5 to define an additional subcategorization of events.

Following the same definitions as in Section 8.2, four event selections are defined for this measurement on detector level. For the 5j3b phase space events with ≥ 5 jets of which ≥ 3 are b tagged jets are selected. Similarly, in the 6j4b phase space, events with ≥ 6 jets of which ≥ 4 are b tagged jets are selected. The two phase space regions with additional light jet radiation, 6j3b3l and 7j4b3l, require ≥ 6 jets of which ≥ 3 are b tagged jets and ≥ 3 are not b tagged jets, and ≥ 7 jets of which ≥ 4 are b tagged jets and ≥ 3 are not b tagged jets, respectively.

The definitions of observables for the respective phase space regions is analogous to the fiducial definitions, using the medium WP of the b tagging algorithm to determine whether a jet is used as a b jet or not. For the definition of light jets from W boson decay in the 6j3b3l and 7j4b3l phase space regions the same procedure is applied, however, the W boson mass is set to 82.8 GeV due to differences in jet energy scales on particle-level and detector-level. Due to the purely particle-level based definition of the observables in Section 8.2 the definition of all observables on detector level can follow the exact same procedures as employed on generator level.

Table 8.5: **Event yields in the two control regions used for the validation of simulated samples.** Event yields are summed across all data-taking eras and hence correspond to the expectations and observations for 138 fb^{-1} of data. The event yields of $t\bar{t}$ are estimated from the PP8 $t\bar{t}$ 5FS simulation. The quoted uncertainties are due to the limited number of simulated events. The uncertainty on the multijet contribution is of the same size as the uncertainty on the total MC yield due to the low number of events in the simulated multijet sample.

	4j event selection	4j2b event selection
$t\bar{t}$	$7\,233\,000 \pm 1000$	$3\,669\,000 \pm 1000$
Single top	$715\,000 \pm 300$	$261\,400 \pm 200$
$t\bar{t}Z$	$12\,000 \pm 10$	6300 ± 10
$t\bar{t}W$	$11\,410 \pm 20$	5340 ± 20
$t\bar{t}H$	9273 ± 4	6487 ± 3
Vjets	$2\,817\,000 \pm 1000$	$74\,000 \pm 200$
Diboson	$57\,700 \pm 100$	2680 ± 30
Multijet	$1\,420\,000 \pm 30\,000$	$69\,000 \pm 4000$
Total MC	$12\,270\,000 \pm 30\,000$	$4\,094\,000 \pm 4000$
Multijet fraction [%]	11.60	1.70
$t\bar{t}$ fraction [%]	58.90	89.60
Data	12 463 467	3 820 959
Data/MC	1.02	0.93

8.4 Validation of simulation

Following the definition of event selections on detector level in Section 8.3, and the introduction of the simulated processes used for the estimation of signal and background contribution to these phase space regions in Section 8.1, control distributions can be produced to validate the proper description of basic observables by the simulation w.r.t. data. This validation is first performed in Section 8.4.1 for event pre-selections that are looser than the ones required for the definition of the measurement regions. Then in Section 8.4.2, the comparison of simulation and data is checked in the measurement regions.

8.4.1 Control regions

In this section, control distributions for simulation and data are provided in two event pre-selections which are supersets of the measurement regions introduced in Section 8.3. A first event selection, 4j, is defined with exactly one electron or muon and ≥ 4 jets and no requirement on the number of b tagged jets (the definition of objects follows Section 8.3). The purpose of this event selection is to check the contribution of other processes to the tighter selections of the measurement regions. In addition to the processes summarized in Section 8.1, the control distributions also include simulations of events where only two bosons (W bosons and Z bosons) are produced together with additional jets, referred to as diboson production, and events containing only jets produced through the strong interaction, referred to as multijet events. The distributions in the 4j region will be accompanied by distributions in the 4j2b region, highlighting the effect of selecting, among the jets, ≥ 2 b tagged jets. The event yields of data and the processes contributing to these event selections are summarized in Table 8.5. This demonstrates that a selection of ≥ 2 b tagged

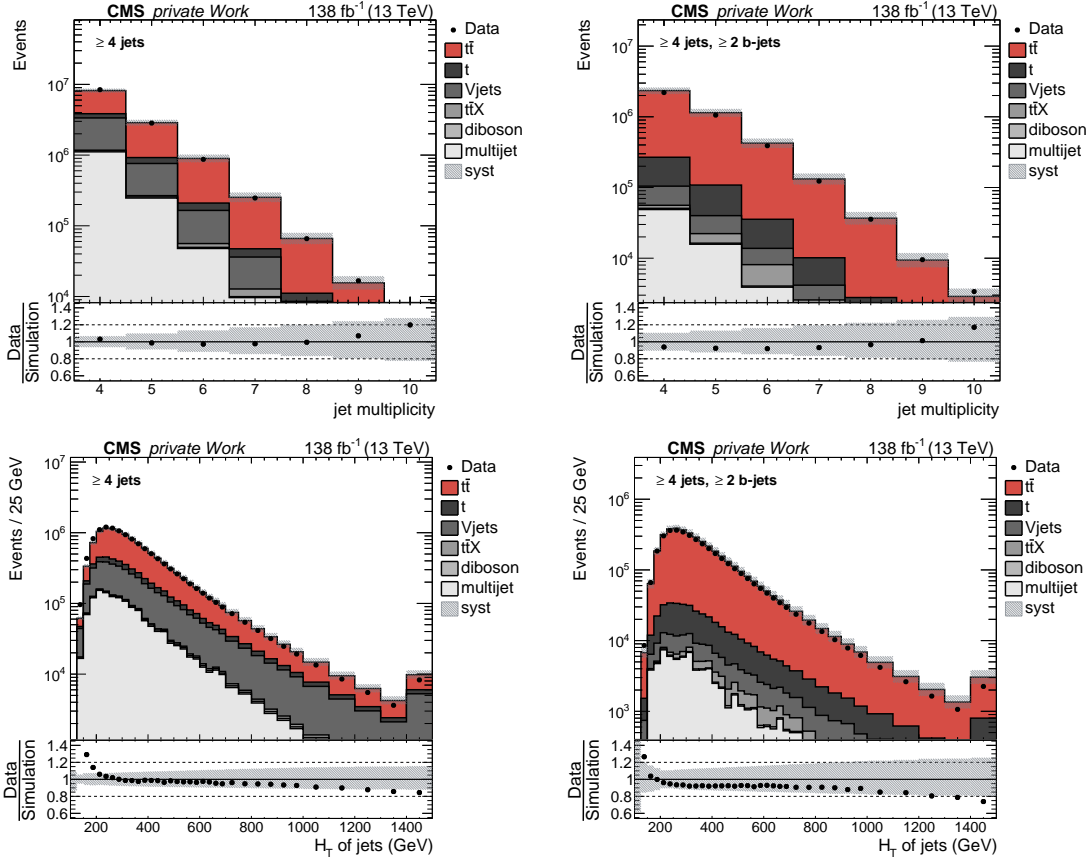


Figure 8.1: **Jet multiplicity (top) and H_T of jets (bottom) in the 4j and 4j2b control regions.** Shown are the contributions of all processes to the detector-level phase space regions as a stack of histograms. The $t\bar{t}$ contribution is estimated from the PP8 $t\bar{t}$ 5FS simulation. Data events are shown as black dots. The lower panel shows the ratio of data to the expectations from simulated events. The shaded bands include all a-priori uncertainties described in Section 8.7.

jets reduces the contributions of most processes, except for the ones containing a pair of top quarks, for which two b jets are expected from the decay of top quarks. Contributions of multijet processes and diboson processes are reduced to levels of $<2\%$ when requiring two or more b tagged jets. The measurement regions require even higher jet and b jet multiplicities, reducing these contributions even further (see discussion in Section 8.4.2).

In Figure 8.1, the jet multiplicity and H_T distributions are shown for the two aforementioned selections of events. The ratio of simulated events relative to data is sufficiently well described in the jet multiplicity distribution. Residual differences between data and simulation are covered by the systematic uncertainties shown as hashed bands. These distributions show that at higher jet multiplicities the relative contribution of $t\bar{t}$ events increases, while other processes like the multijet, diboson, and Vjets contributions decrease steeply. The distribution of the H_T of all jets per event exhibits a clear disagreement between simulation and data where higher H_T values are predicted in simulation relative to what is observed in data, which is further investigated in the discussion of the $t\bar{t}$ +jets measurements in Part III.

Figure 8.2 shows the kinematic distributions of jets, electrons, and muons in the 4j region. The agreement between data and simulation is good in the bulk of the p_T distribution of jets, electrons, and muons (up to around $p_T \leq 200$ GeV). Electrons show trends towards

8 Ingredients for the $t\bar{t}b\bar{b}$ measurement

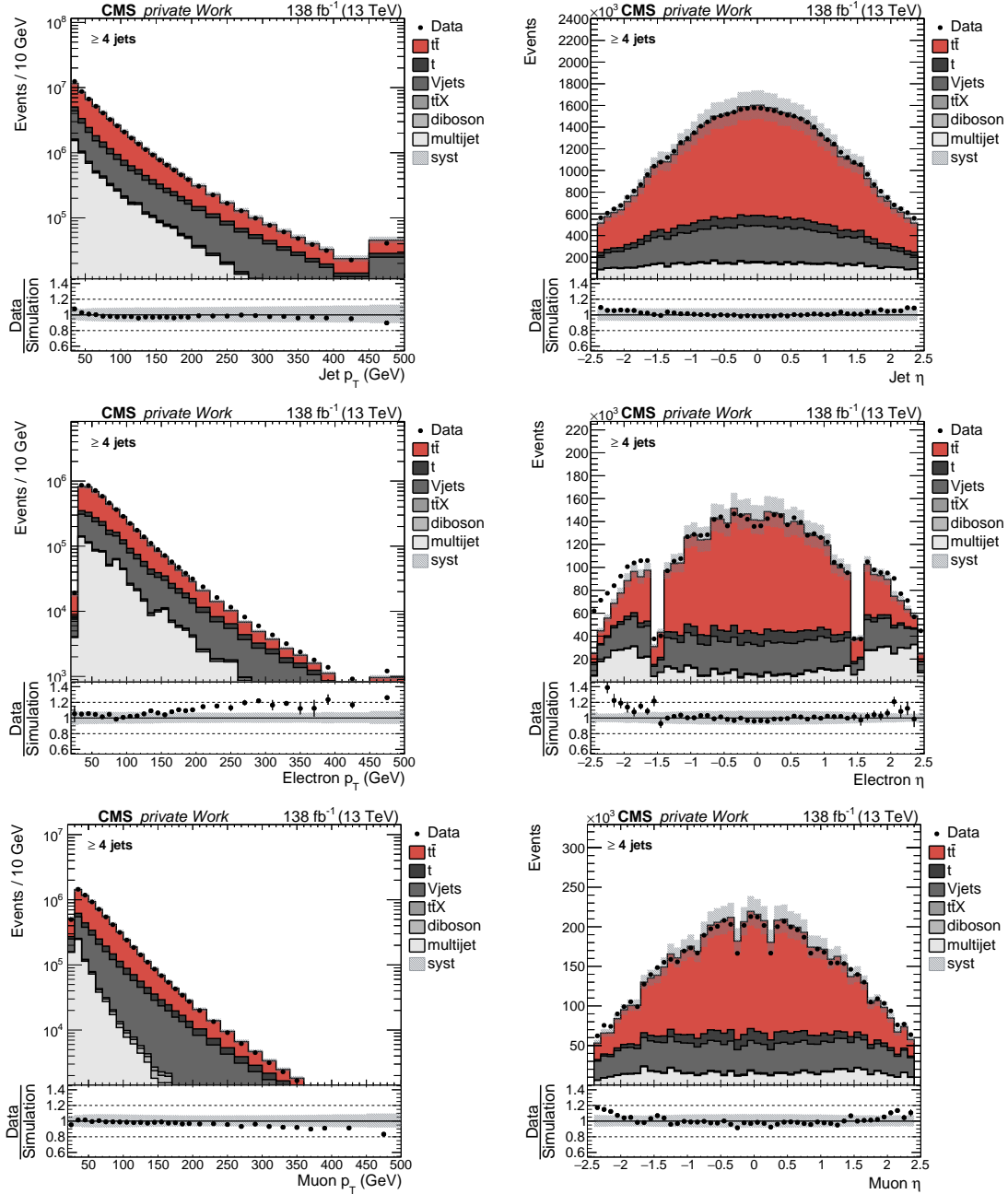


Figure 8.2: **Transverse momentum (left) and η (right) of jets (top), electrons (middle), and muons (bottom) in the 4j control region.** Shown are the contributions of all processes to the detector-level phase space regions as a stack of histograms. The $t\bar{t}$ contribution is estimated from the PP8 $t\bar{t}$ 5FS simulation. Data events are shown as black dots. The lower panel shows the ratio of data to the expectations from simulated events. The shaded bands include all a-priori uncertainties described in Section 8.7.

higher p_T values in data compared to simulation, while the opposite is true for muons. The distributions of the pseudorapidity η show generally good agreement between data and simulation for jets, while for muons, and especially electrons, the regions at large $|\eta|$ exhibit discrepancies between simulation and data. As the event selection for these distributions requires exactly one well-reconstructed charged lepton (electron or muon), the contribution of multijet events to this phase space region originates predominantly from falsely identified leptons. For example, jets could be misidentified as leptons. Due to the

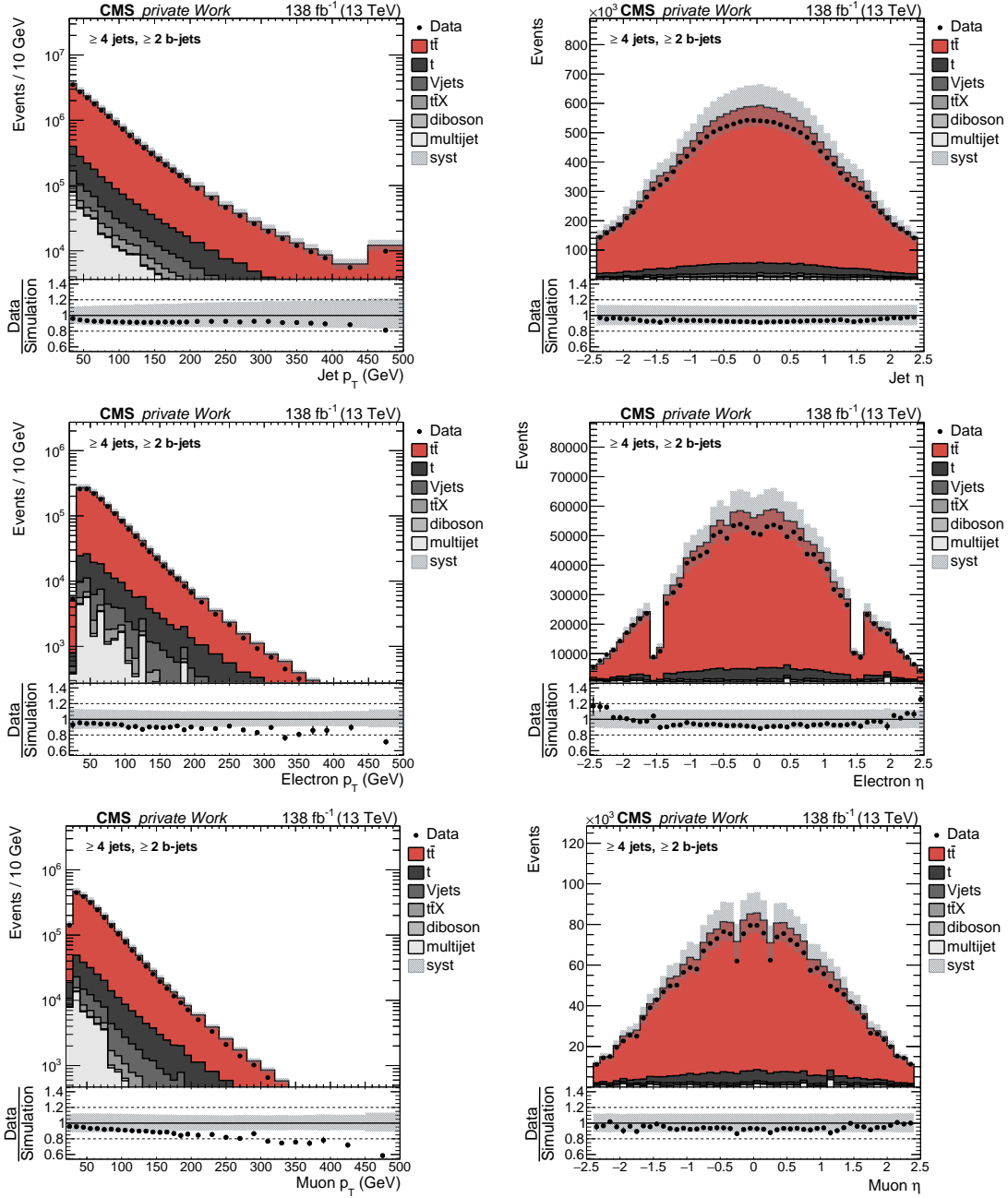


Figure 8.3: Transverse momentum (left) and η (right) of jets (top), electrons (middle), and muons (bottom) in the 4j2b control region. Shown are the contributions of all processes to the detector-level phase space regions as a stack of histograms. The $t\bar{t}$ contribution is estimated from the PP8 $t\bar{t}$ 5FS simulation. Data events are shown as black dots. The lower panel shows the ratio of data to the expectations from simulated events. The shaded bands include all a-priori uncertainties described in Section 8.7.

difficulty of electron reconstruction compared to the reconstruction of muons, the multijet contribution is more dominant in the electron channel. Falsely reconstructed leptons contribute mostly in the high- $|\eta|$ regions, as the detector is less efficient in particle identification in these regions. This is apparent from the increased contribution of multijet events at $|\eta| \geq 1.5$ for the electrons.

8 Ingredients for the $t\bar{t}b\bar{b}$ measurement

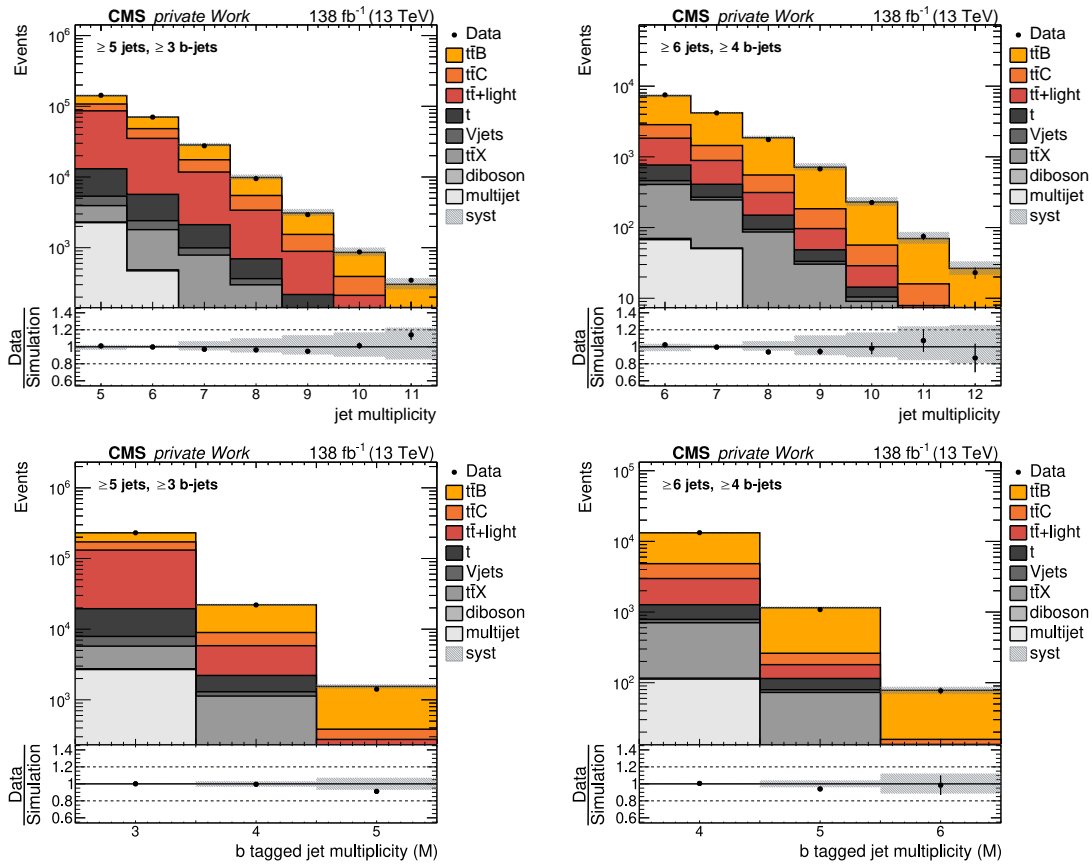


Figure 8.4: **Jet multiplicity (top) and b jet multiplicity (bottom) in the 5j3b (left) and 6j4b (right) measurement regions.** Shown are the contributions of all processes to the detector-level phase space regions as a stack of histograms. The $t\bar{t}B$ contribution is estimated from the PP8 $t\bar{t}b\bar{b}$ 4FS simulation. Data events are shown as black dots. The lower panel shows the ratio of data to the expectations from simulated events. For visualization, the contributions from simulation have been scaled by a common factor to match the yield in data. The shaded bands include all a-priori uncertainties described in Section 8.7. Only effects on the shape of the distributions are considered.

Selecting only events with at least two b jets significantly decreases the rate of multijet and diboson events as these rarely have genuine b jets and are hence suppressed by the selection. The jet, electron, and muon p_T and η distributions for the corresponding 4j2b phase space region are shown in Figure 8.3. The distributions of electron and muon η now show better agreement between data and simulation also at high $|\eta|$, with some residual discrepancies for electrons. The distributions of transverse momenta all show trends towards lower values in data relative to the predictions by simulation. For the p_T of the jets, this is related to the aforementioned top p_T mis-modeling in the simulation. This trend is decreased in the phase space regions of the measurement (5j3b, etc.). The muon region exhibits event yields higher than the electron region by a factor of ~ 1.5 . This is due to the lower electron reconstruction efficiencies relative to the muon reconstruction efficiencies.

8.4.2 Measurement regions

Figure 8.4 shows the distributions of jet multiplicities and b tagged jet multiplicities at the medium b tagging WP after the two event selections 5j3b and 6j4b. Here, the contribution

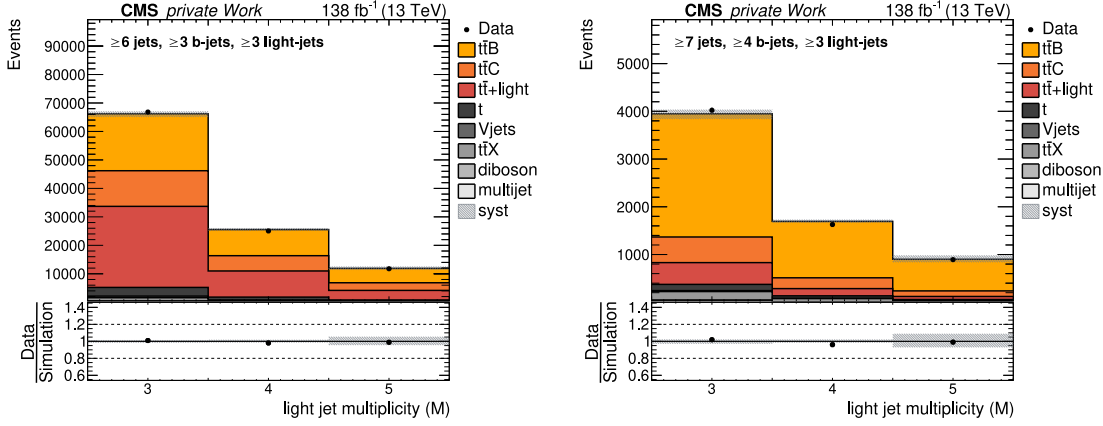


Figure 8.5: **Light jet multiplicity in the 6j3b3l (left) and 7j4b3l (right) measurement regions.** Shown are the contributions of all processes to the detector-level phase space regions as a stack of histograms. The $t\bar{t}B$ contribution is estimated from the PP8 $t\bar{t}b\bar{b}$ 4FS simulation. Data events are shown as black dots. The lower panel shows the ratio of data to the expectations from simulated events. For visualization, the contributions from simulation have been scaled by a common factor to match the yield in data. The shaded bands include all a-priori uncertainties described in Section 8.7. Only effects on the shape of the distributions are considered.

of $t\bar{t}$ is separated into contributions of $t\bar{t}+\text{light}$, $t\bar{t}C$, and $t\bar{t}B$, following the definitions introduced in Section 8.1. The distributions of jet multiplicity and b tagged jet multiplicities are sufficiently well modeled for them to be used in the measurements of the $t\bar{t}b\bar{b}$ processes. As apparent from the distributions, the fraction of $t\bar{t}B$ events increases at higher jet and b jet multiplicities, as expected from the larger number of genuine b jets in these events. Background contributions from single top quark production, Vjets production, or diboson and multijet production decrease steeply with increasing jet and b jet multiplicity, as from these signatures fewer jets and b jets are expected. Figure 8.5 shows the number of light jets, i.e. jets not tagged at the medium b tagging WP in the 6j3b3l and 7j4b3l measurement regions. In each of the measurement regions, no significant differences in the distribution of $t\bar{t}+\text{light}$, $t\bar{t}C$, and $t\bar{t}B$ contributions to the light jet multiplicity can be seen in simulation. This behavior is expected, as light jet radiation in addition to the $t\bar{t}$ system is present in all of these processes.

Even though the event selections in Section 8.3 have been chosen to be as close as possible to the fiducial $t\bar{t}b\bar{b}$ definitions in Section 8.2, these measurement regions still contain a large number of background events. One of the main reasons for this specific measurement is the inefficiency of b tagging. For example, in the 6j4b measurement region, at least four b tagged jets at the medium working point are required in order to be selected in this region. Assuming an approximate b tagging efficiency of 80% at a light jet misidentification rate of 1% (which is a good approximation of the performance of the DEEPJET tagger) this implies that only about 46% of $t\bar{t}b\bar{b}$ events (with four b jets) will pass this selection, but also about 1.5% (0.04%) of events which contain only three (two) true b jets. While the size of the three or two b-jet contributions might seem small in comparison, it has to be emphasized that some processes with fewer b jets have cross sections that are significantly larger than the production cross section of $t\bar{t}b\bar{b}$. The inclusive production cross section of $t\bar{t}$, for example, is about 3500 times larger than the fiducial cross section of $t\bar{t}b\bar{b}$ predicted by the PP8 $t\bar{t}$ 5FS simulation in the 6j4b phase space region. Hence, even a reduction of $t\bar{t}$ events with less than four b jets to the level of 0.04% would result in

Table 8.6: **Event yields in the four measurement regions.** Event yields are summed across all data-taking eras and hence correspond to the expectations and observations for 138 fb^{-1} of data. The event yields of $t\bar{t}B$ are estimated from the PP8 $t\bar{t}b\bar{b}$ 4FS simulation. The event yields of $t\bar{t}C$ and $t\bar{t}+\text{light}$ are estimated from the PP8 $t\bar{t}$ 5FS simulation. The quoted uncertainties are due to the limited number of simulated events. The uncertainty on the multijet contribution is of the same size as the uncertainty on the total MC yield due to the low number of events in the simulated multijet sample.

Event selection	5j3b	6j3b3l	6j4b	7j4b3l
$t\bar{t}B$	$78\,700 \pm 100$	$37\,120 \pm 70$	$10\,240 \pm 40$	4980 ± 30
$t\bar{t}C$	$46\,420 \pm 70$	$22\,310 \pm 50$	2130 ± 20	990 ± 10
$t\bar{t}+\text{light}$	$124\,000 \pm 100$	$44\,480 \pm 80$	1950 ± 20	760 ± 10
single top	$13\,420 \pm 50$	4820 ± 30	570 ± 10	224 ± 6
$t\bar{t}V$	1810 ± 10	917 ± 5	173 ± 1	89 ± 1
$t\bar{t}H$	2468 ± 2	1223 ± 1	517 ± 1	239 ± 1
Vjets	2500 ± 40	910 ± 20	97 ± 4	35 ± 2
diboson	77 ± 5	18 ± 3	4 ± 1	1 ± 1
multijet	3100 ± 600	600 ± 100	130 ± 40	50 ± 30
Total MC	$272\,500 \pm 700$	$112\,400 \pm 200$	$15\,860 \pm 60$	7350 ± 50
Multijet fraction [%]	1.10	0.90	0.80	0.70
$t\bar{t}B$ fraction [%]	28.90	33.00	64.60	67.70
Data	254 549	103 638	14 451	6543
Data/MC	0.93	0.92	0.91	0.89

contributions of about the same size as the sought-after $t\bar{t}b\bar{b}$ contribution. Alternative approaches of defining the event selection via a WP of the b tagging algorithm with lower light jet misidentification rates were also explored. An approximation of this selection with a b tagging efficiency of 60% at a light jet misidentification rate of 0.1% would lead to $t\bar{t}b\bar{b}$ selection efficiencies of around 13% (using the same calculation as above), while events with two b jets are reduced by another factor of 50. With the chosen b tagging WPs (medium) the selection efficiency of the $t\bar{t}b\bar{b}$ ($t\bar{t}b$) process in the 6j4b (5j3b) measurement regions are around 13% (22%). This is, of course, not only affected by the b tagging requirements but also by lepton identification efficiencies and the detector acceptance. In the end, this alternative approach was discarded, as it resulted in larger uncertainties in the measurements due to the lower signal selection efficiencies.

In Table 8.6, the event yields of the different processes after the four event selections are summarized. The drastic decrease in data statistics from increased jet and b jet multiplicity requirements can be inferred from this table. In the most restricted measurement region, 7j4b3l, only 6543 data events are recorded in the 138 fb^{-1} of data analyzed. In the more restricted measurement regions, however, the fraction of $t\bar{t}B$ events is largest, surpassing 60% in the 6j4b and 7j4b3l event selections. While $t\bar{t}+\text{light}$ and $t\bar{t}C$ are the dominating contributions in the 5j3b and 6j3b3l regions, their contributions decrease to small fractions in the other regions, suppressed by the b jet multiplicity requirements. Contributions of multijet and diboson processes are reduced to around 1% in all of the measurement regions, based on the estimate from simulation. The number of simulated multijet events in these event selections is relatively small, as these selections occupy only a niche phase space region of the inclusive multijet production phase space. Hence,

the uncertainty on the contribution of multijet events to these event selections is large in comparison to the uncertainties from other processes. As this makes the prediction of multijet contributions to the measurement regions as a function of the measured observables unreliable, and because the contribution is estimated to be quite subdominant, this contribution is not considered in the measurements. Similarly, the contribution of diboson processes is not considered further due to its small contributions to the measurement regions. Contributions of $t\bar{t}H$ and $t\bar{t}V$ processes are of comparable sizes as the multijet contributions, but occupy, due to their similarity with the $t\bar{t}B$ process, similar regions of phase space as the $t\bar{t}B$ process also in the measured observables. Hence, their contribution is not neglected, even though it might be minor compared to the $t\bar{t}B$ process. The ratio of data relative to the expectations from simulation (Data/MC) is around 0.9 for all of the measurement regions. This is explained via the overestimation of the $t\bar{t}B$ cross section from the PP8 $t\bar{t}b\bar{b}$ 4FS simulation, as will be discussed in Section 9.2.

8.5 Ancillary variables

For the measurement of the $t\bar{t}B$ process an ancillary variable is defined. This variable is used to separate the events in the measurement regions in different, so-called, ancillary regions, which have different compositions of signal and background processes. The variable chosen for this measurement is the number of b tagged jets at the tight b tagging WP, corresponding to a 0.1% light jet misidentification rate. In Figure 8.6, the distribution of the tight b jet multiplicity is shown in the four measurement regions.

The choice of this ancillary variable is motivated from the difference between the $t\bar{t}B$ process and the major background contributions ($t\bar{t}+\text{light}$ and $t\bar{t}C$). From the $t\bar{t}B$ signature, three to four b jets are expected, while for the dominant backgrounds of $t\bar{t}C$ and $t\bar{t}+\text{light}$ only two b jets are expected from the $t\bar{t}$ decay. Hence, by requiring a strong b tagging criterion, these backgrounds can be separated from the $t\bar{t}B$ signal. As explained in the previous section, this is already, to some level, exploited via the definition of the measurement regions via the medium b tagging WP, which reduces the contribution of these background processes. The events are further subcategorized based on the ancillary variable. The 5j3b region is separated into three categories, ≤ 1 , 2, or ≥ 3 tight-tagged b jets. Due to the more stringent selections of the 6j4b region, the events are only separated into two categories, ≤ 2 and ≥ 3 tight-tagged b jets. The definition of ancillary regions in the 6j3b3l (7j4b3l) phase space region corresponds to the one in the 5j3b (6j4b) phase space region. Figure 8.6 indicates the chosen ancillary regions via vertical dashed lines. This subcategorization of events generates bins in the maximum likelihood fit that are enriched in the background processes and other bins that are enriched in the $t\bar{t}b\bar{b}$ process. This increases the sensitivity to the normalization and distribution of the background processes in the background enriched regions, as these regions are signal depleted, and the fit to data in these regions is dominated by the variation of the backgrounds. This information can be transferred in-situ to the region enriched in the $t\bar{t}b\bar{b}$ process. This improved knowledge of the background processes in the $t\bar{t}b\bar{b}$ -enriched region enables the determination of the POIs with higher accuracy.

8.6 Out-of-acceptance process definitions

A difficulty of this measurement is the proper definition and separation of signal and background processes and the treatment of the systematic uncertainties associated with these processes.

8 Ingredients for the $t\bar{t}b\bar{b}$ measurement

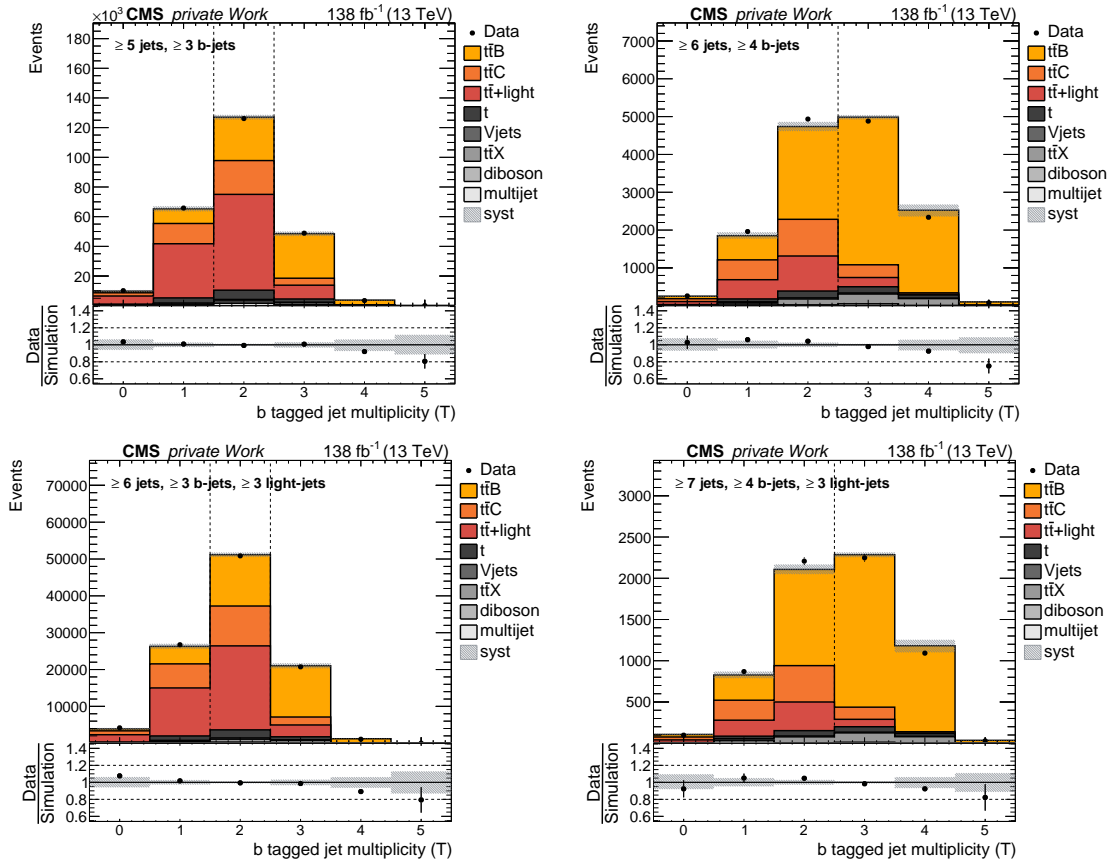


Figure 8.6: **b jet multiplicity at the tight b tagging WP in the four measurement regions.** Shown are the contributions of all processes to the detector-level phase space regions as a stack of histograms. The $t\bar{t}B$ contribution is estimated from the PP8 $t\bar{t}b\bar{b}$ 4FS simulation. Data events are shown as black dots. The lower panel shows the ratio of data to the expectations from simulated events. The vertical dashed lines indicate the ancillary regions used for the measurements of the $t\bar{t}b\bar{b}$ process. For visualization, the contributions from simulation have been scaled by a common factor to match the yield in data. The shaded bands include all a-priori uncertainties described in Section 8.7. Only effects on the shape of the distributions are considered.

The definitions of the fiducial signal phase space regions of Section 8.2 and the corresponding event selections of Section 8.3 are chosen such that they correspond to each other as closely as possible. This leads to a high signal fraction in these phase space regions and also is an attempt to keep the fraction of $t\bar{t}B$ events that do not fulfill the fiducial requirements low for the phase space under scrutiny. These $t\bar{t}B$ events outside the fiducial volume are referred to as OOA events and are treated as background processes for the purpose of this measurement. Events can be identified as out-of-acceptance (OOA) if, for example, this event passes the 6j4b event selection but only has three b jets passing the fiducial requirements on particle level, e.g. because one b jet is below the p_T threshold or outside the $|\eta|$ range of the fiducial definition. This event can still pass the 6j4b event selection with four b jets passing the medium b tagging working point, e.g. because of a mistag of a light jet or the jet on reconstruction level associated to the missing particle-level jet being inside of the detector acceptance. Another contribution to OOA events are the lepton selection criteria, where only events with exactly one lepton on particle level are considered part of the signal. Hence, contributions that pass the jet requirements on particle level but have too many or not enough leptons will also be designated as OOA

Table 8.7: **Fractions of signal, OOA and other processes to the four measurement regions.** All fractions are given in %. Estimated from the PP8 $t\bar{t}b\bar{b}$ 4FS simulation. The uncertainties on these values from a limited sample size are less than 1% and are hence omitted.

Event selection	5j3b	6j3b3l	6j4b	7j4b3l
Fid. signal	26	20	40	41
$t\bar{t}b$ OOA	3	13	17	17
$t\bar{t}b\bar{b}$ OOA	—	—	7	10
Other	71	67	36	32

events. The fiducial definitions and event selections have been chosen such that this OOA contribution is kept small, which is possible only to a limited degree in some of the phase space regions. In order to define OOA contributions a distinction has to be made between $t\bar{t}$ induced processes which contain b jets outside of the $t\bar{t}$ system (additional b jets), and processes which do not. For this purpose the previous definition of $t\bar{t}B$ is used, to draw a well-defined boundary. This definition has been verified to include all fiducial phase space definitions as subsets. As aforementioned, this $t\bar{t}B$ definition is not based purely on particle level anymore, as it references the Monte-Carlo history of the top quarks. As this is, however, only used to draw the boundary between $t\bar{t}$ processes with and without additional b jet radiation, but not to define the signal, this is still a valid approach. Events passing the $t\bar{t}B$ definition and the event selections, but not the respective fiducial signal definitions are therefore classified as OOA $t\bar{t}B$ events. In the phase space regions with at least four b jets (6j4b and 7j4b3l) an additional distinction is made between OOA events which contain only one (OOA $t\bar{t}b$) or at least two (OOA $t\bar{t}b\bar{b}$) additional b jets. This distinction is made as OOA $t\bar{t}b\bar{b}$ events show more similarities to the signal processes in these phase space regions than the OOA $t\bar{t}b$ events and therefore call for a different treatment when considering systematic uncertainties and their correlations. As the OOA contributions in the phase space regions with three b jets (5j3b and 6j3b3l) is smaller in comparison, and the signal process contains both signal events with three or more b jets, no such distinction is made in these phase space regions. Table 8.7 summarizes the fractions of signal and OOA contributions to the respective event selections.

8.7 Systematic uncertainties

Systematic uncertainties are considered in this measurement as nuisance parameters in the maximum likelihood fit as introduced in Section 4.1. Variation of the processes according to most of the uncertainty estimations have an impact on the distribution of events of these processes and are hence implemented as shape uncertainties following the implementation described in Section 4.1.1. A few uncertainty sources only have an overall effect on the rate of a process and are therefore implemented as rate uncertainties.

Generally, the uncertainty sources affecting the measurement can be grouped into two different sets; experimental uncertainties, arising from uncertainties in auxiliary measurements, e.g. the SF derivation procedures described in Chapter 6, and theory uncertainties, arising from uncertainties in calculations or simulations, e.g. uncertainties due to the choice of renormalization scale for the signal simulation. In the following, the uncertainty sources are separated into these two groups. Unless stated otherwise, the uncertainty source described is considered a shape-changing uncertainty. Following the uncertainty description, in Section 8.7.4 a smoothing procedure is described, where the variation of

Table 8.8: **Systematic uncertainties considered in the $t\bar{t}b\bar{b}$ measurements.** Systematic uncertainties smoothed with the procedure described in Section 8.7.4 are indicated via '✓'.

Uncertainty source	Type	# sources	Era corr.	smooth.	Comment
$t\bar{t}B$ μ_R scale	shape	2/group	✓	✓	groups: $t\bar{t}B + t\bar{t}b\bar{b}$ OOA; $t\bar{t}b$ OOA
$t\bar{t}B$ μ_F scale	shape	1/group	✓	✓	groups: $t\bar{t}B + t\bar{t}b\bar{b}$ OOA; $t\bar{t}b$ OOA
$t\bar{t}B$ PS scale ISR	shape	1/group	✓	✓	groups: $t\bar{t}B + t\bar{t}b\bar{b}$ OOA; $t\bar{t}b$ OOA
$t\bar{t}B$ PS scale FSR	shape	1/group	✓	✓	groups: $t\bar{t}B + t\bar{t}b\bar{b}$ OOA; $t\bar{t}b$ OOA
$t\bar{t}B$ h_{damp}	shape	1/group	✓	✓	groups: $t\bar{t}B + t\bar{t}b\bar{b}$ OOA; $t\bar{t}b$ OOA
Other μ_R scale	shape	1/group	✓	✓	groups: $t\bar{t} + \text{light} + t\bar{t}C$; all others
Other μ_F scale	shape	1/group	✓	✓	groups: $t\bar{t} + \text{light} + t\bar{t}C$; all others
Other PS scale ISR	shape	1/group	✓	✓	groups: all separately
Other PS scale FSR	shape	1/group	✓	✓	groups: all separately
Other h_{damp}	shape	1	✓	✓	Only for $t\bar{t} + \text{light} + t\bar{t}C$
pdf	shape	2	✓		Not applied to single top
$t\bar{t}C$ cross section	rate	1	✓		Only for $t\bar{t}C$
Luminosity	rate	1/year + 2	partially		See Table 8.9
Lepton scale factors	shape	5	✓		Two for electrons, three for muons
Trigger efficiency	shape	2/year	—		One for electrons, one for muons
L1 pre-fire correction	shape	1	✓		
Pileup	shape	1	✓		
Jet energy scale	shape	3/year + 7	partially	✓	
Jet energy resolution	shape	1/year	—	✓	
b tagging (light)	shape	2/year + 1	partially		
b tagging (b, c)	shape	2/year + 8	partially		
Size of MC samples	shape	1/bin	—		

some uncertainty sources is smoothed, and in some cases converted from shape-changing to rate-changing parameters (if no relevant shape-changing effect is present), or removed entirely (if also no relevant rate-changing effect is present). A summary table of all systematic uncertainties is shown in Table 8.8. This also includes the number of nuisance parameters in the maximum likelihood fit (see Section 4.1) and the correlation of nuisance parameters across eras.

8.7.1 Uncertainties from theory sources

pdfs: The pdf set used for the description of the proton is obtained from a fit to multiple experimental results of pdf measurements, as explained in Section 5.1. Replicas of the NNPDF set are provided, estimated from variations in the fit of the pdf set. For the 4FS pdf sets, the uncertainties are estimated using the root-mean-square of the residuals of all replicas as the replicas are sampled from the covariance matrix of the pdf fit. For the 5FS pdf sets, the uncertainties are estimated via the quadratic sum of all replicas as these correspond to the eigenvectors of the covariance matrix of the pdf fit. This difference in the treatment is only employed due to the difference in how the variations are stored in the simulated samples and cover the same effects. In addition, the pdf set is also supplied with variations taking into account the uncertainty in the assumed value of the strong coupling constant α_s during the determination of the pdf set. This is treated as a separate variation.

Renormalization and factorization scales: The choices of renormalization (μ_R) and factorization (μ_F) scales for the signal and $t\bar{t}$ simulations are discussed in Section 7.2 and

Section 8.1. These choices can be rather arbitrary and are often motivated by phenomenological observations on how a scale choice best reflects the process compared to data. To account for these scale choices, the μ_R and μ_F scales are varied independently by factors of 0.5 and 2. These variations are generated already during the ME calculation in the simulation of the processes and are stored as additional weights in the simulated samples. One uncertainty source is associated with each of the μ_R and μ_F scale variations. These are further divided into separate uncertainty sources for the signal process, the OOA process, a combination of $t\bar{t}C$ and $t\bar{t}+\text{light}$, and separately for $t\bar{t}H$, $t\bar{t}V$, single top, and Vjets. For the signal process, changes in the expected cross section per generator-level bin (see discussion in Section 9.1) from these variations are normalized such that these uncertainty sources only have an effect on the selection efficiency and the distribution of the signal process, but not its cross section. For the OOA process, the uncertainty source corresponding to the renormalization scale is split into a component varying only the rate of the process, and one component varying the distribution of the process. This has been introduced to the measurement, as the renormalization scale variations show large normalization effects ($\sim 40\%$). Hence, the separation of this uncertainty source in shape- and rate-changing parameters introduces an additional degree of freedom in the maximum likelihood fits beneficial for more freedom in the description of the OOA contribution. In the 6j4b and 7j4b3l measurements where the OOA contribution is split into a $t\bar{t}b\bar{b}$ OOA and $t\bar{t}b$ OOA contribution, the μ_R and μ_F uncertainties for $t\bar{t}b\bar{b}$ OOA are correlated with the signal process, while the uncertainties applied to the $t\bar{t}b$ OOA process remain uncorrelated, as in the 5j3b and 6j3b3l measurements. This choice is motivated by the high similarity of the signal and the $t\bar{t}b\bar{b}$ OOA contribution, justifying a correlated treatment of uncertainties related to the process modeling.

The measurements performed in this thesis can give important insight into the scale choices of the signal models, as the differential results obtained in Section 9.3 can be compared to the signal models using alternative configurations of the scale choices, and thereby improve the modeling of the signal process. A study of the scale choices of the signal models with the results from the measurements in this thesis is discussed in Section 9.4.

ME and PS matching (h_{damp}): The matching between ME calculation and the PS is adjusted via the h_{damp} parameter in the POWHEG event generator. The h_{damp} parameter regulates the damping of real emissions in the NLO calculation when matching to a parton shower. To estimate the impact of this choice of matching scale, the h_{damp} scale is varied to $h_{\text{damp}} = 2.305 \cdot m_t$ and $h_{\text{damp}} = 0.874 \cdot m_t$. Additional $t\bar{t}$ and $t\bar{t}b\bar{b}$ simulations (as introduced in Section 8.1) with adjusted h_{damp} parameter are used and the difference between nominal simulation and variation in the distributions used in the fits are considered as the uncertainty.

Parton shower scales ISR/FSR: In the simulation of the PS, the initial-state radiation (ISR) and final-state radiation (FSR) is generated using a chosen value of the strong coupling constant α_s . Uncertainties arising from this choice are estimated by varying the scale at which the additional radiation is generated by factors of 0.5 and 2. This is considered for initial-state and final-state radiation independently. The uncertainty sources are in addition decorrelated for each background process, the OOA process(es), and the signal process. In the 6j4b and 7j4b3l measurements the $t\bar{t}b\bar{b}$ OOA uncertainties are correlated with the signal process, following the same line of argumentation as for the μ_R and μ_F scales.

Table 8.9: **Uncertainties in the measurement of the integrated luminosity per data-taking era.** From Refs. [159–161].

	2016	2017	2018
Uncorrelated 2016	1.0%		
Uncorrelated 2017		2.0%	
Uncorrelated 2018			1.5%
Correlated 2016/2017/2018	0.6%	0.9%	2.0%
Correlated 2017/2018		0.6%	0.2%

Cross section of $t\bar{t}C$: An uncertainty of 20% is applied to events categorized as $t\bar{t}C$. This reflects the uncertainty in the cross section measurement of the $t\bar{t}C$ process, also introduced in Section 7.4.1. This uncertainty is implemented as a rate-changing uncertainty.

8.7.2 Experimental uncertainty sources

Luminosity: The integrated luminosity for each data-taking era, as described in Section 2.3, is measured from auxiliary measurements, described in Refs. [159–161]. The integrated luminosity for data in 2016, 2017, and 2018 is measured with uncertainties of, respectively, 1.2%, 2.3%, and 2.5%. The uncertainty on the full data set is 1.6%. The uncertainties summarized Table 8.9 are applied to all processes contributing to the respective data-taking years, where some of these uncertainties are correlated between years. Each of these uncertainties is implemented as a rate-changing parameter.

Pileup reweighting: As described in Section 6.1, a reweighting procedure of the number of pileup interactions per event is applied to match the pileup profile observed in data with simulated events. To estimate the uncertainty of this procedure, the assumed inelastic proton-proton cross section is varied by $\pm 4.6\%$. The effect of this variation is propagated to the distributions used in the measurements.

L1 pre-firing: As described in Section 6.2, trigger objects can be associated with wrong bunch crossings under certain circumstances, leading to events self-vetoing. The uncertainty source for this pre-firing effect is estimated from each object (photon, muon, jet) independently by adding in quadrature the statistical uncertainty of the pre-fire efficiency determination and a flat 20% relative uncertainty.

Trigger efficiencies: The SFs described in Section 6.3 to correct the trigger efficiency in simulation to match the efficiencies in data are associated with uncertainties of the SF derivation procedure. These are dominated by uncertainties due to the limited statistics of the SF derivation regions.

Electron identification efficiencies: The measurement of electron identification efficiencies is described in Section 6.4. Uncertainties in the determination of each of the factorized efficiencies (identification and reconstruction) are propagated to the distributions used for the measurements in this thesis. The impact of these uncertainties on the measurements in this thesis is generally small, which is why only one combined uncertainty is used per efficiency measurement encompassing both systematic and statistical effects from the efficiency derivation procedure.

Muon identification efficiencies: Uncertainties on the determination of muon identification efficiencies are, similar to electrons, considered as combined systematic and statistical uncertainties for each the identification, reconstruction, and isolation of the muons.

Jet energy scales: The jet energy scale corrections introduced in Section 6.6 exhibit a range of uncertainties from the different levels of jet energy correction. Uncertainty sources are considered in this measurement by varying the jet momenta according to the uncertainties of the jet energy scale determination. Uncertainties are grouped into ten sources. Two uncertainties are from the calibration of the absolute jet scale determination, where one source contains all uncertainties correlated across eras, and the other contains all uncertainties decorrelated across eras. Two uncertainties are dedicated to the relative jet energy scale calibration and cover the momentum imbalance of the dijet system and the difference between samples used for the correction. Four uncertainties are used to describe differences in calibration due to flavor differences in PYTHIA and HERWIG, separated by bottom, charm, gluon, and light flavor-initiated jets. The final two uncertainty sources cover all remaining uncertainties of the calibration, separated into uncertainty sources correlated and uncorrelated across the eras.

Jet energy resolution: As described in Section 6.6, a correction of the jet energy resolution is applied to simulated jets by smearing their transverse momenta. To account for uncertainties in this procedure, the smearing procedure is repeated with different settings, corresponding to the uncertainties of the jet energy resolution measured in data.

b jet tagging efficiencies: In this measurement, the fixedWP b jet tagging SFs, as introduced in Section 6.7, are used. In total, 13 separate uncertainty sources are considered in the measurement. Ten of these originate from the derivation of SFs for b jets, and three in the derivation of light jets. The uncertainties and SFs for b jets are also applied to c jets, but doubled in size to account for the missing calibration of their contribution. The b jet uncertainties are separated into effects from h_{damp} , jet energy scale variations, renormalization and factorization scales, initial-state radiation, final-state radiation, pileup, and the uncertainty on the top quark mass. Remaining systematic uncertainties specific to only a subset of b jet SF derivation procedures are merged into a separate source of uncertainty, referred to as type3. Two statistical uncertainties of the SF derivation procedure are considered, separated by WP, and decorrelated between eras. For the light jet SFs, one correlated uncertainty source and two statistical uncertainty sources, separated by WP and decorrelated between eras, are used.

8.7.3 Statistical uncertainty sources

As detailed in Section 8.1, all background and signal estimations rely on simulated events. Uncertainties are considered to account for the limited statistics of simulated events. For every bin in the distributions used in the fits, a Gaussian nuisance parameter is introduced, varying the predicted event yields for all processes simultaneously. This is a simplification of the Barlow-Beeston approach introduced in Refs. [162, 163].

8.7.4 Smoothing and filtering of shape-changing variations

The uncertainty model as introduced in this section is customized for each separate measurement of the normalized differential cross sections. An algorithm to smooth the variations from jet energy calibration uncertainties, renormalization and factorization scale uncertainties, parton shower uncertainties, and the h_{damp} uncertainty is applied, but could in principle also be extended to other systematic variations. This algorithm is applied, because fluctuations and inhomogeneities (which are not based on real physics effects, but due to limited statistics in simulated events) in the estimation of uncertainties can introduce biases in the fits performed to estimate the normalized differential cross sections. For example, the uncertainty estimates of jet energy calibrations are prone to fluctuations due to the migration of jets in and out of the event selection phase space regions.

Large fluctuations in the templates for uncertainty estimation can introduce biases or non-physical constraints of the associated nuisance parameters. Similarly, the estimation of the h_{damp} variation relies on a separate simulation of the relevant processes, which is only performed with a reduced number of simulated events. This can also lead to unwanted fluctuations in the uncertainty estimates. In Figure 8.7, two examples are shown, one for a jet energy calibration uncertainty, and one for the h_{damp} uncertainty. The variations of the predicted event yields in the displayed observables show large fluctuations and inhomogeneities. This is corrected via a LOWESS smoothing algorithm [164]. The smoothing is performed on the averaged ratio, considering both the upward and downward variation of the systematic uncertainty under scrutiny. The ratio r_i relative to the nominal event yield prediction N_i in each bin i is obtained from

$$r_i = \frac{N_i^+ - N_i^-}{2N_i}, \quad (8.5)$$

where N_i^\pm are event yields from the upwards and downwards variations. The smoothed ratio \hat{r}_i is obtained via the LOWESS smoothing algorithm. As the smoothing is performed on the ratio which considers both the upwards and downwards variations, the resulting smoothed variations are symmetrized in shape for upwards and downwards variations. The smoothed event yields \hat{N}_i^\pm of the variations are obtained via

$$\hat{N}_i^\pm = (1 \pm s_\pm \hat{r}_i) \cdot N_i. \quad (8.6)$$

Here, s_\pm are scale parameters chosen to minimize the χ_\pm^2 difference between the smoothed and original systematic variation,

$$\chi_\pm^2 = \sum_i (\hat{N}_i^\pm - N_i^\pm)^2. \quad (8.7)$$

Figure 8.7 also includes the resulting smoothed variations of the example distributions. For the jet energy calibration uncertainties, the smoothing procedure is performed separately per data-taking era, distribution, lepton channel, and process, while for the h_{damp} variation, the smoothing is performed on the distributions summed across all data-taking eras and lepton channels, as no difference in the variations is expected for data-taking eras and lepton channels.

After the smoothing procedure, an additional decision algorithm is applied in order to determine whether an uncertainty exhibits a significant shape-changing effect or no effect at all. First, a χ^2 -test (taking into account the uncertainty of the prediction due to the limited sample size) is performed between the nominal distribution and the unsmoothed variation, without considering normalization effects. Correspondingly, a p -value is calculated. If the p -value is larger than 5% the uncertainty is converted into a rate-changing uncertainty, as the shape effect is determined to be negligible. If there is no rate-changing effect of that variation, i.e. the variation is compatible with one or smaller than 1%, the uncertainty is discarded. This procedure is performed independently for each observable, nuisance parameter and process. As this pruning procedure is performed independently per each observable, the final configuration of systematic uncertainties differs slightly in each fit.

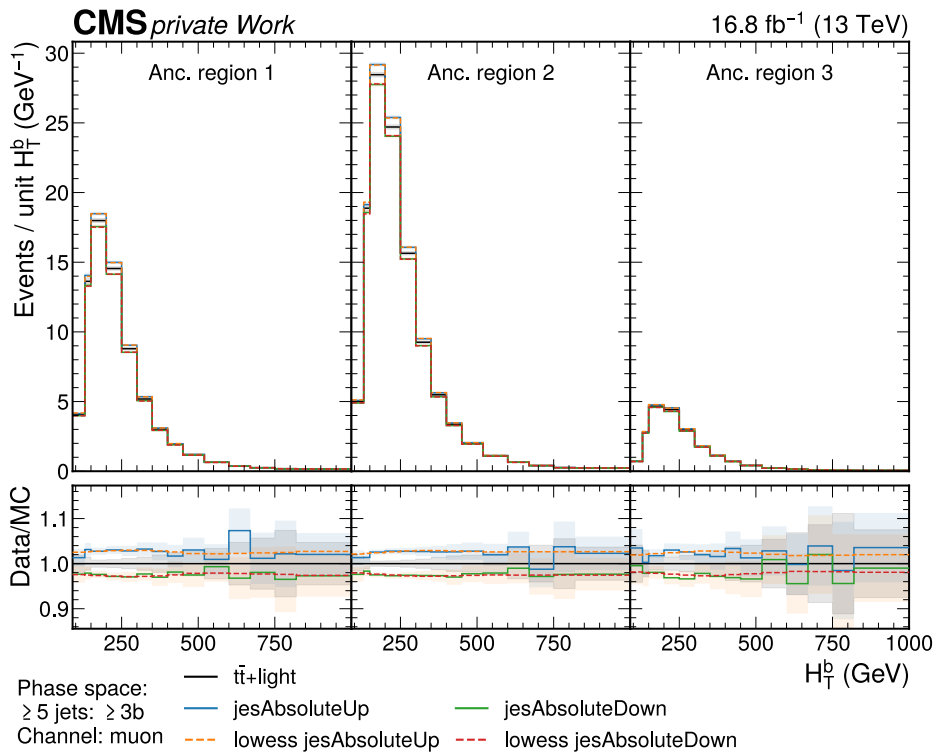
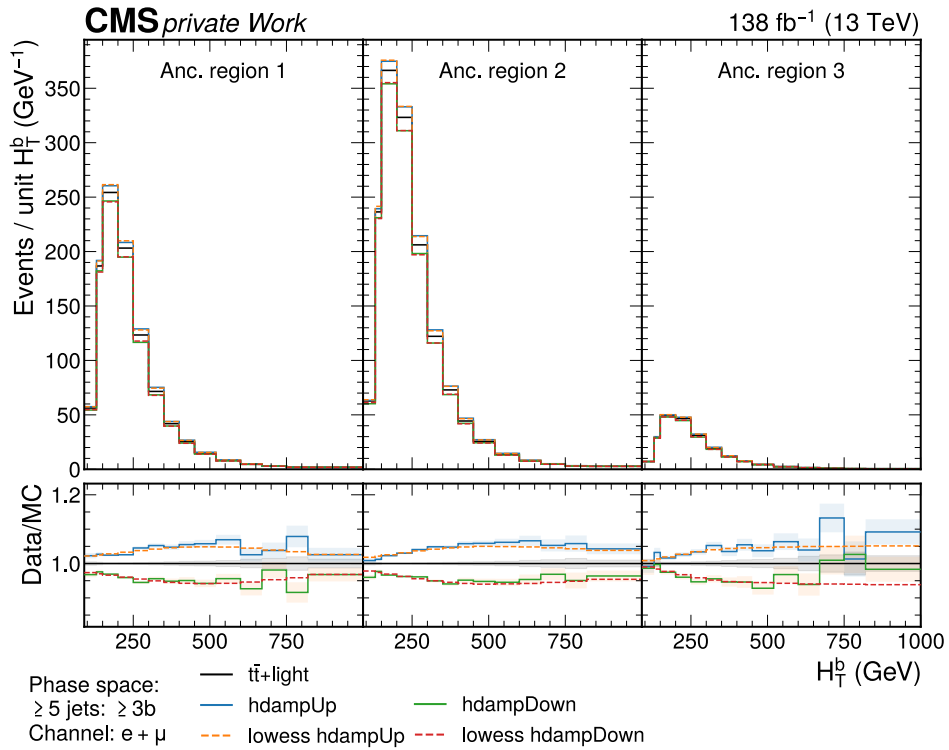


Figure 8.7: **Examples for smoothing of systematic uncertainties.** The variations of the h_{damp} parameter (top) and the absolute jet energy scale (bottom) are shown for the H_T^b observable in the 5j3b region for the $t\bar{t}$ +light process. The original variations are shown as solid lines. The smoothed variations (marked as LOWESS) are shown as dashed lines.

9 Measurement of the $t\bar{t}b\bar{b}$ process

In this chapter, the measurement of the $t\bar{t}b\bar{b}$ process is described. This measurement is published in Ref. [136] and has been adapted for this thesis relative to the published version. The procedure to extract the fiducial and normalized differential cross sections based on the measurement regions defined in Section 8.3 is outlined in Section 9.1. Then, the results of the fiducial and differential cross section measurements are discussed in Section 9.2 and Section 9.3, respectively. In Section 9.4, the results of the measurement are interpreted regarding the scale choices of the PP8 $t\bar{t}b\bar{b}$ 4FS model.

9.1 Extraction of fiducial and normalized differential cross sections

The strategy of this measurement will be elaborated based on two example observables in detail. The strategy for all remaining observables is the same and will not be repeated. The two observables discussed in this section are the angular separation in the (η, ϕ) -plane, ΔR , of the two b jets closest to each other, $\Delta R(bb^{\text{extra}})$, in the 6j4b phase space region, and the scalar sum of transverse momenta of all jets, H_T^{jets} , in the 5j3b region.

The differential measurements of this thesis target observables defined in the fiducial phase space regions on generator level. The corresponding distributions are shown in Figure 9.1 for the two example observables. The figure contains predictions of two generator setups (PP8 $t\bar{t}b\bar{b}$ 4FS and PP8 $t\bar{t}$ 5FS), as introduced in Section 8.1. The nominal signal model (PP8 $t\bar{t}b\bar{b}$ 4FS) is shown as a colorized histogram. A second signal model (PP8 $t\bar{t}$ 5FS) is shown as a line. These different simulation approaches with their generator settings yield significantly different predictions of the rate of the $t\bar{t}b\bar{b}$ process in the respective phase space regions, as well as in the differential observable. The PP8 $t\bar{t}$ 5FS model predicts a lower fiducial cross section than the PP8 $t\bar{t}b\bar{b}$ 4FS model in both phase space regions. In addition, it predicts, on average, a softer H_T spectrum and larger $\Delta R(bb^{\text{extra}})$. Especially the differences in the $\Delta R(bb^{\text{extra}})$ observable are of interest for the study of the modeling of the $t\bar{t}b\bar{b}$ process. As explained in Section 8.2, this observable is sensitive to the additional b jets (b jets outside the $t\bar{t}$ system), which originate in most cases from $g \rightarrow b\bar{b}$ splitting. In the PP8 $t\bar{t}$ 5FS simulation approach, this aspect is modeled by the PS, as the ME simulation only consists of $t\bar{t}$ at NLO accuracy, i.e. can only account for, at maximum, one additional radiation outside of the $t\bar{t}$ system. In the PP8 $t\bar{t}b\bar{b}$ 4FS simulation approach, this aspect is predominantly modeled by the ME simulation itself, as it

9 Measurement of the $t\bar{t}b\bar{b}$ process

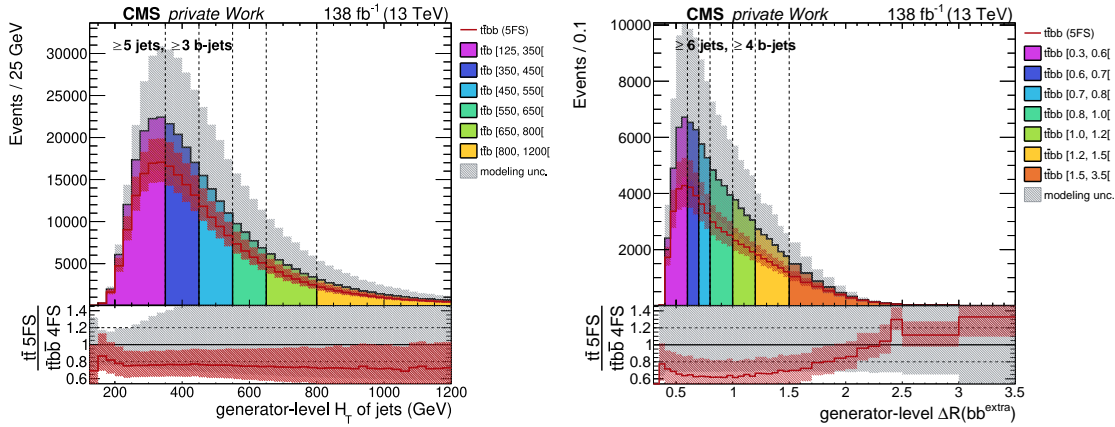


Figure 9.1: Sum of jet transverse momenta (H_T^{jets}) and the ΔR of the two closest b jets ($\Delta R(\text{bb}^{\text{extra}})$), in the $5j3b$ and $6j4b$ generator-level phase space regions. The predicted number of events from the nominal signal model (PP8 $t\bar{t}b\bar{b}$ 4FS) and one alternative model (PP8 $t\bar{t}$ 5FS) are shown as colored histograms and lines, respectively. The number of expected events is based on an integrated luminosity of 138 fb^{-1} . The nominal signal model is separated into generator-level bins (different colors) corresponding to pre-defined ranges of the observable (also indicated as vertical dashed lines). Modeling uncertainties due to renormalization and factorization scale choices and the initial-state and final-state PS radiation are indicated as hatched uncertainty bands. The lower panels show the ratio of the alternative signal model relative to the nominal signal model.

contains a $t\bar{t}b\bar{b}$ ME calculation at NLO. Figure 9.1 also includes estimations of the modeling uncertainties due to variation of renormalization and factorization scales, as well as initial-state and final-state radiation in the PS. Their estimation is described in Section 8.7.1. As explained in Section 7.2, $t\bar{t}b\bar{b}$ simulation at the ME-level exhibits a strong dependence on the renormalization scale due to its $\alpha_s^4(\mu_R)$ scaling, leading to variations of up to 40% in the fiducial cross section. In comparison, the assumed uncertainties on the PP8 $t\bar{t}$ 5FS simulation approach are smaller, but most likely underestimate the effects of missing higher-order corrections for a description of $t\bar{t}b\bar{b}$.

In order to gain insight into which of the modeling approaches and generator settings best describes the $t\bar{t}b\bar{b}$ process as measured in data, differential measurements of these observables have to be performed. For that purpose, the observables are separated into so-called generator-level bins, indicated by the different colors in Figure 9.1. In the differential cross section measurement, each of these generator-level bins is treated as an independent parameter of interest (POI), i.e. is scaled with an independent signal-strength modifier μ_i , as introduced in Chapter 4. The bins are chosen based on the resolution of the observable and other limitations, such as the number of expected signal events in the fiducial phase space regions and after the event selections on reconstruction level. If an observable were to be reconstructed perfectly on reconstruction level the bins for the differential cross section measurement could be chosen to be narrower. Similarly, if the number of events is large enough to allow for a precise determination of the fraction and number of signal events in the bins of the measurement, more bins are possible. For example, the measurement of the transverse momentum p_T of a jet underlies inefficiencies in the energy measurement and spatial resolution due to detector inefficiencies, misreconstruction of jets, missing particles like neutrinos, etc.. For the measurement of the differential cross section this means that accessing the generator-level observable is difficult as the distribution of the observable is smeared on detector level. This is visualized

9.1 Extraction of fiducial and normalized differential cross sections

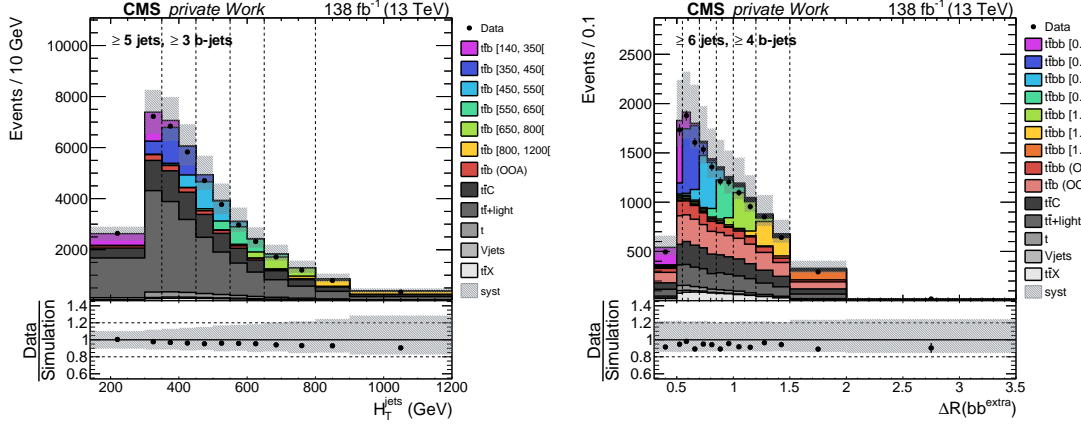


Figure 9.2: **Detector-level distribution of H_T^{jets} after the 5j3b event selection (left) and $\Delta R(\text{bb}^{\text{extra}})$ after the 6j4b event selection (right).** The upper plots show the contributions of all processes to the detector-level phase space regions as a stack of histograms. The contributions from the nominal $\text{t}\bar{\text{t}}\text{B}$ signal model (PP8 $\text{t}\bar{\text{t}}\text{b}\bar{\text{b}}$ 4FS) are separated based on the pre-defined generator-level bins indicated by different colors. Data events are shown as black dots. The lower panel shows the ratio of data w.r.t. the simulated events. Uncertainties on the simulated events from systematic uncertainty sources are indicated as grey bands.

in Figure 9.2, where the observable is shown on detector level (following the detector-level selections introduced in Section 8.3) where the contribution of the process of interest is again separated into the generator-level bins introduced above. The clear separation into the pre-defined generator-level bins is now washed out and events from the same generator-level bin are distributed over a broader kinematic range. Furthermore, it can also be seen that with the event selections on reconstruction-level also background processes are present that have to be accounted for in the measurement.

It is apparent that the events generated in a certain generator-level bin are not always reconstructed in the corresponding bin on detector-level, but are prone to migrations in neighboring bins. To quantify this, migration matrices are constructed, as shown in Figure 9.3. These show the migrations of each of the generator-level bins (on the vertical axis) to the same range of the observable, but defined on detector level (on the horizontal axis). The migration matrices are normalized per generator-level bin, i.e. per row of the matrix. Events for which the detector-level quantity is reconstructed in the same bin (i.e. same range of the observable) as generated on generator level will be on the diagonal of the matrix. Due to the normalization of the matrix, these values hence correspond to the fraction of events of a certain generator-level bin also reconstructed in the corresponding bin on detector-level, referred to as the stability. Figure 9.3 also contains panels showing the efficiency (panel on the vertical axis) and the purity (panel on the horizontal axis). The efficiency is defined as the fraction of signal events of a certain generator-level bin passing the detector-level event selection. The choice of generator-level and detector-level definitions heavily influences the efficiency at which the events passing the generator-level definitions (fiducial events) enter the detector-level selections. The purity is defined as the fraction of events in a certain detector-level bin associated with the corresponding generator-level bin (i.e. the vice-versa of the stability). The choice of the width and number of generator-level bins influences the stability and purity numbers. For example, by choosing narrower bins, a larger fraction of events migrate away from the corresponding bin on detector level, leading to lower purities and stabilities. This negatively impacts

9 Measurement of the $t\bar{t}b\bar{b}$ process

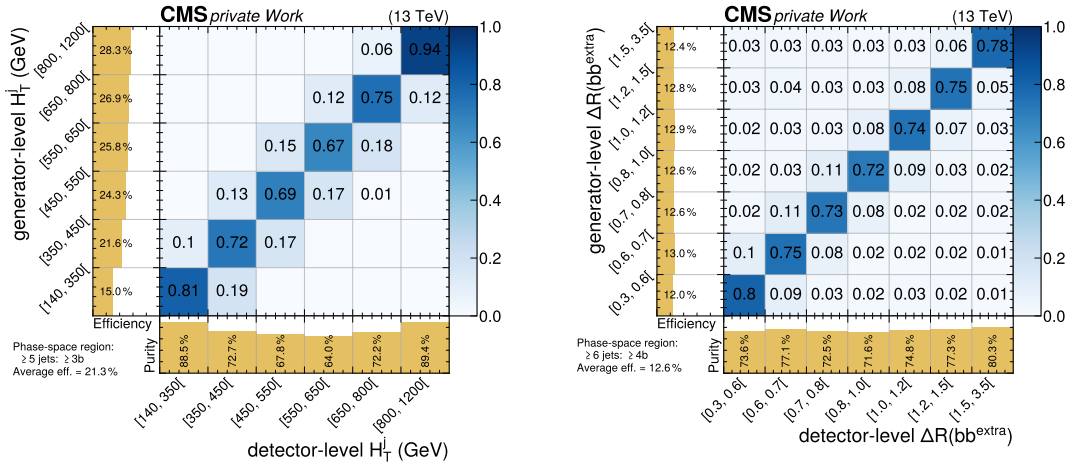


Figure 9.3: Migration matrices of the sum of jet transverse momenta (H_T^{jets}) and the ΔR of the two closest b jets ($\Delta R(\text{bb}^{\text{extra}})$), in the 5j3b and 6j4b phase space regions. The generator-level observable is shown on the vertical axis and the detector-level observable on the horizontal axis. The migration matrix corresponds to the generator-level bins defined for the corresponding observables. Entries in the migration matrix are normalized per generator-level bin (i.e. horizontally). The panel on the vertical axis shows the selection efficiency per generator-level bin. The panel on the horizontal axis shows the purity of events per detector-level bin.

the maximum likelihood fits performed to obtain the differential cross section results, as the signal contributions of (especially) neighboring generator-level bins will be strongly correlated in the fits, and reduce the sensitivity on each of the associated POIs. In essence, if a range of bins on detector level is enriched only in events from a single generator-level bin, the determination of the signal-strength μ of the associated POI is free of any influence from the other differential cross section POIs. The purity and stability values of around 70–80% in these observables are large enough to enable differential cross section measurements with high precision. The migration matrices of all other observables are shown in Appendix A.1.

The migrations of the two example observables also exhibit some systematic features which are inherent to the observables of this measurement. In the migration matrix of the H_T observable, for example, (almost) only contributions in diagonal entries and the neighboring entries are present for this choice of binning which has been chosen to contain this resolution effect. As this observable requires no dedicated identification algorithm on generator level or detector level, the source of the migrations is mostly jet energy mismeasurements. Hence, the detector-level values are rarely too far away from the corresponding generator level to migrate into further away bins. Also, a systematic trend towards lower values is visible, i.e. the fraction of events in the lower off-diagonal bins is higher than the values in the higher off-diagonal bins on the detector level. This can be explained via the difference in the minimal jet p_T requirement of the jets on detector level (30 GeV) and generator level (25 GeV) and the steeply falling H_T spectrum. For the $\Delta R(\text{bb}^{\text{extra}})$ observable, a notable amount of migration from each generator-level bin into all detector-level bins is present. This is due to the associated identification method of the observable, where the pair of b jets is chosen that is closest in ΔR . On detector level, for example, a pair of b jets can be chosen that does not correspond to the same pair on generator level if one of the b jets fails the b -tagging requirement. Hence, events where the bb^{extra} jets are different on generator level and reconstruction level appear as a con-

9.1 Extraction of fiducial and normalized differential cross sections

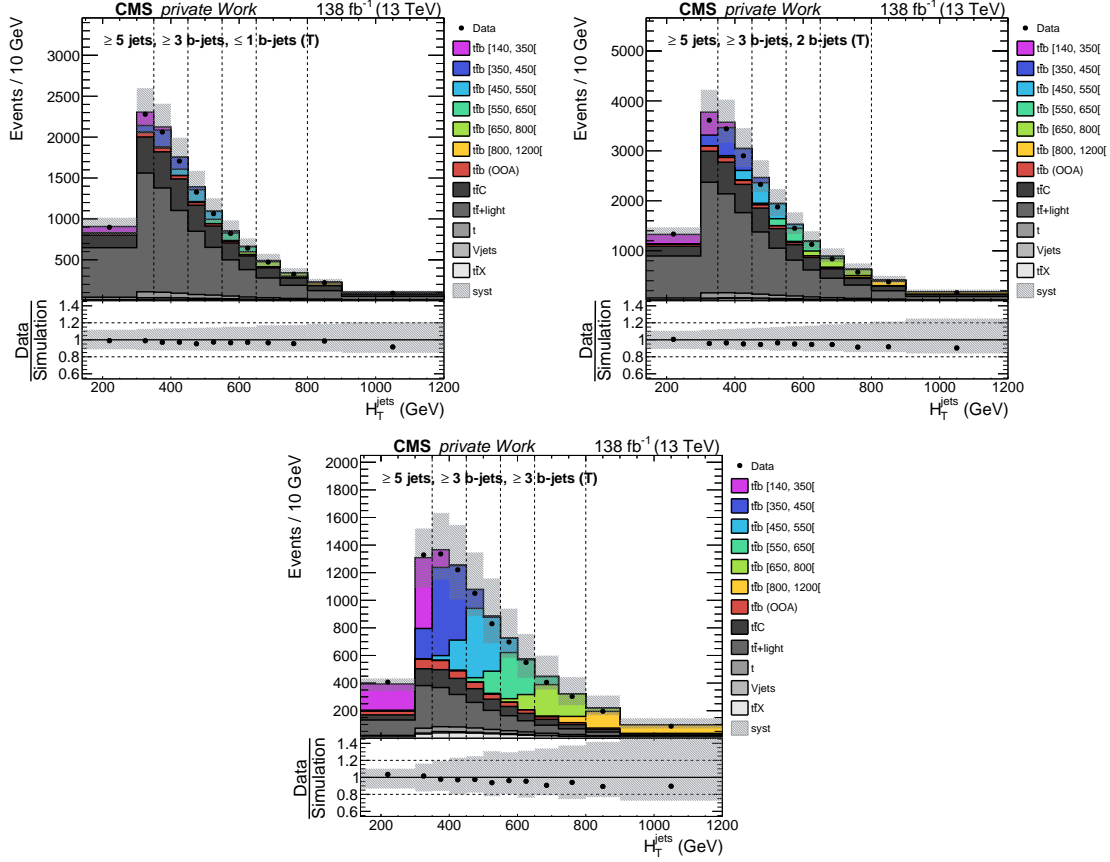


Figure 9.4: Sum of jet transverse momenta (H_T) in the 5j3b detector-level phase space region separated into ancillary regions based on the tight b jet multiplicity. Shown are the contributions of all processes to the detector-level phase space regions as a stack of histograms. The contributions from the nominal $t\bar{t}B$ signal model (PP8 $t\bar{t}b\bar{b}$ 4FS) are separated based on the pre-defined generator-level bins indicated by different colors. Data events are shown as black dots.

stant distribution of a few percent throughout the matrix. In the other cases, where the correct association is made, the migrations into off-diagonal bins are small, as the angular resolution of jets, relevant for this observable, is better than the momentum resolution, relevant for the H_T^{jets} observable.

The selection efficiencies as a function of the two observables show further systematic trends. For the $\Delta R(b\bar{b}^{\text{extra}})$ observable the efficiency is constant around approximately 13%. The efficiency exhibits no dependence on the generator-level bin, as the acceptance of jets is relatively uniform in the (η, ϕ) -plane. For the H_T^{jets} observable, the selection efficiency is significantly smaller in the low- H_T region compared to the high- H_T region. This is due to the lower efficiency of reconstructing jets in the threshold region (jets with p_T around 30 GeV) which accumulates in the low- H_T region. The difference between detector-level jet p_T threshold (30 GeV) and generator-level jet p_T threshold (25 GeV) additionally contributes to this effect. Altogether, the overall selection efficiency in the 5j3b region is larger than in the 6j4b region, which is explained, as aforementioned, with the efficiency of b jet tagging.

Ancillary regions, as introduced in Section 8.4.2, are employed, separating the events into regions of b jet multiplicity at the tight b tagging WP. This enables a separation of fiducial signal events and background processes entering the detector level to some

9 Measurement of the $t\bar{t}b\bar{b}$ process

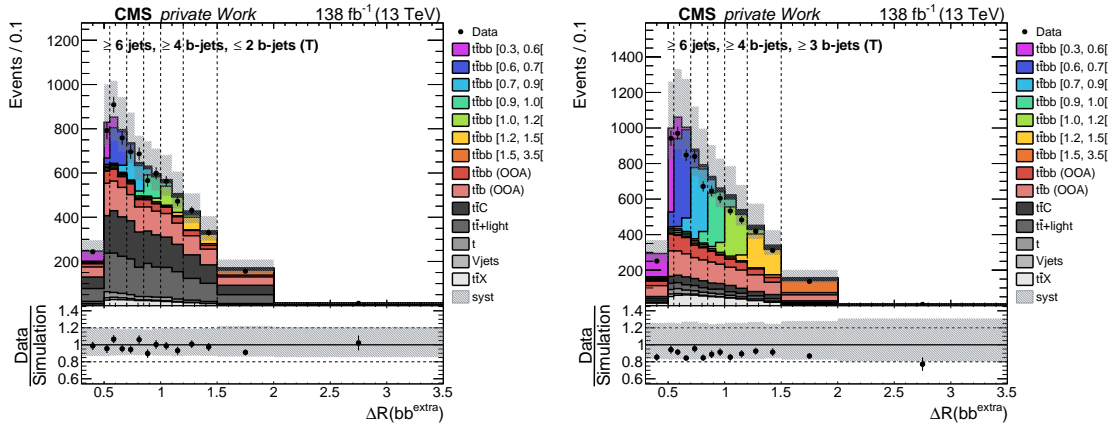


Figure 9.5: ΔR of the two closest b jets ($\Delta R(bb^{\text{extra}})$) in the 6j4b detector-level phase space region separated into ancillary regions based on the tight b jet multiplicity. Shown are the contributions of all processes to the detector-level phase space regions as a stack of histograms. The contributions from the nominal $t\bar{t}B$ signal model (PP8 $t\bar{t}b\bar{b}$ 4FS) are separated based on the pre-defined generator-level bins indicated by different colors. Data events are shown as black dots.

degree, as $t\bar{t}b\bar{b}$ events have, on average, more b jets than the background processes. In the 5j3b phase space, events are separated into a region with fewer than two tight b tagged jets, exactly two b tagged jets, and more than two tight b tagged jets. In the 6j4b phase space, events are separated into a region with fewer or equal two tight b tagged jets and more than two tight b tagged jets. In the light-jet enriched regions, the regions defined for the 6j3b3l (7j4b3l) phase space follow the definitions of the 5j3b (6j4b) phase space. In Figures 9.4 and 9.5, the distributions of the example observables are shown separated into the ancillary regions. The contributions of the fiducial $t\bar{t}b\bar{b}$ events to the ancillary regions are around 12%, 20%, and 59% in the 5j3b phase space region, and 22% and 59% in the 6j4b event selection. This can be compared to the average fraction of fiducial $t\bar{t}b\bar{b}$ events to the 5j3b and 6j4b measurement regions of 26% and 40%, respectively, as summarized in Table 8.7. This shows the increased fraction of fiducial $t\bar{t}b\bar{b}$ events in the ancillary bins with large b jet multiplicity requirement compared to the average fiducial $t\bar{t}b\bar{b}$ event contributions.

In order to measure the normalized differential cross sections of the $t\bar{t}b\bar{b}$ process for the selected observables, the distributions shown in Figures 9.4 and 9.5 are used in maximum likelihood fits. For the fits, the distributions are additionally separated per data-taking era and lepton flavor in order to account for differences in the detector conditions and the leptons. The normalized differential cross sections are measured with the maximum likelihood parameterizations introduced in Chapter 4. Accordingly, the POIs in the maximum likelihood fit are the fiducial cross section of the $t\bar{t}b\bar{b}$ process in the phase space region under scrutiny, σ_{fid} , and for all generator-level bins, except the last one, the fraction of $t\bar{t}b\bar{b}$ events in this bin, f_i . The contribution of the last bin is scaled according to eq. (4.18), in order to retain the appropriate number of degrees of freedom. In the following sections, the results of all measurements are discussed.

9.2 Inclusive cross section results

The cross section of the $t\bar{t}b\bar{b}$ process is measured in four different phase space regions, each of them defined purely on stable-particle level. The fiducial regions overlap and

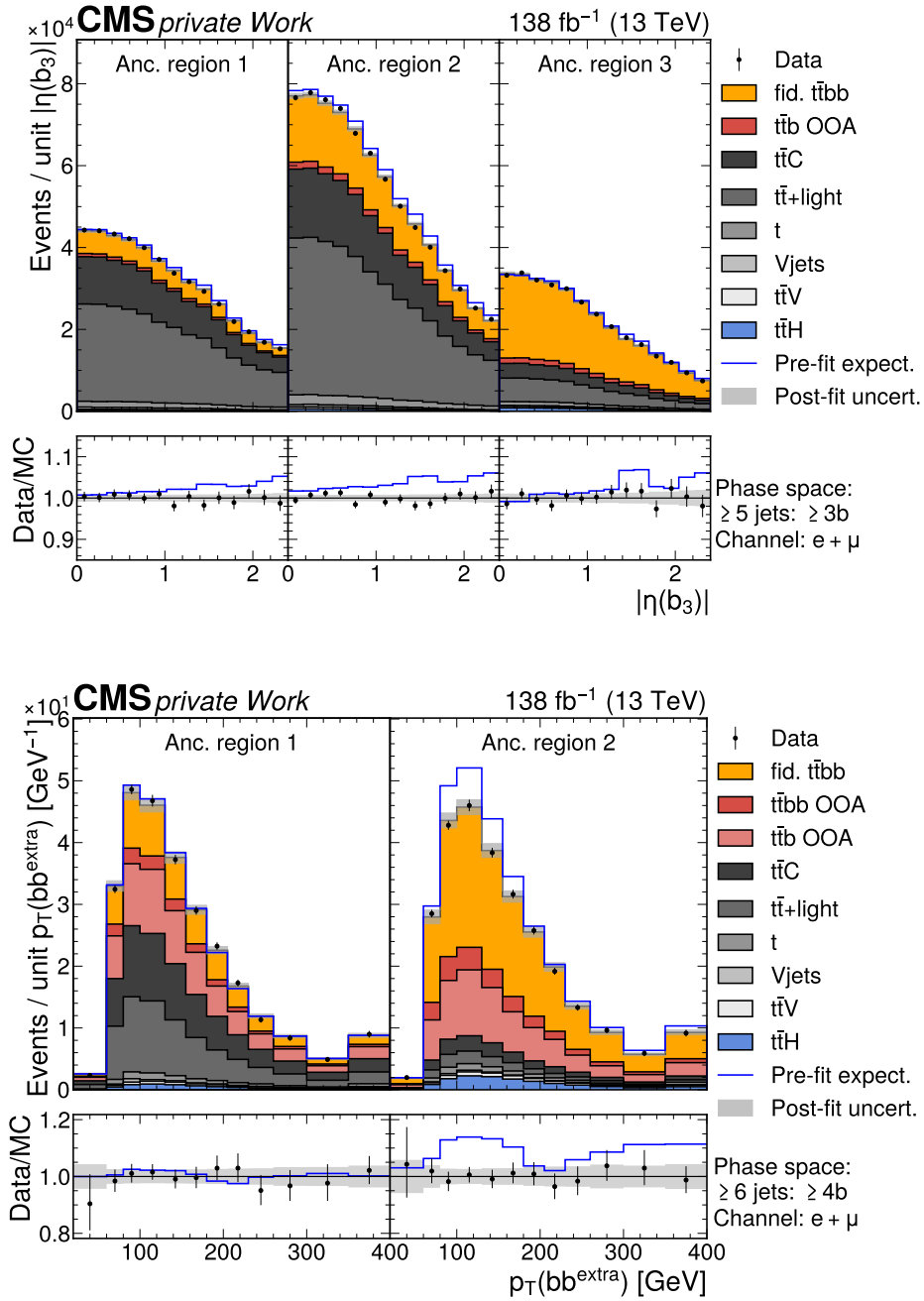


Figure 9.6: **Representative observables in the 5j3b and 6j4b phase space regions after the fit to data.** Shown are $|\eta(b_3)|$ in the 5j3b phase space (top), and $p_T(bb^{\text{extra}})$ in the 6j4b phase space (bottom). The contributions of all processes to the detector-level phase space regions after the fit to data are shown as a stack of histograms. The distributions are shown separately for each ancillary region but are combined across all eras and the lepton channels. The blue line indicates the sum of all processes before the fit to data using the PP8 $t\bar{t}b\bar{b}$ 4FS sample for the estimation of the $t\bar{t}B$ contribution. The lower panel shows the ratio of data to the processes after the fit to data. The shaded bands include all uncertainties described in Section 8.7 after profiling the nuisance parameters in the fit, estimated by sampling the predicted yields from the fit covariance matrix. Modified from Ref. [136].

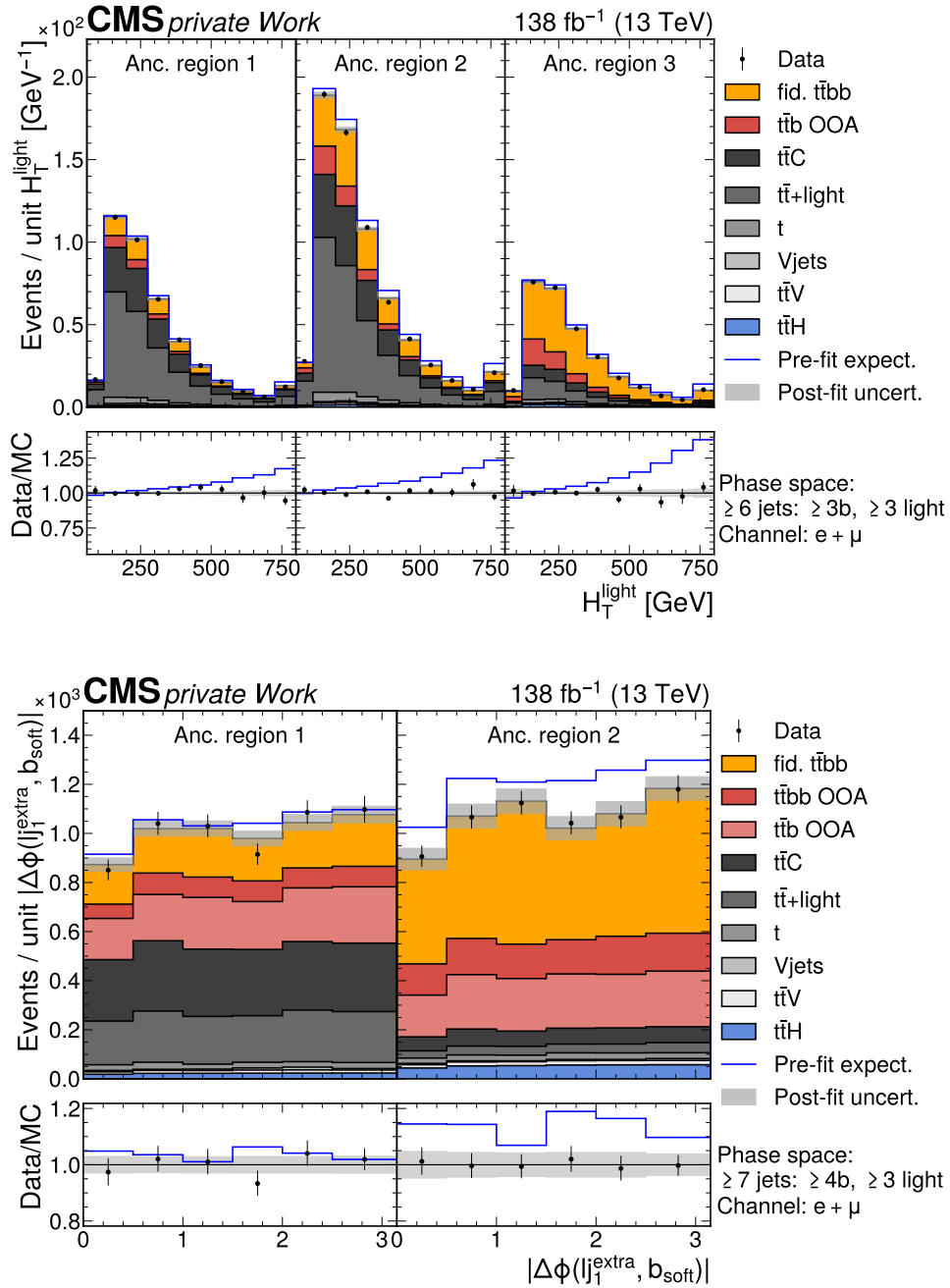


Figure 9.7: **Representative observables in the 6j3b3l and 7j4b3l phase space regions after the fit to data.** Shown are H_T^{light} in the 6j3b3l phase space (top), and $|\Delta\phi(l_{j_1}^{\text{extra}}, b_{\text{soft}})|$ in the 7j4b3l phase space (bottom). The contributions of all processes to the detector-level phase space regions after the fit to data are shown as a stack of histograms. The distributions are shown separately for each ancillary region but are combined across all eras and the lepton channels. The blue line indicates the sum of all processes before the fit to data using the PP8 $t\bar{t}b\bar{b}$ 4FS sample for the estimation of the $t\bar{t}B$ contribution. The lower panel shows the ratio of data to the processes after the fit to data. The shaded bands include all uncertainties described in Section 8.7 after profiling the nuisance parameters in the fit, estimated by sampling the predicted yields from the fit covariance matrix. Modified from Ref. [136].

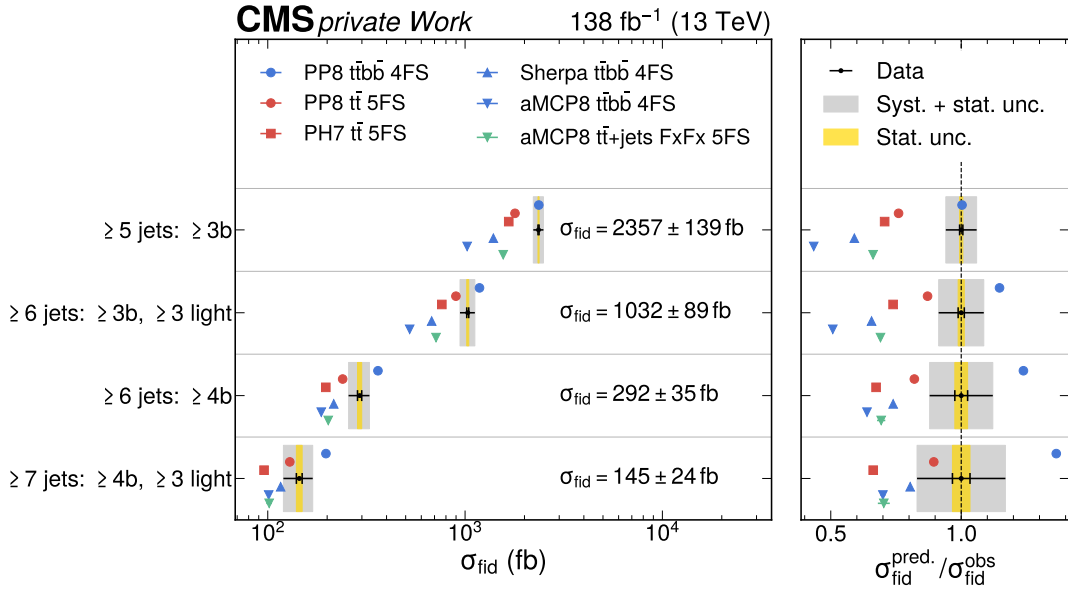


Figure 9.8: **Fiducial cross sections measured in each of the four phase space regions.** The measured cross sections in data are indicated with black dots, with inner (outer) vertical bars indicating the systematic (total) uncertainties, also represented as gray (yellow) bands. The cross section predictions from different modeling approaches as introduced in Section 8.1 are shown as colored symbols with different shapes. The panel on the right shows the ratio between the predicted and measured cross sections. Modified from Ref. [136].

target different aspects of the $t\bar{t}b\bar{b}$ process, as explained in Section 8.2. In Table 8.3 all observables are listed for which a normalized differential cross section measurement is performed. In each of the measurements, the fiducial cross section of the respective phase space region is measured as one of the POIs. Due to variations in the post-fit values of the nuisance parameters in each of the measurements, the resulting cross section values show some variations between the different measurements. In order to provide a representative cross section for each of the fiducial phase space regions, the observable for which the fiducial cross section value is closest to the mean of all measured cross section values in that phase space region is chosen as a representative observable. In the four phase space regions, these observables are $|\eta(b_3)|$ in the 5j3b phase space, H_T^{light} in the 6j3b3l phase space, $p_T(b\bar{b}^{\text{extra}})$ in the 6j4b phase space, and $|\Delta\phi(lj_1^{\text{extra}}, b_{\text{soft}})|$ in the 7j4b3l phase space. The distributions of these observables after the fit to data (post-fit) are shown in Figure 9.6 for the 5j3b and 6j4b phase space regions, and in Figure 9.7 for the 6j3b3l and 7j4b3l phase space regions. The post-fit distributions of all other observables are shown in Appendix A.2. The measured fiducial cross sections from these four observables are shown in Figure 9.8 and Table 9.1 together with the predictions of the different signal models introduced in Section 8.1.

The measured cross sections in the four fiducial phase space regions are all larger than the predictions, except for the prediction of the PP8 $t\bar{t}b\bar{b}$ 4FS simulation. This confirms previous measurements by the ATLAS and CMS Collaborations, where cross sections of $t\bar{t}b\bar{b}$ were similarly under-predicted in simulation (see discussion in Section 7.4.1). The PP8 $t\bar{t}$ 5FS simulation, used e.g. in the background estimation of $t\bar{t}H(b\bar{b})$ measurements in the past (see Section 7.4.2), shows an under-prediction of 10–30%, depending on the

Table 9.1: **Measured and predicted fiducial cross section values.** All cross sections are given in fb. Modified from Ref. [136].

Fiducial phase space	5j3b	6j3b3l	6j4b	7j4b3l
Measured cross section	2357	1032	292	144
	± 139 (syst)	± 89 (syst)	± 35 (syst)	± 24 (syst)
	± 14 (stat)	± 12 (stat)	± 7 (stat)	± 5 (stat)
PP8 $t\bar{t}b\bar{b}$ 4FS	2361	1183	361	197
PP8 $t\bar{t}$ 5FS	1791	899	240	129
PH7 $t\bar{t}$ 5FS	1665	762	197	95
SHERPA $t\bar{t}b\bar{b}$ 4FS	1391	677	216	116
AMCP8 $t\bar{t}b\bar{b}$ 4FS	1024	524	187	101
AMCP8 $t\bar{t}$ +jets FFX 5FS	1560	712	203	101

fiducial phase space region. The other simulation approaches exhibit even higher levels of under-prediction with the generator settings used in the simulation, ranging up to around 50%. In the 5j3b phase space region the PP8 $t\bar{t}b\bar{b}$ 4FS simulation agrees with the measurement. In all other phase space regions this simulation approach over-predicts the fiducial cross section, increasingly in the phase space regions requiring more jets and b jets. Similar trends are exhibited by the other $t\bar{t}b\bar{b}$ ME simulation approaches (AMCP8 $t\bar{t}b\bar{b}$ 4FS, SHERPA $t\bar{t}b\bar{b}$ 4FS), albeit with a large offset predicting smaller cross sections than measured. The simulation approaches using a $t\bar{t}$ ME (PP8 $t\bar{t}$ 5FS, PH7 $t\bar{t}$ 5FS) or the AMCP8 $t\bar{t}$ +jets FFX 5FS simulation approach predict a more even off-set w.r.t. the measurement, suggesting that the jet, b jet, and light jet multiplicities are better modeled with these generator setups compared to the generator setups using a $t\bar{t}b\bar{b}$ ME.

For each normalized differential cross section measurement, the correlations of the POIs, i.e. the fiducial cross section and the differential fractions, are shown in Appendix A.3.

9.2.1 Sensitivity and limitations of measurements

The measurement of the four fiducial cross section values exhibits uncertainties between 6–17%, depending on the phase space region. These constitute the highest precision on the measurement of the $t\bar{t}b\bar{b}$ cross sections to date. In Table 9.2, the contributions to these uncertainties are broken down into groups of uncertainties following their introduction in Section 8.7. The measurements of the fiducial cross sections are mostly limited by systematic uncertainties, where the dominant groups of uncertainties are uncertainties in μ_R and μ_F scales and the parton shower (PS) modeling, as well as uncertainties in b tagging efficiency determination and jet energy corrections. These limitations are expected from the design of the measurement using phase space regions with large jet multiplicity and b jet multiplicity requirements, and the nominal signal model (PP8 $t\bar{t}b\bar{b}$ 4FS), which is associated with large modeling uncertainties.

On the theory modeling side, the estimation of the signal process especially depends strongly on the μ_R scale choice and exhibits large prior uncertainties due to this scale (see Section 7.2). Similarly, both the $t\bar{t}b\bar{b}$ and $t\bar{t}$ modeling, relevant for the estimation of the majority of the contributions to the measurement regions, rely on accurate descriptions of the additional radiation from the parton showering processes in the high jet multiplicity phase space regions. Hence, uncertainties in the additional radiation described by the PS are expected to limit these measurements.

On the experimental side, the design of measurement regions with large jet and b jet multiplicities are expected to have limitations in the measurement precision due to the

Table 9.2: **Contributions of the sources of uncertainty considered to the total uncertainty on the fiducial cross section measurements.** For each group, the impact of the corresponding nuisance parameters on the fiducial cross section are combined, taking into account their correlations in the maximum likelihood fit. The numbers show the relative uncertainty on the fiducial cross section, given in %. The statistical uncertainty is obtained as the difference, in quadrature, between the total uncertainty and the sum of all systematic uncertainties. Modified from Ref. [136].

Uncertainty source	5j3b	6j3b3l	6j4b	7j4b3l
Luminosity	1.6	1.6	2.6	1.8
Lepton and trigger	1.2	0.9	1.0	1.9
JES, JER	2.1	1.6	1.3	5.8
b tagging	4.4	4.0	6.3	9.2
Pileup	0.2	0.8	0.2	0.6
PDF	0.2	0.8	1.1	1.9
μ_R and μ_F scales	2.7	6.8	8.9	12.2
PS modelling	2.9	2.6	0.9	1.7
h_{damp}	0.4	1.1	1.4	2.3
$t\bar{t}C$ normalization	0.5	0.4	1.3	2.4
MC statistical	0.7	1.6	2.5	2.7
Total systematic uncertainty	5.9	8.6	11.9	16.6
Statistical uncertainty	0.6	1.2	2.5	3.4
Total uncertainty	5.9	8.6	12.1	16.9

determination of jet energy corrections and the calibration of b jets. Even small uncertainties in these calibrations can have large effects when considering the large number of jets and b jets they influence. The b jet calibration uncertainties also add to the limitations due to the choice of defining the ancillary regions via the tight b tagging WP (see Section 8.5), but their use outweighs the increase in uncertainty by improving the control over background processes.

In Figure 9.9 the 30 nuisance parameters of the maximum likelihood fit with the largest impact on the fiducial cross section in the 5j3b phase space region are shown. The figure contains the post-fit nuisance parameter values, which are defined with pre-fit value zero and unity uncertainty. Hence, derivations of the central nuisance parameter value from zero indicate that the nuisance parameter value changed during the fit. The uncertainty of the post-fit nuisance parameter value can be smaller than unity, indicating that the value of the nuisance parameter was constrained beyond its a-priori uncertainty. This is possible in cases where the measurement is sensitive to a nuisance parameter, e.g. in the case of the uncertainty of the renormalization scale μ_R on the OOA $t\bar{t}b\bar{b}$ contribution, which has a large a-priori rate-changing effect of up to 40%. In the fit, the associated nuisance parameter can be determined with higher precision, constraining the variation on the post-fit nuisance parameter. Similarly, uncertainties related to b tagging and jet energy calibrations can be constrained to a moderate level due to the high sensitivity in changes to the jet and b jet-related observables in this measurement. The figure also contains the relative impact of nuisance parameters on the fiducial cross section measurement in the 5j3b phase space region. These relative impacts are obtained by fixing the nuisance parameter under scrutiny at its post-fit $\pm 1\sigma$ variations (indicated by the error bars in the post-fit nuisance parameter values), and repeating the fit with that configuration. The

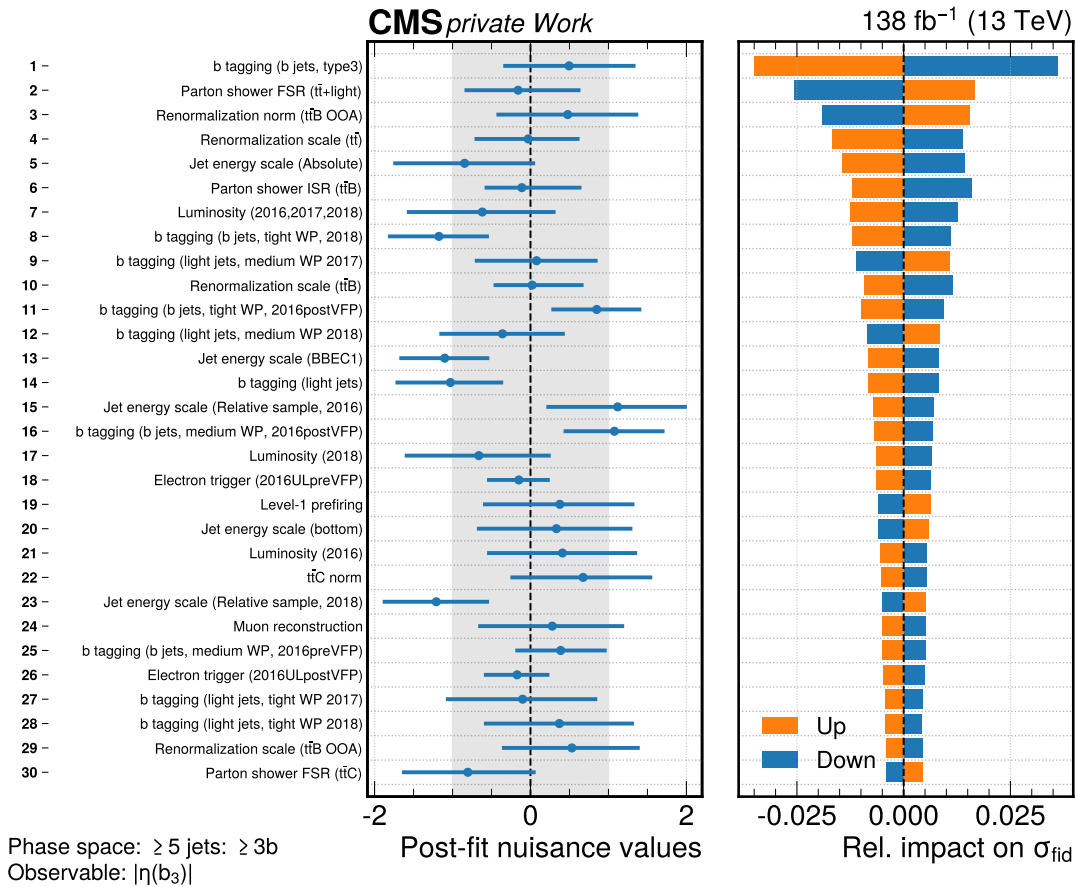


Figure 9.9: **Post-fit nuisance parameter values (left) and relative impacts on the fiducial cross section (right) in the 5j3b phase space.** The nuisance parameters are defined such that the pre-fit value is zero with unity uncertainty. Shown are the thirty nuisance parameters with the largest impact on the fiducial cross section measurement. Modified from Ref. [136].

relative impact then quantifies the difference between the central σ_{fid} value and the σ_{fid} value obtained with this modification in the fit. The relative impact is given relative to the central σ_{fid} value. The nuisance parameter with the highest impact on the fiducial cross section in this fit is the type3 b tagging uncertainty (see Section 8.7.2) and exhibits a relative impact of around 3% in both directions. Compared to the total uncertainty on the σ_{fid} measurement of 6%, this is a sizable contribution. Other nuisance parameters with large impacts on the fiducial cross section measurement are associated with the modeling of signal and background processes, e.g. the PS FSR variation of the $t\bar{t}$ +light process, which is the dominant contribution in this measurement region, or the renormalization scale of the OOA contribution. Other nuisance parameters associated with b tagging and jet energy calibrations are also present in the leading impacts. The uncertainties on the luminosity also show large impacts on the fiducial cross section measurement, as these uncertainties change the rate of all simulated processes simultaneously, e.g. by 1.6%, and hence have a relatively high impact on this precise cross section measurement.

9.2.2 Comparison to other measurements

The measurement of the fiducial $t\bar{t}b\bar{b}$ cross section by the ATLAS Collaboration in Ref. [145] (see Section 7.4.1) uses similar fiducial phase space definitions and also performs mea-

measurements in (slightly different) 6j4b and 5j3b phase space regions. The ATLAS measurement uses electrons with $p_T \geq 25$ GeV (compared to $p_T \geq 29$ GeV here) and muons with $p_T \geq 25$ GeV and $|\eta| \leq 2.5$ (compared to $p_T \geq 26$ GeV and $|\eta| \leq 2.4$ here). Furthermore, jets in the ATLAS measurement are defined using $|\eta| \leq 2.5$, while this measurement uses $|\eta| \leq 2.4$. The clustering of jets in the ATLAS measurement also includes neutrinos, which are not considered in this measurement. For the definition of b jets via ghost-hadron matching (see Section 5.8.1), ATLAS uses a $p_T \geq 5$ GeV threshold for the B hadrons, while no such threshold is applied here. This difference is estimated to be less than 0.1%, given that B hadrons in the jets usually carry large momentum fractions, making this low p_T threshold irrelevant. In summary, the fiducial volume of the ATLAS measurement is larger than what is presented here. When using the ATLAS fiducial definitions, the fiducial cross section of the PP8 $t\bar{t}b\bar{b}$ 4FS model with the generator settings used in this thesis is 2685 fb (440 fb) in the 5j3b (6j4b) phase space region. These values are larger by 14% (22%) relative to the fiducial phase space definitions of this measurement (see Table 9.1). This matches the expectations due to the increased size of the ATLAS fiducial volume. The cross section predictions corresponding to the ATLAS fiducial definitions can be compared to the ATLAS measurements of 2370 fb (331 fb). This shows that the PP8 $t\bar{t}b\bar{b}$ 4FS simulation approach with its generator settings overpredicts the fiducial cross sections measured by the ATLAS Collaboration by a factor of 13% (30%), which is compatible with the overprediction of 0% (25%) observed in this measurement when taking into account the measurement uncertainties of 28% (17%) in the ATLAS measurement. The ATLAS measurement is dominated by uncertainties from similar sources as the measurements presented in this thesis.

The measurement of the fiducial $t\bar{t}b\bar{b}$ cross section by the CMS Collaboration in Ref. [148] also provides a measurement in a fiducial volume similar to the 6j4b measurement presented in this thesis. In the previous CMS measurement, leptons are defined with $|\eta| \leq 2.4$ and $p_T \geq 30$ GeV in the single-lepton channel, while in the measurement presented in this thesis electrons are defined with $|\eta| \leq 2.5$ and $p_T \geq 29$ GeV, and muons are defined with $p_T \geq 26$ GeV. Furthermore, jets are defined with $p_T \geq 20$ GeV in the previous CMS measurement, while in this thesis a threshold of $p_T \geq 25$ GeV is used. In summary, for the fiducial phase space definition in Ref. [148], the PP8 $t\bar{t}$ 5FS simulation with its generator settings predicts a cross section of 520 fb, which, compared to the 240 fb predicted for the 6j4b phase space in this thesis is larger by 116%. This can mostly be explained by the lower jet p_T threshold. The 6j4b fiducial cross section (with the fiducial definitions of the previous CMS measurement) is measured to be 620 fb with an uncertainty of 11%. The PP8 $t\bar{t}$ 5FS model under-predicts the measured cross section by 17% in the measurement of this thesis and 16% in the previous CMS measurement, indicating that both measurements are compatible.

9.3 Differential cross section results

Normalized differential cross sections are measured as a function of 29 observables, six in the 5j3b phase space, 17 in the 6j4b phase space, and three each in the 6j3b3l and 7j4b3l phase space regions. The results will be discussed in detail in the following. The compatibility of predictions with the measurements is summarized in Figure 9.10, quantified using χ^2 -tests calculated from the normalized distributions of the predictions and the measurement. In the calculation of the χ^2 -tests, the uncertainties and correlations of the measured differential cross section are taken into account, but not the uncertainty on the predictions (e.g. uncertainties from the variation of modeling parameters). The p -values of the χ^2 -tests are converted into z scores, i.e. number of standard deviations from the

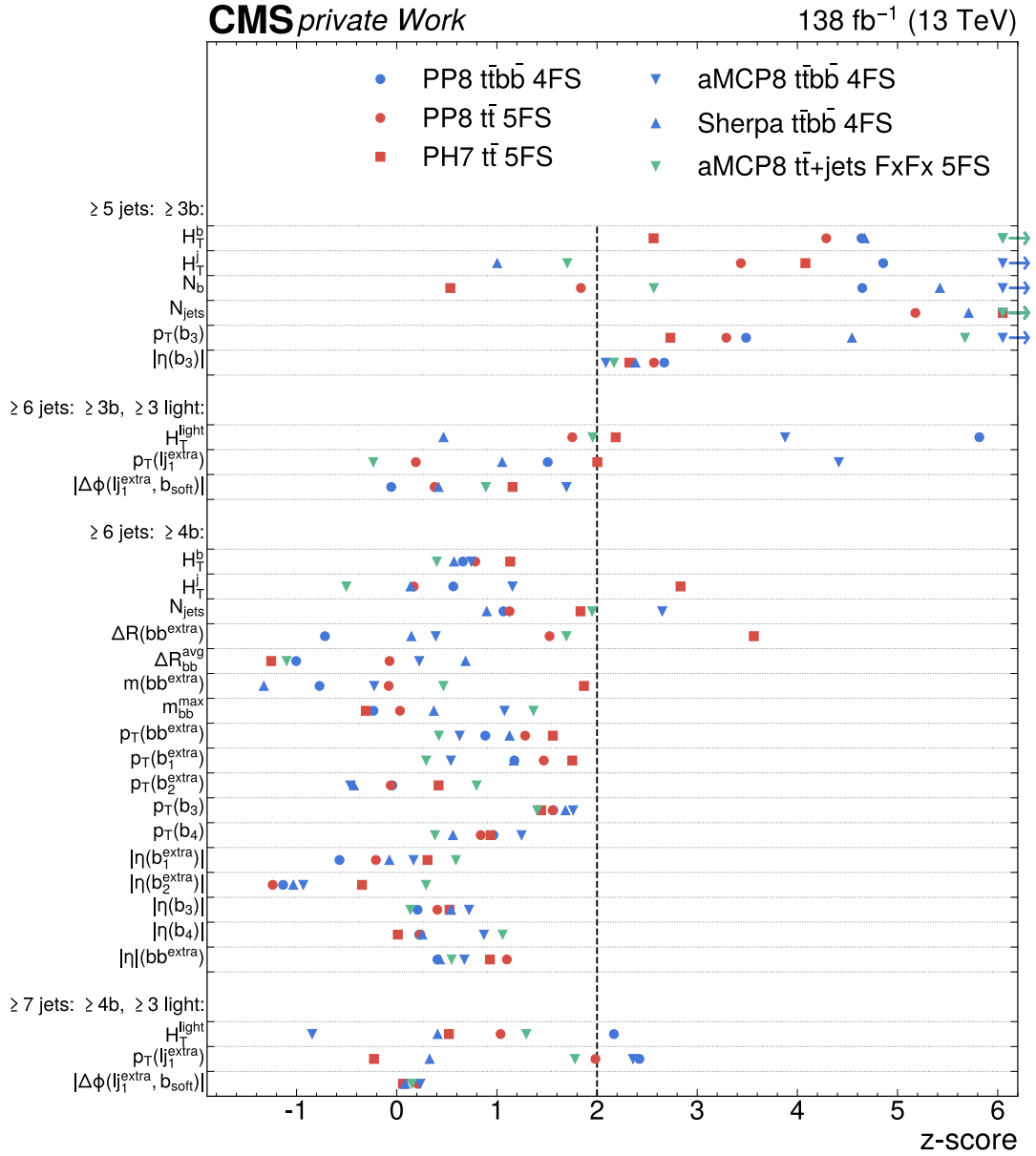


Figure 9.10: **Observed z score for each of the simulation approaches, given the measured normalized differential cross sections and their covariances.** Lower values indicate better agreement between prediction and measurement. The dashed line at $z = 2$ indicates a p -value of 5%. Predictions for which the z score exceeds the visible range of the figure are marked with arrows (\rightarrow). Modified from Ref. [136].

center of a Gaussian distribution¹. A z score of two corresponds to a p -value of 5%, larger values indicate that the description of the observable by the simulation is insufficient.

9.3.1 Results in the 5j3b phase space region

The normalized differential cross sections of the N_{jets} , N_b , H_T^{jets} , and H_T^b observables in the 5j3b phase space region are shown in Figure 9.11. In the N_{jets} distribution, the simulation

¹In this parameterization the sign of the z score is retained for clarity, i.e. a negative z score is possible if the p -value is larger than 50%.

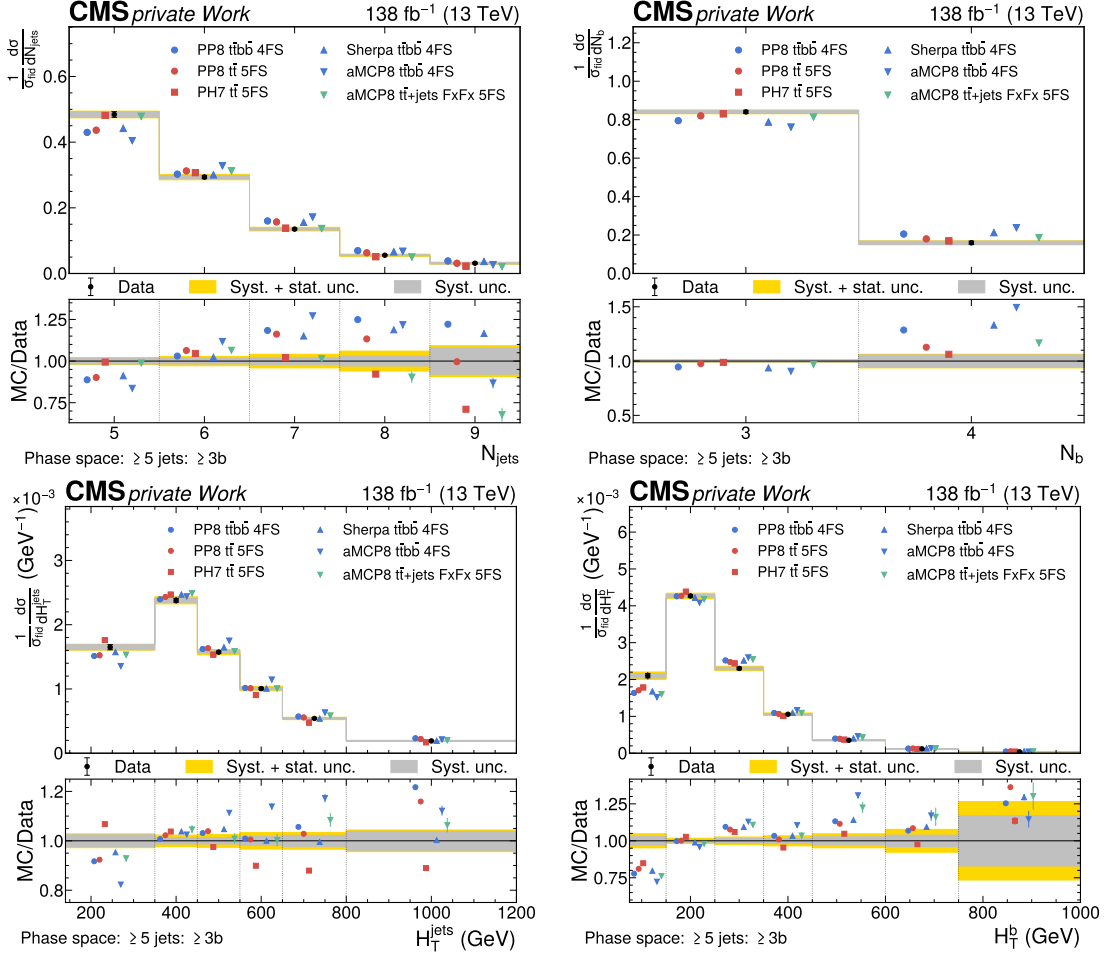


Figure 9.11: Predicted and observed normalized differential cross sections of the N_{jets} (top left), N_{b} (top right), $H_{\text{T}}^{\text{jets}}$ (bottom left), and H_{T}^{b} (bottom right) observables in the 5j3b phase space region. The measured cross sections in data are indicated with black dots, with inner (outer) vertical bars indicating the systematic (total) uncertainties, also represented as gray (yellow) bands. The cross section predictions from different modeling approaches as introduced in Section 8.1 are shown as colored symbols with different shapes. Where the observable can exceed the visible range, the last bin contains the overflow. Modified from Ref. [136].

approaches in which the $t\bar{t}b\bar{b}$ process is described at the ME (PP8 $t\bar{t}b\bar{b}$ 4FS, AMCP8 $t\bar{t}b\bar{b}$ 4FS, SHERPA $t\bar{t}b\bar{b}$ 4FS) show similar trends in simulation relative to the measurement, where all of these simulation approaches predict more jets than observed in data. This is similarly reflected in the measurement of N_{b} , where all of these simulation approaches predict a larger fraction of events with ≥ 4 b jets than observed in data. This is related to the observed disagreements in the fiducial cross section measurements discussed in the previous section. The estimation obtained with the PP8 $t\bar{t}$ 5FS simulation shows similar trends as the $t\bar{t}b\bar{b}$ ME simulation approaches. An opposite (albeit smaller) trend in the description of the N_{jets} observable is present for the PH7 $t\bar{t}$ 5FS and AMCP8 $t\bar{t}$ +jets FxFx 5FS simulation approaches in which fewer jets are predicted than observed in data. Comparing the PH7 $t\bar{t}$ 5FS and PP8 $t\bar{t}$ 5FS simulation approaches suggests that the PYTHIA PS and its tune describe the jet multiplicity of $t\bar{t}b\bar{b}$ better than the HERWIG PS and its tune, although both descriptions are insufficient based on the z scores in Figure 9.10. In the N_{b} measurement, the NLO $t\bar{t}$ simulation approaches (PP8 $t\bar{t}$ 5FS and PH7 $t\bar{t}$ 5FS) show

9 Measurement of the $t\bar{t}b\bar{b}$ process

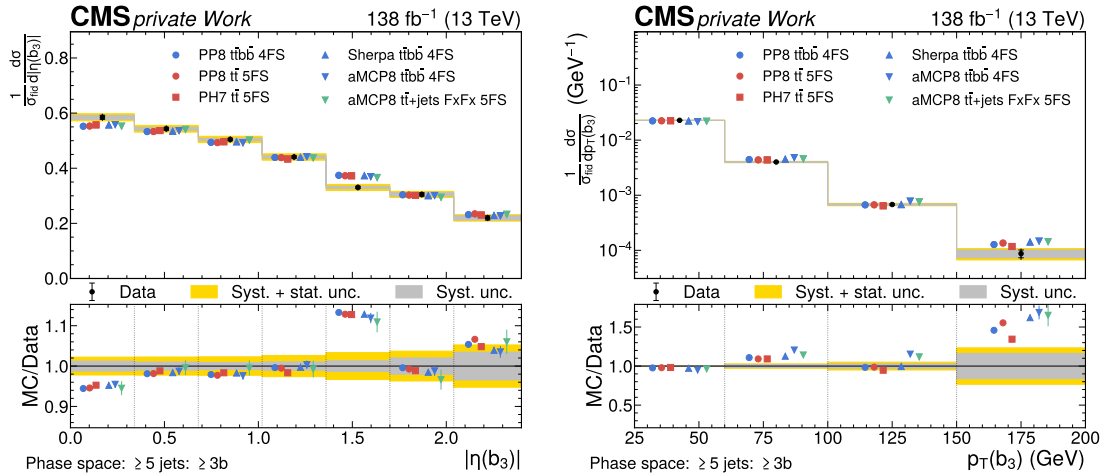


Figure 9.12: **Predicted and observed normalized differential cross sections of the $|\eta(\mathbf{b}_3)|$ (left), and $p_T(\mathbf{b}_3)$ (right) observables in the 5j3b phase space region.** The measured cross sections in data are indicated with black dots, with inner (outer) vertical bars indicating the systematic (total) uncertainties, also represented as gray (yellow) bands. The cross section predictions from different modeling approaches as introduced in Section 8.1 are shown as colored symbols with different shapes. Where the observable can exceed the visible range, the last bin contains the overflow. Modified from Ref. [136].

the best agreement with data, while the AMCP8 $t\bar{t}b\bar{b}$ 4FS simulation shows the largest disagreement quantified by the z score.

In the H_T^{jets} measurement strong trends are observed for the AMCP8 $t\bar{t}b\bar{b}$ 4FS and PH7 $t\bar{t}$ 5FS simulation approaches, where the former tends towards higher and the latter towards lower H_T^{jets} values than observed in data. Compared to the PH7 $t\bar{t}$ 5FS simulation, the PP8 $t\bar{t}$ 5FS prediction agrees somewhat better with the measurement, suggesting that the momentum content of the $t\bar{t}b\bar{b}$ events is better described by the PYTHIA PS and its tune compared to the HERWIG PS and its tune. Both however have z scores >2 , indicating that the description of the observable is insufficient. Only the SHERPA $t\bar{t}b\bar{b}$ 4FS and AMCP8 $t\bar{t}$ +jets FxFx 5FS simulations seem to describe the observable sufficiently well. In the H_T^b measurement, most of the simulation approaches show trends towards larger H_T^b values than observed in data, and all simulation approaches have troubles with the region at small H_T^b values, all predicting a smaller fraction than observed in data. The trend of the PH7 $t\bar{t}$ 5FS simulation in H_T^{jets} is not present in H_T^b , suggesting that the mis-modeling of H_T^{jets} originates mostly in the description of light jets. Based on the z scores, none of the simulation approaches appear to describe the H_T^b observable well, but among them, the PH7 $t\bar{t}$ 5FS still exhibits the best description.

Figure 9.12 shows the measurements of the $|\eta(\mathbf{b}_3)|$ and $p_T(\mathbf{b}_3)$ observables in the 5j3b phase space. In both observables the distributions of the different predictions are similar. In the $|\eta(\mathbf{b}_3)|$ observable all simulations show small trends towards larger $|\eta|$ compared to data. Similarly, in the $p_T(\mathbf{b}_3)$ observable all simulations show small trends towards larger p_T compared to data. None of the simulation approaches is able to describe either observable sufficiently well based on the z scores in Figure 9.10. For the $|\eta(\mathbf{b}_3)|$ observable this can most likely be attributed to the fluctuation in the measurement in the fifth bin as otherwise the distribution is described relatively well. Among the simulation approaches the inclusive $t\bar{t}$ simulations at NLO (PP8 $t\bar{t}$ 5FS and PH7 $t\bar{t}$ 5FS) are able to describe the $p_T(\mathbf{b}_3)$ best and show the smallest level of disagreement, while the simulations using

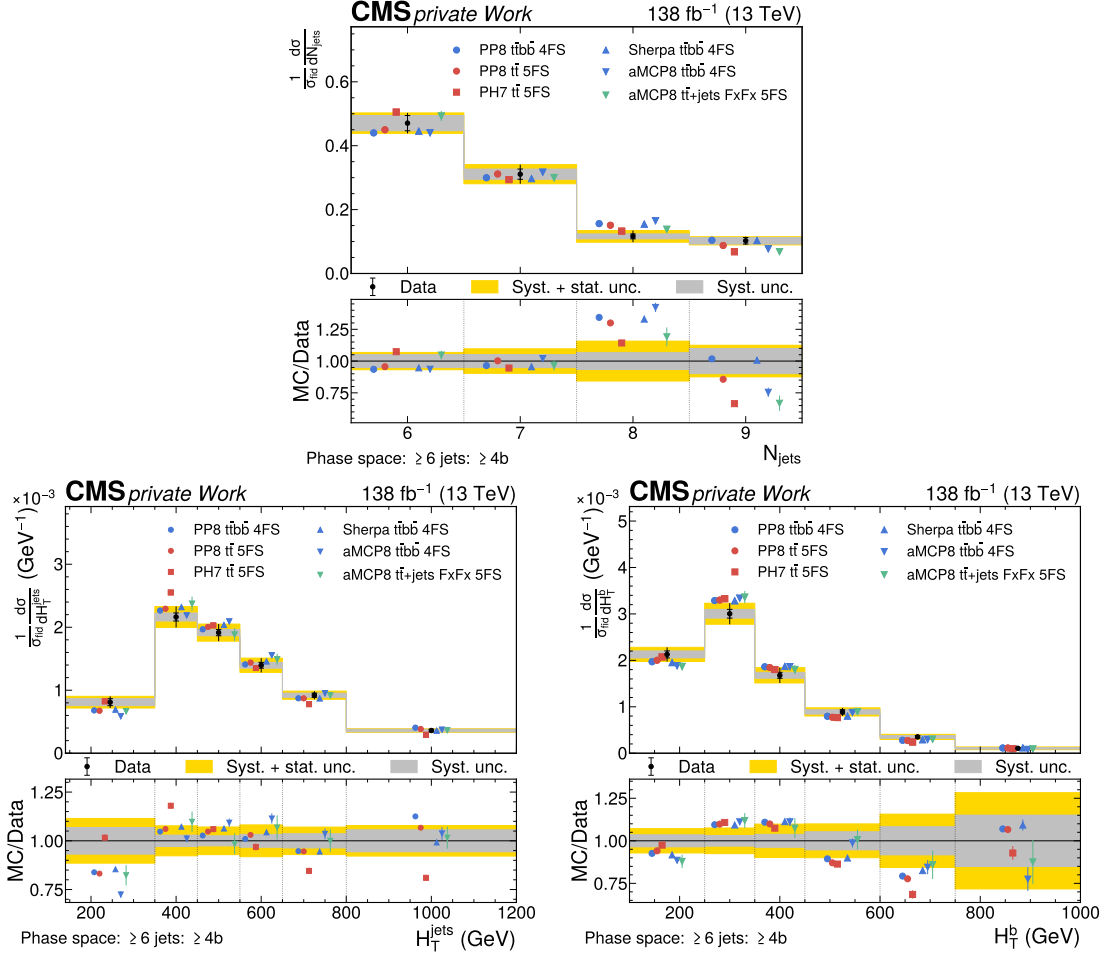


Figure 9.13: **Predicted and observed normalized differential cross sections of N_{jets} (top), $H_{\text{T}}^{\text{jets}}$ (bottom left), and H_{T}^{b} (bottom right) observables in the 6j4b phase space region.** The measured cross sections in data are indicated with black dots, with inner (outer) vertical bars indicating the systematic (total) uncertainties, also represented as gray (yellow) bands. The cross section predictions from different modeling approaches as introduced in Section 8.1 are shown as colored symbols with different shapes. Where the observable can exceed the visible range, the last bin contains the overflow. Modified from Ref. [136].

MADGRAPH5_aMC@NLO MEs (AMCP8 $t\bar{t}b\bar{b}$ 4FS and AMCP8 $t\bar{t}+\text{jets}$ FxFx 5FS) show the largest disagreements.

9.3.2 Results in the 6j4b phase space region

In the 6j4b phase space region the compatibility between simulation approaches and the measurement results is generally better if using the z scores for quantifying the agreement, as the measurement uncertainties in this phase space region are larger than in the 5j3b region. In Figure 9.13, the measurements of the N_{jets} , $H_{\text{T}}^{\text{jets}}$, and H_{T}^{b} observables in the 6j4b phase space region are shown. The N_{jets} observable is described well by all simulation approaches except the AMCP8 $t\bar{t}b\bar{b}$ 4FS simulation which fails to describe the larger jet multiplicity regions. Similar trends are seen in the AMCP8 $t\bar{t}+\text{jets}$ FxFx 5FS and PH7 $t\bar{t}$ 5FS simulation approaches, but are not as pronounced. The $H_{\text{T}}^{\text{jets}}$ observable is described sufficiently well by all simulation approaches except the PH7 $t\bar{t}$ 5FS simulation, which already showed similar mis-modeling in the 5j3b phase space, predicting on aver-

9 Measurement of the $t\bar{t}b\bar{b}$ process

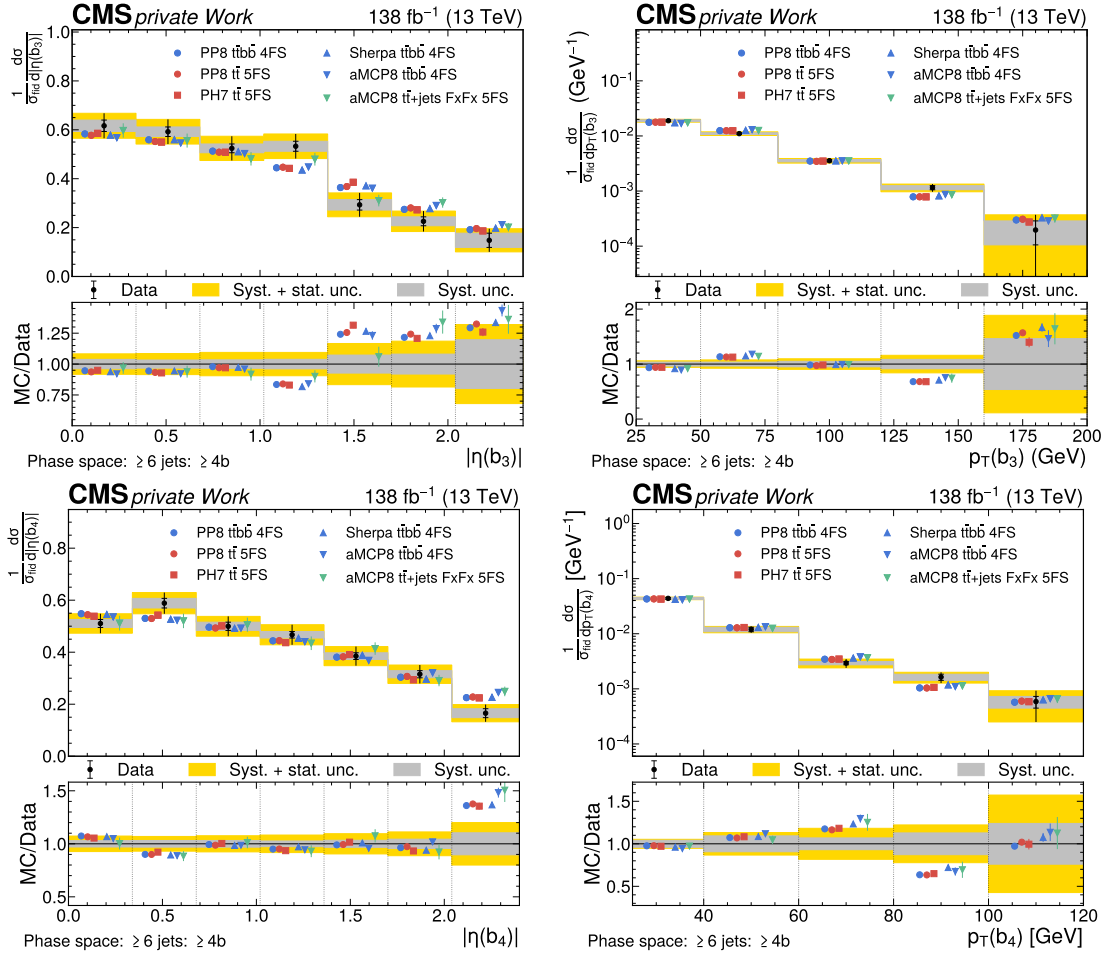


Figure 9.14: Predicted and observed normalized differential cross sections of $|\eta(\mathbf{b}_3)|$ (top left), $p_T(\mathbf{b}_3)$ (top right), $|\eta(\mathbf{b}_4)|$ (bottom left), and $p_T(\mathbf{b}_4)$ (bottom right) observables in the 6j4b phase space region. The measured cross sections in data are indicated with black dots, with inner (outer) vertical bars indicating the systematic (total) uncertainties, also represented as gray (yellow) bands. The cross section predictions from different modeling approaches as introduced in Section 8.1 are shown as colored symbols with different shapes. Where the observable can exceed the visible range, the last bin contains the overflow. Modified from Ref. [136].

age lower H_T^{jets} values than observed in data. This again suggests that the configuration of the PYTHIA PS and tune as used for the PP8 $t\bar{t}$ 5FS simulation is better suited for the description of this observable compared to the HERWIG PS and its tune. The H_T^b observable is described well by all simulation approaches.

Figure 9.14 shows the measurements of the $|\eta(\mathbf{b}_3)|$, $p_T(\mathbf{b}_3)$, $|\eta(\mathbf{b}_4)|$, and $p_T(\mathbf{b}_4)$ observables in the 6j4b phase space. All simulation approaches are able to describe the observables sufficiently well based on the z scores in Figure 9.10. The simulation approaches predict similar distributions for a given observable. These results suggest that the b jets with lower energies are modeled well and similar in the different modeling approaches probed. Small differences between the modeling approaches accumulate more in observables relating to the full event content, like the N_{jets} and H_T^{jets} or H_T^b measurements discussed above, and hence emphasize the differences, while in the description of a single jet, as shown here, the differences are small, and the agreement with data is generally good.

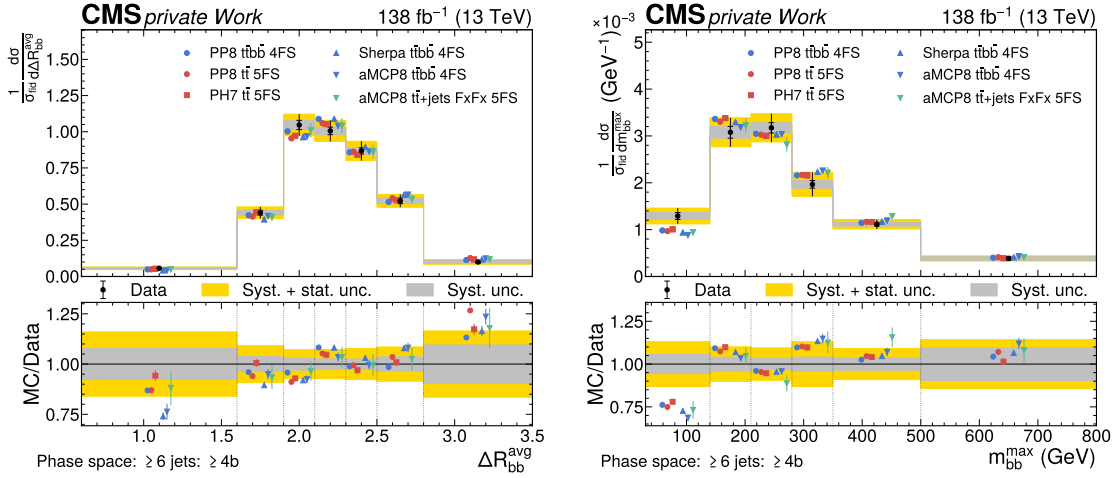


Figure 9.15: Predicted and observed normalized differential cross sections of $\Delta R_{bb}^{\text{avg}}$ (left), and m_{bb}^{max} (right) observables in the 6j4b phase space region. The measured cross sections in data are indicated with black dots, with inner (outer) vertical bars indicating the systematic (total) uncertainties, also represented as gray (yellow) bands. The cross section predictions from different modeling approaches as introduced in Section 8.1 are shown as colored symbols with different shapes. Where the observable can exceed the visible range, the last bin contains the overflow. Modified from Ref. [136].

Figure 9.15 shows the results of the measurement of the $\Delta R_{bb}^{\text{avg}}$ and m_{bb}^{max} observables in the 6j4b phase space, which again reference more than a single jet and take into account all jet kinematics in the fiducial events. Due to the size of the measurement uncertainties, all simulation approaches are able to describe the $\Delta R_{bb}^{\text{avg}}$ observable well based on the z scores in Figure 9.10. Some simulation approaches however exhibit trends towards larger $\Delta R_{bb}^{\text{avg}}$ values than measured in data, most pronounced for the SHERPA $t\bar{t}b\bar{b}$ 4FS and AMCP8 $t\bar{t}b\bar{b}$ 4FS simulation approaches. Even though at this point the quality of the description of this observable with the aforementioned simulation approaches cannot be criticized, future measurements with a larger amount of data could reduce the measurement uncertainties (which are dominated by data statistics in this phase space region), and thereby quantify possible disagreements between the simulation approaches and data. Based on the indication that the PP8 $t\bar{t}b\bar{b}$ 4FS simulation is closer to the measurement compared to the AMCP8 $t\bar{t}b\bar{b}$ 4FS simulation, this suggests that the angular distribution of b jets in $t\bar{t}b\bar{b}$ events is somewhat better described using the POWHEG-BOX-RES ME simulation with the chosen simulation settings rather than the MADGRAPH5_aMC@NLO ME simulation with the chosen simulation settings. In the m_{bb}^{max} observable all simulation approaches show similar trends towards higher masses compared to the measurement. These trends are, however, not very pronounced and the interpretation is limited due to the size of the measurement uncertainties.

In Figure 9.16, the measurements relating to the single b jets of the pair of b jets closest in ΔR are shown, i.e. $|\eta(b_1^{\text{extra}})|$, $p_T(b_1^{\text{extra}})$, $|\eta(b_2^{\text{extra}})|$, and $p_T(b_2^{\text{extra}})$. Similar to Figure 9.14, the simulation approaches exhibit similar descriptions for each of the four measured observables and all simulation approaches are compatible with data indicated by the z scores.

Finally, in Figure 9.17 the four remaining observables related to the pair of b jets closest in ΔR are shown, i.e. $|\eta(bb^{\text{extra}})|$, $\Delta R(bb^{\text{extra}})$, $m(bb^{\text{extra}})$, and $p_T(bb^{\text{extra}})$. As these observables are designed to probe the collinear gluon splitting regime ($g \rightarrow b\bar{b}$) in the simulation of $t\bar{t}b\bar{b}$ events, differences in the description of these observables are expected because of

9 Measurement of the $t\bar{t}b\bar{b}$ process

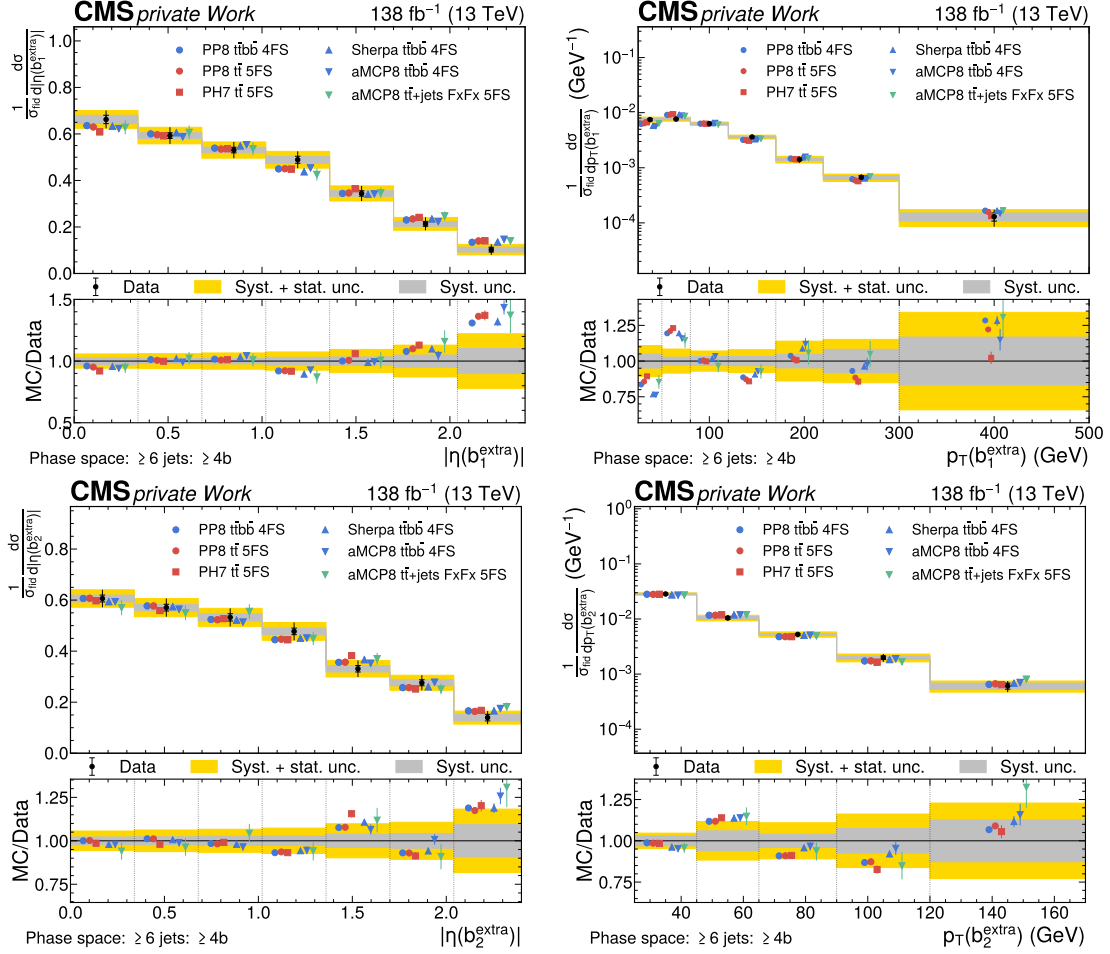


Figure 9.16: Predicted and observed normalized differential cross sections of $|\eta(\mathbf{b}_1^{\text{extra}})|$ (top left), $p_{\text{T}}(\mathbf{b}_1^{\text{extra}})$ (top right), $|\eta(\mathbf{b}_2^{\text{extra}})|$ (bottom left), and $p_{\text{T}}(\mathbf{b}_2^{\text{extra}})$ (bottom right) observables in the 6j4b phase space region. The measured cross sections in data are indicated with black dots, with inner (outer) vertical bars indicating the systematic (total) uncertainties, also represented as gray (yellow) bands. The cross section predictions from different modeling approaches as introduced in Section 8.1 are shown as colored symbols with different shapes. Where the observable can exceed the visible range, the last bin contains the overflow. Modified from Ref. [136].

the differences in the simulation of the $g \rightarrow b\bar{b}$ splitting in the different signal models. In the $\Delta R(bb^{\text{extra}})$ observable a significant trend towards smaller ΔR values is seen for the PH7 $t\bar{t}$ 5FS and AMCP8 $t\bar{t}+\text{jets}$ FxFx 5FS simulation approaches relative to the measurement, i.e. showing that these simulation approaches predict b jets from $g \rightarrow b\bar{b}$ splitting that are too close to each other when compared with the measurement. The simulation approaches using a description of $t\bar{t}b\bar{b}$ at the ME level (PP8 $t\bar{t}b\bar{b}$ 4FS, AMCP8 $t\bar{t}b\bar{b}$ 4FS, SHERPA $t\bar{t}b\bar{b}$ 4FS) show good agreement with the measurement. This suggests that the description of the collinear $g \rightarrow b\bar{b}$ splitting regime in $t\bar{t}b\bar{b}$ events is described more accurately in the ME simulations compared to NLO $t\bar{t}$ simulation approaches in which the description of the $g \rightarrow b\bar{b}$ splitting relies mostly on the PS. Further, comparing the PH7 $t\bar{t}$ 5FS and PP8 $t\bar{t}$ 5FS simulation approaches shows that the PYTHIA PS and its tune are able to describe this observable sufficiently well while the HERWIG PS and its tune is not able to describe this observable well. The invariant mass of the bb^{extra} pair shows similar trends as discussed for the $\Delta R(bb^{\text{extra}})$ observable. The PH7 $t\bar{t}$ 5FS and AMCP8 $t\bar{t}+\text{jets}$

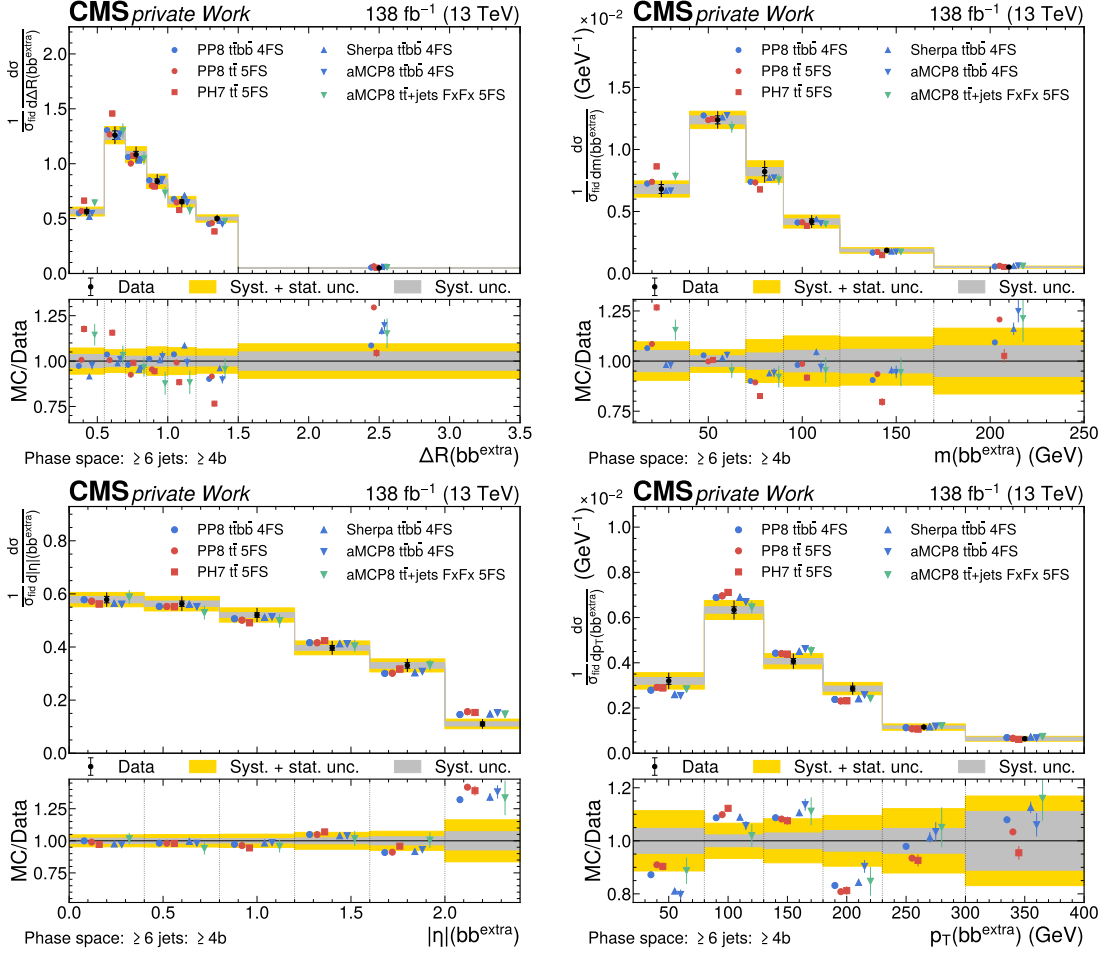


Figure 9.17: Predicted and observed normalized differential cross sections of $|\eta|(\text{bb}^{\text{extra}})$ (top left), $\Delta R(\text{bb}^{\text{extra}})$ (top right), $m(\text{bb}^{\text{extra}})$ (bottom left), and $p_T(\text{bb}^{\text{extra}})$ (bottom right) observables in the 6j4b phase space region. The measured cross sections in data are indicated with black dots, with inner (outer) vertical bars indicating the systematic (total) uncertainties, also represented as gray (yellow) bands. The cross section predictions from different modeling approaches as introduced in Section 8.1 are shown as colored symbols with different shapes. Where the observable can exceed the visible range, the last bin contains the overflow. Modified from Ref. [136].

FFFX 5FS simulation approaches predict on average smaller masses than measured in data while the simulation approaches using $t\bar{t}b\bar{b}$ MEs (PP8 $t\bar{t}b\bar{b}$ 4FS, AMCP8 $t\bar{t}b\bar{b}$ 4FS, SHERPA $t\bar{t}b\bar{b}$ 4FS) exhibit a better agreement with the measurement. Compared to the $\Delta R(\text{bb}^{\text{extra}})$ measurement the uncertainties in the measurement of the $m(\text{bb}^{\text{extra}})$ observable are larger which yields z scores that are all < 2 , suggesting that the description of the observable is sufficient. The increase in uncertainties can be explained via the increased size of migrations for observables depending on jet energy measurements compared to angular observables like ΔR (see Section 9.1). All simulation approaches are able to describe the $|\eta|(\text{bb}^{\text{extra}})$ and $p_T(\text{bb}^{\text{extra}})$ observables well based on the z scores shown in Figure 9.10. In the $p_T(\text{bb}^{\text{extra}})$ observable trends towards smaller p_T values in the simulation approaches compared to the measurement are indicated, but are not significant enough given the size of the measurement uncertainties. The z scores suggest that the angle ($|\eta|$) and momentum (p_T) of the intermediate gluon before $g \rightarrow b\bar{b}$ splitting is modeled sufficiently well with the probed modeling approaches. However, given that no attempt

9 Measurement of the $t\bar{t}b\bar{b}$ process

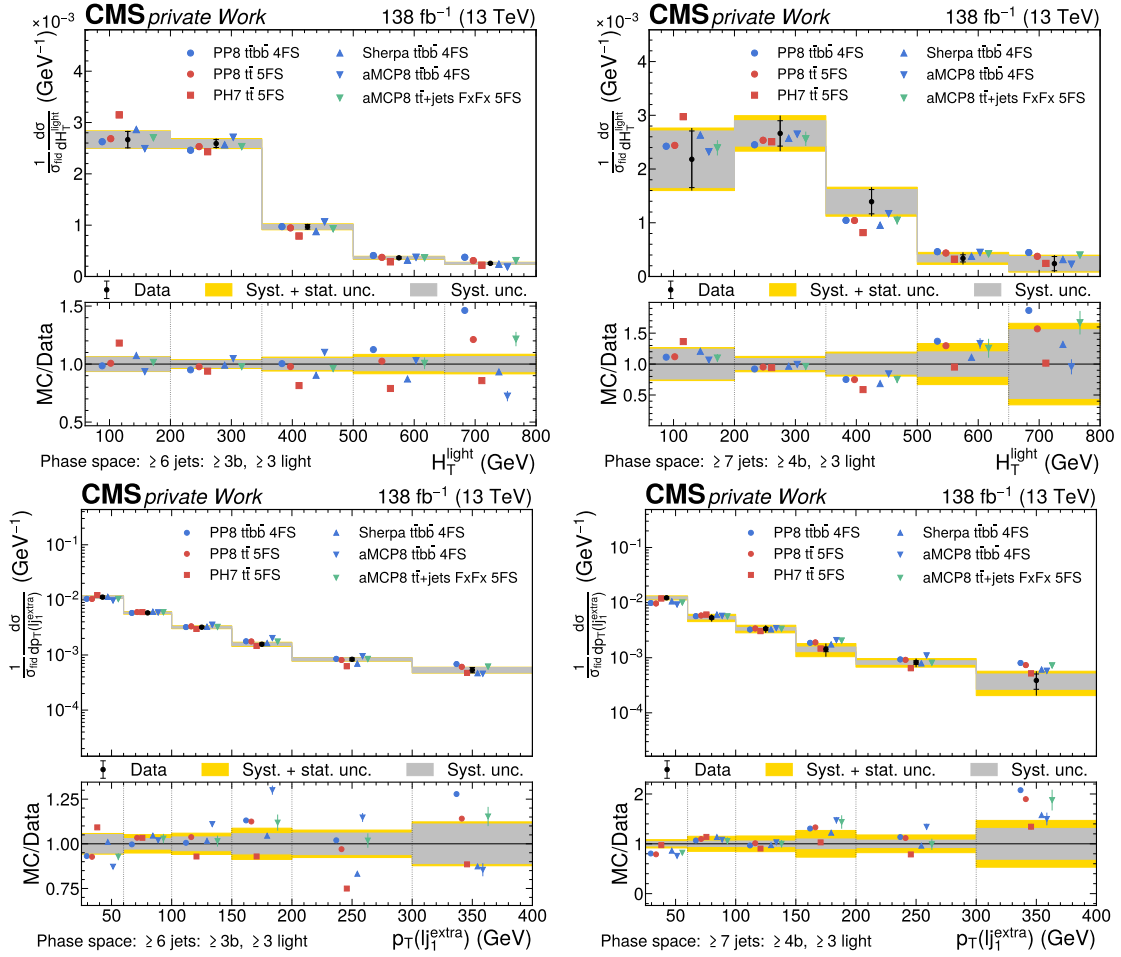


Figure 9.18: Predicted and observed normalized differential cross sections of H_T^{light} (top) and $p_T(lj_1^{\text{extra}})$ (bottom) observables in the 6j3b3l (left) and 7j4b3l (right) phase space regions. The measured cross sections in data are indicated with black dots, with inner (outer) vertical bars indicating the systematic (total) uncertainties, also represented as gray (yellow) bands. The cross section predictions from different modeling approaches as introduced in Section 8.1 are shown as colored symbols with different shapes. Where the observable can exceed the visible range, the last bin contains the overflow. Modified from Ref. [136].

at identifying the origin of the $b\bar{b}^{\text{extra}}$ pair is made for these observables, and hence the exact fraction of cases in which the two $b\bar{b}^{\text{extra}}$ jets originate from $g \rightarrow b\bar{b}$ splitting is unknown, the interpretation of this is limited.

9.3.3 Results in the 6j3b3l and 7j4b3l phase space regions

In Figure 9.18, the measurements of the H_T^{light} and $p_T(lj_1^{\text{extra}})$ observables are shown in the 6j3b3l and 7j4b3l phase space regions. As the phase 6j3b3l phase space is significantly larger than the 7j4b3l phase space, the z scores in Figure 9.10 are generally better in 7j4b3l than 6j3b3l. The H_T^{light} observable is not described well by the PP8 $t\bar{t}b\bar{b}$ 4FS simulation in both phase space regions, indicated by z scores > 2 . In both phase space regions, the PP8 $t\bar{t}b\bar{b}$ 4FS simulation exhibits a trend towards larger H_T^{light} values compared to the measurements. Contrary trends are observed for the PH7 $t\bar{t}$ 5FS and aMCP8 $t\bar{t}b\bar{b}$ 4FS simulation approaches, which predict on average smaller H_T^{light} values compared to the measurements, but only significant enough in the 6j3b3l phase space. The PP8 $t\bar{t}$ 5FS

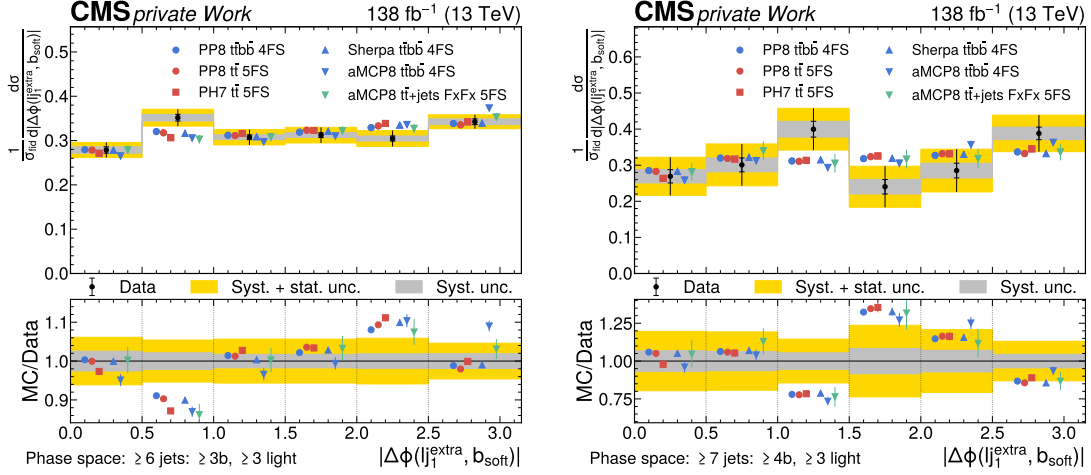


Figure 9.19: **Predicted and observed normalized differential cross sections of $|\Delta\phi(lj_1^{\text{extra}}, b_{\text{soft}})|$ observable in the 6j3b3l (left) and 7j4b3l (right) phase space regions.** The measured cross sections in data are indicated with black dots, with inner (outer) vertical bars indicating the systematic (total) uncertainties, also represented as gray (yellow) bands. The cross section predictions from different modeling approaches as introduced in Section 8.1 are shown as colored symbols with different shapes. Where the observable can exceed the visible range, the last bin contains the overflow. Modified from Ref. [136].

simulation approach can describe the H_T^{light} observable well in both phase space regions, suggesting that the light jets in $t\bar{t}b\bar{b}$ events are better described with the PYTHIA PS and its tune compared to the HERWIG PS and its tune. This confirms the results discussed for the H_T^b observable, which showed a better description by the PH7 $t\bar{t}$ 5FS simulation approach compared to the H_T^{jets} observable, suggesting that the origin of the mis-modeling is the description of the light jets, i.e. H_T^{light} . In the $p_T(lj_1^{\text{extra}})$ observable similar trends can be observed, showing trends towards smaller p_T values for PH7 $t\bar{t}$ 5FS compared to the measurements, and trends towards larger p_T values for AMCP8 $t\bar{t}b\bar{b}$ 4FS compared to the measurements. The description of the $p_T(lj_1^{\text{extra}})$ observable by the PP8 $t\bar{t}b\bar{b}$ 4FS simulation approach appears to be better than its description of the H_T^{light} observable, suggesting that the origin of the mis-modeling observed in the H_T^{light} observable originates not from the hardest light jet radiation but potentially from softer jets or the light jets from top quark decays. The hardest light jet radiation in PP8 $t\bar{t}b\bar{b}$ 4FS can be described via the ME using the NLO $t\bar{t}b\bar{b}$ ME calculation, suggesting that the origin of the mis-modeling seen in the H_T^{light} observable could originate from the PS simulation.

In Figure 9.19, the measurements of the $|\Delta\phi(lj_1^{\text{extra}}, b_{\text{soft}})|$ observables in the 6j3b3l and 7j4b3l phase space regions are shown. All simulation approaches are able to describe these observables sufficiently well based on the z scores in Figure 9.10, in part also due to the large measurement uncertainties. The observables are described similarly by all simulation approaches.

9.3.4 Sensitivity and limitation of measurements

Contrary to the fiducial cross sections, the normalized differential cross sections are limited in sensitivity by data statistics. The measurements exhibit a wide range of uncertainty sizes, ranging from about 2% in some bins in the 5j3b phase space to up to 50% in some bins in other phase space regions. For one representative observable the contributions of groups of uncertainties as introduced in Section 8.7 to the total uncertainty in each

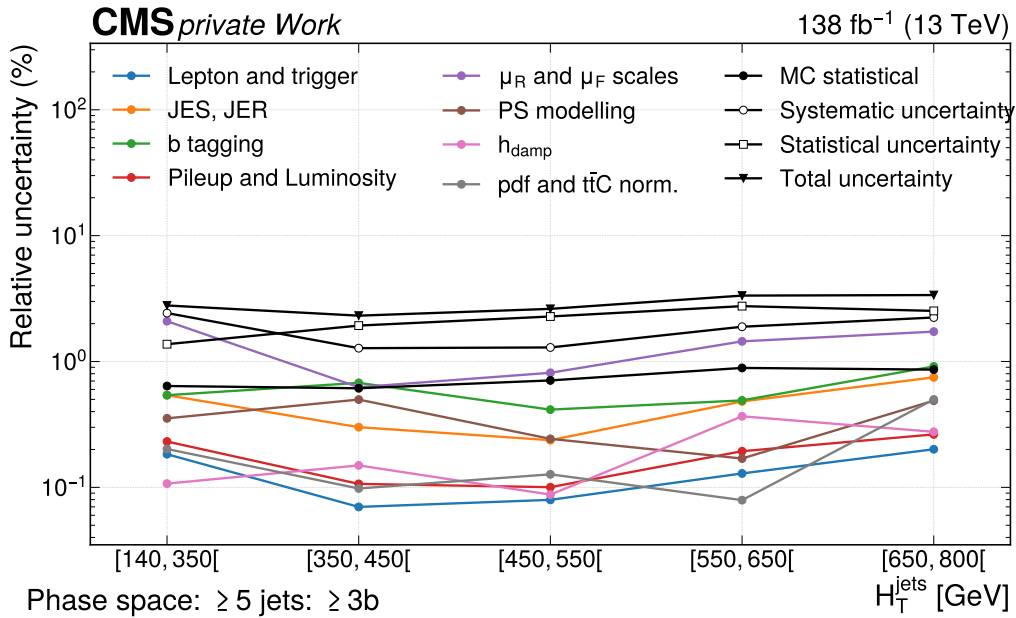


Figure 9.20: **Effect of sources of uncertainties on the measurement of the normalized differential cross section of the H_T^{jets} in the 5j3b phase space region.** The impacts of the nuisance parameters associated to the displayed uncertainty groups are obtained by combining their impacts taking into account their correlation in the fit.

of the measured bins is shown in Figure 9.20. As can be seen, the statistical uncertainty due to the limited amount of data dominates the uncertainty in each of the bins already in the largest phase space (5j3b), exceeding the combined contribution of all systematic uncertainties in most of the bins. Subdominant contributions arise from uncertainties on the μ_R and μ_F scales and the size of simulated samples, followed by b tagging, PS modeling, and jet energy calibrations.

9.4 Scale choices of the nominal signal model

The nominal signal model (PP8 $t\bar{t}b\bar{b}$ 4FS) exhibits a strong dependence on the choices of renormalization (μ_R) and factorization (μ_F) scales in the calculation of the hard scattering MEs. As explained in Section 7.2, this is due to the dependence of the $t\bar{t}b\bar{b}$ cross section on the renormalization scale through the strong coupling constant with $\sim \alpha_s(\mu_R)^4$. In Ref. [137], inclusive and fiducial cross section predictions of the PP8 $t\bar{t}b\bar{b}$ 4FS model are discussed assuming scales with $\xi_R = \xi_F = 1$ (see eqs. (7.1) and (7.3)), while in this measurement as nominal scales these factors are set to $\xi_R = \xi_F = 0.5$ (see eq. (8.2)). In the $t\bar{t}H(b\bar{b})$ and $t\bar{t}t\bar{t}$ measurements by the ATLAS Collaboration [149, 152] the $t\bar{t}b\bar{b}$ background is modelled using $\xi_R = \xi_F = 1$, but is seen to predict $t\bar{t}b\bar{b}$ cross sections that are too low compared to what is seen in data (see Section 7.4.2). Hence in this section, the results of the measurements in this thesis are compared to different μ_F and μ_R scale choices of the PP8 $t\bar{t}b\bar{b}$ 4FS simulation. This study does not include a full simulation of PP8 $t\bar{t}b\bar{b}$ 4FS events with adjusted scales but takes as basis for the comparison the simulation of PP8 $t\bar{t}b\bar{b}$ 4FS events with the nominal scale choices reweighted to other μ_R and μ_F scales. The PP8 $t\bar{t}b\bar{b}$ 4FS signal model is compared between its nominal μ_R and μ_F scale choices and both of these scales independently varied up ($\xi_R/\xi_F = 1$) and down ($\xi_R/\xi_F = 0.25$) by a factor of two. This does not constitute a full simulation of the process with adjusted

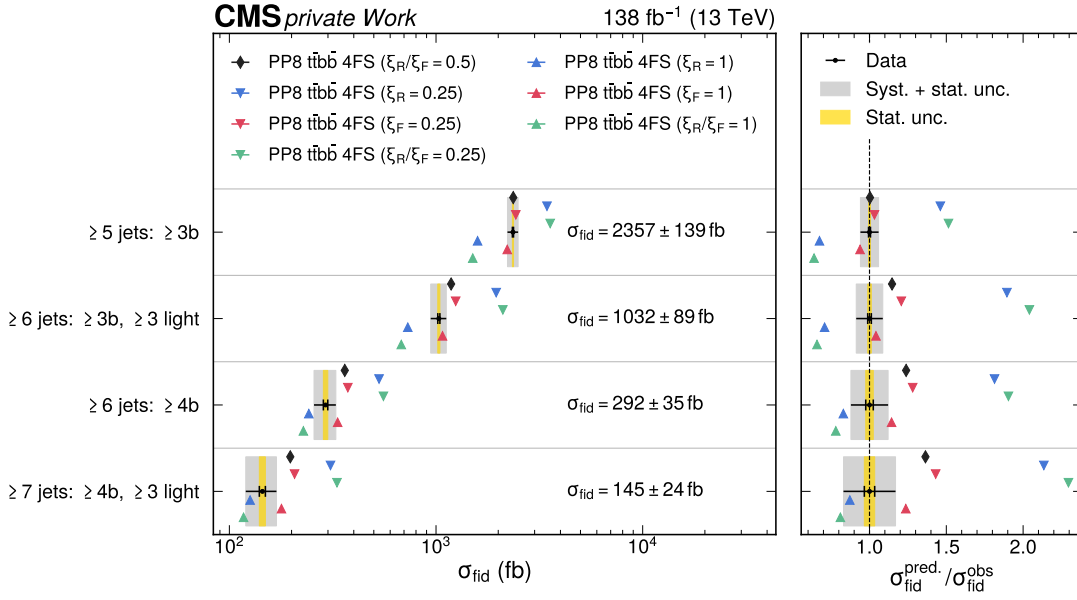


Figure 9.21: **Fiducial cross sections measurement compared to the PP8 $t\bar{t}b\bar{b}$ 4FS signal model and alternative μ_R and μ_F scale choices.** The measured cross sections in data are indicated with black dots, with inner (outer) vertical bars indicating the systematic (total) uncertainties, also represented as gray (yellow) bands. The cross section predictions of the PP8 $t\bar{t}b\bar{b}$ 4FS simulation are shown as black diamonds. Variations of the μ_R and μ_F scales by factors of two up and down are indicated via triangles. The panel on the right shows the ratio between the predictions and measured cross sections.

scales and is therefore only an approximation. For a more accurate comparison, the full simulation would have to be repeated with adjusted settings, which is beyond the scope of this thesis.

In Figure 9.21, the measurements of the fiducial cross sections from Figure 9.8 are shown again, but are compared to the different μ_R and μ_F scale choices of the PP8 $t\bar{t}b\bar{b}$ 4FS model. As explained in Section 7.2, individual or simultaneous increase of μ_R and μ_F by a factor of two ($\xi_R/\xi_F = 1$) decreases the predicted fiducial cross sections, while a decrease of μ_R and μ_F by a factor of two ($\xi_R/\xi_F = 0.25$) increases the predicted fiducial cross sections. The μ_R scale steers the value of the strong coupling constant α_s at which the calculation of the scattering ME is performed (see Section 5.2). Following the discussions in Ref. [142], variations of $\mu_R \rightarrow \xi_R \mu_R$ affect the strong coupling constant to first order as

$$\alpha_s(\xi\mu_R) = \frac{\alpha_s(\mu_R)}{1 + \frac{\ln(\xi)}{\ln(\mu_R/\Lambda_{\text{QCD}})}} \propto \frac{1}{1 + \ln \xi}, \quad (9.1)$$

where Λ_{QCD} is the reference scale for QCD interaction. Hence, an increase in the μ_R scale decreases the coupling constant α_s which decreases the available phase space for the radiation of gluons outside the $t\bar{t}$ system, which reduces the cross section of the process. Similarly, an increase in the μ_F scale increases the scale at which the pdfs are evaluated, which decreases the phase space for the $t\bar{t}b\bar{b}$ ME, decreasing its cross section. With these considerations, the decrease of the predicted fiducial $t\bar{t}b\bar{b}$ cross sections due to an increase in μ_R and μ_F scales in the simulation is expected, as is confirmed by the results in Figure 9.21. The difference in predicted fiducial cross sections is of the order of 50% for

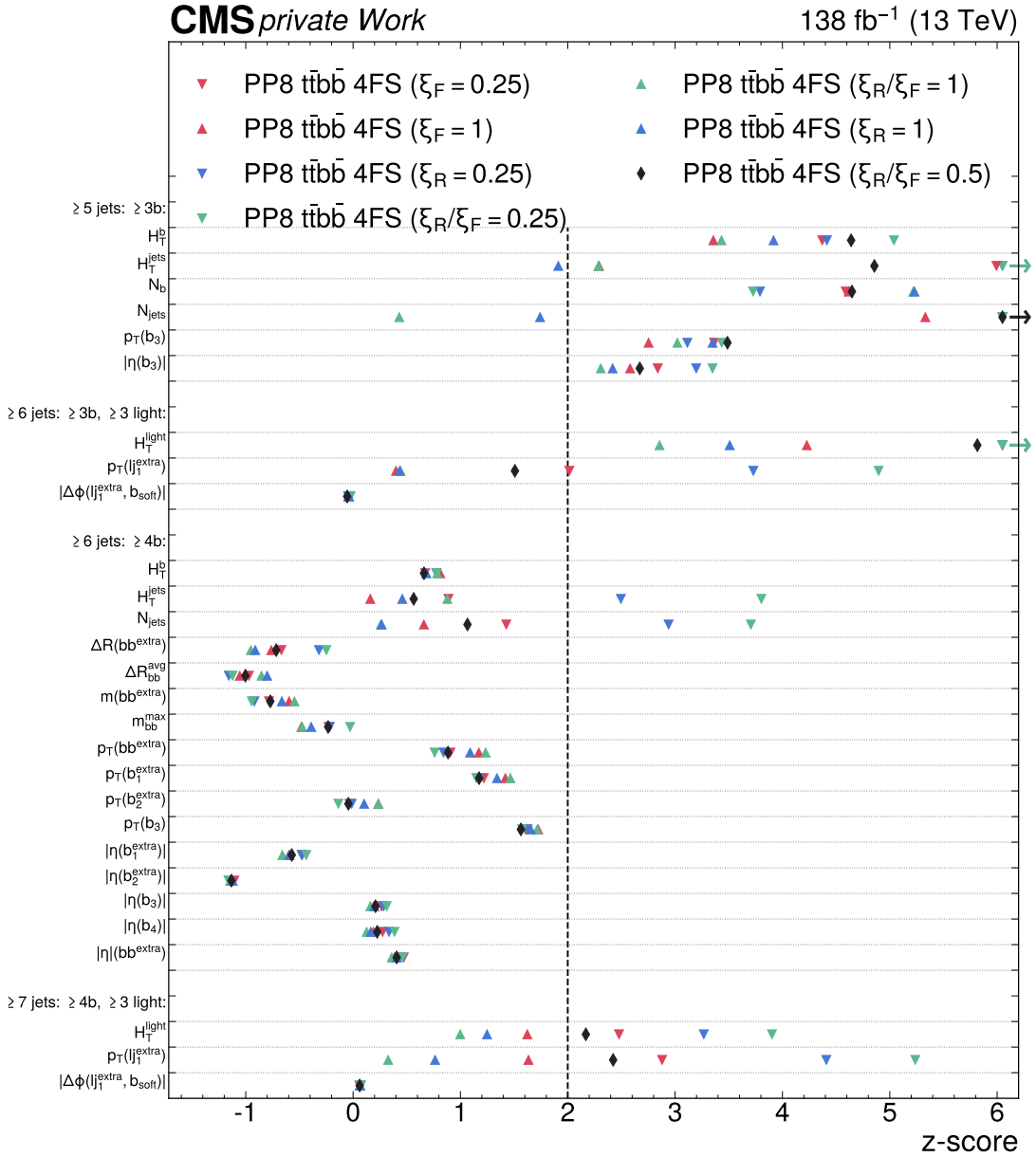


Figure 9.22: **Observed z score for the PP8 $t\bar{t}b\bar{b}$ 4FS simulation approach and alternative μ_R and μ_F scale choices.** Lower values indicate better agreement between prediction and measurement. The z scores of the PP8 $t\bar{t}b\bar{b}$ 4FS simulation are shown as black diamonds. Variations of the μ_R and μ_F scales by factors of two up and down are indicated via triangles. The dashed line at $z = 2$ indicates a p -value of 5%. Predictions for which the z score exceeds the visible range of the figure are marked with arrows (\rightarrow).

the μ_R scale and below 10% for the μ_F scale. The alternatives where the μ_R or μ_F scales are reduced w.r.t. the nominal scale choices overpredict the measured cross sections in each of the fiducial phase space regions, as the nominal PP8 $t\bar{t}b\bar{b}$ 4FS simulation already overpredicts the cross sections in most cases. Increase of the μ_R scale by a factor of two ($\xi_R = 1$) yields, in most cases, cross sections that are lower than the measurement. The increase of the μ_F scale by a factor of two ($\xi_F = 1$) yields cross sections that are in most cases compatible with the measurement, and in each of the phase space regions except for the $5j3b$ phase space closer to the measured cross section values than the nominal

9.4 Scale choices of the nominal signal model

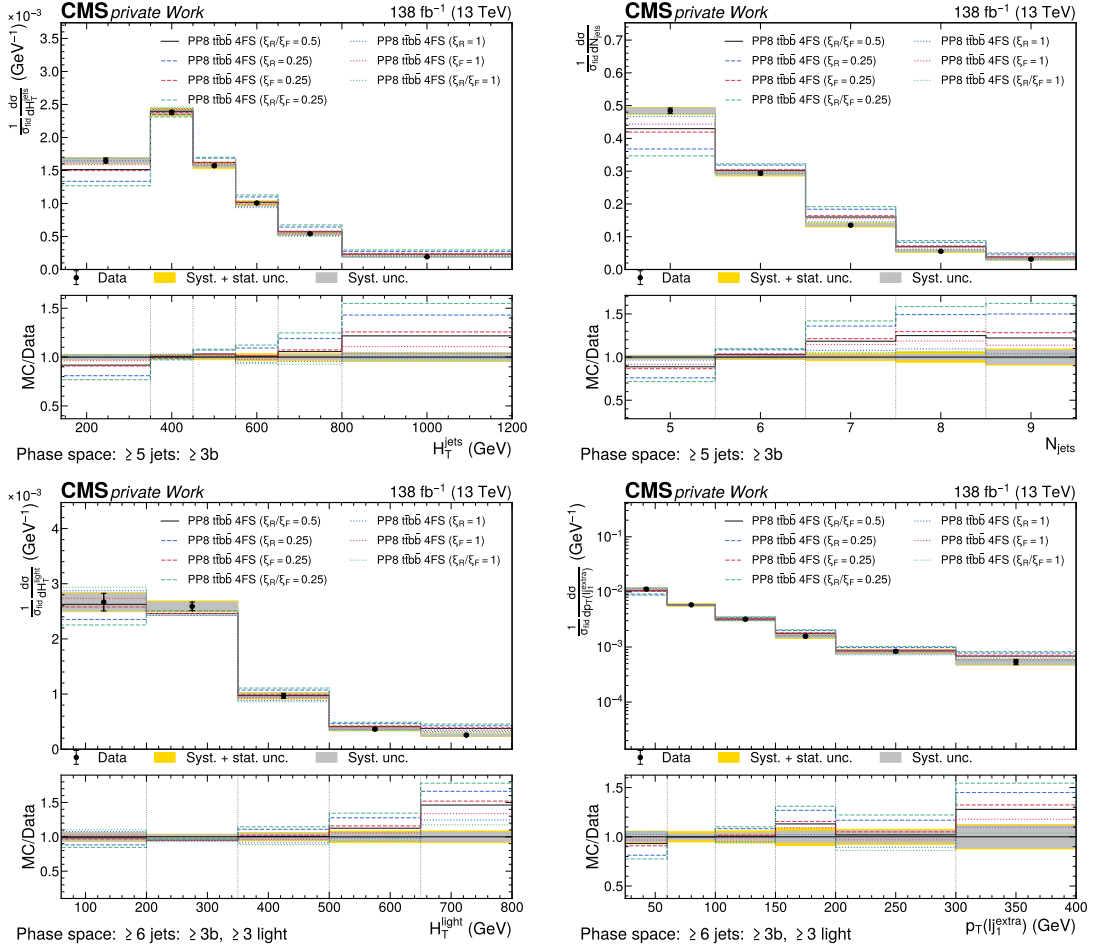


Figure 9.23: Predicted and observed normalized differential cross sections of the H_T^{jets} (top left) and N_{jets} (top right) observables in the 5j3b phase space region, and the H_T^{light} and $p_T(l_1^{\text{extra}})$ observables in the 6j3b3l phase space region. The measured cross sections in data are indicated with black dots, with inner (outer) vertical bars indicating the systematic (total) uncertainties, also represented as gray (yellow) bands. The predictions of the PP8 $t\bar{t}b\bar{b}$ 4FS simulation are shown as black diamonds. Variations of the μ_R and μ_F scales by factors of two up and down are indicated via triangles. Where the observable can exceed the visible range, the last bin contains the overflow.

PP8 $t\bar{t}b\bar{b}$ 4FS model with $\xi_R/\xi_F = 0.5$. This indicates that for the description of the fiducial cross sections, an increased μ_F scale would be beneficial. With the adjusted μ_F scale the configuration of the signal modeling corresponds to the value chosen by the ATLAS Collaboration in the $t\bar{t}b\bar{b}$ modeling studies in Ref. [165]. The scale choices made in the $t\bar{t}H(b\bar{b})$ and $t\bar{t}t\bar{t}$ measurements by the ATLAS Collaboration [149, 152] (see Section 7.4.2), which predate Ref. [165], appear to be too large as the $t\bar{t}b\bar{b}$ background is underestimated in these measurements.

Figure 9.22 summarizes the z scores of the PP8 $t\bar{t}b\bar{b}$ 4FS simulation and the alternative μ_R and μ_F scale choices discussed in this section for all of the measured observables discussed in Section 9.3. While for many observables no significant difference in the z scores is visible when changing the scale choices in the simulation, in some observables the agreement with the measurement changes significantly. As explained in Section 7.2, changes in the μ_R and μ_F scales are expected to not influence the normalized distributions of observables related to the part of the $t\bar{t}b\bar{b}$ process fully described by the ME at NLO,

but predominantly the observables related to the additional radiation [137]. In the 5j3b phase space, where the nominal PP8 $t\bar{t}b\bar{b}$ 4FS signal model is not able to describe either of the six measured observables, variations of the μ_R scale by a factor of two ($\xi_R = 1$) are able to describe two observables, indicated by $z \leq 2$. These observables are H_T^{jets} and N_{jets} , which are shown in Figure 9.23 in the top row for all the scale choices discussed here. These observables include all jets, also the ones not described by the $t\bar{t}b\bar{b}$ ME, and hence show large shape effects with varying the μ_R and μ_F scales, while observables such as H_T^b or N_b show only smaller changes as the b jets are described by the ME. These distributions also indicate that, besides the increased μ_R scale, also the increased μ_F scale is closer to data than the nominal PP8 $t\bar{t}b\bar{b}$ 4FS model. Both these scale variations predict, on average, more H_T and more jets than the nominal PP8 $t\bar{t}b\bar{b}$ 4FS model, which is also the trend observed in data. Variations in which either the μ_R or μ_F scales are decreased show even larger differences in the measurement than the nominal model.

Besides the two aforementioned observables, also observables related to the description of light jets in the 6j3b3l and 7j4b3l phase space regions show significant differences in the signal modeling when changing the μ_R or μ_F scales. As shown representatively in the bottom row of Figure 9.23 for the H_T^{light} and $p_T(\text{1j}_1^{\text{extra}})$ in the 6j3b3l phase space region, an increase of either the μ_R or μ_F scale by a factor of two is able to better describe these observables in the normalized differential cross section.

In order to probe not only variations of $\xi_{R/F}$ by a factor of two, an interpolation of the variations shown in Figure 9.23 is performed. The interpolation is performed linearly, between the symmetrized ratio of upward and downward variations (i.e. assuming that a variation of the scale parameter by half and two has a symmetric effect). For each interpolated point the z score is calculated as shown in Figure 9.24 for the four observables. In the figure, the area where $z < 2$ is indicated via a contour. This simple interpolation suggests that the PP8 $t\bar{t}b\bar{b}$ 4FS model with adjusted scales would be able to describe the observables well. For the four observables shown, the interpolations hint towards increased μ_R and μ_F scales where sufficiently small z scores are obtained for variations smaller than a factor two in most cases.

When taking into account also the fiducial cross sections in Figure 9.21, especially an increased μ_R scale is not able to describe the fiducial cross sections, suggesting that a simple variation of the two parameters ξ_R and ξ_F alone is not able to resolve all the observed issues of the PP8 $t\bar{t}b\bar{b}$ 4FS model simultaneously. Also, the trends in the fiducial cross section agreement between the more inclusive (5j3b) and more exclusive (7j4b3l) phase space regions can apparently not be resolved with these simple variations.

In Ref. [142] also alternative μ_R and μ_F scales are proposed, incorporating (in addition) additional jets outside the $t\bar{t}b\bar{b}$ system e.g. from NLO corrections ($t\bar{t}b\bar{b}j$). One modification that is proposed is

$$\mu_R = \xi_R \left(\mu_{t\bar{t}}^2 \mu_{b\bar{b}}^2 p_{T,j} \right)^{1/5}, \quad (9.2)$$

i.e. introducing the p_T of additional jets j to the geometric average of $\mu_{t\bar{t}}$ and $\mu_{b\bar{b}}$ scales as defined in eq. (7.2). The results presented in this thesis and in the corresponding CMS publication [136] will be able to be compared to such alternative scale choices by the modeling experts in more detail than in this section. This will enable the theory community to update the recommendations of generator scales and settings for future CMS and ATLAS measurements. For the purpose of comparing the results of this measurement with updated $t\bar{t}b\bar{b}$ modeling approaches the results are published in a Rivet routine [166].

9.4 Scale choices of the nominal signal model

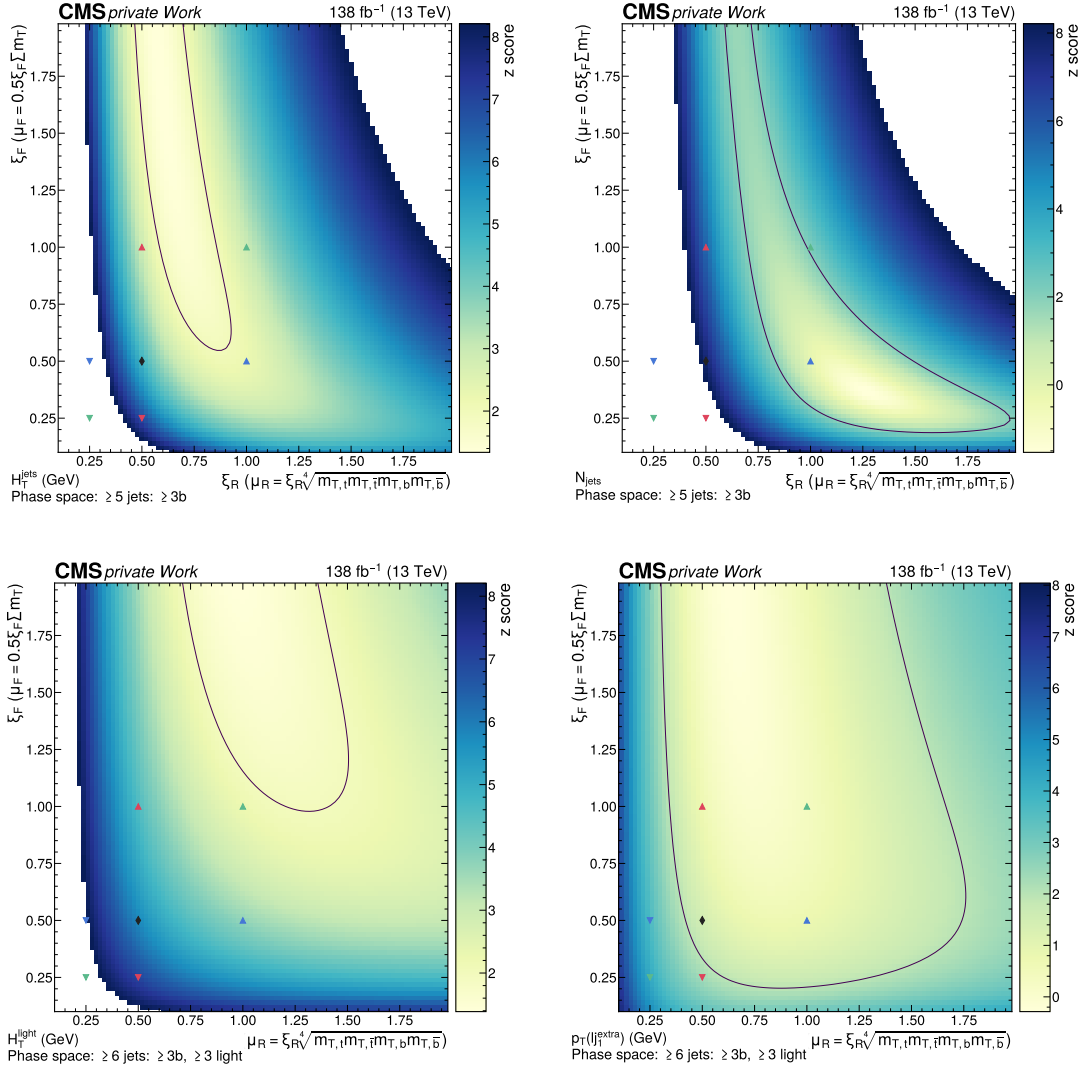


Figure 9.24: Interpolation of z scores in the normalized differential cross section measurement. Shown are the interpolation of z scores from variations of the μ_R and μ_F scales of the PP8 $t\bar{t}b\bar{b}$ 4FS model for the H_T^{jets} (top left) and N_{jets} (top right) observables in the 5j3b phase space region, and the H_T^{light} (bottom left) and $p_T(lj_1^{\text{extra}})$ (bottom right) observables in the 6j3b3l phase space region. The contour indicates $z < 2$.

Part III

Additional studies on $t\bar{t}$ +jets production



10 Introduction

In this part of the thesis, additional studies on $t\bar{t}$ production with additional jets ($t\bar{t}$ +jets) will be presented. In the modeling of the $t\bar{t}$ production process at NLO precision a common issue is the accurate modeling of the top quark momentum, discussed e.g. in Ref. [167], which will be investigated in this part of the thesis for the $t\bar{t}$ production process in association with jets. Observables directly related to the top quark momentum or just related to the general modeling of the $t\bar{t}$ +jets production process are probed via normalized differential cross section measurements, analog to the procedure employed for the $t\bar{t}b\bar{b}$ process in Part II. The measured normalized differential cross sections are compared to cross section predictions from different simulation approaches of the $t\bar{t}$ production process at NLO precision, and one simulation approach reweighted to the expected distribution of top quark momenta in NNLO simulations from Ref. [167]. Also the description of additional jet radiation in $t\bar{t}$ +jets events is probed and compared to simulation approaches of $t\bar{t}$ at NLO precision. Furthermore, the b jet multiplicity distribution is measured, giving additional insight in the description of the $t\bar{t}b\bar{b}$ process as a subset of the $t\bar{t}$ +jets process.

In Section 10.1, first, the available simulation approaches for $t\bar{t}$ +jets production are briefly reviewed. In Section 10.2, the setup of the $t\bar{t}$ +jets measurements is summarized and related to the measurements of $t\bar{t}b\bar{b}$ from Part II. The observables for which a normalized differential cross section measurements are performed are introduced in Section 10.3. In Chapter 11, the results of the measurements are described and interpreted.

10.1 Modeling of $t\bar{t}$ +jets events

For measurements performed in the CMS Collaboration, the usual approach during Run 2 was to estimate the contributions of $t\bar{t}$ production with generator setups modeling $t\bar{t}$ production at NLO precision in the ME, interfaced with a PS. Two examples are the PP8 $t\bar{t}$ 5FS and PH7 $t\bar{t}$ 5FS simulation approaches already studied in the context of $t\bar{t}b\bar{b}$ (see Section 8.1). Analog to the discussion of $t\bar{t}b\bar{b}$ modeling with $t\bar{t}$ NLO simulation approaches, the description of $t\bar{t}$ +jets production relies to a large degree on the description of additional radiation by the PS. As discussed in Section 7.2, this simulation approach describes the $gg/q\bar{q} \rightarrow t\bar{t}g$ process at LO precision on the ME-level, which corresponds to the description of $t\bar{t}$ +1 jet at LO precision. For additional jet radiation the PS is necessary, e.g.

for the description of the gluon splitting $g \rightarrow q\bar{q}/gg$, potentially yielding $t\bar{t}+2$ jets. Additional jet radiation has to be described exclusively by additional gluon radiation in the PS simulation. Consequently, the description of the additional jets mostly relies on the PS with leading-log precision, and is only available at LO precision for one additional jet.

The AMCP8 $t\bar{t}+\text{jets}$ FFX 5FS simulation approach, already discussed in Section 7.2, merges separate simulated samples of $t\bar{t}+0, 1, 2$ jets production at the ME-level based on the number of resolved additional partons which are defined based on a merging scale Q . Hence, the additional jet radiation is only described at the ME-level at larger momenta, potentially providing a more accurate description of additional jet radiation in that kinematic regime.

In $t\bar{t}+\text{jets}$ events with at least two additional jets, these jets can originate from different parts of the process. For example, a $g \rightarrow gg$ splitting in the initial state, described by the PS, could yield one jet radiation, and the additional gluon in the $t\bar{t}g$ process could yield another jet radiation. This implies a smaller angular correlation of additional jet radiation in $t\bar{t}+\text{jets}$ events compared to $t\bar{t}b\bar{b}$ events, where the dominant production process for the additional $b\bar{b}$ pair is from gluon splitting in final state radiation [137]. As shown in Ref. [168], the angular separation of two additional jets in $t\bar{t}+\text{jets}$ events contains a large fraction of dijet pairs with low opening angle ΔR , attributed more dominantly to gluon splitting effects, and a large contribution at larger angles, peaking at $\Delta R = \pi$, attributed more dominantly to two independent radiation processes. The description of this observable will also be probed in this measurement.

10.1.1 Mismodeling of the top quark momentum

Previous measurements of the CMS Collaboration, e.g. in Ref. [169], show that the momentum of the top quark is not accurately modeled in $t\bar{t}$ events simulated at NLO precision in the ME calculation. Ref. [169] also shows that with simulations and calculations of $t\bar{t}$ production at higher orders of perturbation theory, the top quark momentum is modeled more accurately and agrees well with the measurement. The corresponding result of Ref. [169] is shown in Figure 10.1. In this figure, the measurement of the top quark p_T in $t\bar{t}$ events is compared to the PP8 $t\bar{t}$ 5FS model that is also used in this thesis, and differential $t\bar{t}$ calculations of beyond-NLO precision (the details of these models can be found in Section 9.4 of Ref. [169]). The trend of the PP8 $t\bar{t}$ 5FS model to predict, on average, larger p_T for the partonic top quarks is not observed for the beyond-NLO models and the predictions agree well with the measurement. One of the beyond-NLO modeling approaches probed in Ref. [169] is a prediction with full NNLO precision in QCD interfaced with a PS and an appropriate pdf set. The ME calculations use the MiNNLOPS method [170–172] to reach full NNLO precision. This model is a promising candidate for future modeling of $t\bar{t}$ and $t\bar{t}+\text{jets}$ processes. The description of the observables measured in this thesis (both the $t\bar{t}b\bar{b}$ and $t\bar{t}+\text{jets}$ observables) can be compared against predictions from this NNLO model in future works to validate its performance also for $t\bar{t}$ production with additional jet and b jet radiation.

For the interpretation of the results obtained in this part of the thesis, the PP8 $t\bar{t}$ 5FS model is reweighted in order to gauge the effect of improved top quark p_T modeling without explicitly comparing to beyond-NLO simulation approaches which would be beyond the scope of this study presented in this thesis. The reweighting of the top quark p_T description from NLO to NNLO is based on calculations in Ref. [167]. The NNLO/NLO-ratio of the partonic top quark p_T is parameterized as

$$r_{\text{NNLO/NLO}}[p_T] = 0.103 \cdot e^{-11.8 \cdot (p_T/\text{TeV})} - 0.134 \cdot (p_T/\text{TeV}) + 0.973. \quad (10.1)$$

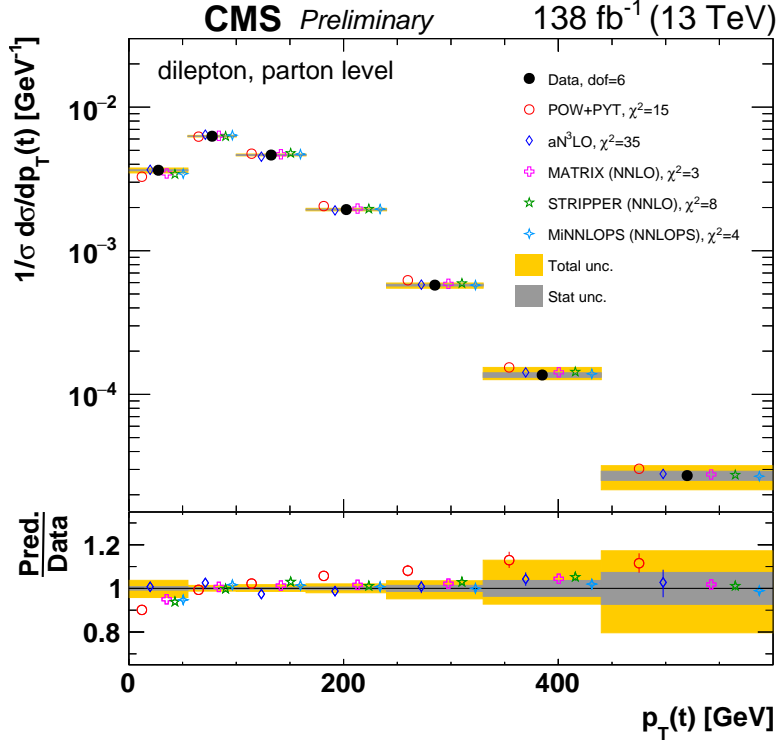


Figure 10.1: Normalized differential $t\bar{t}$ production cross section as a function of the partonic top quark p_T at the parton level. The measured cross sections are shown as filled circles with grey and yellow bands indicating the statistical and total uncertainties, respectively. The cross sections are compared to predictions corresponding to the PP8 $t\bar{t}$ 5FS model (POW+PYT) and simulation approaches with beyond-NLO precision. From Ref. [169].

The $t\bar{t}$ events obtained from the PP8 $t\bar{t}$ 5FS simulation are reweighted using both top quarks on the parton level via

$$w_{\text{NNLO/NLO}} = \sqrt{r[p_T(t)] \cdot r[p_T(\bar{t})]}. \quad (10.2)$$

This reweighting procedure is only used for the interpretation of results and is not considered in the measurement itself.

10.2 Setup of the $t\bar{t}$ +jets measurement

In Part II, $t\bar{t}$ production with additional b jet radiation has been explicitly studied. The focus of that measurement was the overall description of $t\bar{t}b\bar{b}$ events in simulation, and explicitly the focus on observables related to b jet radiation. In this chapter, the measurement is extended to $t\bar{t}$ production with additional jet radiation of any flavor ($t\bar{t}$ +jets), i.e. a more inclusive phase space.

The strategy of the measurement of the $t\bar{t}$ +jets process is equivalent to the measurement of the $t\bar{t}b\bar{b}$ process. Normalized differential cross sections of the $t\bar{t}$ +jets process are measured, using the same strategy as described in Section 9.1. The object definitions on the generator and detector level correspond to what has already been described in Sections 8.2 and 8.3. Two fiducial phase space regions are defined for the measurement of the $t\bar{t}$ +jets process, again based exclusively on the particle-level information. One

10 Introduction

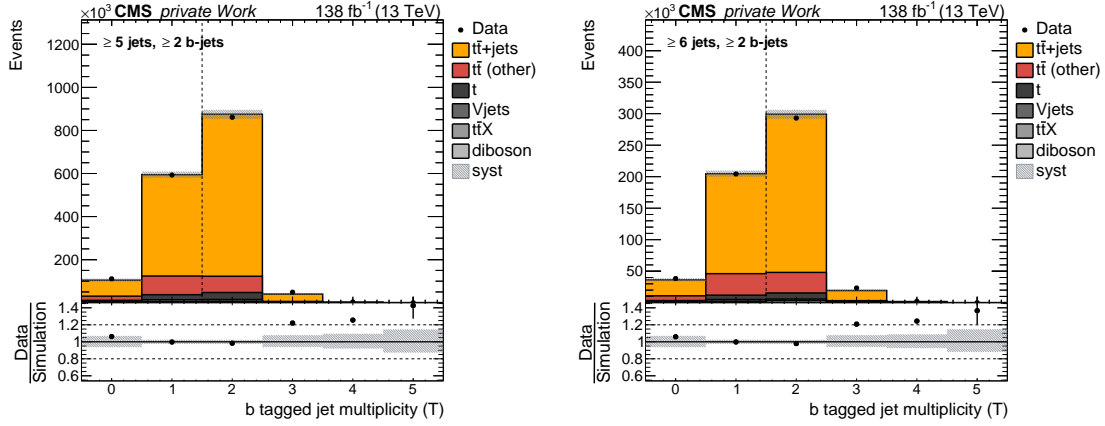


Figure 10.2: **b jet multiplicity at the tight b tagging WP in the 5j2b (left) and 6j2b (right) measurement regions.** The measurement regions are defined via the medium b-tagging WP. Shown are the contributions of all processes to the detector-level phase space regions as a stack of histograms. The $t\bar{t}$ +jets and $t\bar{t}$ (other) contributions are estimated from the PP8 $t\bar{t}$ 5FS simulation. Data events are shown as black dots. The lower panel shows the ratio of data to the expectations from simulated events. The vertical dashed line indicates the ancillary regions used for the measurements of the $t\bar{t}$ +jets process. For visualization, the contributions from simulation have been scaled by a common factor to match the yield in data. The shaded bands include all a-priori uncertainties described in Section 8.7. Only effects on the shape of the distributions are considered.

generator-level phase space, 5j2b, requires at least five jets, of which at least two are b jets. With this selection, events with a $t\bar{t}$ pair and at least one jet are selected. A second generator-level phase space, 6j2b, requires at least six jets, of which at least two are b jets. With this selection, similarly, events with a $t\bar{t}$ pair and at least two jets are selected. This procedure is equivalent to what has been employed for the identification of $t\bar{t}b\bar{b}$ with the 5j3b and 6j4b phase space regions, where one or two b jets in addition to the $t\bar{t}$ system are required. Here, the same is repeated, but agnostic towards the flavor of the additional jet radiation. The modifications of signal phase space regions are also reflected in the event selections for the extraction of the fiducial cross sections. Events are selected by requiring ≥ 5 (≥ 6) jets and ≥ 2 b tagged jets (at the medium WP) for the measurements of the 5j2b (6j2b) phase space regions.

In the $t\bar{t}$ +jets measurements, the PP8 $t\bar{t}$ 5FS simulation is used as the nominal signal model. This also includes the simulation of $t\bar{t}$ events that are not part of the fiducial phase space regions, which are treated similar to the OOA process in the $t\bar{t}b\bar{b}$ measurement (see Section 8.6). These events are referred to as $t\bar{t}$ (other) and for example encompass $t\bar{t}$ events with more or fewer than one fiducial electron or muon, or fewer jets or b jets on generator level than required by the fiducial phase space selections.

Similar to Section 8.5, an ancillary variable is defined, here also the number of b jets at the tight b tagging working point. The event selections are divided into two ancillary regions, one with ≤ 1 tight b jets, and one with ≥ 2 tight b jets. The distributions of the tight b jet multiplicity after the two aforementioned event selections are shown in Figure 10.2. As exactly two b jets are expected from the signal process, the first ancillary region is a bit more enriched in the background processes, to give an additional handle on their contribution. Due to the dominance of the signal process, however, this effect is small and does not add as much value to the measurement as the procedure employed in the $t\bar{t}b\bar{b}$ measurement. In the bins with ≥ 3 b tagged jets the majority of the contribution is expected

Table 10.1: Fractions of $t\bar{t}$ +jets, $t\bar{t}$ (other) and other background processes to the two measurement regions, separated by ancillary region. All fractions are given in %. Estimated from the PP8 $t\bar{t}$ 5FS simulation. The uncertainties on these values from a limited sample size are less than 1% and are hence omitted.

Event selection	5j2b		6j2b	
Anc. region	≤ 1 b	≥ 2 b	≤ 1 b	≥ 2 b
$t\bar{t}$ +jets	78	86	76	84
$t\bar{t}$ (other)	15	8	17	11
Other backgrounds	7	6	7	5

to be from $t\bar{t}B$ events. These control distributions already show a clear mismodeling of the fraction of $t\bar{t}B$ events in the $t\bar{t}$ +jets phase space regions, as was discussed in detail in Section 9.2, and will be discussed again in the context of the $t\bar{t}$ +jets measurements in Section 11.2. In Table 10.1, the fraction of $t\bar{t}$ +jets, $t\bar{t}$ (other), and background processes contributing to the measurement regions are summarized, and separated in the two ancillary regions.

The systematic uncertainties as described for the $t\bar{t}b\bar{b}$ measurement (see Section 8.7) are also applied for the measurements of the $t\bar{t}$ +jets process. The modeling uncertainties which are indicated to be decorrelated between the signal process and the OOA process in Section 8.7 are similarly decorrelated between the $t\bar{t}$ +jets signal and the $t\bar{t}$ (other) process. As the separation in $t\bar{t}$ +light, $t\bar{t}C$, and $t\bar{t}B$ processes is no longer relevant for the $t\bar{t}$ +jets measurements, the uncertainties applied only to the $t\bar{t}$ +light and $t\bar{t}C$ processes are not explicitly considered here.

10.3 Definition of observables

A range of observables targeting different aspects of $t\bar{t}$ +jets production is measured in the 5j2b and 6j2b phase space regions. In both phase space regions, the scalar sum of jet p_T (H_T^{jets}), the jet multiplicity (N_{jets}), and the b jet multiplicity (N_b) are measured. These event observables quantify the overall quality of the $t\bar{t}$ +jets simulation. With the N_b observables also the fraction of $t\bar{t}b\bar{b}$ events in the fiducial $t\bar{t}$ +jets phase space regions can be extracted.

As discussed in Section 10.1.1, the top quark momentum in $t\bar{t}$ events is not described well in $t\bar{t}$ simulation approaches using ME calculations at NLO accuracy in the perturbative ME calculation. In order to access the top quarks, a particle-level reconstruction is employed, referred to as pseudo top quark reconstruction. The reconstruction algorithm is a simplified approach compared to discussions in Ref. [173]. The reconstruction algorithm is described in the following. On both generator-level and detector-level, one b(-tagged) jet and two light(-tagged) jets (i.e. non-b(-tagged) jets) are combined to a hadronic top quark candidate. This aims at mimicking the decay of the top quark, $t \rightarrow b(W \rightarrow q\bar{q})$, in cases where the W boson decays into a pair of quarks (referred to as hadronic top). For each hadronic top quark candidate (i.e. each trijet combination), the invariant mass of the three jets m_{3j} , representing the top quark, and the invariant mass of only the two light jets m_{2j} , representing the W boson, are calculated. The trijet combination with the smallest χ_t^2 value

$$\chi_t^2 = (m_{3j} - m_t)^2 + (m_{2j} - m_W)^2, \quad (10.3)$$

is chosen to represent the pseudo top quark. The parameters $m_t = 172.5 \text{ GeV}$ and $m_W = 80.4 \text{ GeV}$ correspond to the assumed top quark and W boson masses. The transverse momentum $p_T(t_{\text{had}})$ of the pseudo top quark is measured in order to access the top quark momentum.

Similarly, the top quark for which the W boson from the $t \rightarrow Wb$ decay decays into a charged lepton and a neutrino ($W \rightarrow \ell\nu$) can be reconstructed from a combination of a b(-tagged) jet, a charged lepton, and a neutrino (referred to as leptonic top quark). Neutrinos are not reconstructed on the detector-level as they are not detected, and are only accessible via the missing transverse momentum (see Section 3.4). As the longitudinal component and the composition of the missing energy are not known (it could originate from multiple neutrinos or energy mismeasurements), the reconstruction of the leptonic top quark exhibits larger migration effects (of that top quark component) between detector- and generator-level. The identification of the charged lepton is, however, a lot more precise and has only little ambiguity in the assignment of the correct object on detector- and generator-level. In this part of the thesis, only the hadronic top quark is reconstructed and analyzed. As a cross-check, corresponding results of the leptonic pseudo top quark ($p_T(t_{\text{lep}})$) are shown in Appendix B.5. These results do not differ significantly from the hadronic top quark results. A proper measurement of this observable would require additional uncertainties related to the reconstruction of the missing transverse momentum to be considered.

For a more accurate quantification of the top quark momentum mismodeling effect in $t\bar{t}$ +jets events, a definition of the top quark at the parton level would be necessary, in order to access its momentum. Accordingly, suitable observables would have to be constructed on the reconstruction level that correspond to the partonic top quark momentum. This is not possible with simple kinematic reconstruction methods and is therefore not explored in this initial study. In Appendix B.6, the migration matrices and detector-level distributions are shown for the partonic top quark p_T , using the pseudo top reconstruction to model the observable on the detector level. This takes into account the charge of the lepton to assign either the hadronic or leptonic pseudo top quark candidate to the partonic top quark candidate on the detector level. From these distributions, it is apparent that an unbiased measurement is not possible, as the correspondence of generator and detector-level observable is small.

One additional observable is measured in the 6j2b phase space, targeting the radiation of jets outside of the $t\bar{t}$ system. The pseudo top quark reconstruction is applied for the hadronic and leptonic top quarks, and the remaining jets (referred to as additional jets) are identified. For the additional jets, the angular distance between the two jets leading in p_T is probed, $\Delta R(jj^{\text{add}})$. This observable aims at probing the angular correlation of additional jet radiation, as discussed in Section 10.1.

11 Measurement of the $t\bar{t}+\text{jets}$ process

Analog to the $t\bar{t}b\bar{b}$ measurements in Part II, normalized differential cross section measurements are performed for the observables introduced in the previous section. This follows the same strategy as introduced in Section 4.2 and using the same systematic uncertainty model as introduced in Section 8.7 for the $t\bar{t}b\bar{b}$ measurement.

In Figure 11.1, the distribution of events for the $p_T(t_{\text{had}})$ and H_T^{jets} observables in the 5j2b phase space region are shown after detector-level selection, before the fit to data, where the $t\bar{t}+\text{jets}$ process is separated into the generator-level bins. The migration matrices of all observables are shown in Appendix B.1. The H_T^{jets} observable exhibits a high level of correspondence between detector and generator level, as expected (see Section 9.1). The $p_T(t_{\text{had}})$ observable exhibits larger migrations as the reconstruction of the observable on detector and generator level is more prone to differences, e.g. different combinations of three jets could be chosen as the pseudo top quark, leading to larger migrations.

For each normalized differential cross section measurement, the correlations of the POIs, i.e. the fiducial cross section and the differential fractions, are shown in Appendix B.3.

11.1 Inclusive cross section results

The fiducial cross sections in the 5j2b and 6j2b phase space regions are representatively shown for the measurements of the H_T^{jets} observable in Figure 11.2. The distributions of the H_T^{jets} observable after the fit to data in both phase space regions are shown in Figure 11.3. The distributions of all other observables are shown in Appendix B.2. The H_T^{jets} observable is chosen as the representative observable for the fiducial cross section as it exhibits the best correspondence between generator and detector level and hence allows for a larger number of bins in the measurement, increasing the measurement precision. The cross sections are measured with a precision of around 2% and 5% in the 5j2b and 6j2b phase space regions, owing to the statistically rich measurement regions. In Table 11.1, the contributions to the measurement uncertainties are shown separated into groups of uncertainties. The statistical uncertainty is negligible ($<0.2\%$), while uncertainties such as the luminosity, jet energy calibrations, b tagging calibrations, and the variation of the ME-PS matching scale (h_{damp}) have the largest impact on the measurements.

The measurement is compared to the three modeling approaches that have already been probed for $t\bar{t}b\bar{b}$ (see Section 8.1) that describe the full $t\bar{t}$ phase space, namely PP8 $t\bar{t}$ 5FS,

11 Measurement of the $t\bar{t}$ +jets process

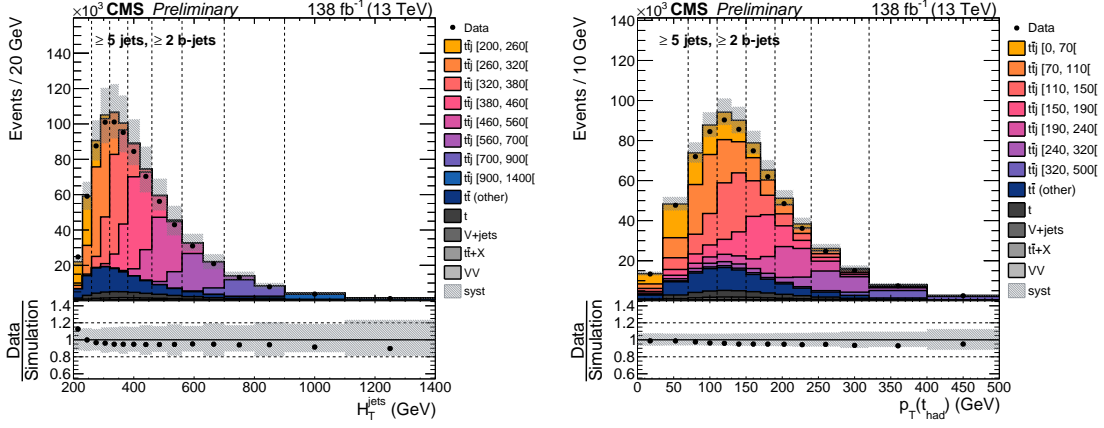


Figure 11.1: The H_T^{jets} observable (left) and $p_T(t_{\text{had}})$ observable (right) in the 5j2b detector-level phase space region. The upper plots show the contributions of all processes to the detector-level phase space regions as a stack of histograms. The contributions from the signal model are separated based on the pre-defined generator-level bins indicated by different colors. Data events are shown as black dots. The lower panel shows the ratio of data w.r.t. the simulated events. Uncertainties on the simulated events from systematic uncertainty sources are indicated as gray bands.

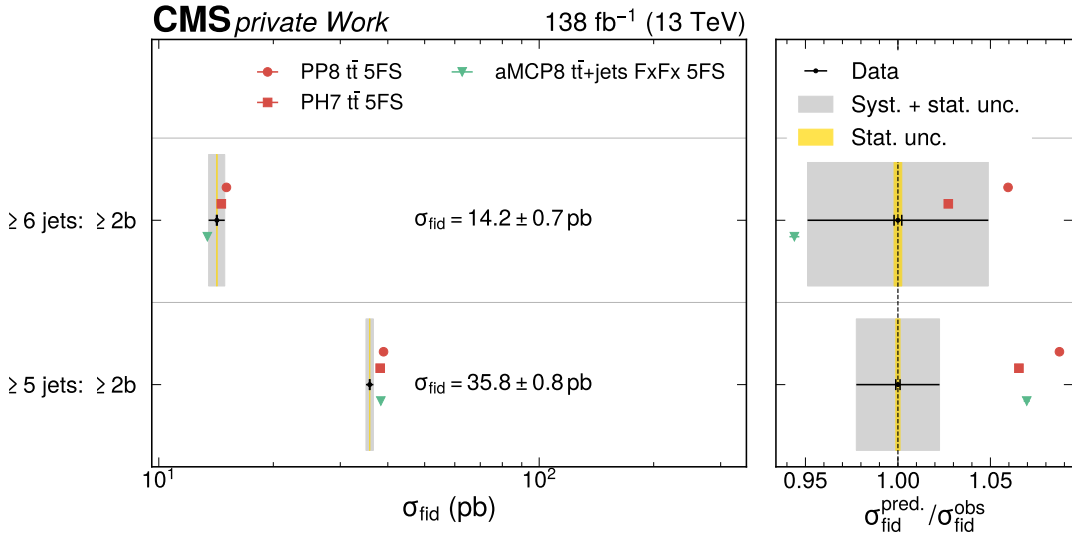


Figure 11.2: Fiducial cross sections of $t\bar{t}$ +jets measured in the 5j2b and 6j2b phase space regions. The measured cross sections in data are indicated with black dots, with inner (outer) vertical bars indicating the systematic (total) uncertainties, also represented as gray (yellow) bands. The cross section predictions from different $t\bar{t}$ modeling approaches as introduced in Section 8.1 are shown as colored symbols with different shapes. The panel on the right shows the ratio between the predicted and measured cross sections.

PH7 $t\bar{t}$ 5FS, and AMCP8 $t\bar{t}$ +jets FXXF 5FS. The fiducial cross section of these three models are obtained from the predicted fraction of fiducial $t\bar{t}$ +jets events in the two phase space regions, all assuming an inclusive $t\bar{t}$ cross section of $\sigma(t\bar{t}) = 833.7$ pb based on NNLO+NNLL calculations [59, 154]. In the 5j2b phase space, the three modeling approaches are shown to overestimate the fiducial cross section by $>5\%$, while the predic-

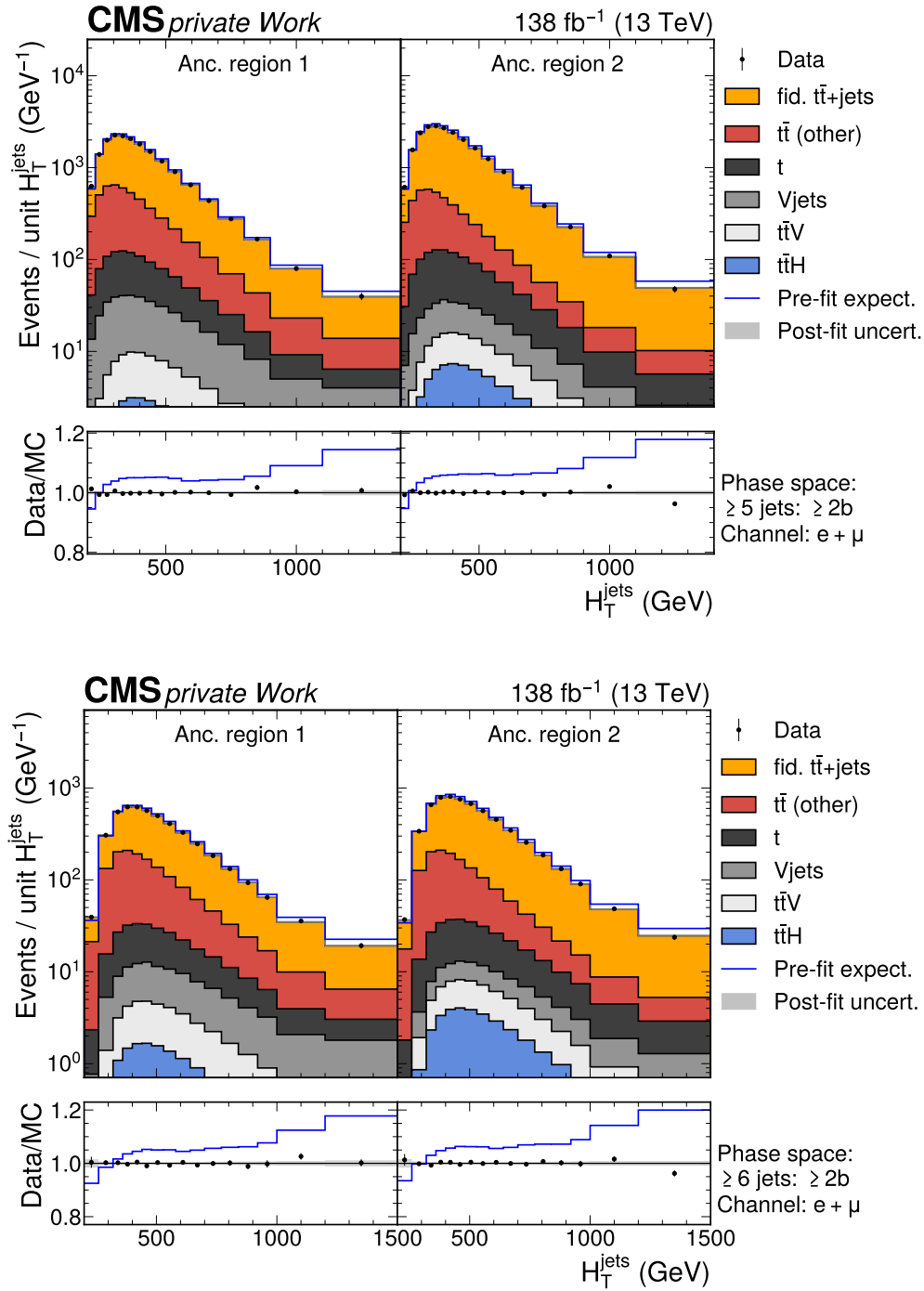


Figure 11.3: **Distributions of H_T^{jets} in the 5j2b and 6j2b phase space regions after the fit to data.** The contributions of all processes to the detector-level phase space regions after the fit to data are shown as a stack of histograms. The distributions are shown separately for each ancillary region, but are combined across all eras and the lepton channels. The blue line indicates the sum of all processes before the fit to data. The lower panel shows the ratio of data to the processes after the fit to data. The shaded bands include all uncertainties described in Section 8.7 after profiling the nuisance parameters in the fit, estimated by sampling the predicted yields from the fit covariance matrix.

Table 11.1: **Contributions of the sources of uncertainty considered to the total uncertainty on the fiducial cross section measurements.** For each group, the impact of the corresponding nuisance parameters on the fiducial cross section are combined, taking into account their correlations in the maximum likelihood fit. The numbers show the relative uncertainty on the fiducial cross section, given in %. The statistical uncertainty is obtained as the difference, in quadrature, between the total uncertainty and the sum of all systematic uncertainties.

Uncertainty source	5j2b	6j2b
Luminosity	1.4	1.7
Lepton and trigger	0.7	0.6
JES, JER	0.8	2.2
b tagging	1.2	2.3
Pileup	0.3	0.2
PDF	0.3	2.8
μ_R and μ_F scales	0.3	0.5
PS modelling	0.2	0.8
h_{damp}	0.7	1.5
MC statistical	0.4	1.0
Total systematic uncertainty	2.2	4.9
Statistical uncertainty	0.1	0.2
Total uncertainty	2.2	4.9

tions are compatible with the measurement in the 6j2b phase space. Relating the measured fiducial cross section values to the inclusive cross section of $t\bar{t}$ yields fractions of

$$\sigma(t\bar{t}+\text{jets}_{5j2b})/\sigma(t\bar{t}) = (4.3 \pm 0.1)\%, \quad \text{and} \quad (11.1)$$

$$\sigma(t\bar{t}+\text{jets}_{6j2b})/\sigma(t\bar{t}) = (1.7 \pm 0.1)\%, \quad (11.2)$$

only considering the measurement uncertainties. The measurement in the 5j2b phase space suggests that the corresponding fraction is overestimated from the NLO $t\bar{t}$ simulation approaches.

11.2 Differential cross section results

The measurement of the normalized differential cross sections of $t\bar{t}$ +jets production are summarized in the following. The sources of uncertainty of the differential measurements are shown in Figure 11.4 as an example for measurement of the H_T^{jets} observable in the 5j2b phase space region. The precision of the normalized differential cross sections is limited to approximately equal parts by data statistics and systematic uncertainties. Among the systematic uncertainties, the jet energy calibration and b tagging calibration have the largest impact on the results. The total uncertainties of the normalized differential cross sections are, in most cases, below 5%.

In Figure 11.5, the measurements of the N_{jets} and N_b observables are shown. In both fiducial phase space regions, the probed modeling approaches do not describe either observable well, all showing trends to underpredict the high jet and b jet multiplicity regions. In the measurements of N_{jets} , the trend is the largest for the AMCP8 $t\bar{t}$ +jets FFX 5FS simulation approach, which predicts up to 50% smaller fractions of events at high jet

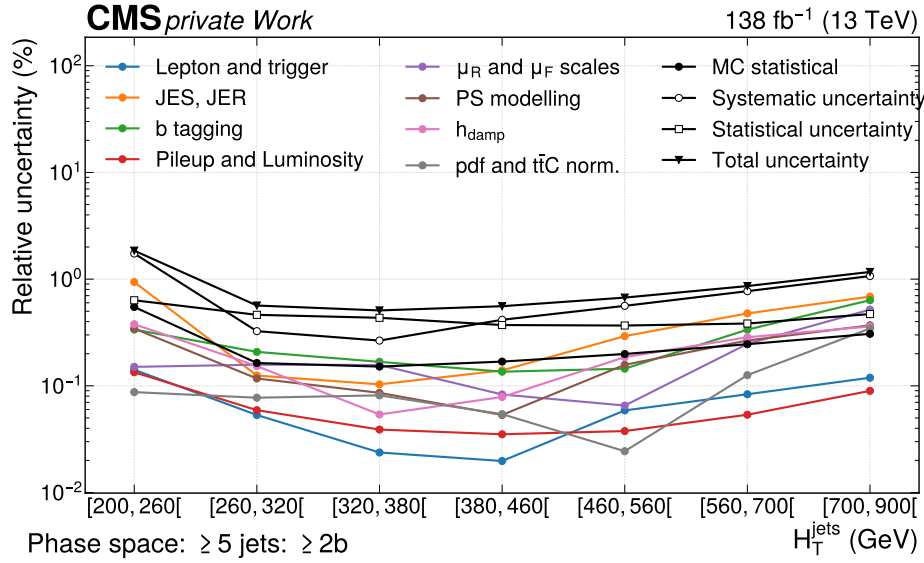


Figure 11.4: Effect of sources of uncertainties on the measurement of the normalized differential cross section of the H_T^{jets} in the 5j2b phase space region. The impacts of the nuisance parameters associated with the displayed uncertainty groups are obtained by combining their impacts taking into account their correlation in the fit.

multiplicity compared to the measurement. This is contrary to the expectation towards the AMCP8 $t\bar{t}$ +jets FFX 5FS modeling, which should show a better description of at least the five and six jet bins compared to the other two modeling approaches, as these additional jet radiation processes are in part simulated at the ME-level. This implies that this $t\bar{t}$ +jets model requires an improved tuning of its modeling parameters to better describe the jet multiplicity distribution (and by extension other distributions). The PP8 $t\bar{t}$ 5FS simulation approach, used as the nominal background and signal model for the $t\bar{t}$ process by the CMS Collaboration during Run 2, is able to describe the lower jet multiplicities well but starts to deviate from the measurement at around eight jets. These regions of large jet multiplicity are relevant for the background estimation for example in measurements of $t\bar{t}t\bar{t}$ production. This measurement suggests that the background from $t\bar{t}$ production is underestimated in these measurements. In Appendix B.4, variations of the PS scales, the ME scales (μ_R and μ_F), the ME-PS matching scale, and the reweighting of the top quark p_T (see Section 10.1.1) are probed for the PP8 $t\bar{t}$ 5FS simulation approach. These variations show that a decrease of either ME or PS scales, or an increase of the h_{damp} scale provides a better description of the N_{jets} observable than the nominal scale choices of the PP8 $t\bar{t}$ 5FS model. The reweighting of the top quark momenta to NNLO does not improve the description of the observable.

In the measurements of N_b , all NLO $t\bar{t}$ simulation approaches significantly underpredict the fraction of fiducial events with ≥ 3 b jets, while slightly overpredicting the fraction of fiducial events with two b jets. As the fiducial definitions of the $t\bar{t}$ +jets process are equivalent to the fiducial definitions of the $t\bar{t}b\bar{b}$ process, minus the b jet multiplicity requirements, this measurement of N_b quantifies the fraction of $t\bar{t}b\bar{b}$ events in the fiducial phase space of $t\bar{t}$ +jets. In the 5j2b phase space region, the N_b bin with ≥ 3 b jets corresponds to the 5j3b fiducial phase space defined in Section 8.2. All three NLO $t\bar{t}$ simulation approaches predict around 30% lower fractions of 5j3b events compared to the

11 Measurement of the $t\bar{t}$ +jets process

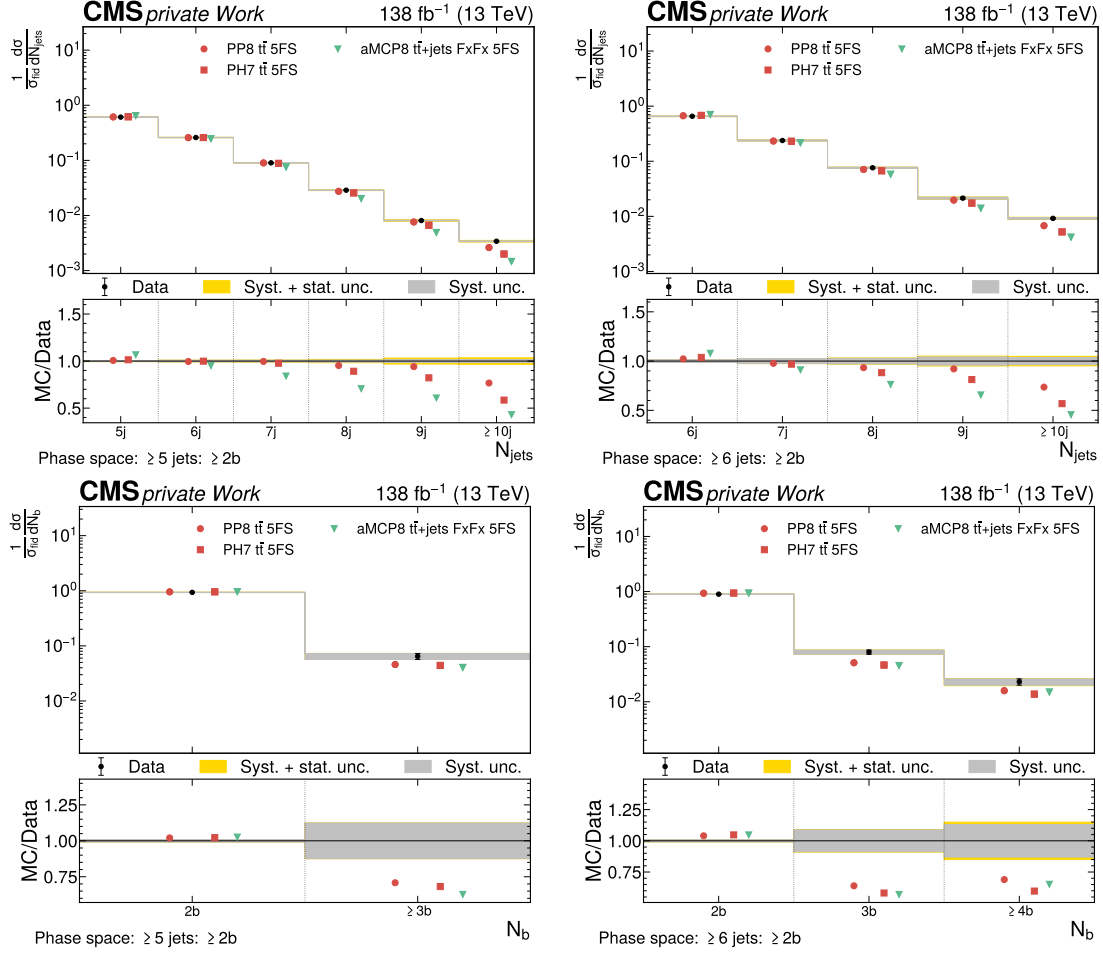


Figure 11.5: Predicted and observed normalized differential cross sections of the N_{jets} (top) and N_{b} (bottom) observables in the 5j2b (left) and 6j4b (right) phase space regions. The measured cross sections in data are indicated with black dots, with inner (outer) vertical bars indicating the systematic (total) uncertainties, also represented as gray (yellow) bands. The cross section predictions from different $t\bar{t}$ modeling approaches as introduced in Section 8.1 are shown as colored symbols with different shapes. Where the observable can exceed the visible range, the last bin contains the overflow.

measurement. Explicitly, the measurement yields

$$f_{\geq 3\text{b}}^{\text{obs.}} = \sigma(t\bar{t}b\bar{b}_{5j3b})/\sigma(t\bar{t}+\text{jets}_{5j2b}) = (6.5 \pm 0.8)\%, \quad (11.3)$$

while with the PP8 $t\bar{t}$ 5FS simulation approach a value of $f_{\geq 3\text{b}}^{\text{PP8 } t\bar{t} \text{ 5FS}} = 4.6\%$ is predicted, corresponding to a relative fraction of

$$\mu_{\geq 3\text{b}} = f_{\geq 3\text{b}}^{\text{obs.}}/f_{\geq 3\text{b}}^{\text{PP8 } t\bar{t} \text{ 5FS}} = 1.41 \pm 0.17. \quad (11.4)$$

In the uncertainty on this value only the uncertainty of the measurement and not of the prediction is considered. This relative fraction is consistent with the measurement of the fiducial 5j3b cross section in Section 9.2. In the 6j2b phase space region, three b jet multiplicity bins are measured, containing two, three and at least four b jets. The last bin corresponds to the fiducial definition of the 6j4b phase space in Section 8.2. For this bin the measurement yields

$$f_{\geq 4\text{b}}^{\text{obs.}} = \sigma(t\bar{t}b\bar{b}_{6j4b})/\sigma(t\bar{t}+\text{jets}_{6j2b}) = (2.3 \pm 0.3)\%, \quad (11.5)$$

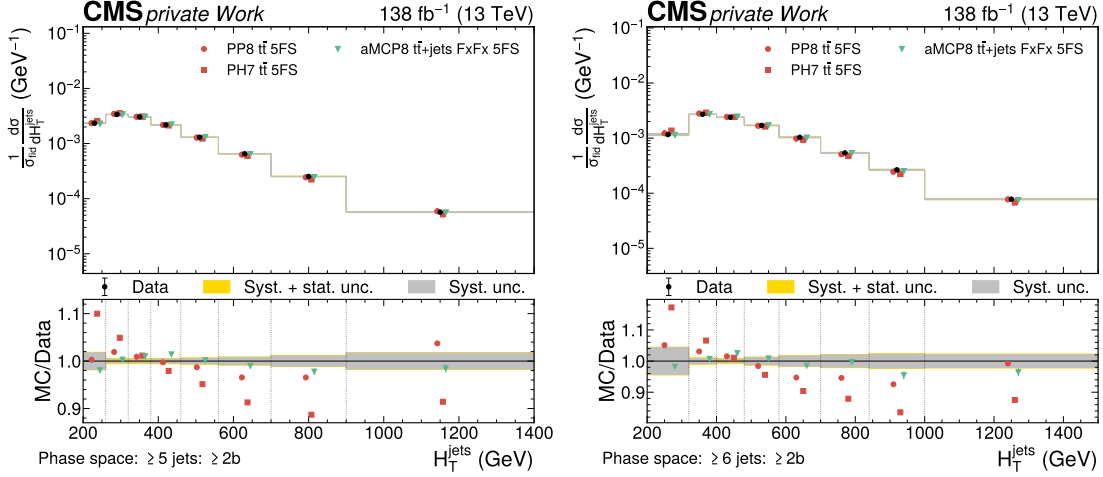


Figure 11.6: **Predicted and observed normalized differential cross sections of the H_T^{jets} observable in the 5j2b (left) and 6j4b (right) phase space regions.** The measured cross sections in data are indicated with black dots, with inner (outer) vertical bars indicating the systematic (total) uncertainties, also represented as gray (yellow) bands. The cross section predictions from different $t\bar{t}$ modeling approaches as introduced in Section 8.1 are shown as colored symbols with different shapes. Where the observable can exceed the visible range, the last bin contains the overflow.

while the PP8 $t\bar{t}$ 5FS simulation approach predicts a value of $f_{\geq 4b}^{\text{PP8 } t\bar{t} \text{ 5FS}} = 1.6\%$, corresponding to a relative fraction of

$$\mu_{\geq 4b} = f_{\geq 4b}^{\text{obs.}} / f_{\geq 4b}^{\text{PP8 } t\bar{t} \text{ 5FS}} = 1.44 \pm 0.19. \quad (11.6)$$

This value is also consistent with the measurement of the fiducial 6j4b cross section in Section 9.2.

This measurement can be compared to a previous measurement by the ATLAS Collaboration in Ref. [145], as discussed in Section 7.4.1. In Ref. [145], a measurement of the b jet multiplicity in a fiducial phase space with ≥ 2 jets is performed, showing similar levels of disagreement of NLO $t\bar{t}$ simulation approaches at larger b jet multiplicity (also around 40%). In that measurement, the uncertainty on the normalized differential cross section is of the order of 30% in the bins with ≥ 3 b jets, while in the measurements of this thesis uncertainties of around 15% are achieved. This increase in measurement precision makes the difference between prediction and measurement more significant, further confirming the mismodeling of the b jet radiation fraction in $t\bar{t}$ +jets simulation. As shown in Appendix B.4, among variations of the PS scales, the ME scales (μ_R and μ_F) and the ME-PS matching scales in the PP8 $t\bar{t}$ 5FS simulation approach, the variation of the amount of final state radiation from the PS shows the largest effect on the modeling of the N_b observable, but none of the tested variations are able to properly describe the b jet multiplicity. In NLO simulations of $t\bar{t}$, the description of the b jets outside the $t\bar{t}$ system, and by extension the b jet multiplicity distribution at ≥ 3 b jets are expected to be described by the PS. The results suggest that the tuning of the PS requires a readjustment in order to better describe the b jet multiplicity, and by extension the $t\bar{t}b\bar{b}$ fiducial cross sections.

In Figure 11.6, the measurement of the H_T^{jets} observable is shown for the 5j2b and 6j2b phase space regions. Similar trends are observed in both fiducial regions, where the PH7 $t\bar{t}$ 5FS simulation approach shows on average H_T^{jets} values significantly smaller than the measurement. This suggests that the HERWIG PS requires improved tuning to describe the momentum distribution of jets in $t\bar{t}$ events. Among the three probed modeling

11 Measurement of the $t\bar{t}$ +jets process

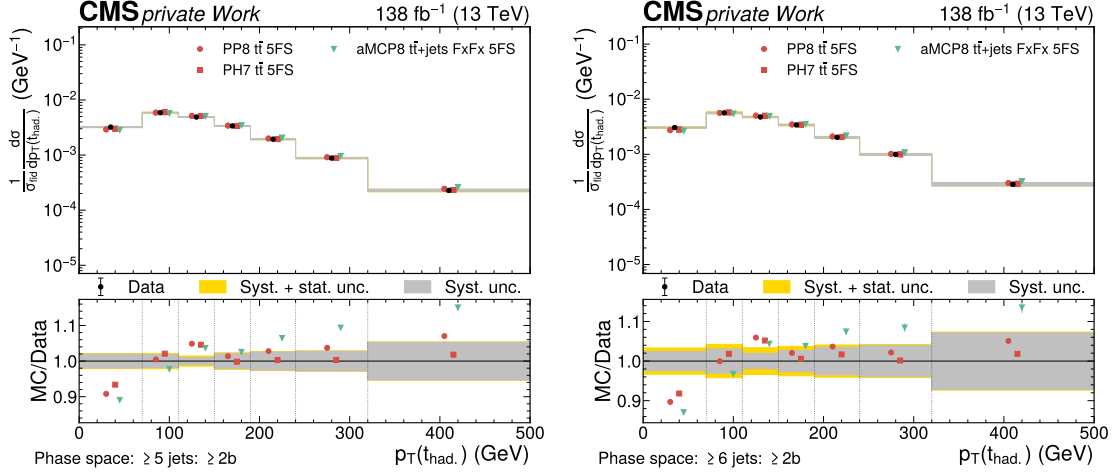


Figure 11.7: **Predicted and observed normalized differential cross sections of the $p_T(t_{\text{had}})$ observable in the 5j2b (left) and 6j4b (right) phase space regions.** The measured cross sections in data are indicated with black dots, with inner (outer) vertical bars indicating the systematic (total) uncertainties, also represented as gray (yellow) bands. The cross section predictions from different $t\bar{t}$ modeling approaches as introduced in Section 8.1 are shown as colored symbols with different shapes. Where the observable can exceed the visible range, the last bin contains the overflow.

approaches, the aMCP8 $t\bar{t}$ +jets FxFx 5FS simulation is able to describe the H_T^{jets} observable best, but still exhibits small trends towards smaller H_T^{jets} values than measured in data. Similar to the measurements in the fiducial $t\bar{t}b\bar{b}$ regions in Section 9.3, the PP8 $t\bar{t}$ 5FS simulation approach also predicts on average smaller H_T^{jets} values than measured in data, but does not deviate as much from the measurement as the PH7 $t\bar{t}$ 5FS model. Also for this observable, variations of the modeling parameters and a reweighting of the top quark p_T is performed and compared to the measurement (see Appendix B.4). The trend towards smaller values than predicted in data is mitigated to some degree via decreased ME or (to a lesser extent) PS scales, or (best) an increased h_{damp} scale. The reweighting of the top quark p_T does not improve the modeling of the H_T^{jets} observable and rather enhances the discrepancy with respect to the measurement. This suggests that the origin of the discrepancies of jet momentum distributions, which collimate in the description of the H_T^{jets} observable, is not due to the poor description of the top quark momentum, but can rather be associated with an insufficient tuning of the ME or PS.

To probe the top quark p_T , the measurements of the $p_T(t_{\text{had}})$ observable (the p_T of the pseudo top quark reconstructed on particle level) are shown in Figure 11.7 in both phase space regions. In all NLO $t\bar{t}$ modeling approaches probed, a trend towards higher $p_T(t_{\text{had}})$ values compared to the measurement is observed, the smallest deviations from the measurement are present in the PH7 $t\bar{t}$ 5FS model. The trend of the PP8 $t\bar{t}$ 5FS simulation approach is similar as in the measurement of the partonic top quark p_T from Ref. [169] in $t\bar{t}$ events, shown in Figure 10.1. For the PP8 $t\bar{t}$ 5FS simulation, again variations in the modeling parameters are tested as shown in Appendix B.4. The variations of ME and PS scale choices and the h_{damp} parameter only have small effects on the $p_T(t_{\text{had}})$ distribution. As expected, a larger difference is observed for the PP8 $t\bar{t}$ 5FS simulation reweighted to the NNLO partonic top quark p_T spectrum. The reweighted distribution generally agrees better with the measurement than the nominal description obtained with the NLO $t\bar{t}$ simulation, but still exhibits some residual differences.

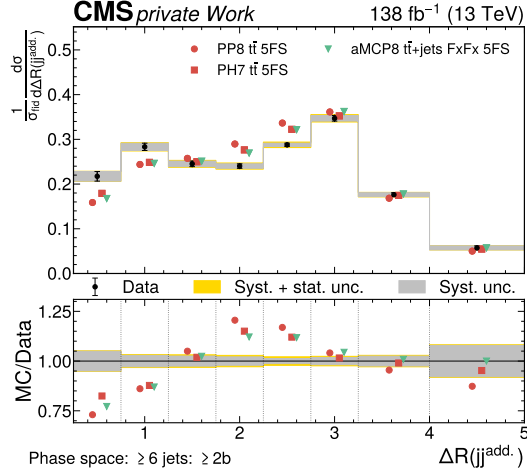


Figure 11.8: **Predicted and observed normalized differential cross sections of the $\Delta R(\text{jj}^{\text{add.}})$ observable in the 6j4b phase space region.** The measured cross sections in data are indicated with black dots, with inner (outer) vertical bars indicating the systematic (total) uncertainties, also represented as gray (yellow) bands. The cross section predictions from different $t\bar{t}$ modeling approaches as introduced in Section 8.1 are shown as colored symbols with different shapes. Where the observable can exceed the visible range, the last bin contains the overflow.

Finally, in Figure 11.8 the measurement of the $\Delta R(\text{jj}^{\text{add.}})$ observable in the 6j2b phase space is shown. This observable is, as $p_{\text{T}}(t_{\text{had}})$, only a proxy for the measurement of the angular distance of non- $t\bar{t}$ jets defined on the parton level. The measurement shows two peaks in the $\Delta R(\text{jj}^{\text{add.}})$ spectrum, one at small ΔR , which can be associated with collinear gluon splitting ($g \rightarrow q\bar{q}/gg$) in $t\bar{t} + \text{jets}$ events, and one peak around $\Delta R = \pi$, corresponding to back-to-back emission of the additional jet radiation attributed to different origins of the jet radiation (see Section 10.1). In the probed $t\bar{t}$ simulation approaches at NLO, the collinear region is significantly underpredicted, while the bulk of the distribution at moderate ΔR is overpredicted. This result hints towards a mismodeling of the angular correlation of additional jet radiation in the parton shower (PS) probed here, as the additional jets are predominantly modeled with the PS and not at the ME-level. Simulations of $t\bar{t} + \text{jets}$ at the ME-level with NLO precision are expected to provide more accurate modeling of this observable as discussed in Ref. [168]. The variations of ME and PS and h_{damp} scales do not have any noteworthy effect on the predicted distributions and are hence not shown.

Summary and Outlook

Precision measurements of the particles and interactions of the standard model are an active field of study in high-energy physics and at the LHC. In this thesis, the differential cross section measurement of the $t\bar{t}b\bar{b}$ process is presented. Normalized differential cross sections are measured as a function of 29 observables across four fiducial phase space regions. The measurements make use of pp collision events recorded at the CMS detector between 2016 and 2018 with either one electron or muon and at least five jets. The differential cross sections probe observables related to the b jets in the $t\bar{t}b\bar{b}$ system, as well as global observables describing the full event signatures. The four fiducial phase space regions probe different aspects of $t\bar{t}$ production with additional b jets. In the most inclusive phase space region, where at least one b jet in addition to the $t\bar{t}$ system is required, the fiducial cross section is measured with a precision of 6% and constitutes the most precise measurement of $t\bar{t}$ production in association with a b jet to date. More exclusive phase space regions, requiring additional b jet and light jet radiation, are measured with precisions of 9–17%. The limitations of these fiducial cross section measurements are mostly attributed to uncertainties in the modeling of the $t\bar{t}b\bar{b}$ signal simulation and b jet tagging and jet energy calibrations.

The results are compared to six different modeling approaches of $t\bar{t}b\bar{b}$. Some of these modeling approaches fully describe the $t\bar{t}b\bar{b}$ process at the ME-level at NLO accuracy, while some other approaches use a description of $t\bar{t}$ at the ME-level at NLO accuracy and obtain a description of $t\bar{t}b\bar{b}$ with the PS, where $g \rightarrow b\bar{b}$ splitting processes are modeled. These comparisons show that the probed generator setups and their chosen generator settings are not able to simultaneously describe all measured observables and the fiducial cross sections well. Large differences are seen between the predicted fiducial cross sections and the measurements, where most of the generator setups predict fiducial cross sections that are lower than the measurement, except for the PP8 $t\bar{t}b\bar{b}$ 4FS model which uses an ME simulation of $t\bar{t}b\bar{b}$. This generator setup is able to describe the fiducial cross section in the 5j3b phase space region well but is seen to overpredict the fiducial cross sections in the more exclusive phase space regions. An important observation is made in the measurement of the jet and b jet multiplicity observables, showing that the simulation approaches using a $t\bar{t}$ ME describe the b jet multiplicity, and to some degree also the jet multiplicity, more accurately than the simulation approaches using a $t\bar{t}b\bar{b}$ ME, i.e. tend to be more suitable for the description of the relative rate of $t\bar{t}b\bar{b}$ events with different jet and b jet multiplicities. At the same time, the angular separation of the two b jets clos-

Summary and Outlook

est to each other is described well with the generator setups using a $t\bar{t}b\bar{b}$ ME, while the other simulation approaches do not describe the observable comparably well. This can be traced back to potential mis-modeling in the PS settings as these simulation approaches rely on the PS for the simulation of these b jets.

Variations of the renormalization and factorization scale choices of the PP8 $t\bar{t}b\bar{b}$ 4FS model are tested and show that an increase of the renormalization and factorization scales could improve the description of some observables such as the jet multiplicity or the scalar p_T sum of all jets. However, simple variations of these two scales were not able to resolve all differences in the differential measurements and the fiducial cross sections. Especially the trend to overpredict the fiducial cross sections in the more exclusive phase space regions cannot be resolved with these scale variations.

In this thesis, also studies on $t\bar{t}$ production with additional jet radiation of any flavor are performed as an extension of the $t\bar{t}b\bar{b}$ measurements. Measurements are performed for the jet and b jet multiplicities, showing that for example the relative rate of $t\bar{t}$ events with and without additional b jets is modeled poorly with the probed generator setups. All three generator setups which describe the full $t\bar{t}$ phase space show that the fraction of events with additional b jet radiation is significantly underpredicted, but all of them also show that this mis-modeling is relatively homogeneous also for larger b jet multiplicities, confirming the results of the $t\bar{t}b\bar{b}$ measurements.

Measurements of the top quark momentum are performed with a particle-level-based reconstruction of top quarks, confirming that simulation approaches using a $t\bar{t}$ ME at NLO accuracy are not able to describe the momentum of top quarks well. The results are compared to the PP8 $t\bar{t}$ 5FS simulation approach in which the top quark momenta are reweighted to the expected top quark momentum distribution at NNLO. These show an improved description of the top quark momentum. The modeling of the top quark momentum has been probed in inclusive $t\bar{t}$ phase space regions, but has not been probed in $t\bar{t}$ events which explicitly require additional jet radiation.

For future measurements at the CMS and ATLAS experiments, the choices made for the modeling of the $t\bar{t}b\bar{b}$ process will have to be reevaluated. Important feedback from the experts on $t\bar{t}b\bar{b}$ modeling is expected based on the results presented in this thesis. For example, alternative choices of modeling parameters, such as the renormalization and factorization scales, will have to be tested against the measurements provided in this thesis. More detailed studies on the modeling choices will have to be performed in order to update and implement the recommendations for data analysis. Future measurements of the $t\bar{t}H$ process or the $t\bar{t}t\bar{t}$ process will continue to rely on accurate modeling of the $t\bar{t}b\bar{b}$ process and will greatly benefit from updated modeling prescriptions, with a better estimate of the contributions of the $t\bar{t}b\bar{b}$ process to the measurement regions.

Similar measurements, as have been performed for the $t\bar{t}b\bar{b}$ process in this thesis, should, in the future, be performed also for $t\bar{t}$ production in association with charm jets ($t\bar{t}C$) and the $t\bar{t}b\bar{b}$ process where the two b jets from $g \rightarrow b\bar{b}$ splitting are close enough to be clustered into one large-radius jet. The dedicated measurement of the $t\bar{t}C$ process will give additional insight into the background contributions for measurements of $t\bar{t}H$ where the Higgs boson decays into a pair of charm quarks ($t\bar{t}H(c\bar{c})$). Measurements of the $t\bar{t}H(c\bar{c})$ process will be able to constrain, or even discover, the coupling of the Higgs boson to the charm quark, which is one of the major milestones expected in the physics program at the LHC in the coming years. Such a measurement would rely on an accurate background description of $t\bar{t}C$ production, which has as of yet not been probed differentially. With the advances in jet flavor tagging, e.g. via tagging algorithms using graph networks, the accurate identification of c jets and their differentiation from b jets is possible, giving a

good opportunity for measuring the $t\bar{t}C$ process. Similarly, the advances in jet flavor tagging of large-radius jets, where, for example, the decay of the Higgs boson to a pair of b or c quarks is clustered in a single jet, make the measurements of $t\bar{t}H(b\bar{b})$ and $t\bar{t}H(c\bar{c})$ with these high- p_T signatures more promising than was possible before. For successful measurements of these large-radius jet signatures in $t\bar{t}H$, a good understanding of the background from $t\bar{t}b\bar{b}$ and $t\bar{t}C$ with similar signatures is necessary, and has also not yet been probed explicitly.

To summarize, the measurements presented in this thesis provide valuable input for the physics program at the LHC Run 3, which started in 2022, and beyond, where the observations of the $t\bar{t}H(b\bar{b})$ process and the coupling of the Higgs boson to the charm quark are expected, both benefiting from these results.

Appendix

A Supplemental material for the $t\bar{t}b\bar{b}$ measurement

A.1 Migration matrices

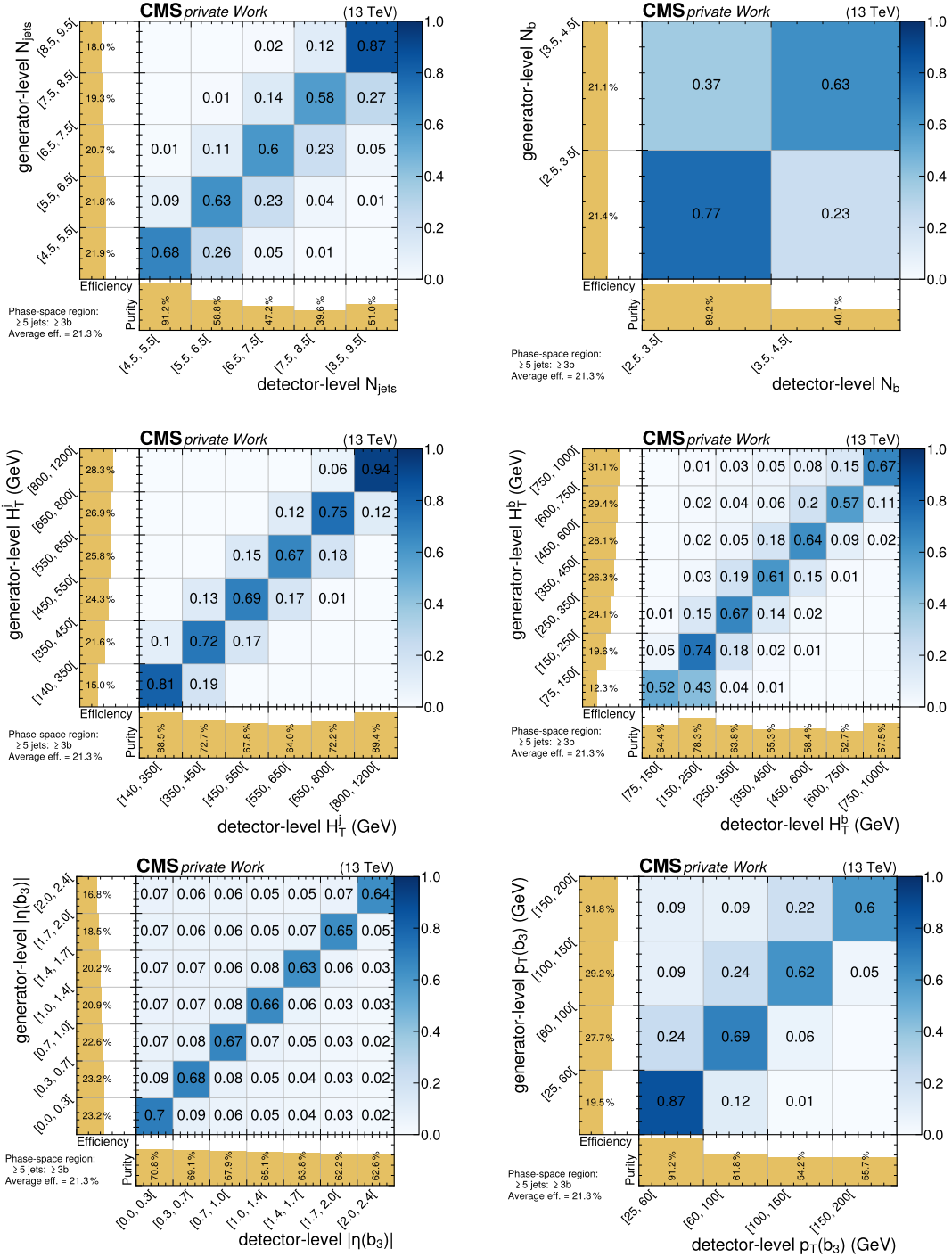


Figure A.1: Migration matrices of the observables in the 5j3b phase space region. The generator-level observable is shown on the vertical axis and the detector-level observable on the horizontal axis. The migration matrix corresponds to the generator-level bins defined for the corresponding observables. Entries in the migration matrix are normalized per generator-level bin (i.e. horizontally). The panel on the vertical axis shows the selection efficiency per generator-level bin. The panel on the horizontal axis shows the purity of events per detector-level bin.

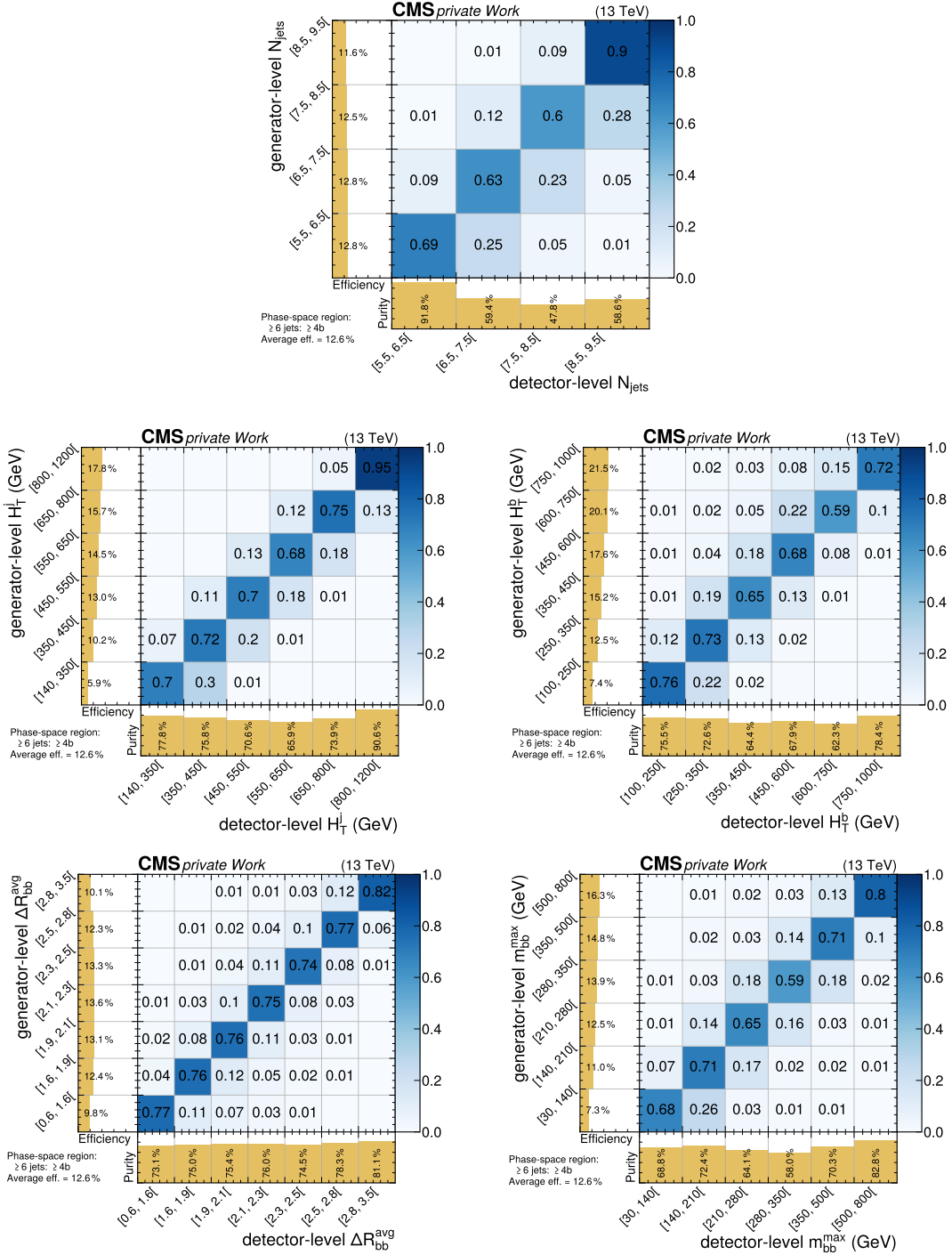


Figure A.2: Migration matrices of observables in the 6j4b phase space region. The generator-level observable is shown on the vertical axis and the detector-level observable on the horizontal axis. The migration matrix corresponds to the generator-level bins defined for the corresponding observables. Entries in the migration matrix are normalized per generator-level bin (i.e. horizontally). The panel on the vertical axis shows the selection efficiency per generator-level bin. The panel on the horizontal axis shows the purity of events per detector-level bin.

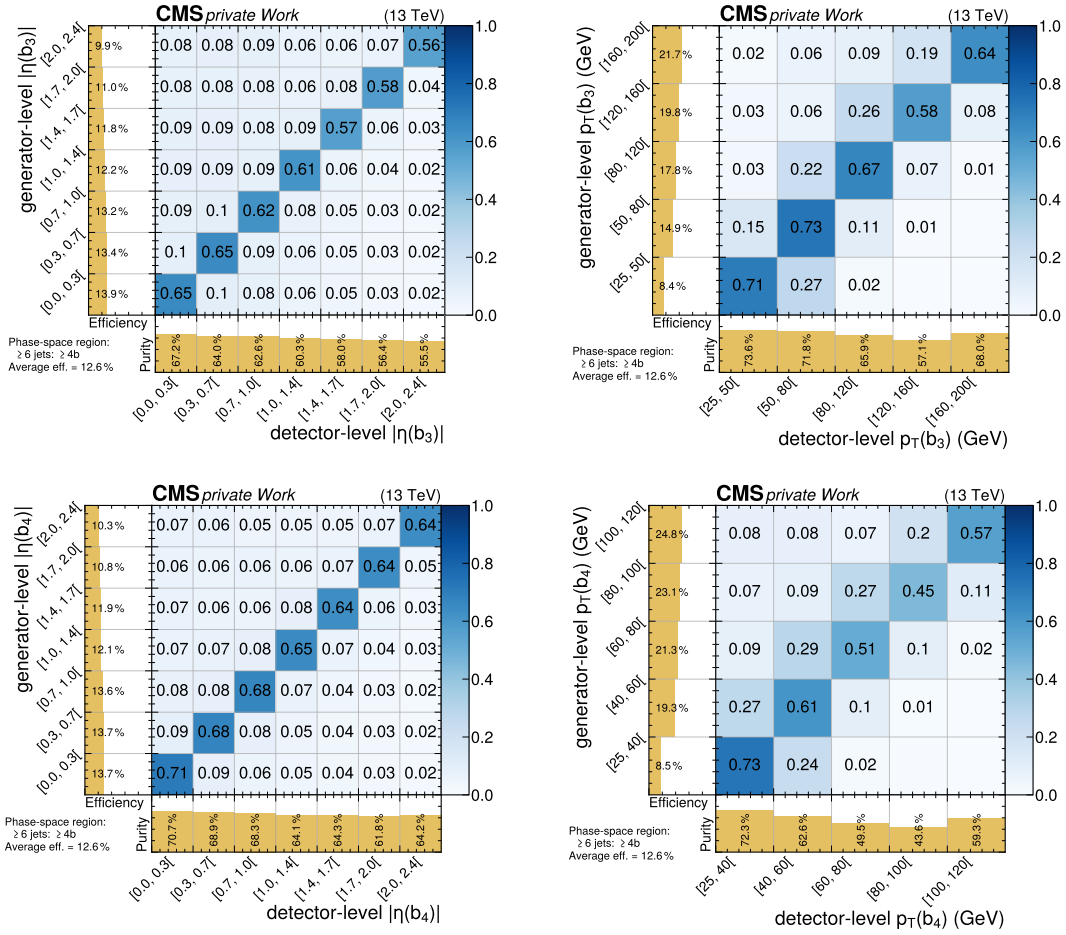


Figure A.3: Migration matrices of observables in the 6j4b phase space region. The generator-level observable is shown on the vertical axis and the detector-level observable on the horizontal axis. The migration matrix corresponds to the generator-level bins defined for the corresponding observables. Entries in the migration matrix are normalized per generator-level bin (i.e. horizontally). The panel on the vertical axis shows the selection efficiency per generator-level bin. The panel on the horizontal axis shows the purity of events per detector-level bin.

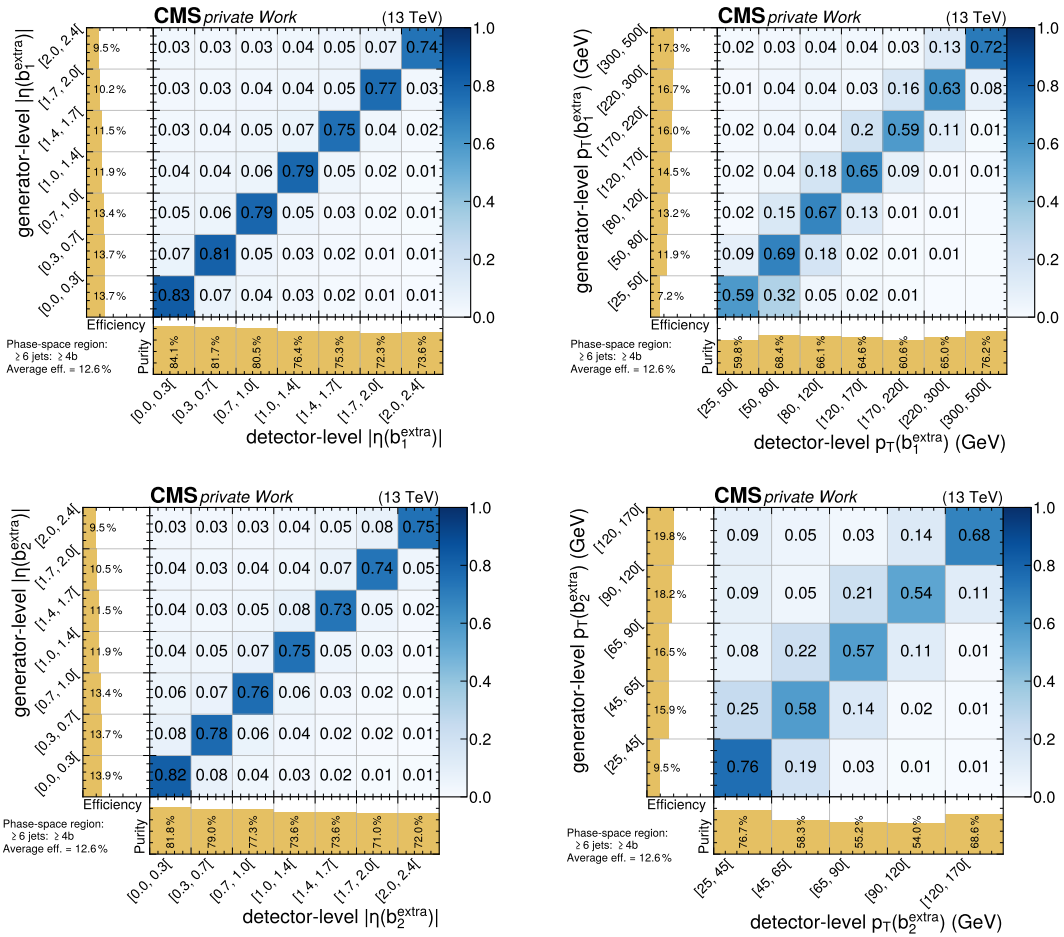


Figure A.4: Migration matrices of observables in the 6j4b phase space region. The generator-level observable is shown on the vertical axis and the detector-level observable on the horizontal axis. The migration matrix corresponds to the generator-level bins defined for the corresponding observables. Entries in the migration matrix are normalized per generator-level bin (i.e. horizontally). The panel on the vertical axis shows the selection efficiency per generator-level bin. The panel on the horizontal axis shows the purity of events per detector-level bin.

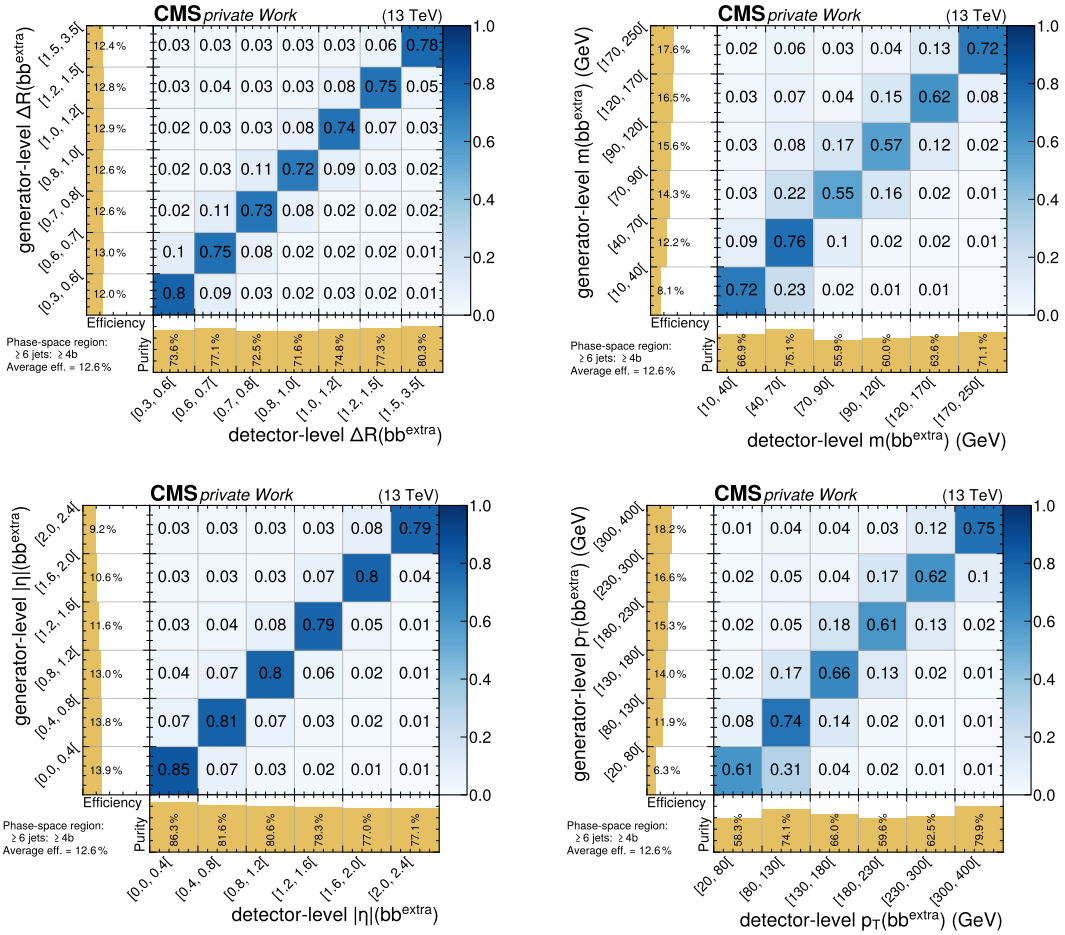


Figure A.5: Migration matrices of observables in the 6j4b phase space region. The generator-level observable is shown on the vertical axis and the detector-level observable on the horizontal axis. The migration matrix corresponds to the generator-level bins defined for the corresponding observables. Entries in the migration matrix are normalized per generator-level bin (i.e. horizontally). The panel on the vertical axis shows the selection efficiency per generator-level bin. The panel on the horizontal axis shows the purity of events per detector-level bin.

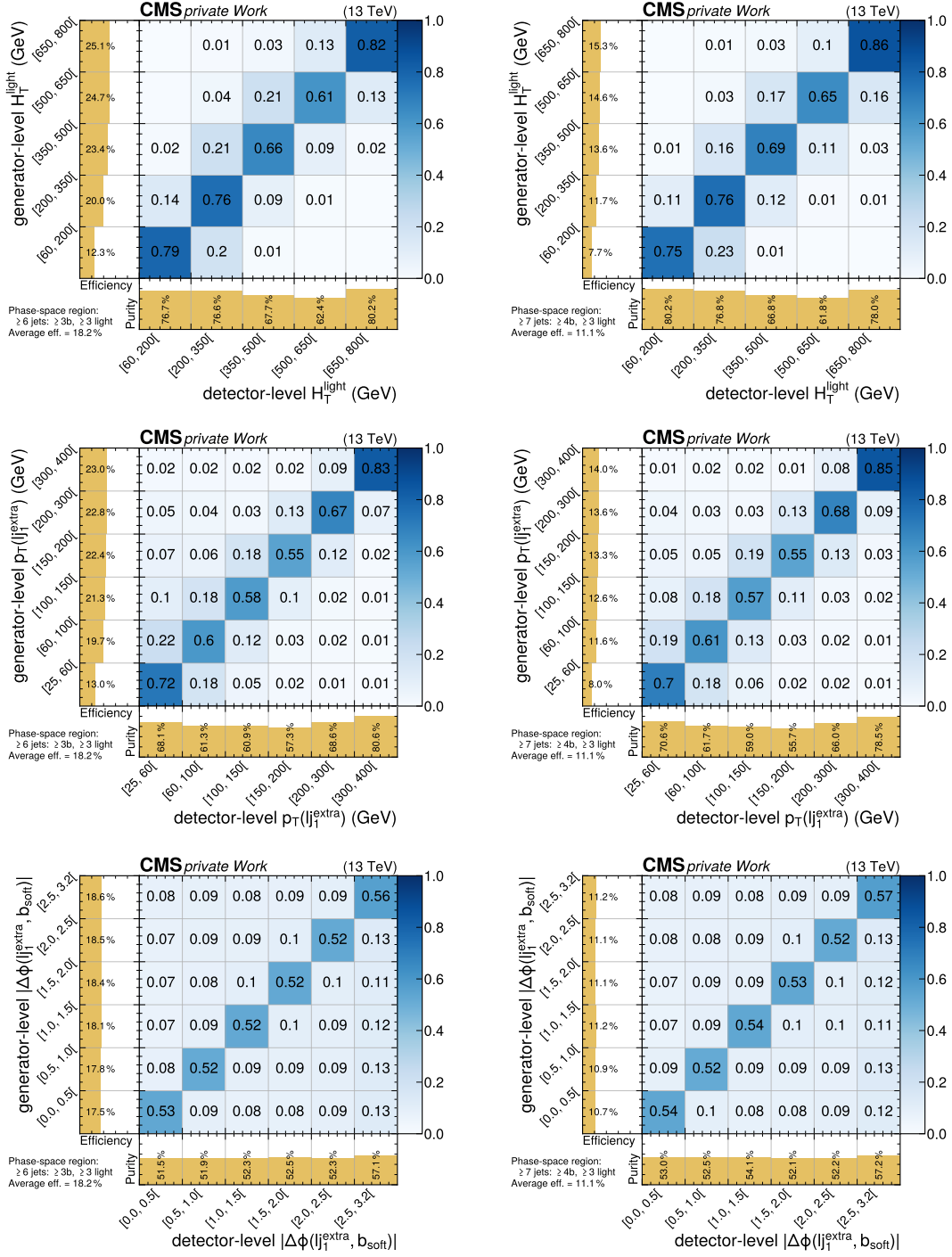


Figure A.6: Migration matrices of observables in the 6j3b3l (left) and 7j4b3l (right) phase space regions. The generator-level observable is shown on the vertical axis and the detector-level observable on the horizontal axis. The migration matrix corresponds to the generator-level bins defined for the corresponding observables. Entries in the migration matrix are normalized per generator-level bin (i.e. horizontally). The panel on the vertical axis shows the selection efficiency per generator-level bin. The panel on the horizontal axis shows the purity of events per detector-level bin.

A.2 Post-fit distributions

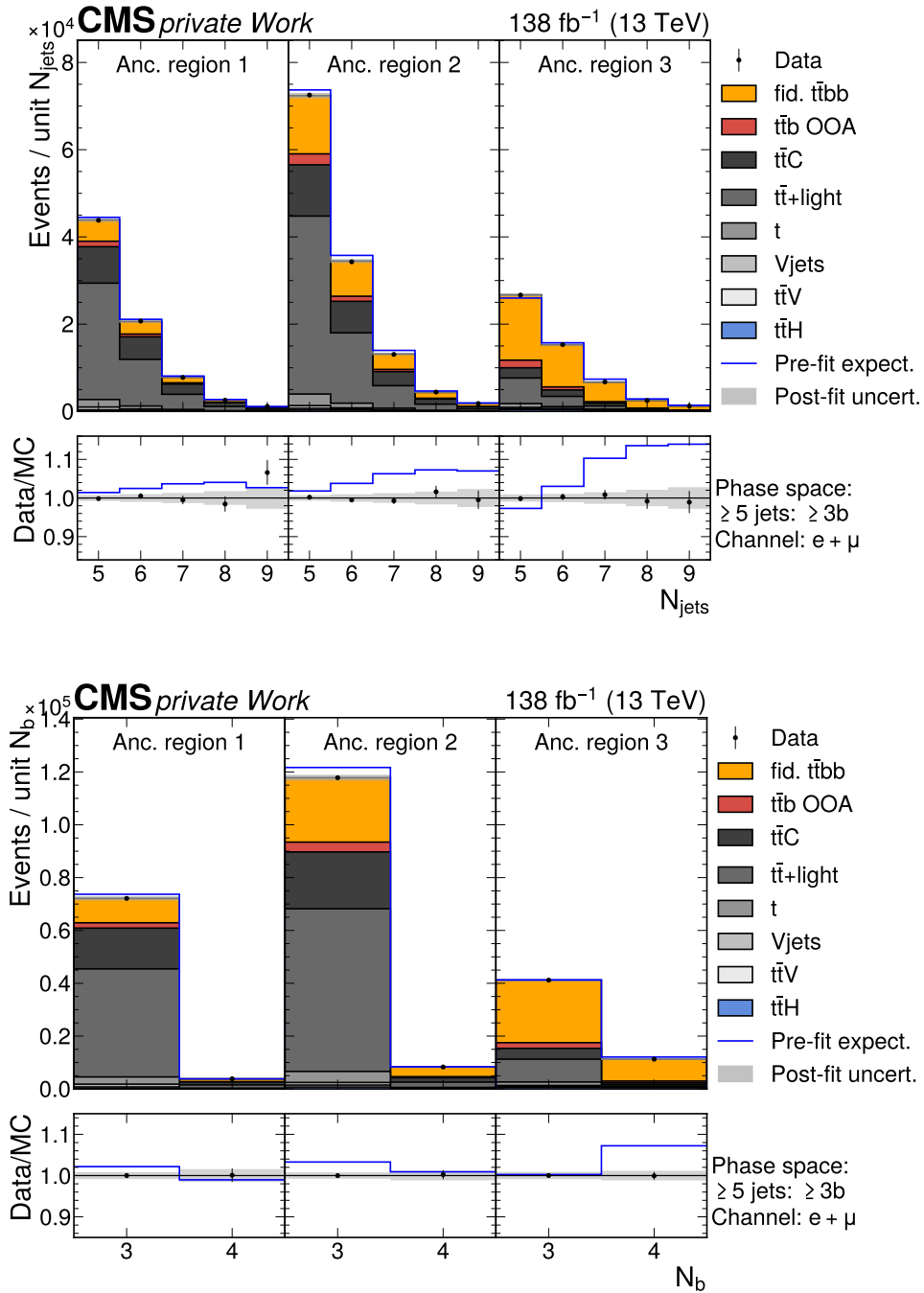


Figure A.7: Distributions of N_{jets} and N_b in the 5j3b phase space region after the fit to data. The contributions of all processes to the detector-level phase space regions after the fit to data are shown as a stack of histograms. The distributions are shown separately for each ancillary region, but are combined across all eras and the lepton channels. The blue line indicates the sum of all processes before the fit to data using the PP8 $t\bar{t}b\bar{b}$ 4FS sample for the estimation of the $t\bar{t}B$ contribution. The lower panel shows the ratio of data to the processes after the fit to data. The shaded bands include all uncertainties described in Section 8.7 after profiling the nuisance parameters in the fit, estimated by sampling the predicted yields from the fit covariance matrix.

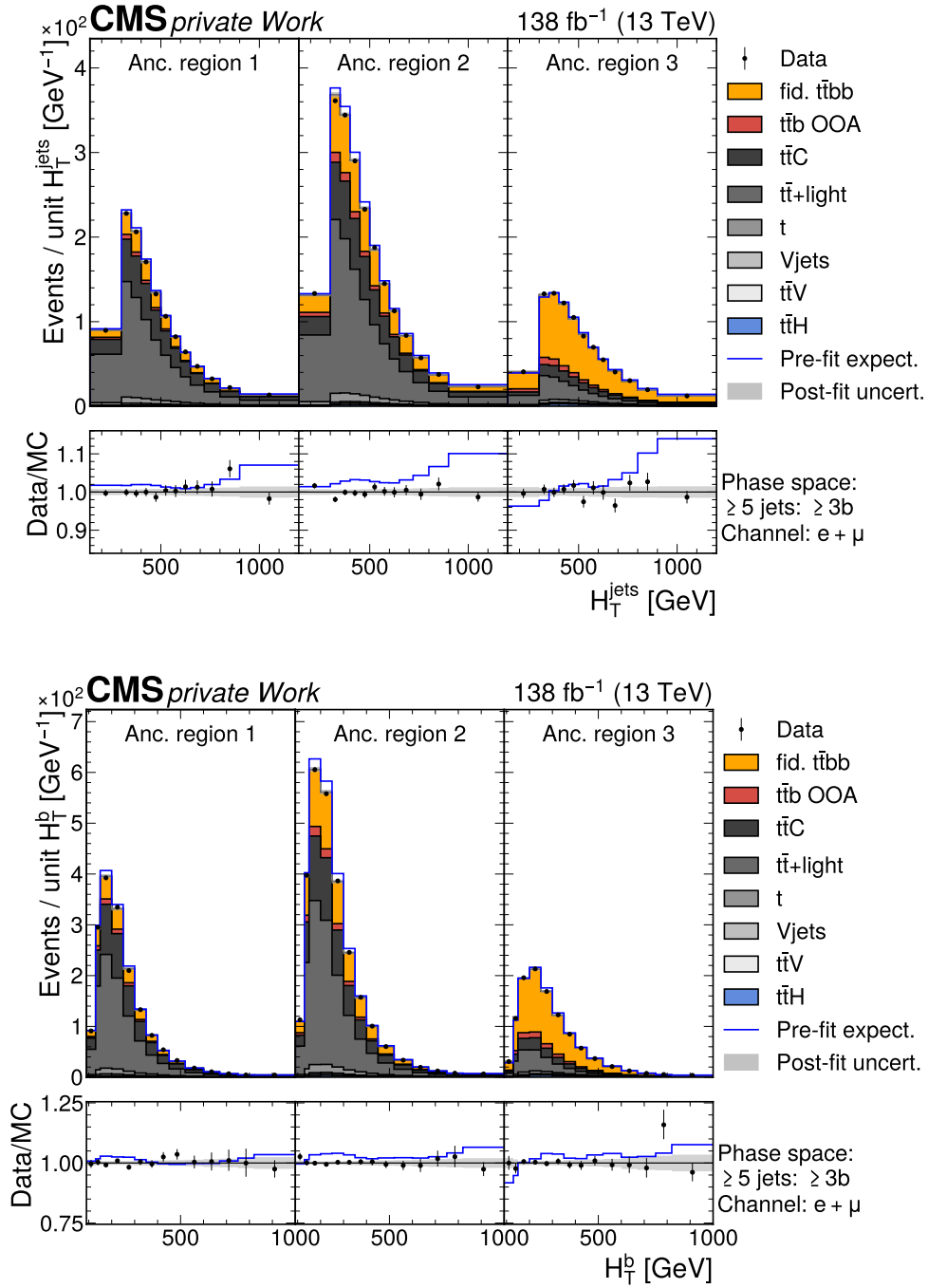


Figure A.8: Distributions of H_T^{jets} and H_T^b in the 5j3b phase space region after the fit to data. The contributions of all processes to the detector-level phase space regions after the fit to data are shown as a stack of histograms. The distributions are shown separately for each ancillary region, but are combined across all eras and the lepton channels. The blue line indicates the sum of all processes before the fit to data using the PP8 $t\bar{t}b\bar{b}$ 4FS sample for the estimation of the $t\bar{t}B$ contribution. The lower panel shows the ratio of data to the processes after the fit to data. The shaded bands include all uncertainties described in Section 8.7 after profiling the nuisance parameters in the fit, estimated by sampling the predicted yields from the fit covariance matrix.

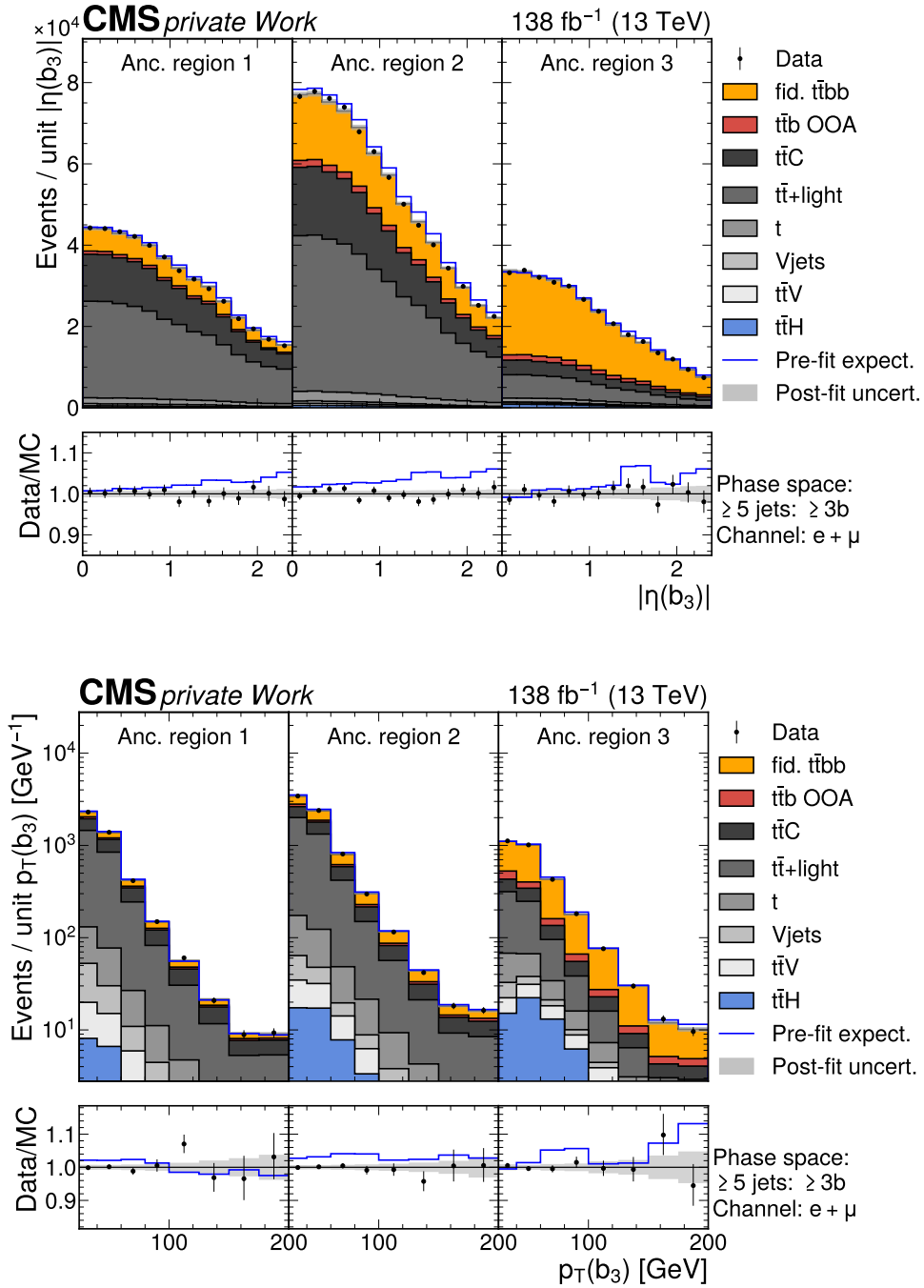


Figure A.9: **Distributions of $|\eta(b_3)|$ and $p_T(b_3)$ in the 5j3b phase space region after the fit to data.** The contributions of all processes to the detector-level phase space regions after the fit to data are shown as a stack of histograms. The distributions are shown separately for each ancillary region, but are combined across all eras and the lepton channels. The blue line indicates the sum of all processes before the fit to data using the PP8 $t\bar{t}b\bar{b}$ 4FS sample for the estimation of the $t\bar{t}B$ contribution. The lower panel shows the ratio of data to the processes after the fit to data. The shaded bands include all uncertainties described in Section 8.7 after profiling the nuisance parameters in the fit, estimated by sampling the predicted yields from the fit covariance matrix.

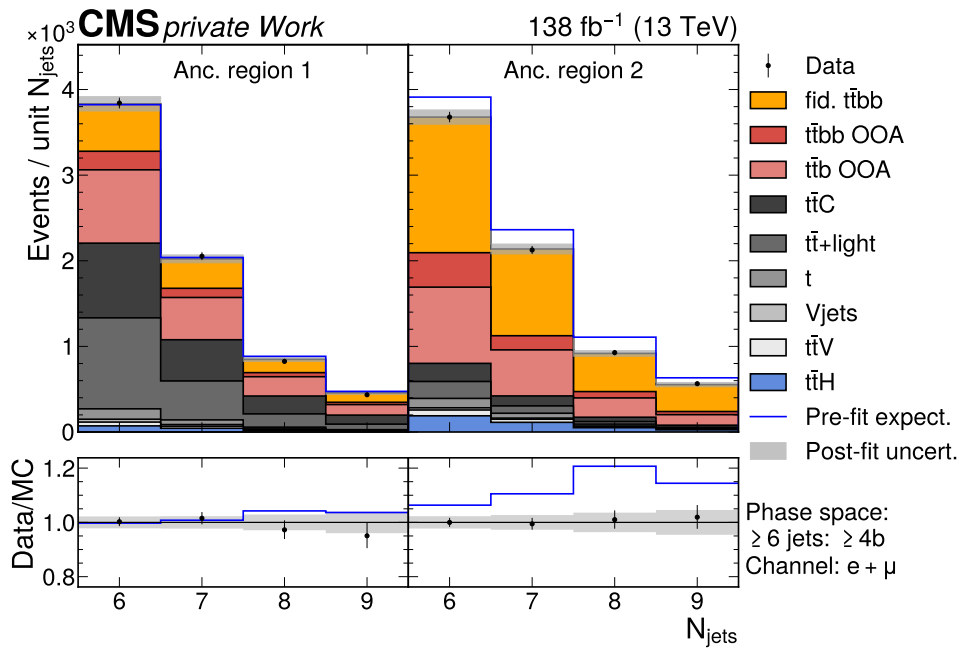


Figure A.10: **Distribution of N_{jets} in the 6j4b phase space region after the fit to data.** The contributions of all processes to the detector-level phase space regions after the fit to data are shown as a stack of histograms. The distributions are shown separately for each ancillary region, but are combined across all eras and the lepton channels. The blue line indicates the sum of all processes before the fit to data using the PP8 $t\bar{t}b\bar{b}$ 4FS sample for the estimation of the $t\bar{t}B$ contribution. The lower panel shows the ratio of data to the processes after the fit to data. The shaded bands include all uncertainties described in Section 8.7 after profiling the nuisance parameters in the fit, estimated by sampling the predicted yields from the fit covariance matrix.

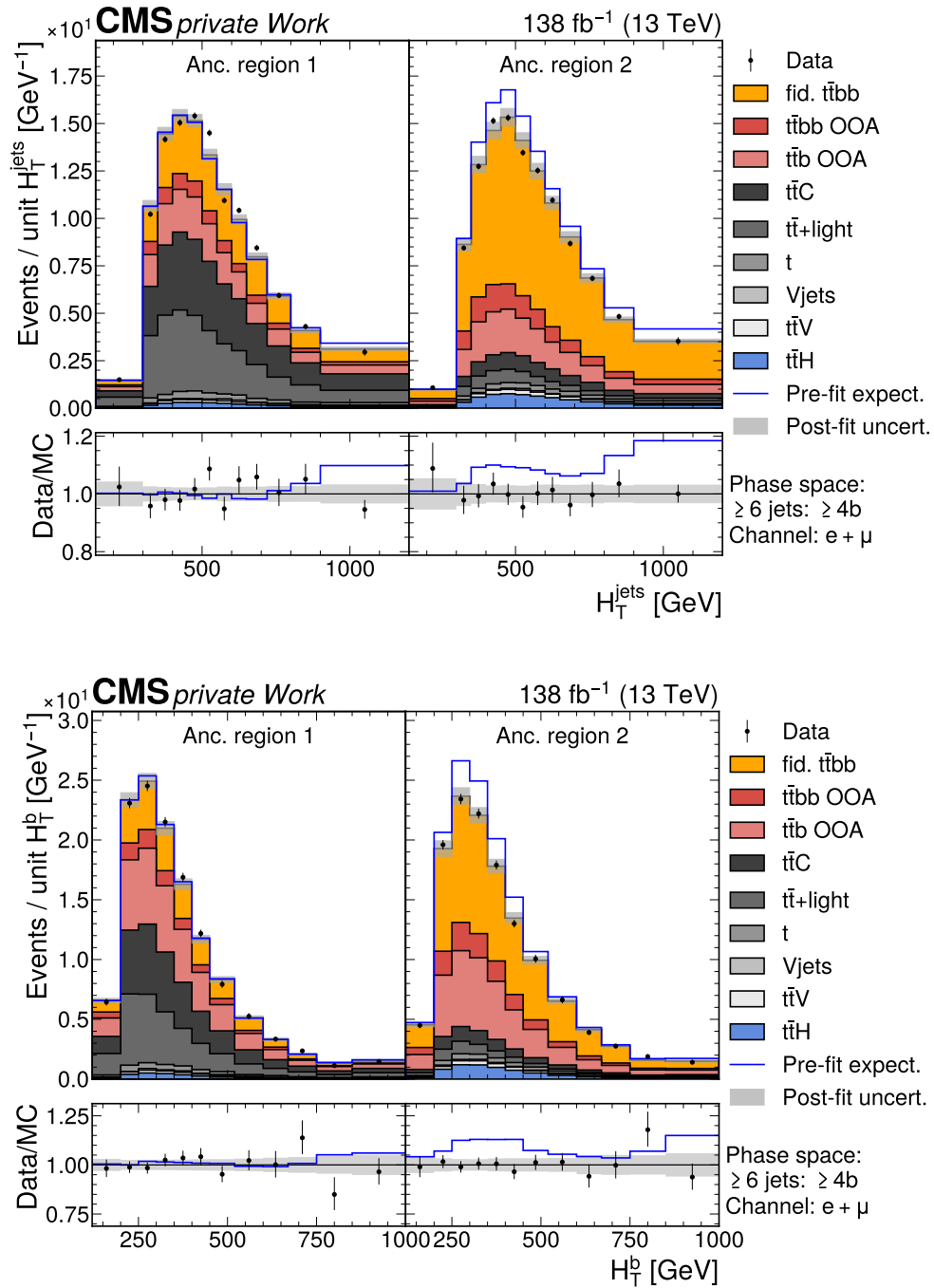


Figure A.11: **Distributions of H_T^{jets} and H_T^b in the 6j4b phase space region after the fit to data.** The contributions of all processes to the detector-level phase space regions after the fit to data are shown as a stack of histograms. The distributions are shown separately for each ancillary region, but are combined across all eras and the lepton channels. The blue line indicates the sum of all processes before the fit to data using the PP8 $t\bar{t}b\bar{b}$ 4FS sample for the estimation of the $t\bar{t}B$ contribution. The lower panel shows the ratio of data to the processes after the fit to data. The shaded bands include all uncertainties described in Section 8.7 after profiling the nuisance parameters in the fit, estimated by sampling the predicted yields from the fit covariance matrix.

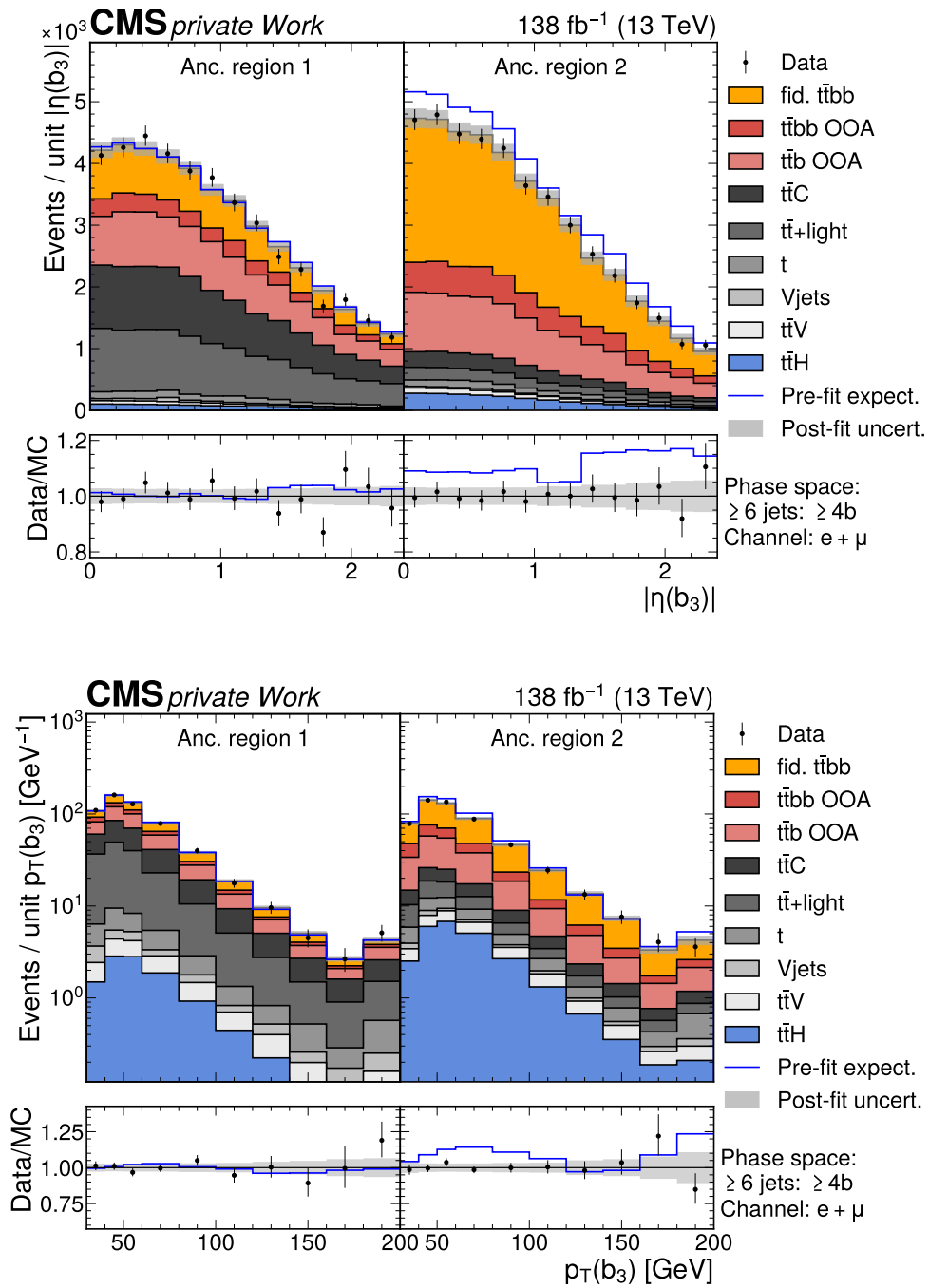


Figure A.12: **Distributions of $|\eta(b_3)|$ and $p_T(b_3)$ in the 6j4b phase space region after the fit to data.** The contributions of all processes to the detector-level phase space regions after the fit to data are shown as a stack of histograms. The distributions are shown separately for each ancillary region, but are combined across all eras and the lepton channels. The blue line indicates the sum of all processes before the fit to data using the PP8 $t\bar{t}b\bar{b}$ 4FS sample for the estimation of the $t\bar{t}B$ contribution. The lower panel shows the ratio of data to the processes after the fit to data. The shaded bands include all uncertainties described in Section 8.7 after profiling the nuisance parameters in the fit, estimated by sampling the predicted yields from the fit covariance matrix.

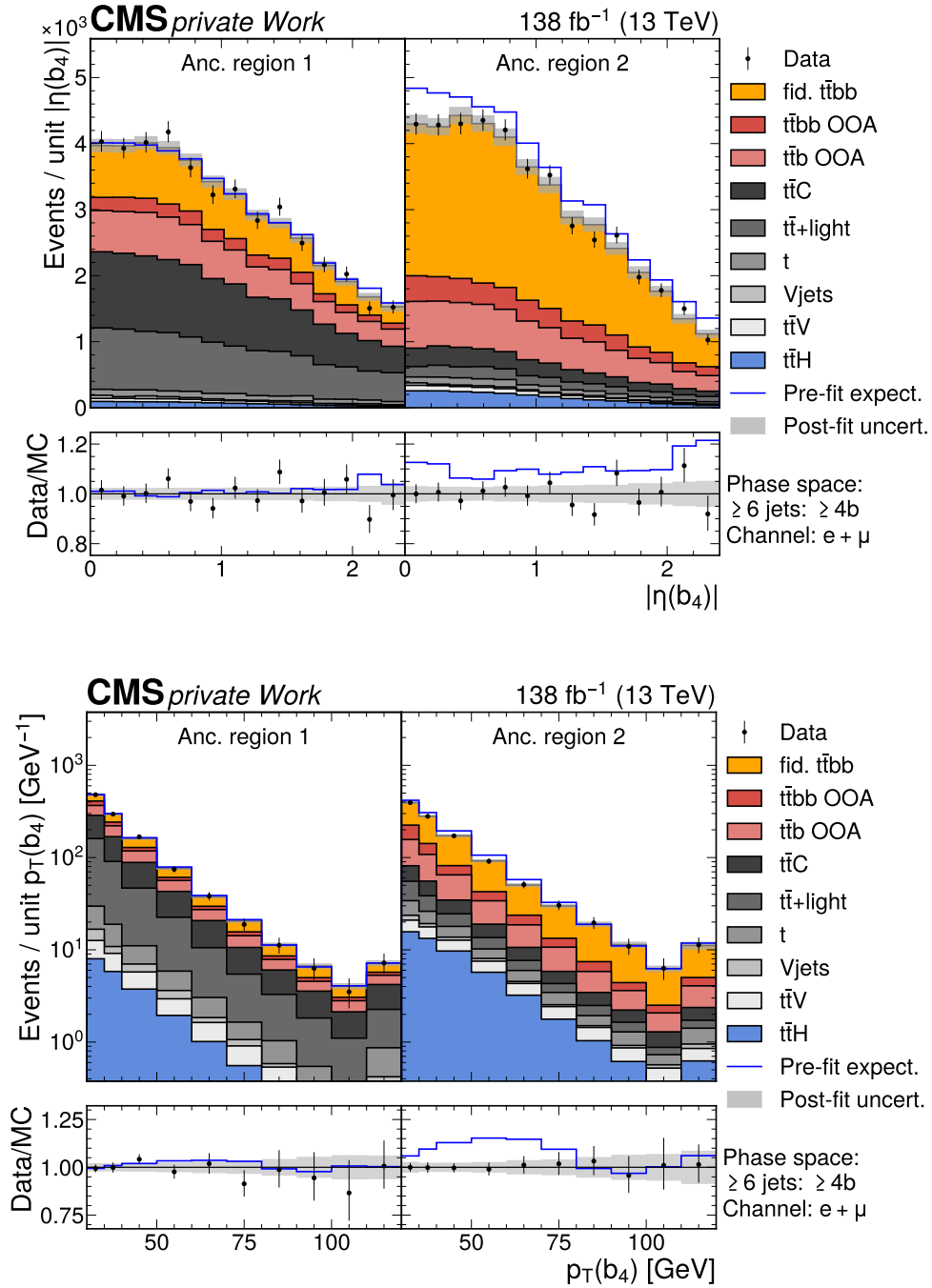


Figure A.13: **Distributions of $|\eta(b_4)|$ and $p_T(b_4)$ in the 6j4b phase space region after the fit to data.** The contributions of all processes to the detector-level phase space regions after the fit to data are shown as a stack of histograms. The distributions are shown separately for each ancillary region, but are combined across all eras and the lepton channels. The blue line indicates the sum of all processes before the fit to data using the PP8 $t\bar{t}b\bar{b}$ 4FS sample for the estimation of the $t\bar{t}B$ contribution. The lower panel shows the ratio of data to the processes after the fit to data. The shaded bands include all uncertainties described in Section 8.7 after profiling the nuisance parameters in the fit, estimated by sampling the predicted yields from the fit covariance matrix.

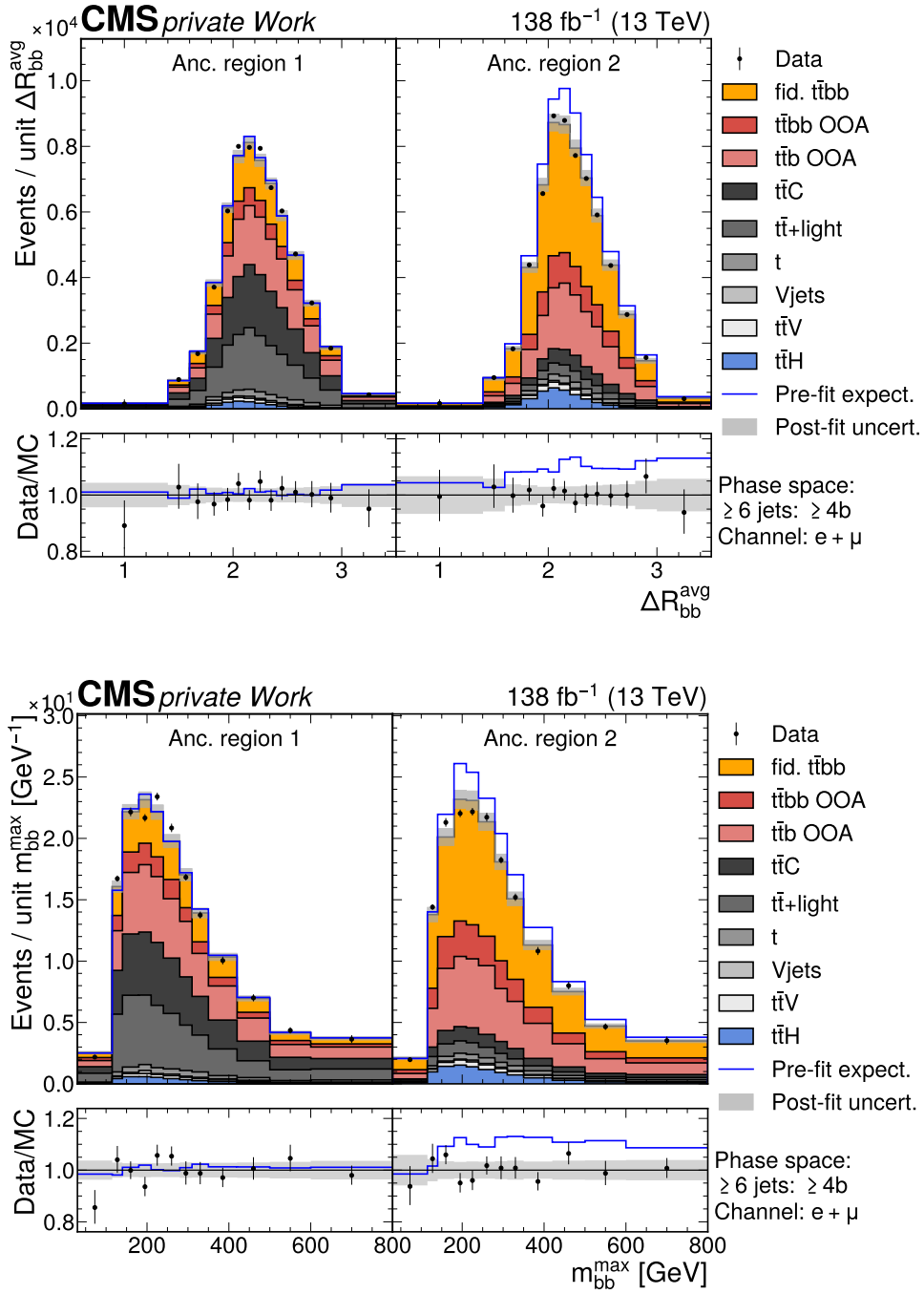


Figure A.14: Distributions of ΔR_{bb}^{avg} and m_{bb}^{max} in the 6j4b phase space region after the fit to data. The contributions of all processes to the detector-level phase space regions after the fit to data are shown as a stack of histograms. The distributions are shown separately for each ancillary region, but are combined across all eras and the lepton channels. The blue line indicates the sum of all processes before the fit to data using the PP8 $t\bar{t}b\bar{b}$ 4FS sample for the estimation of the $t\bar{t}B$ contribution. The lower panel shows the ratio of data to the processes after the fit to data. The shaded bands include all uncertainties described in Section 8.7 after profiling the nuisance parameters in the fit, estimated by sampling the predicted yields from the fit covariance matrix.

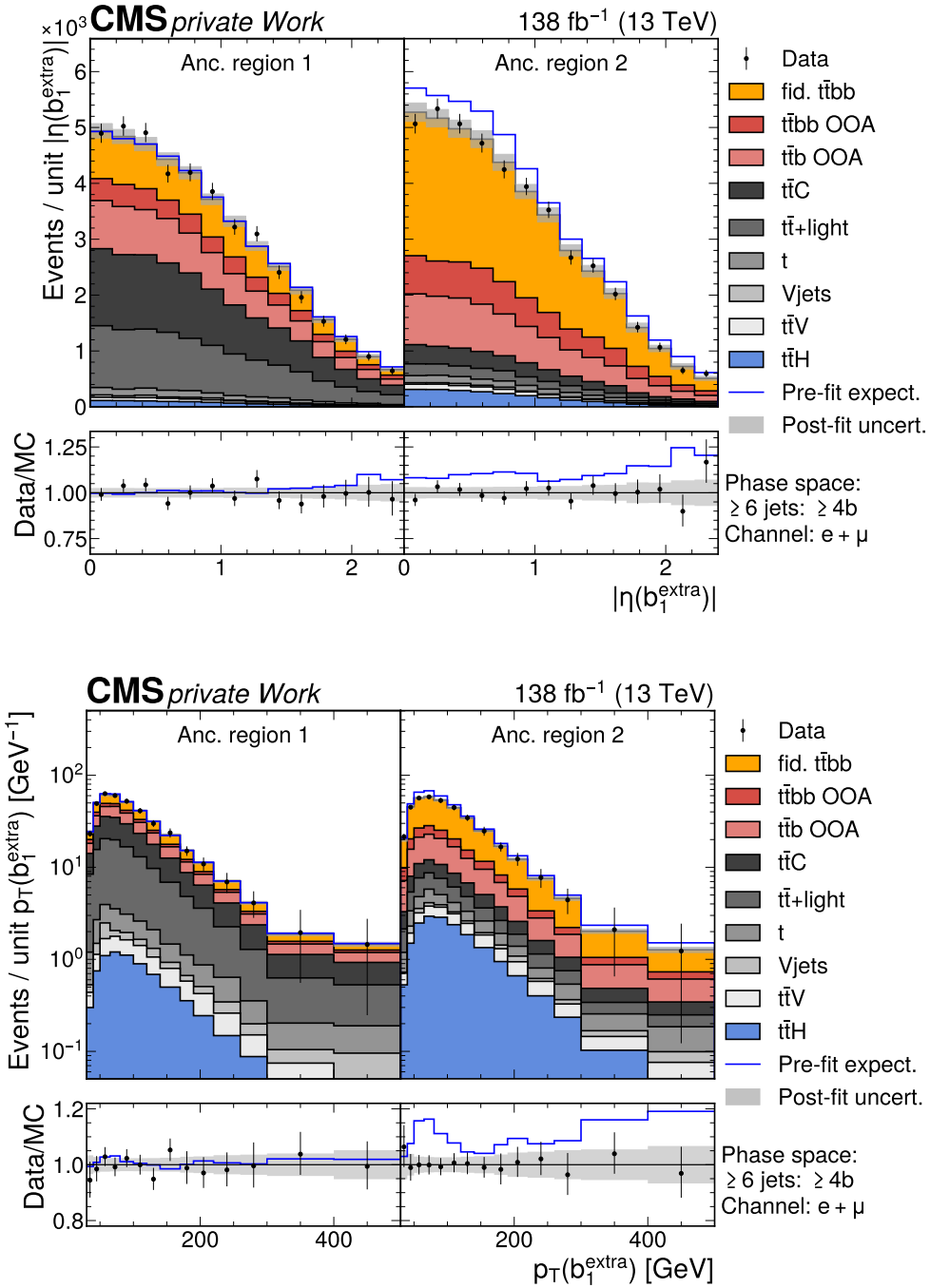


Figure A.15: **Distributions of $|\eta(\mathbf{b}_1^{\text{extra}})|$ and $p_T(\mathbf{b}_1^{\text{extra}})$ in the 6j4b phase space region after the fit to data.** The contributions of all processes to the detector-level phase space regions after the fit to data are shown as a stack of histograms. The distributions are shown separately for each ancillary region, but are combined across all eras and the lepton channels. The blue line indicates the sum of all processes before the fit to data using the PP8 $t\bar{t}b\bar{b}$ 4FS sample for the estimation of the $t\bar{t}B$ contribution. The lower panel shows the ratio of data to the processes after the fit to data. The shaded bands include all uncertainties described in Section 8.7 after profiling the nuisance parameters in the fit, estimated by sampling the predicted yields from the fit covariance matrix.

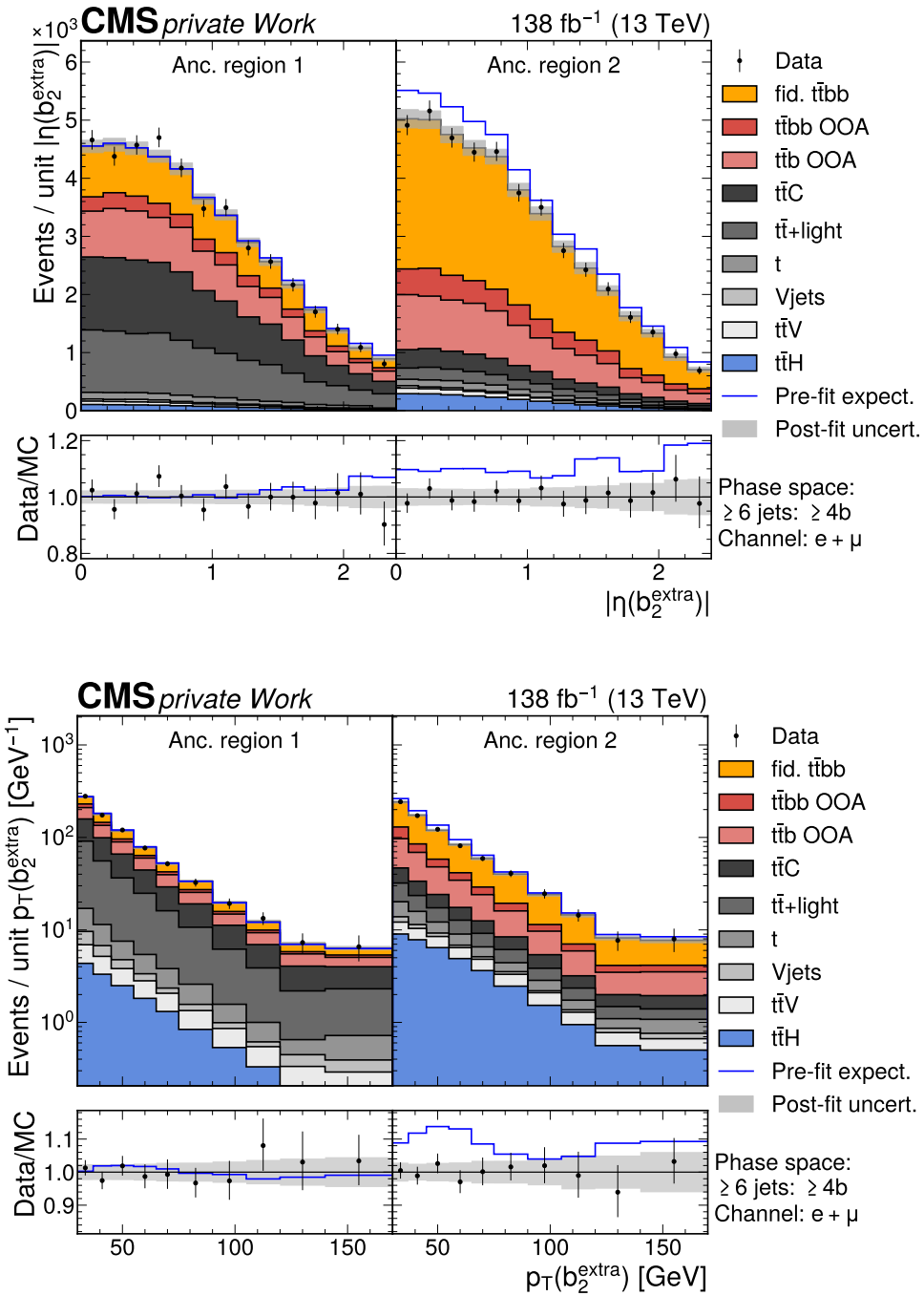


Figure A.16: **Distributions of $|\eta(b_2^{\text{extra}})|$ and $p_T(b_2^{\text{extra}})$ in the 6j4b phase space region after the fit to data.** The contributions of all processes to the detector-level phase space regions after the fit to data are shown as a stack of histograms. The distributions are shown separately for each ancillary region, but are combined across all eras and the lepton channels. The blue line indicates the sum of all processes before the fit to data using the PP8 $t\bar{t}b\bar{b}$ 4FS sample for the estimation of the $t\bar{t}B$ contribution. The lower panel shows the ratio of data to the processes after the fit to data. The shaded bands include all uncertainties described in Section 8.7 after profiling the nuisance parameters in the fit, estimated by sampling the predicted yields from the fit covariance matrix.

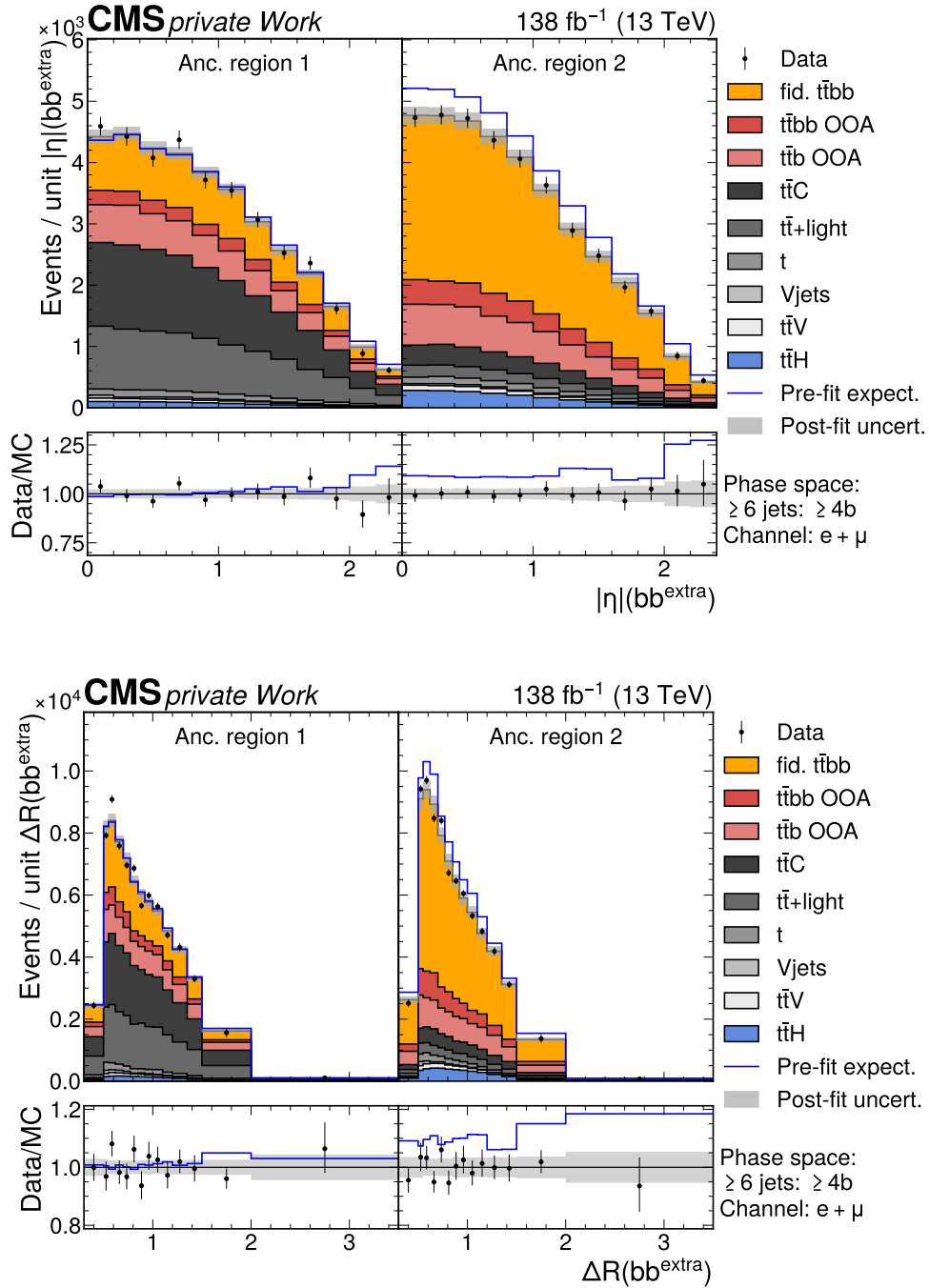


Figure A.17: Distributions of $|\eta|(\text{bb}^{\text{extra}})$ and $\Delta R(\text{bb}^{\text{extra}})$ in the 6j4b phase space region after the fit to data. The contributions of all processes to the detector-level phase space regions after the fit to data are shown as a stack of histograms. The distributions are shown separately for each ancillary region, but are combined across all eras and the lepton channels. The blue line indicates the sum of all processes before the fit to data using the PP8 $t\bar{t}b\bar{b}$ 4FS sample for the estimation of the $t\bar{t}B$ contribution. The lower panel shows the ratio of data to the processes after the fit to data. The shaded bands include all uncertainties described in Section 8.7 after profiling the nuisance parameters in the fit, estimated by sampling the predicted yields from the fit covariance matrix.

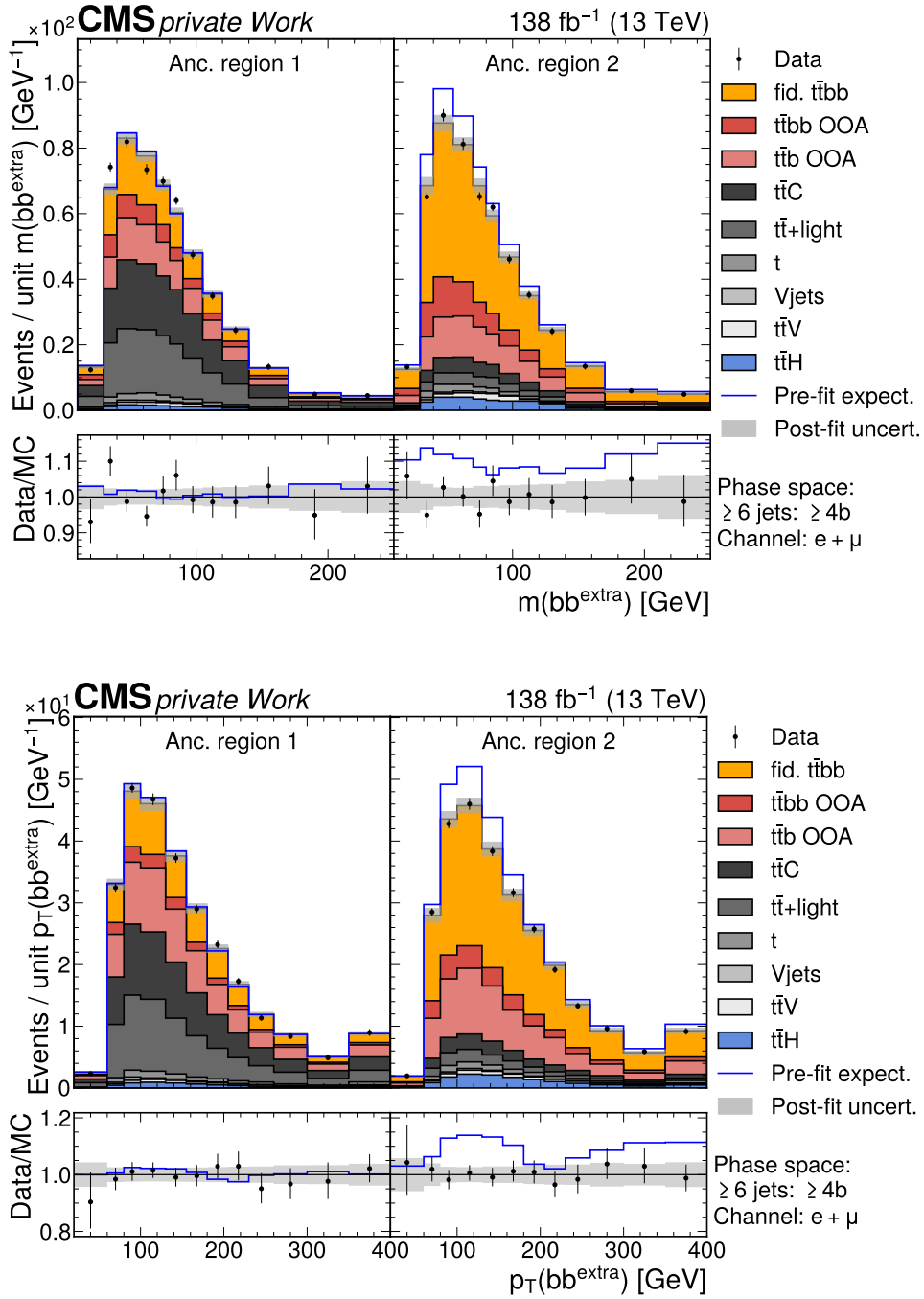


Figure A.18: Distributions of $m(bb^{\text{extra}})$ and $p_T(bb^{\text{extra}})$ in the 6j4b phase space region after the fit to data. The contributions of all processes to the detector-level phase space regions after the fit to data are shown as a stack of histograms. The distributions are shown separately for each ancillary region, but are combined across all eras and the lepton channels. The blue line indicates the sum of all processes before the fit to data using the PP8 $t\bar{t}b\bar{b}$ 4FS sample for the estimation of the $t\bar{t}B$ contribution. The lower panel shows the ratio of data to the processes after the fit to data. The shaded bands include all uncertainties described in Section 8.7 after profiling the nuisance parameters in the fit, estimated by sampling the predicted yields from the fit covariance matrix.

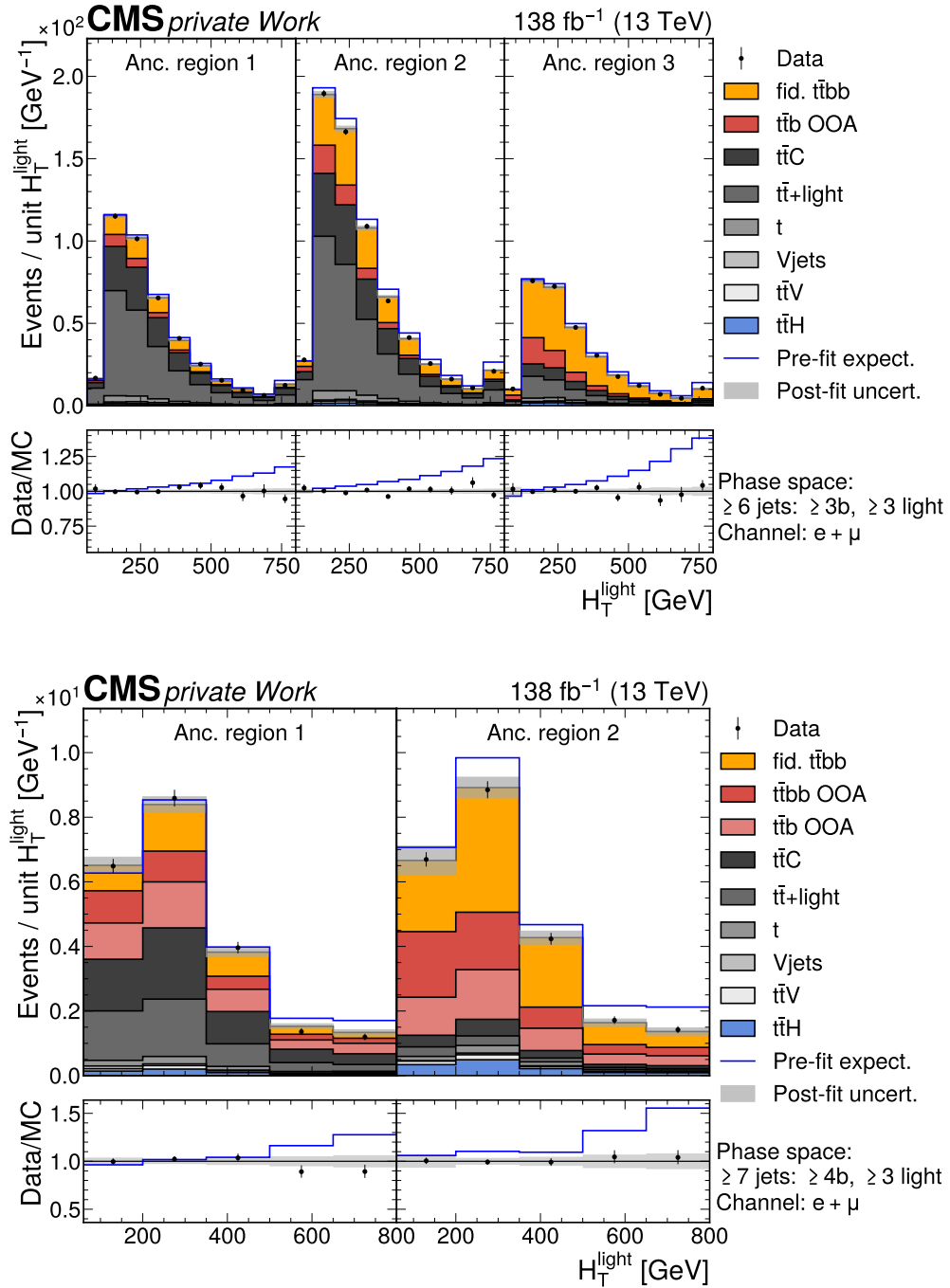


Figure A.19: Distributions of H_T^{jets} in the 6j3b3l and 7j4b3l phase space regions after the fit to data. The contributions of all processes to the detector-level phase space regions after the fit to data are shown as a stack of histograms. The distributions are shown separately for each ancillary region, but are combined across all eras and the lepton channels. The blue line indicates the sum of all processes before the fit to data using the PP8 $t\bar{t}b\bar{b}$ 4FS sample for the estimation of the $t\bar{t}B$ contribution. The lower panel shows the ratio of data to the processes after the fit to data. The shaded bands include all uncertainties described in Section 8.7 after profiling the nuisance parameters in the fit, estimated by sampling the predicted yields from the fit covariance matrix.

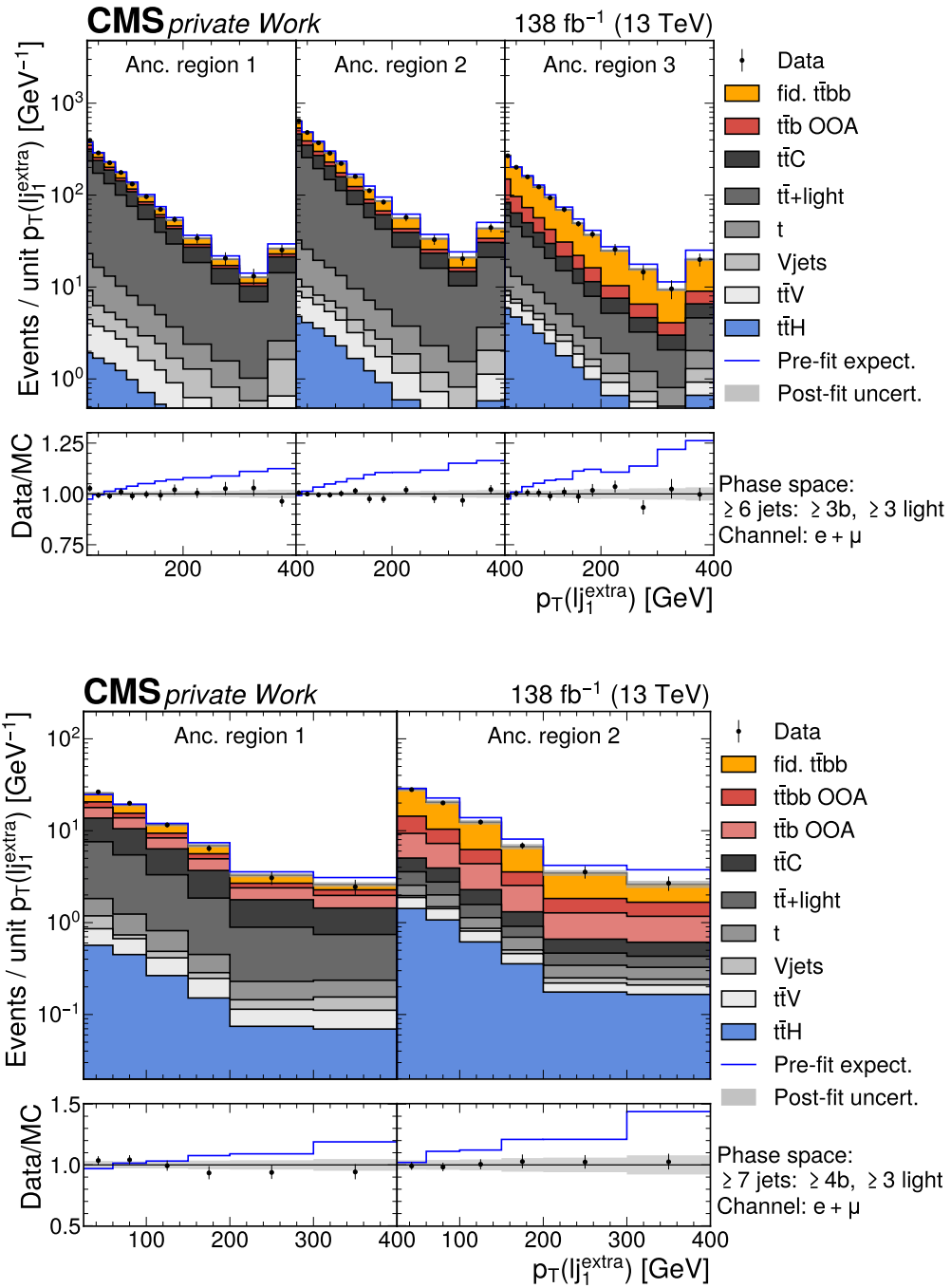


Figure A.20: Distributions of $p_T(lj_1^{\text{extra}})$ in the 6j3b3l and 7j4b3l phase space regions after the fit to data. The contributions of all processes to the detector-level phase space regions after the fit to data are shown as a stack of histograms. The distributions are shown separately for each ancillary region, but are combined across all eras and the lepton channels. The blue line indicates the sum of all processes before the fit to data using the PP8 $t\bar{t}b\bar{b}$ 4FS sample for the estimation of the $t\bar{t}B$ contribution. The lower panel shows the ratio of data to the processes after the fit to data. The shaded bands include all uncertainties described in Section 8.7 after profiling the nuisance parameters in the fit, estimated by sampling the predicted yields from the fit covariance matrix.

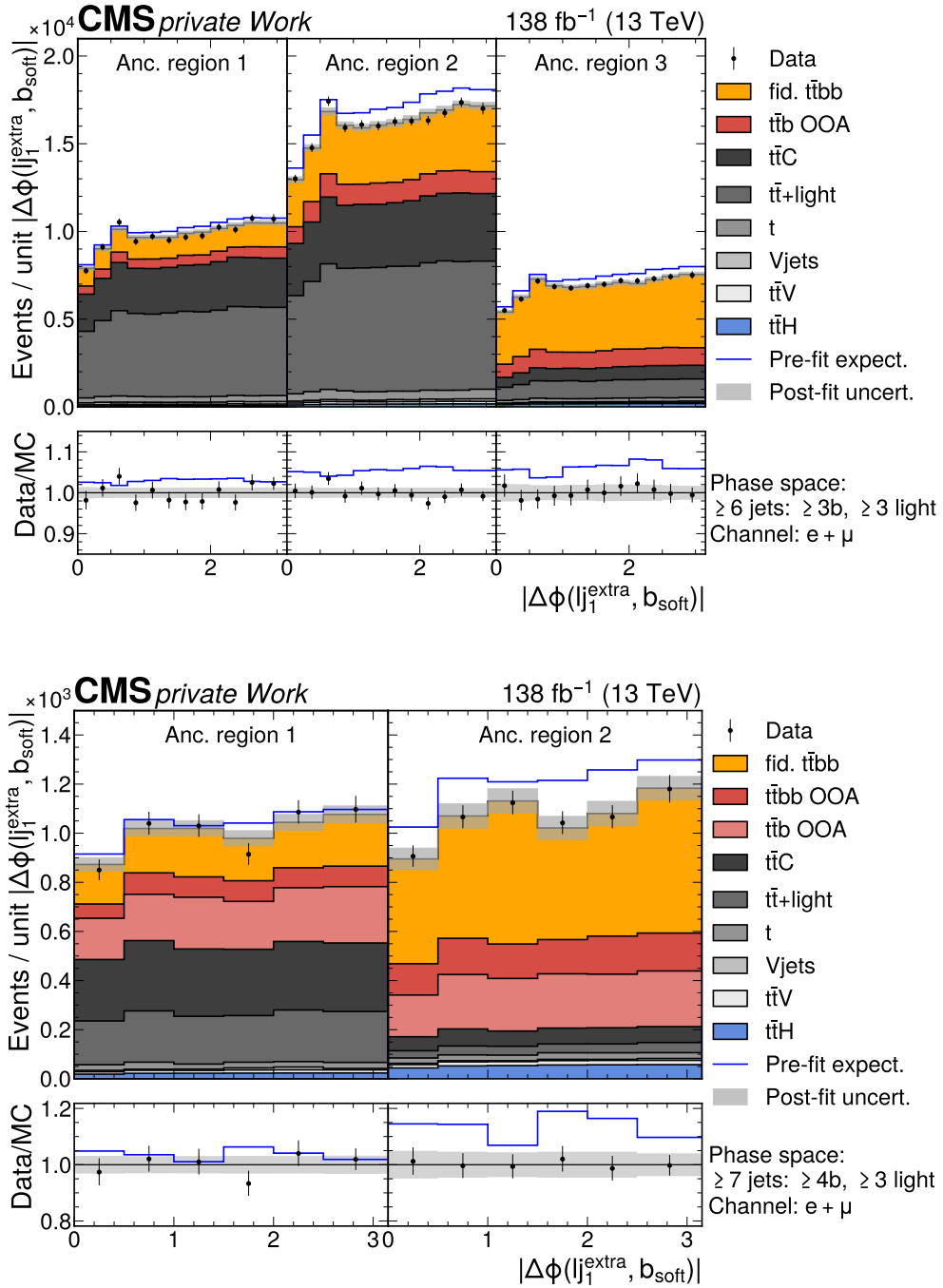


Figure A.21: Distributions of $|\Delta\phi(lj_1^{\text{extra}}, b_{\text{soft}})|$ in the 6j3b3l and 7j4b3l phase space regions after the fit to data. The contributions of all processes to the detector-level phase space regions after the fit to data are shown as a stack of histograms. The distributions are shown separately for each ancillary region, but are combined across all eras and the lepton channels. The blue line indicates the sum of all processes before the fit to data using the PP8 $t\bar{t}b\bar{b}$ 4FS sample for the estimation of the $t\bar{t}B$ contribution. The lower panel shows the ratio of data to the processes after the fit to data. The shaded bands include all uncertainties described in Section 8.7 after profiling the nuisance parameters in the fit, estimated by sampling the predicted yields from the fit covariance matrix.

A.3 Correlation of POIs

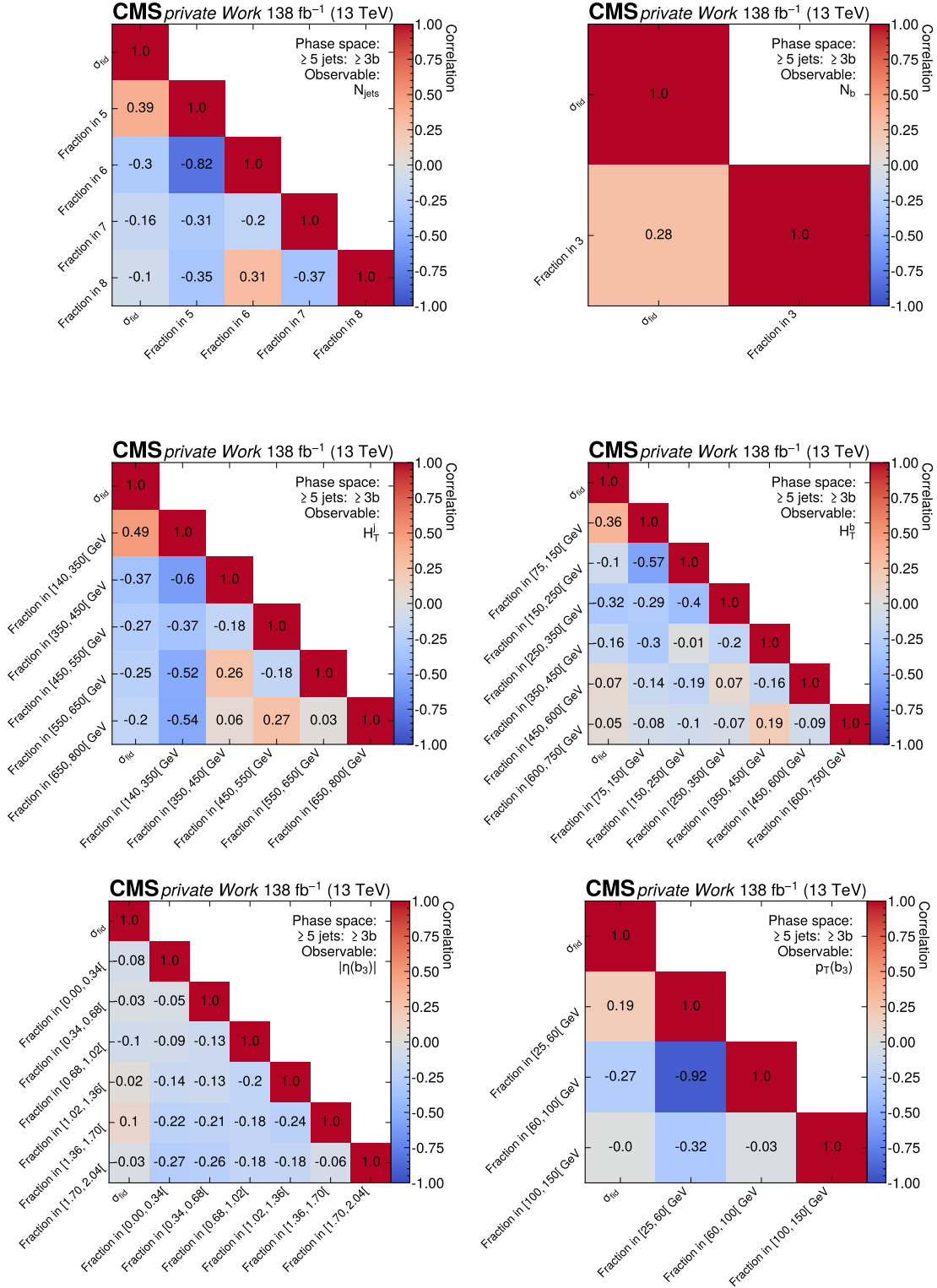


Figure A.22: Correlations between the parameters of interest $\vec{\mu}$ for the observables in the 5j3b phase space region.

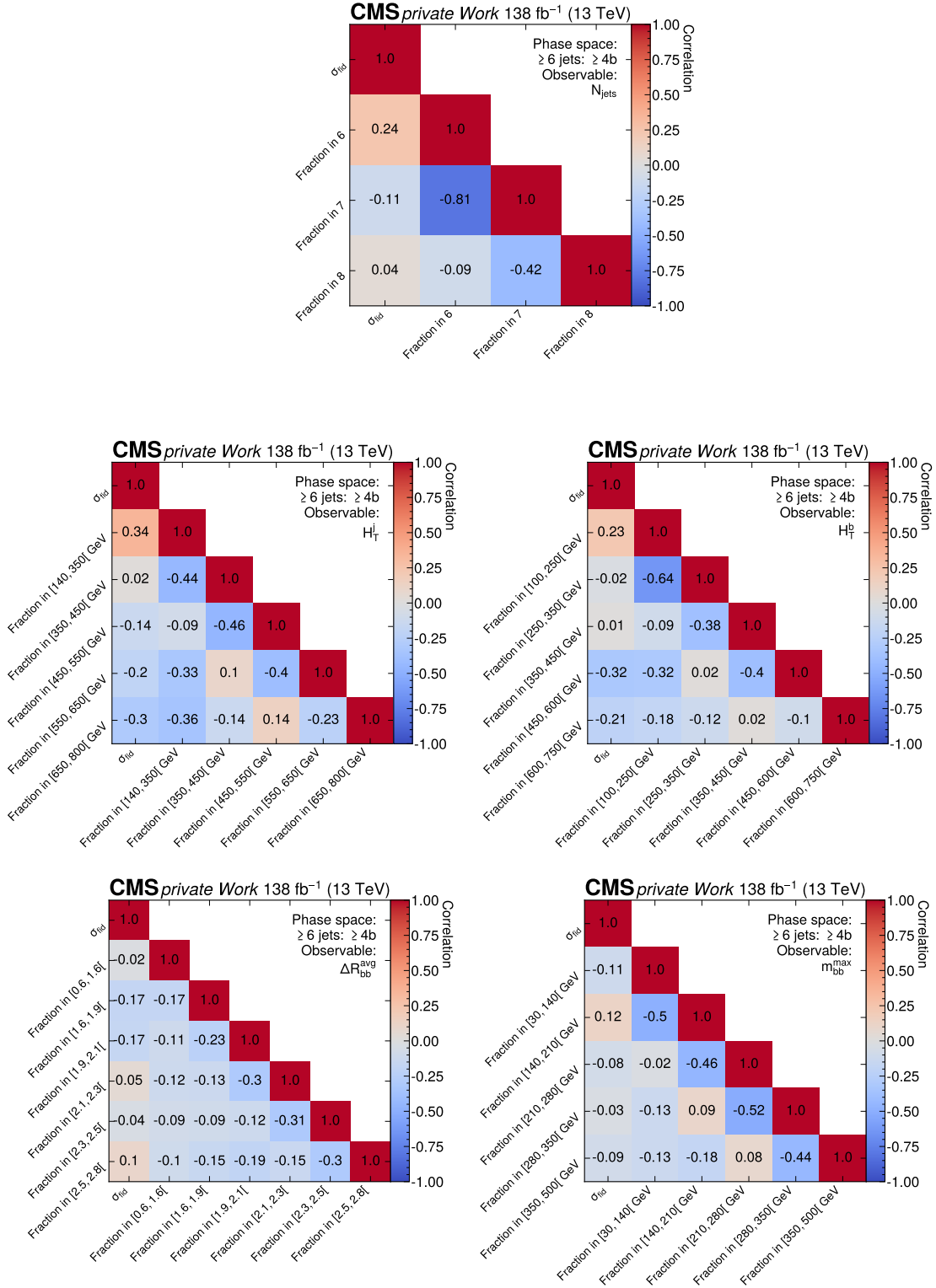


Figure A.23: Correlations between the parameters of interest $\vec{\mu}$ for the N_{jets} , H_T^{jets} , H_T^b , $\Delta R_{\text{bb}}^{\text{avg}}$ and $m_{\text{bb}}^{\text{max}}$ observables in the 6j4b phase space region.

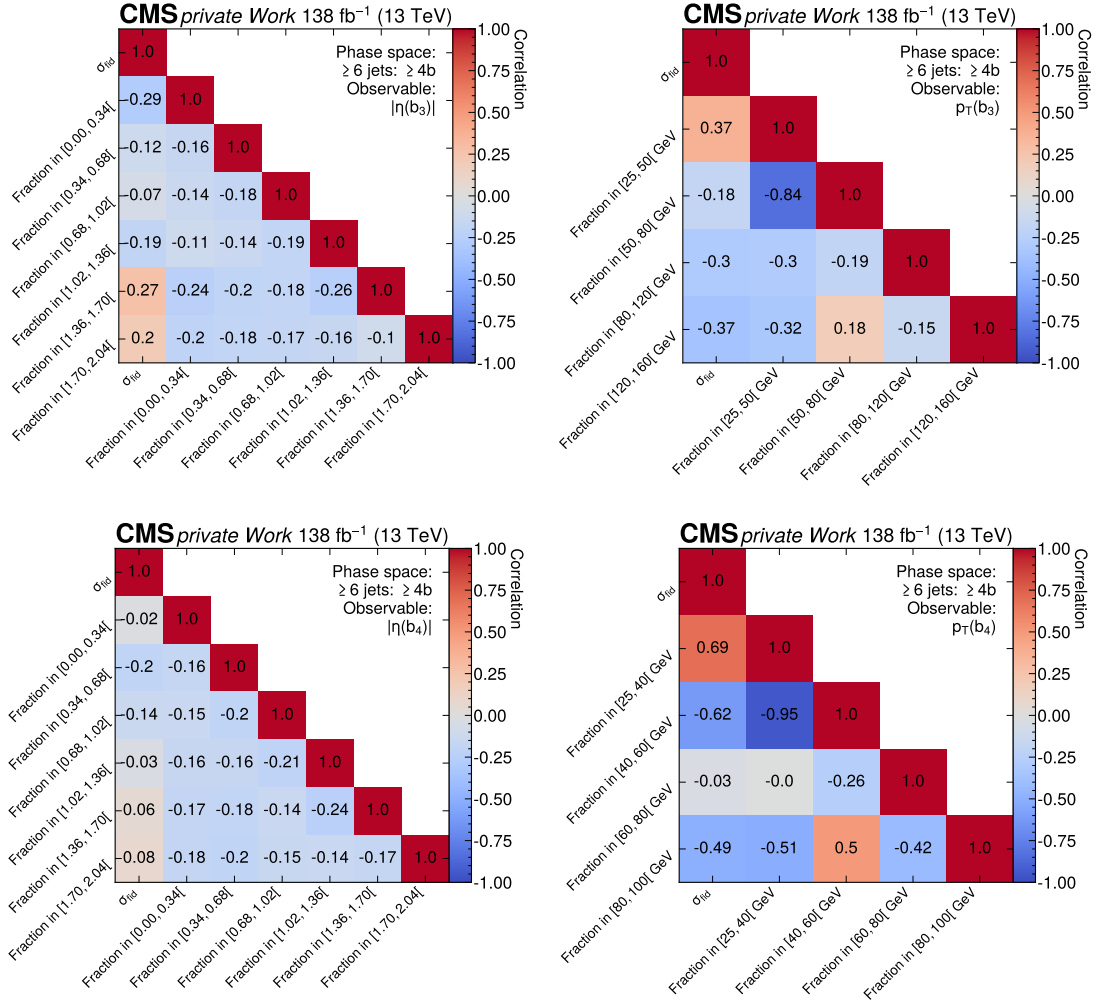


Figure A.24: Correlations between the parameters of interest $\vec{\mu}$ for the $p_{\text{T}}(\mathbf{b}_3)$, $p_{\text{T}}(\mathbf{b}_4)$, $|\eta(\mathbf{b}_3)|$ and $|\eta(\mathbf{b}_4)|$ observables in the 6j4b phase space region.

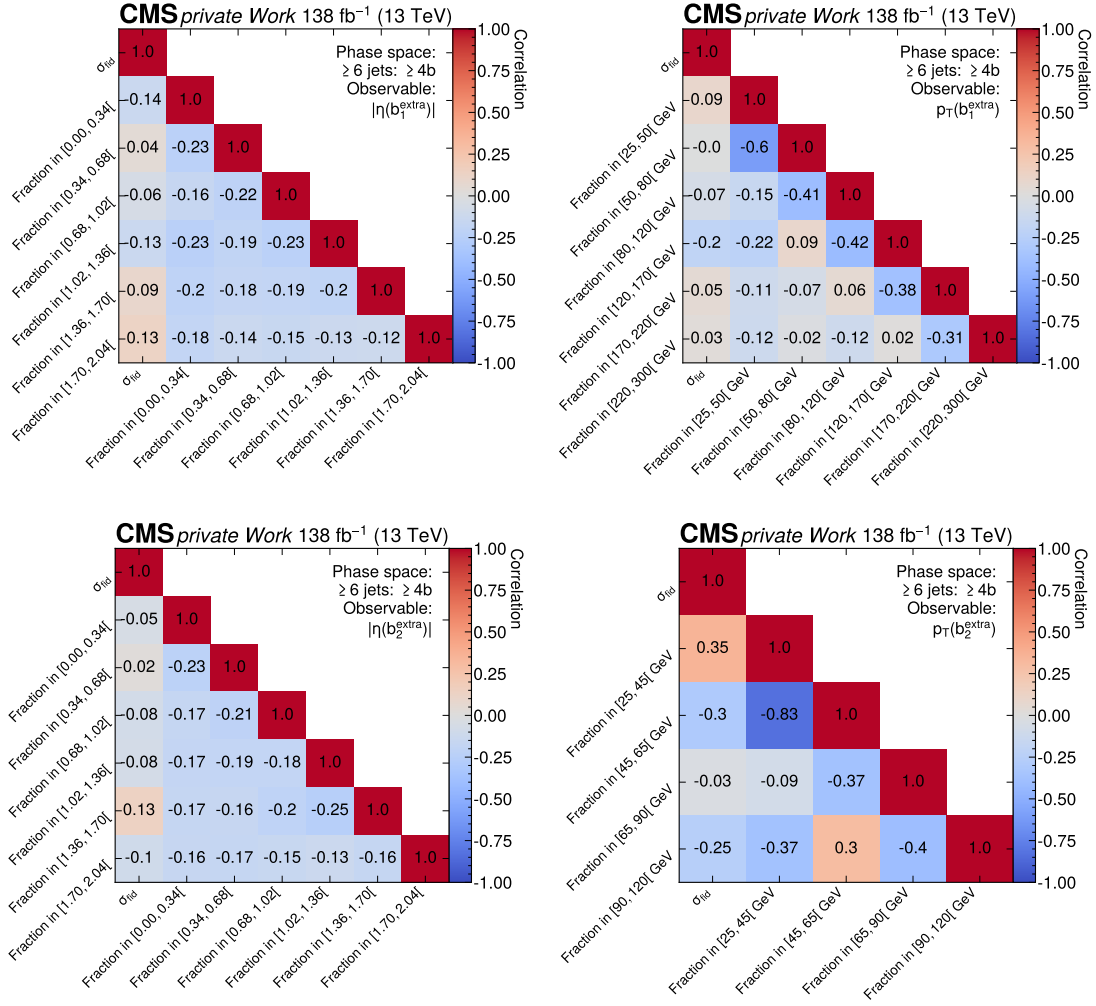


Figure A.25: Correlations between the parameters of interest $\vec{\mu}$ for the $p_T(b_1^{\text{extra}})$, $p_T(b_2^{\text{extra}})$, $|\eta(b_1^{\text{extra}})|$ and $|\eta(b_2^{\text{extra}})|$ observables in the 6j4b phase space region.

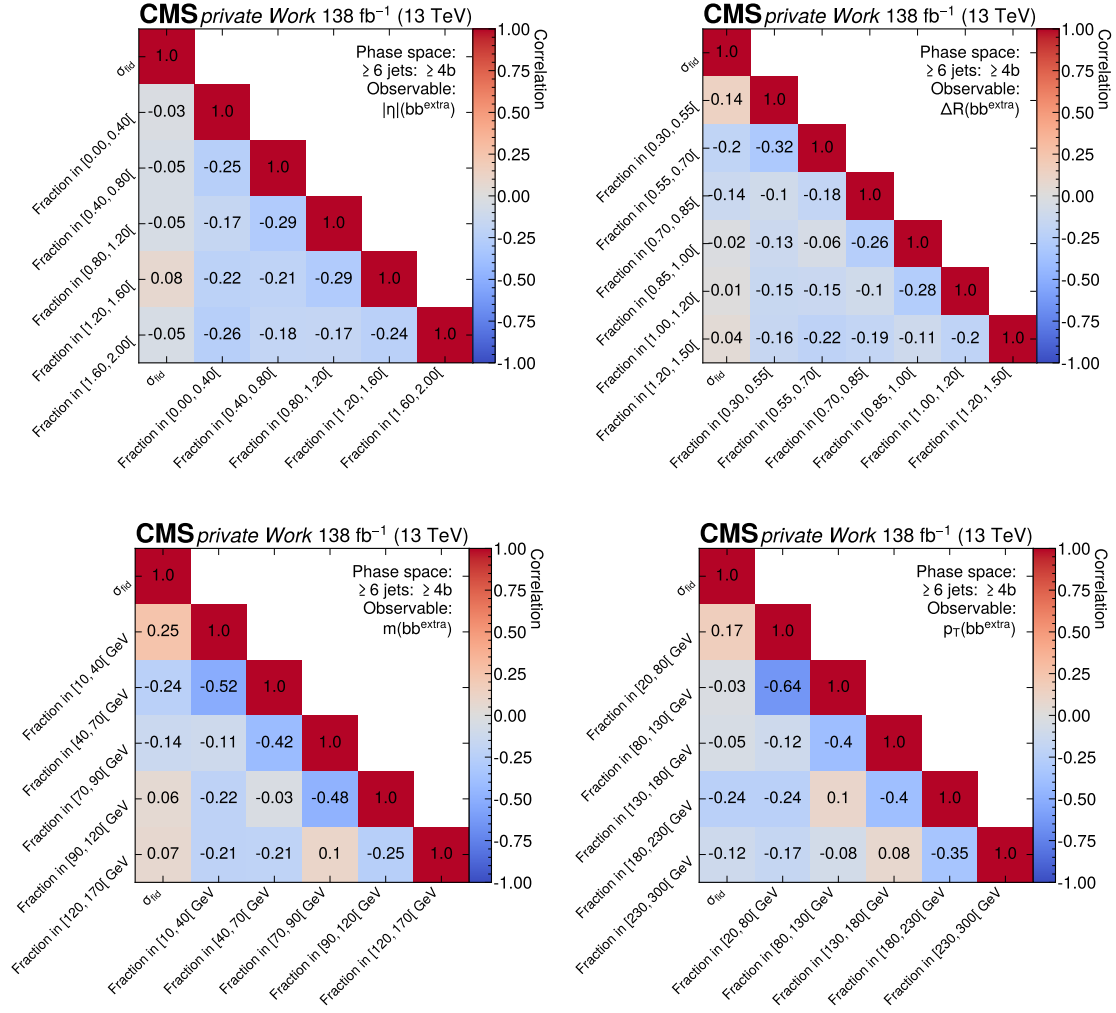


Figure A.26: Correlations between the parameters of interest $\vec{\mu}$ for the $\Delta R(\text{bb}^{\text{extra}})$, $|\eta|(\text{bb}^{\text{extra}})$, $m(\text{bb}^{\text{extra}})$ and $p_{\text{T}}(\text{bb}^{\text{extra}})$ observables in the 6j4b phase space region.

Appendix

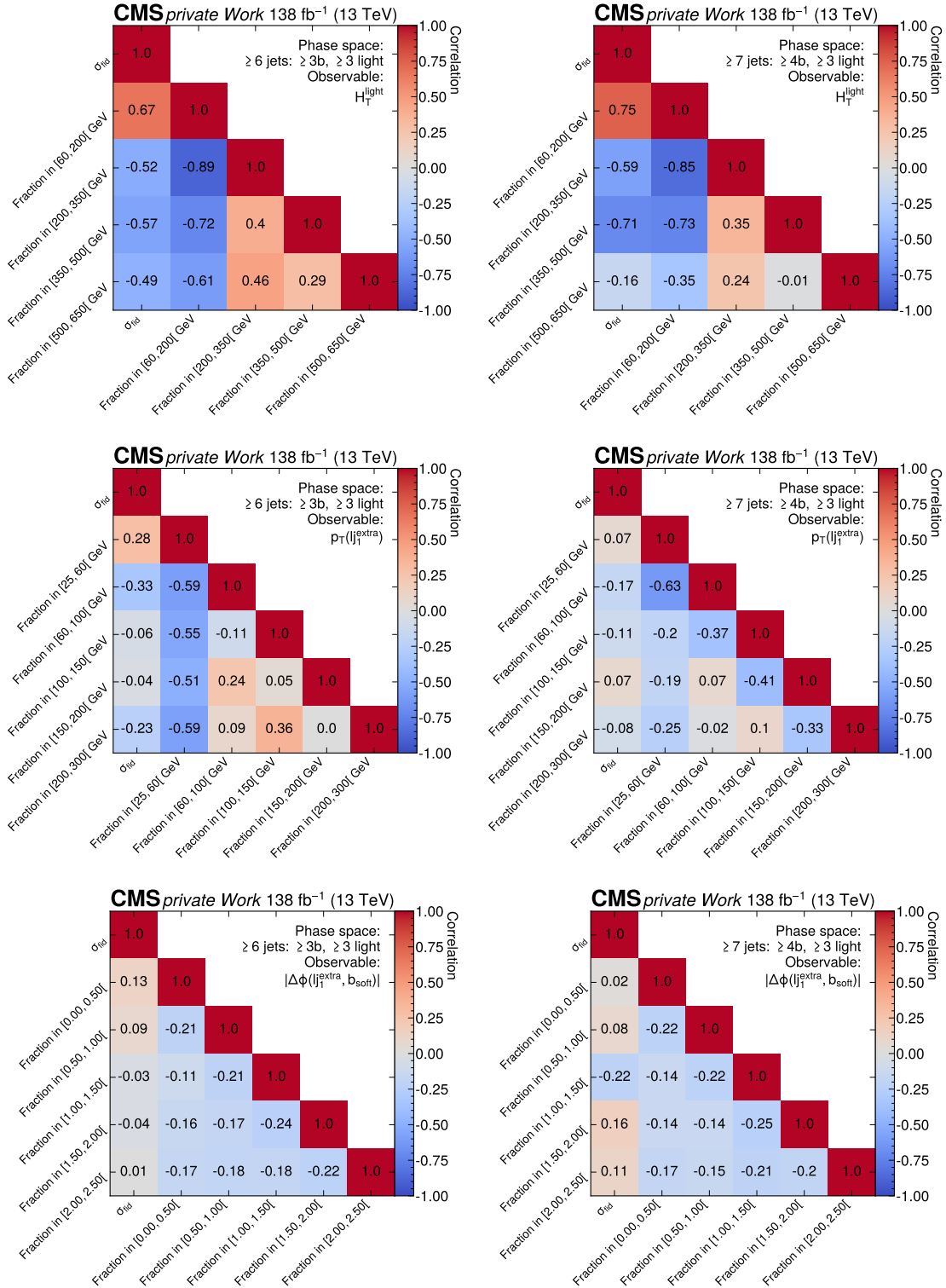


Figure A.27: Correlations between the parameters of interest $\vec{\mu}$ for the observables in the 6j3b3l and 7j4b3l phase space regions.

B Supplemental material for the $t\bar{t}$ +jets measurement

B.1 Migration matrices

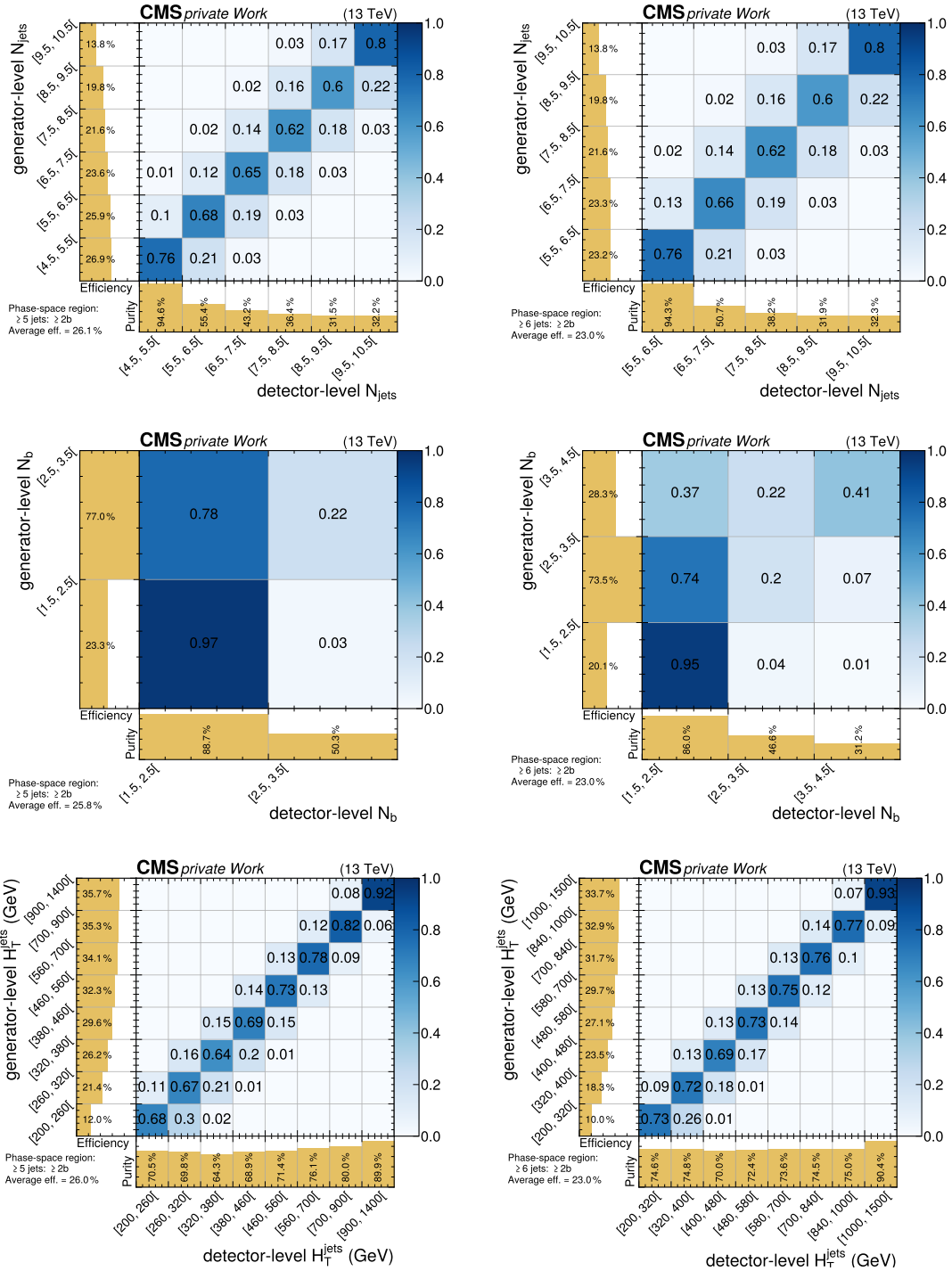


Figure B.28: Migration matrices of the observables in the 5j2b and 6j2b phase space regions. The generator-level observable is shown on the vertical axis and the detector-level observable on the horizontal axis. The migration matrix corresponds to the generator-level bins defined for the corresponding observables. Entries in the migration matrix are normalized per generator-level bin (i.e. horizontally). The panel on the vertical axis shows the selection efficiency per generator-level bin. The panel on the horizontal axis shows the purity of events per detector-level bin.

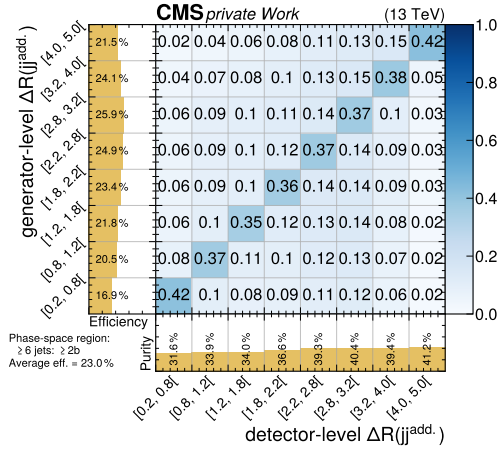


Figure B.29: Migration matrices of the observables in the 5j2b and 6j2b phase space regions relating to additional jets. The generator-level observable is shown on the vertical axis and the detector-level observable on the horizontal axis. The migration matrix corresponds to the generator-level bins defined for the corresponding observables. Entries in the migration matrix are normalized per generator-level bin (i.e. horizontally). The panel on the vertical axis shows the selection efficiency per generator-level bin. The panel on the horizontal axis shows the purity of events per detector-level bin.

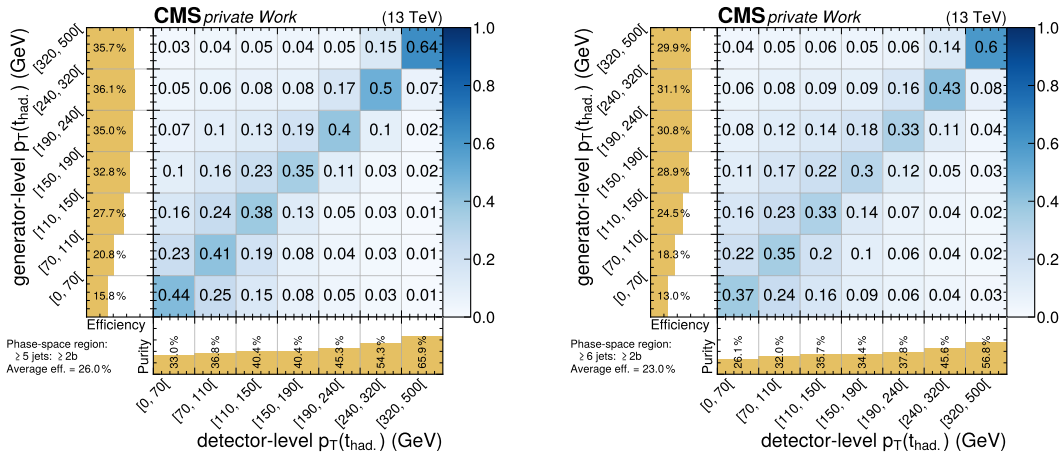


Figure B.30: Migration matrices of the observables in the 5j2b and 6j2b phase space regions relating to top quarks. The generator-level observable is shown on the vertical axis and the detector-level observable on the horizontal axis. The migration matrix corresponds to the generator-level bins defined for the corresponding observables. Entries in the migration matrix are normalized per generator-level bin (i.e. horizontally). The panel on the vertical axis shows the selection efficiency per generator-level bin. The panel on the horizontal axis shows the purity of events per detector-level bin.

B.2 Post-fit distributions

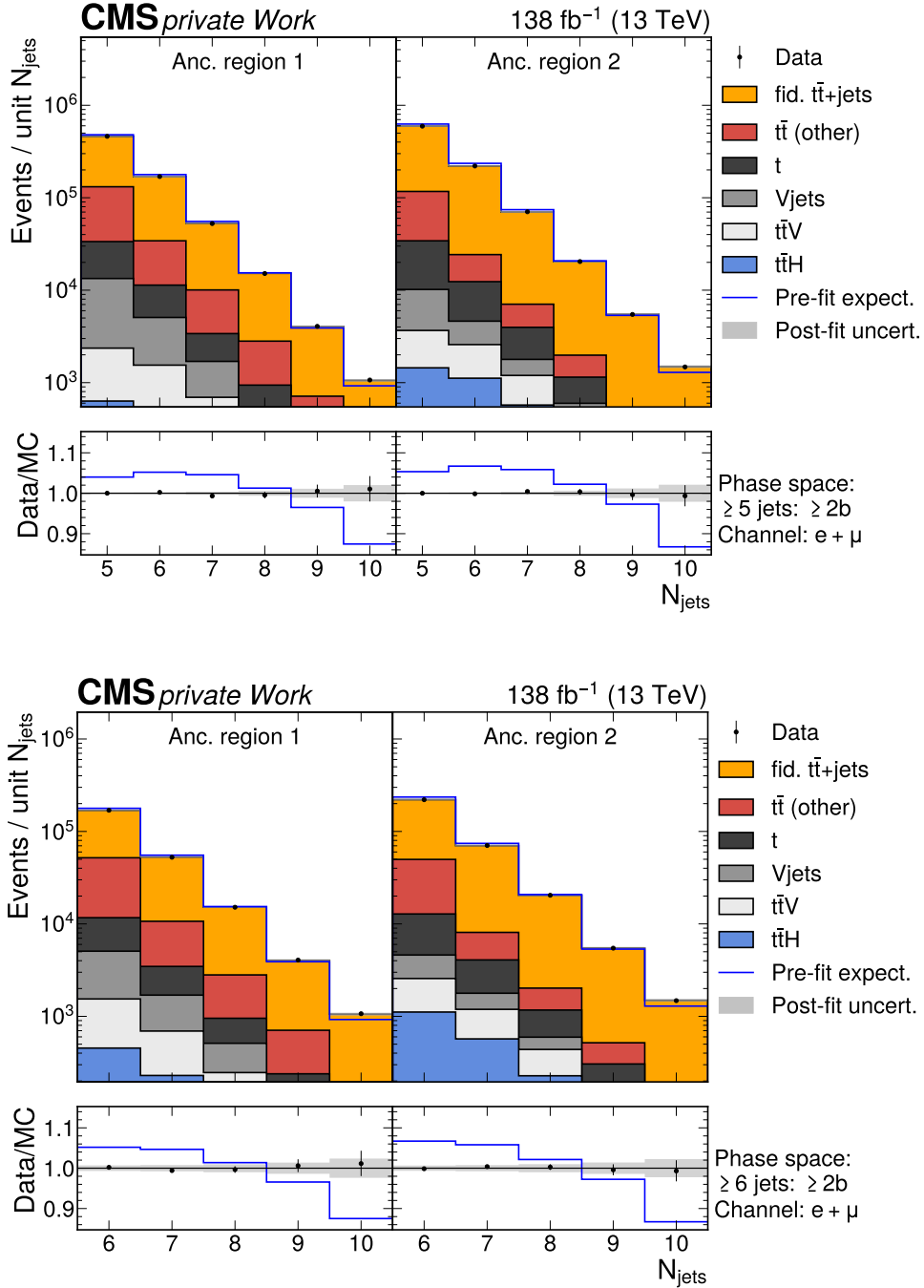


Figure B.31: **Distributions of N_{jets} in the 5j2b and 6j2b phase space regions after the fit to data.** The contributions of all processes to the detector-level phase space regions after the fit to data are shown as a stack of histograms. The distributions are shown separately for each ancillary region, but are combined across all eras and the lepton channels. The blue line indicates the sum of all processes before the fit to data. The lower panel shows the ratio of data to the processes after the fit to data. The shaded bands include all uncertainties described in Section 8.7 after profiling the nuisance parameters in the fit, estimated by sampling the predicted yields from the fit covariance matrix.

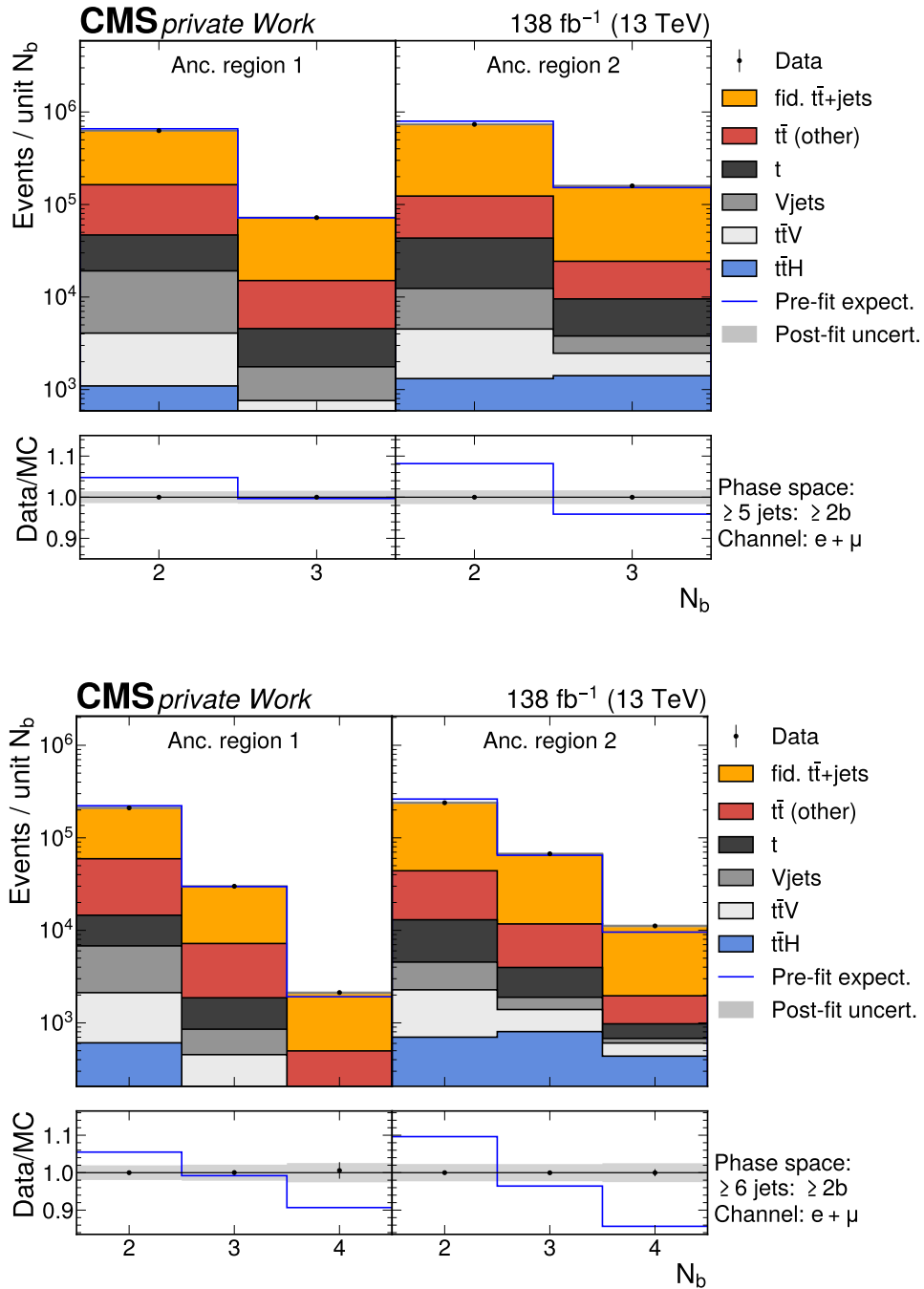


Figure B.32: Distributions of N_b in the 5j2b and 6j2b phase space regions after the fit to data. The contributions of all processes to the detector-level phase space regions after the fit to data are shown as a stack of histograms. The distributions are shown separately for each ancillary region, but are combined across all eras and the lepton channels. The blue line indicates the sum of all processes before the fit to data. The lower panel shows the ratio of data to the processes after the fit to data. The shaded bands include all uncertainties described in Section 8.7 after profiling the nuisance parameters in the fit, estimated by sampling the predicted yields from the fit covariance matrix.

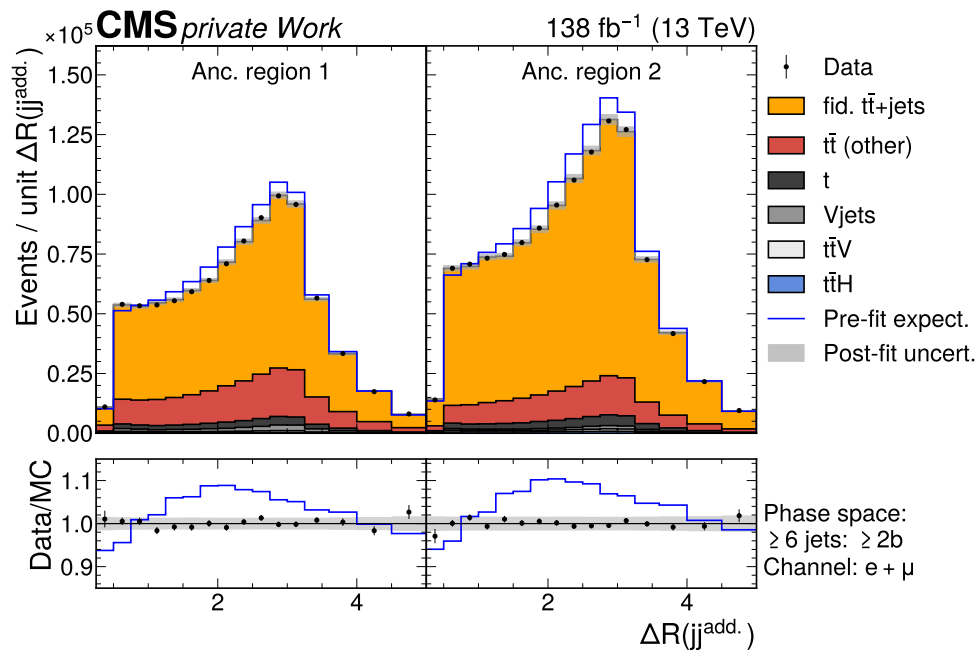


Figure B.33: **Distributions of $\Delta R(jj^{\text{add.}})$ in the 6j2b phase space region after the fit to data.** The contributions of all processes to the detector-level phase space regions after the fit to data are shown as a stack of histograms. The distributions are shown separately for each ancillary region, but are combined across all eras and the lepton channels. The blue line indicates the sum of all processes before the fit to data. The lower panel shows the ratio of data to the processes after the fit to data. The shaded bands include all uncertainties described in Section 8.7 after profiling the nuisance parameters in the fit, estimated by sampling the predicted yields from the fit covariance matrix.

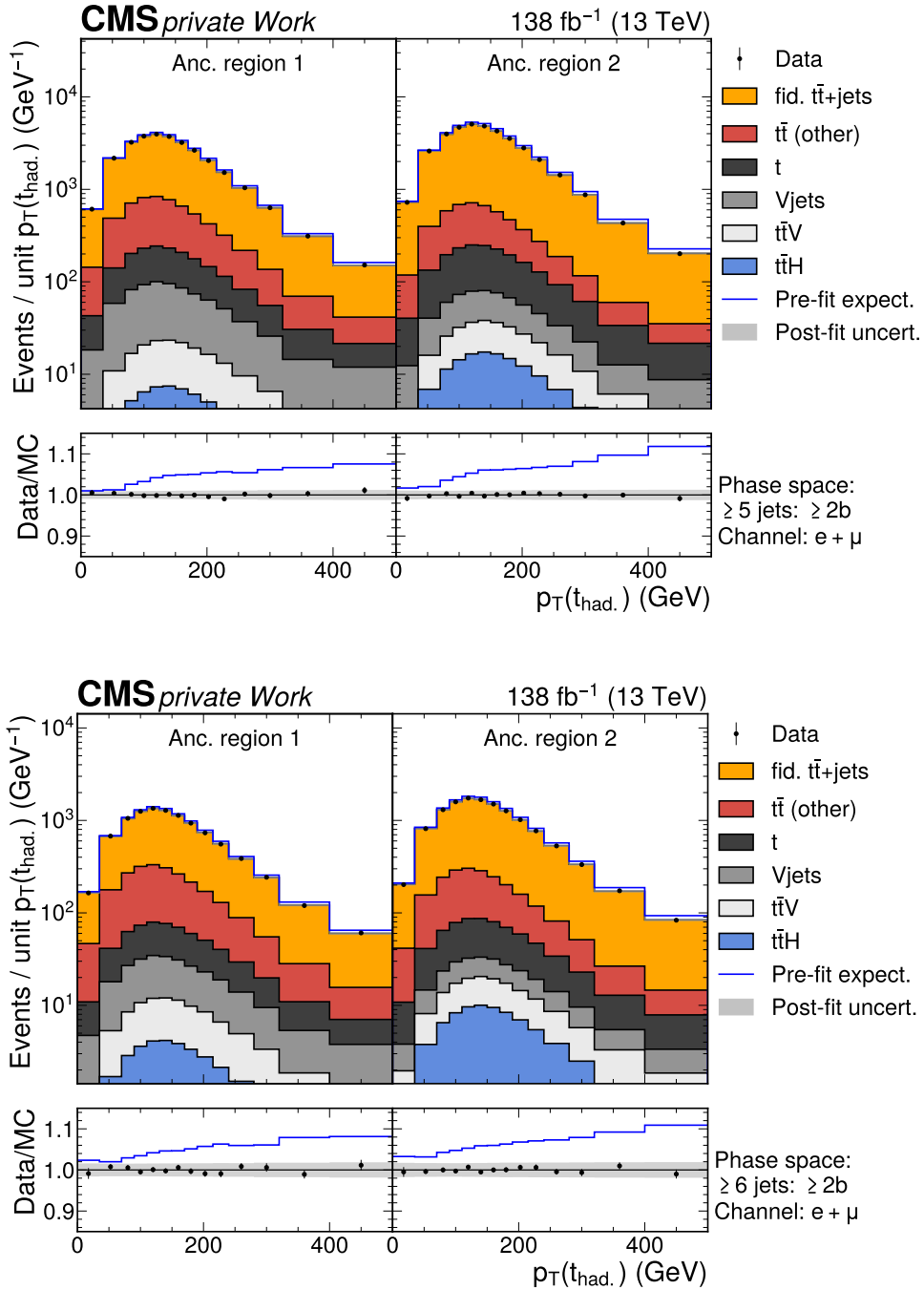


Figure B.34: **Distributions of $p_T(t_{\text{had.}})$ in the 5j2b and 6j2b phase space regions after the fit to data.** The contributions of all processes to the detector-level phase space regions after the fit to data are shown as a stack of histograms. The distributions are shown separately for each ancillary region, but are combined across all eras and the lepton channels. The blue line indicates the sum of all processes before the fit to data. The lower panel shows the ratio of data to the processes after the fit to data. The shaded bands include all uncertainties described in Section 8.7 after profiling the nuisance parameters in the fit, estimated by sampling the predicted yields from the fit covariance matrix.

B.3 Correlation of POIs

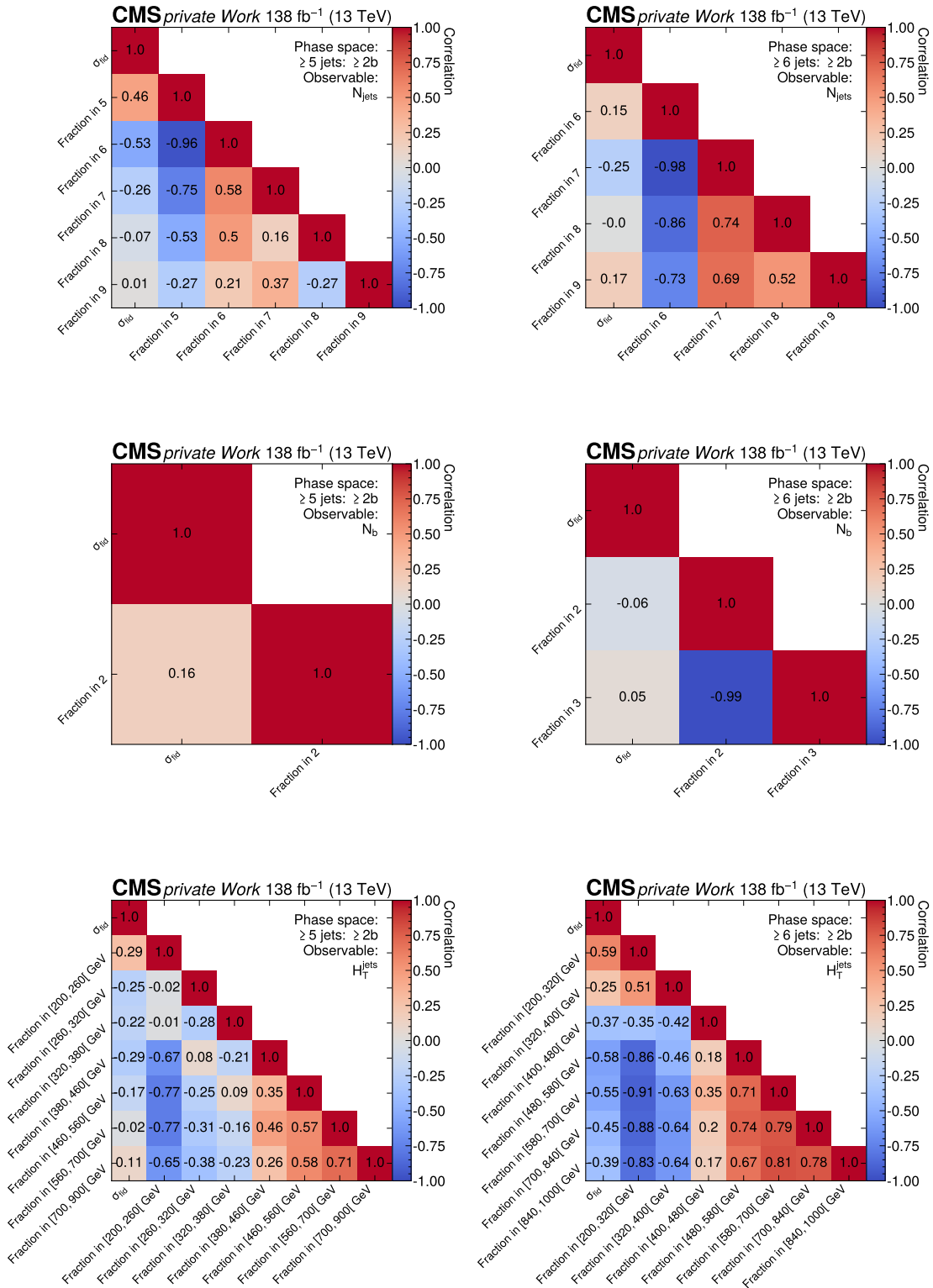


Figure B.35: Correlations between the parameters of interest $\vec{\mu}$ for the global event observables in the 5j2b (left) and 6j2b (right) phase space regions.

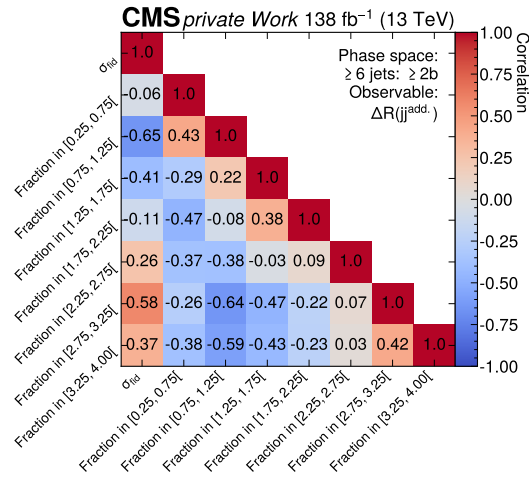


Figure B.36: Correlations between the parameters of interest $\vec{\mu}$ for the $\Delta R(jj^{\text{add.}})$ observable in the 6j2b phase space region.

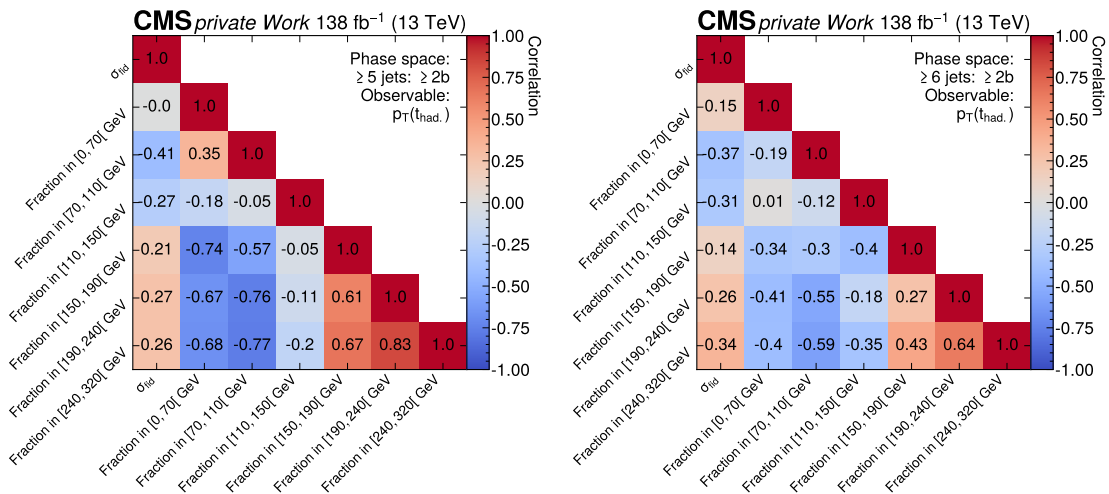


Figure B.37: Correlations between the parameters of interest $\vec{\mu}$ for the $p_T(t_{\text{had}})$ observables in the 5j2b (left) and 6j2b (right) phase space region.

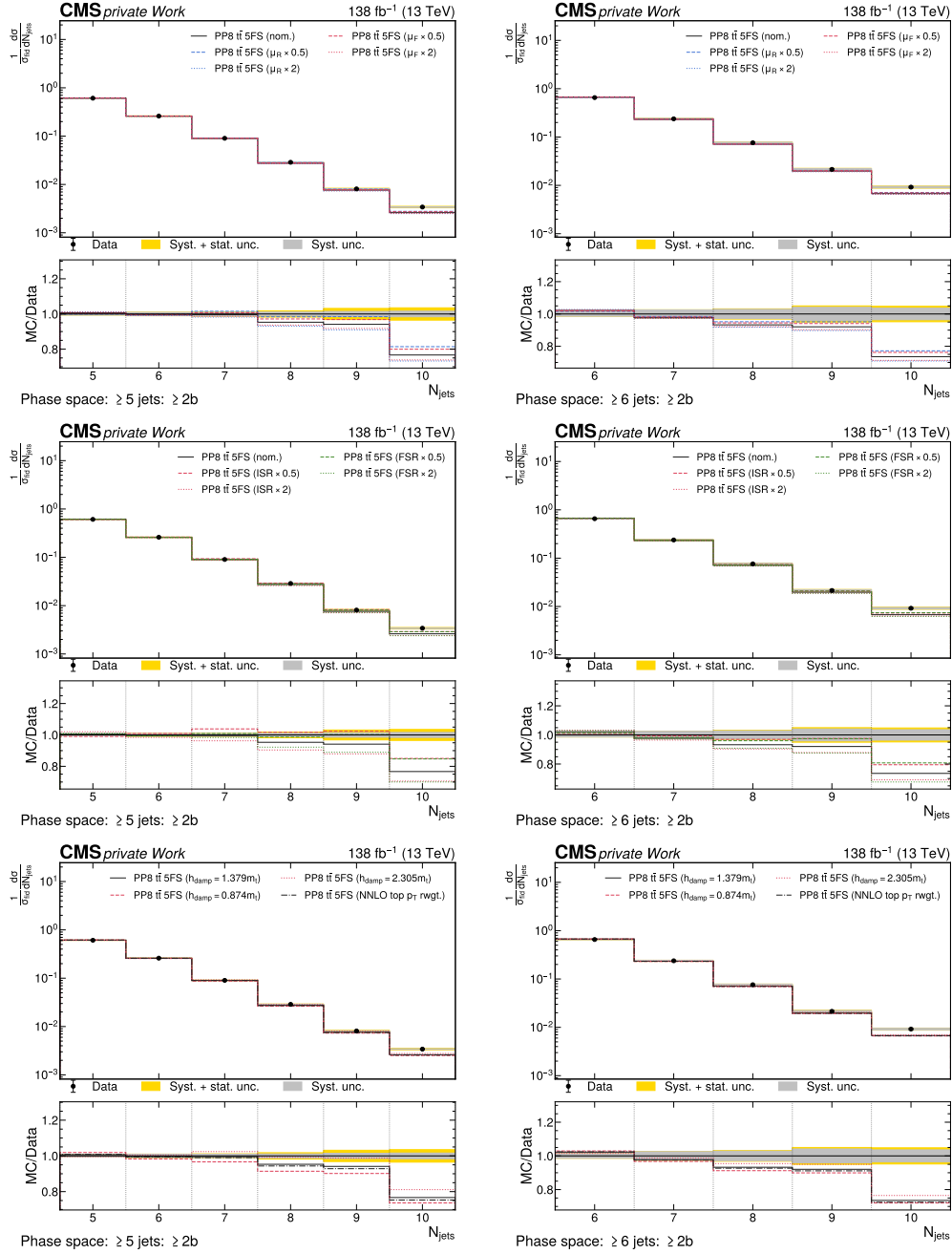
B.4 Variation of modeling parameters in the PP8 $t\bar{t}$ 5FS model

Figure B.38: Predicted and observed normalized differential cross sections of the N_{jets} observable in the 5j2b (left) and 6j2b phase space region compared to variations of modeling uncertainties in the PP8 $t\bar{t}$ 5FS model. The measured cross sections in data are indicated with black dots, with inner (outer) vertical bars indicating the systematic (total) uncertainties, also represented as gray (yellow) bands. The predictions of the PP8 $t\bar{t}$ 5FS simulation are shown in black. The plots in the first row show variations of the μ_R and μ_F scales by factors of two up and down. The plots in the second row show variations of the PS initial-state and final-state radiation by factors of two up and down. The plots in the third row show variations of the h_{damp} parameter and the reweighting of the signal model to NNLO predictions of the top quark p_T (see Section 10.1.1).

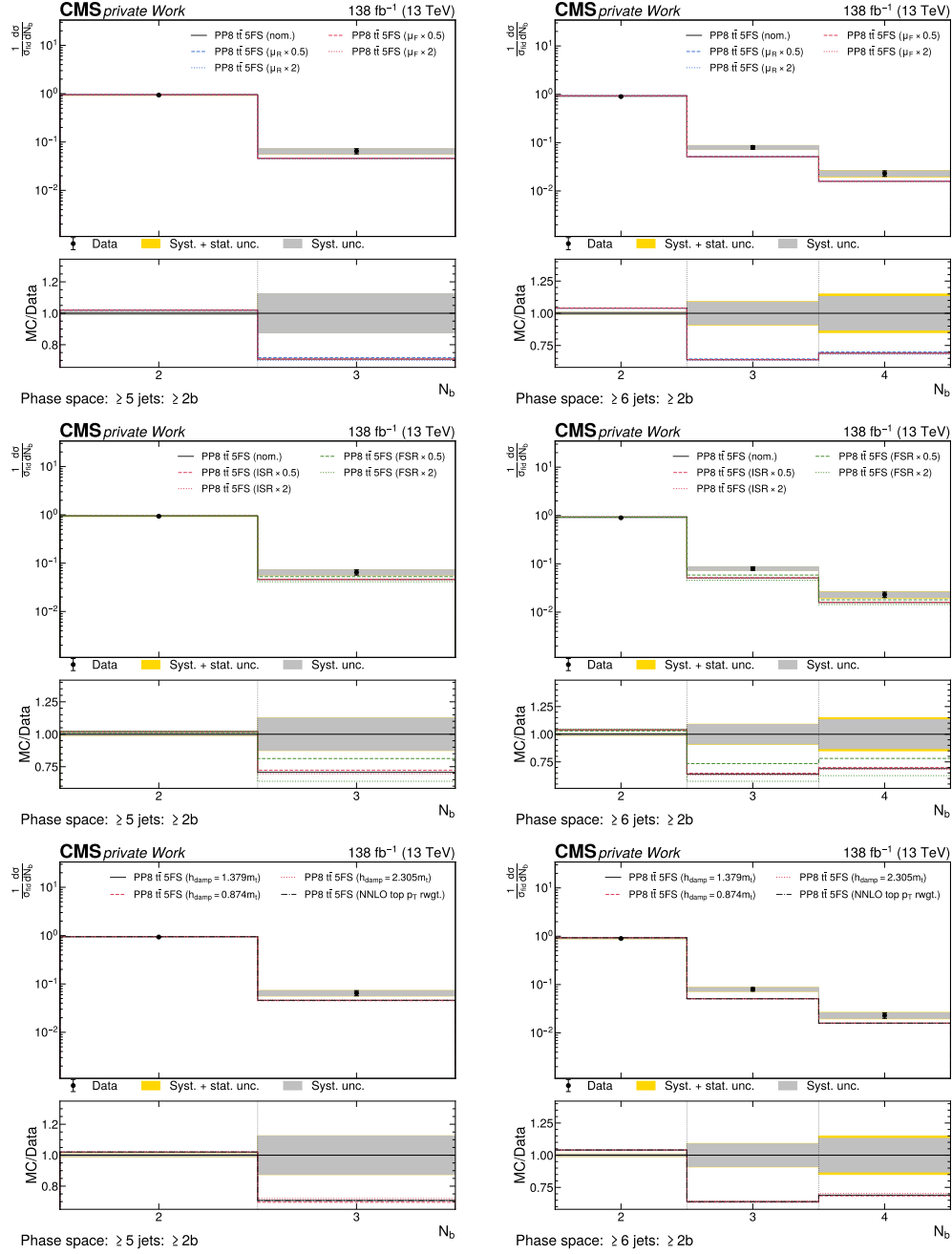


Figure B.39: Predicted and observed normalized differential cross sections of the N_b observable in the 5j2b (left) and 6j2b phase space region compared to variations of modeling uncertainties in the PP8 $t\bar{t}$ 5FS model. The measured cross sections in data are indicated with black dots, with inner (outer) vertical bars indicating the systematic (total) uncertainties, also represented as gray (yellow) bands. The predictions of the PP8 $t\bar{t}$ 5FS simulation are shown in black. The plots in the first row show variations of the μ_R and μ_F scales by factors of two up and down. The plots in the second row show variations of the PS initial-state and final-state radiation by factors of two up and down. The plots in the third row show variations of the h_{damp} parameter and the reweighting of the signal model to NNLO predictions of the top quark p_T (see Section 10.1.1).

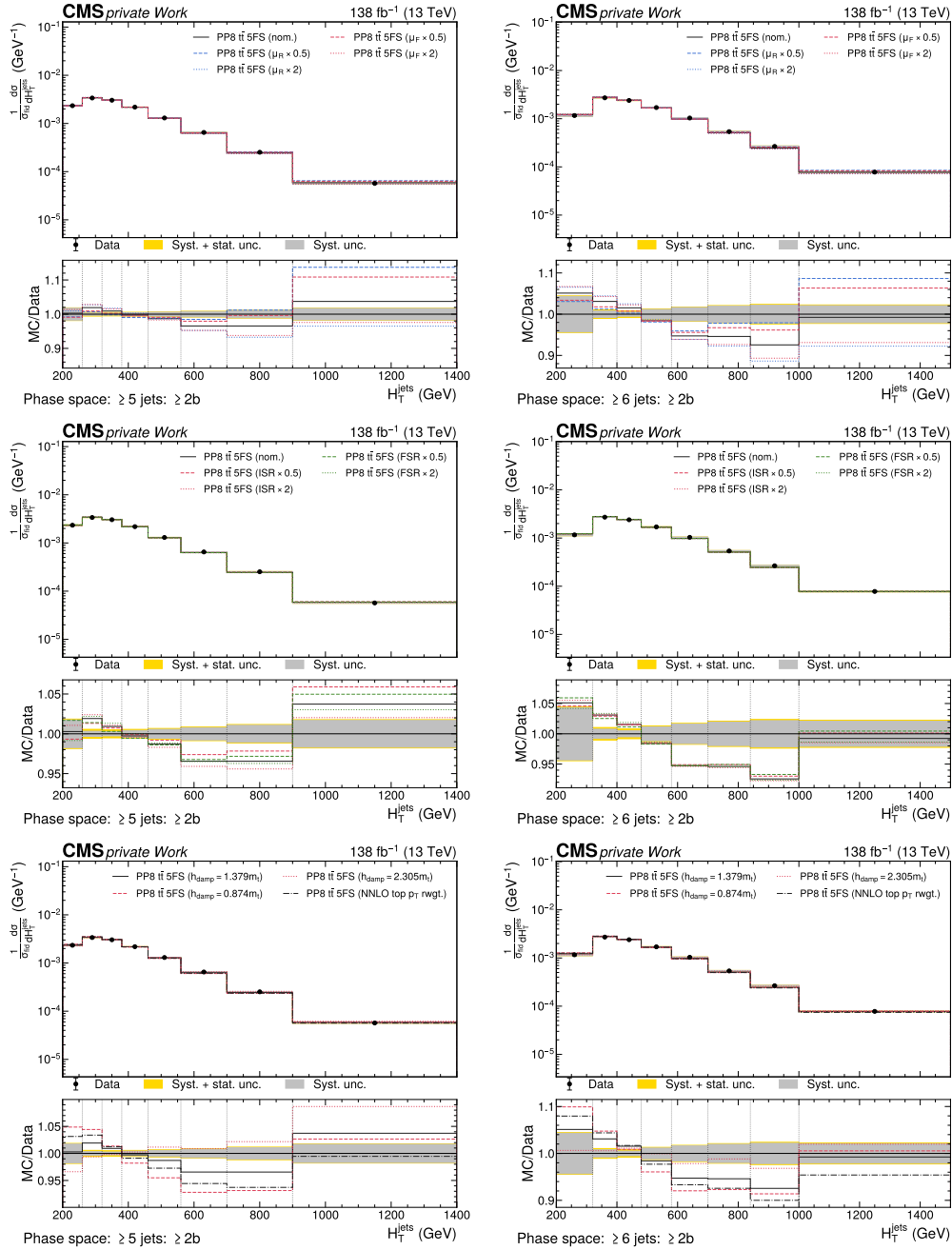


Figure B.40: Predicted and observed normalized differential cross sections of the H_T^{jets} observable in the 5j2b (left) and 6j2b phase space region compared to variations of modeling uncertainties in the PP8 $t\bar{t}$ 5FS model. The measured cross sections in data are indicated with black dots, with inner (outer) vertical bars indicating the systematic (total) uncertainties, also represented as gray (yellow) bands. The predictions of the PP8 $t\bar{t}$ 5FS simulation are shown in black. The plots in the first row show variations of the μ_R and μ_F scales by factors of two up and down. The plots in the second row show variations of the PS initial-state and final-state radiation by factors of two up and down. The plots in the third row show variations of the h_{damp} parameter and the reweighting of the signal model to NNLO predictions of the top quark p_T (see Section 10.1.1).

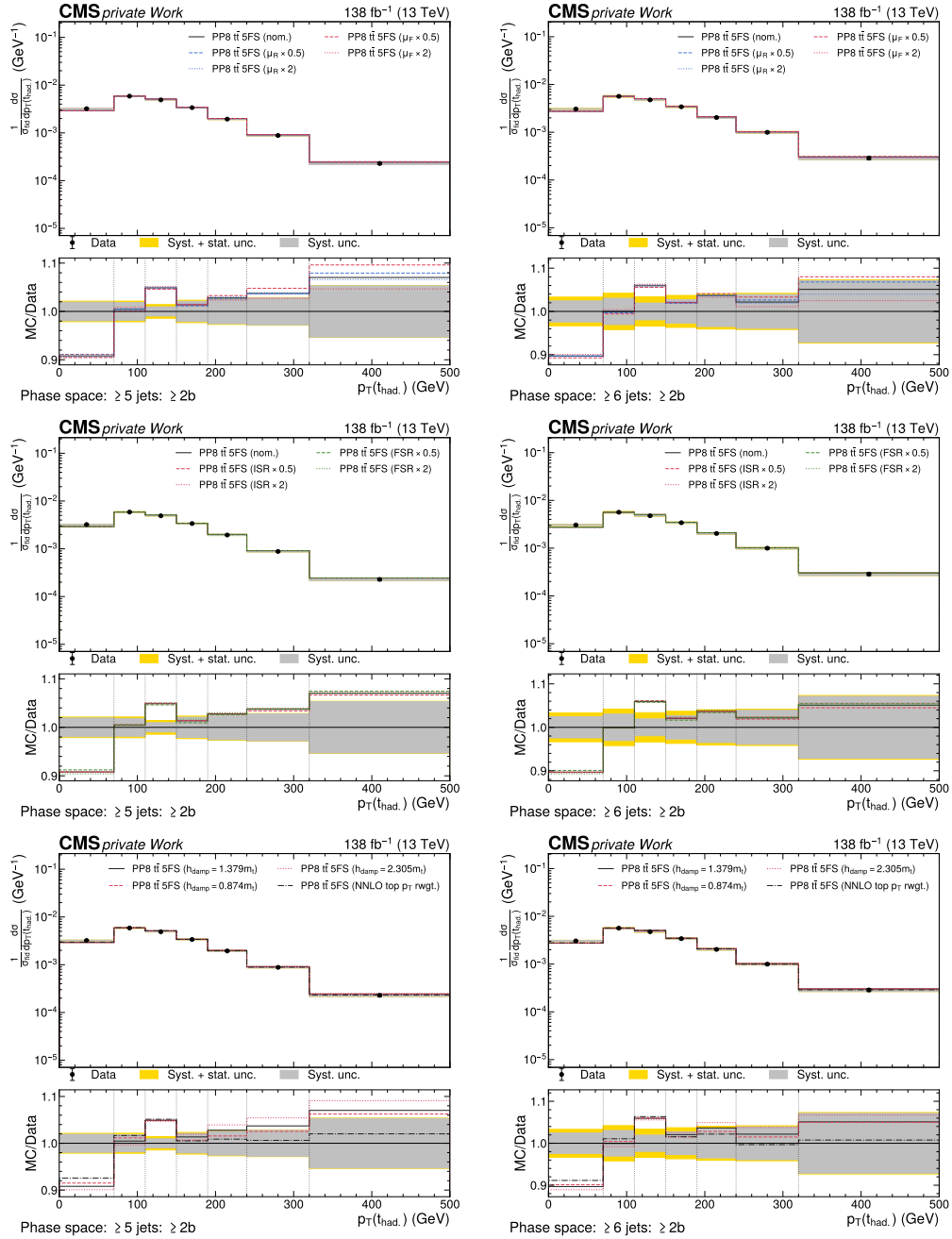


Figure B.41: Predicted and observed normalized differential cross sections of the $p_T(t_{\text{had}})$ observable in the 5j2b (left) and 6j2b phase space region compared to variations of modeling uncertainties in the PP8 $t\bar{t}$ 5FS model. The measured cross sections in data are indicated with black dots, with inner (outer) vertical bars indicating the systematic (total) uncertainties, also represented as gray (yellow) bands. The predictions of the PP8 $t\bar{t}$ 5FS simulation are shown in black. The plots in the first row show variations of the μ_R and μ_F scales by factors of two up and down. The plots in the second row show variations of the PS initial-state and final-state radiation by factors of two up and down. The plots in the third row show variations of the h_{damp} parameter and the reweighting of the signal model to NNLO predictions of the top quark p_T (see Section 10.1.1).

B.5 Unfolding of leptonic pseudo top quark momentum

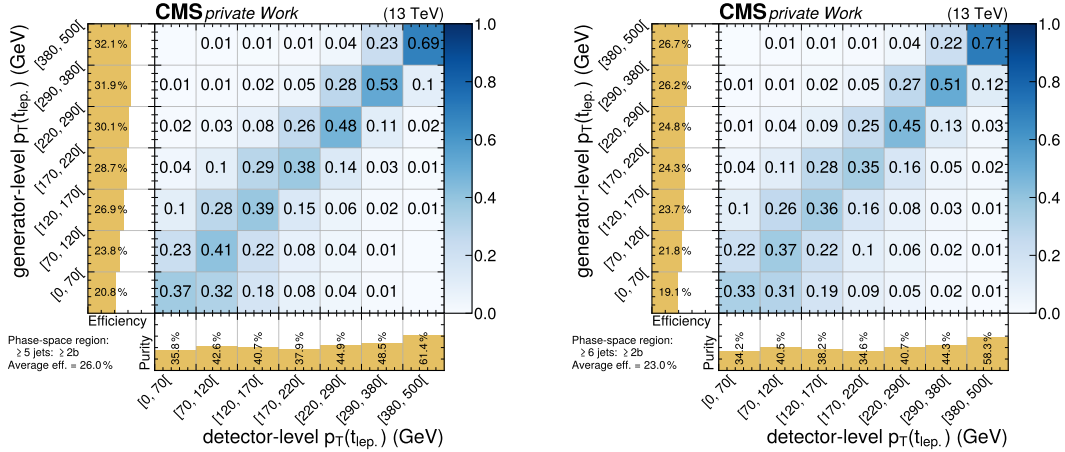


Figure B.42: Migration matrices of the $p_T(t_{lep})$ observable in the 5j2b and 6j2b phase space regions. The generator-level observable is shown on the vertical axis and the detector-level observable on the horizontal axis. The migration matrix corresponds to the generator-level bins defined for the corresponding observables. Entries in the migration matrix are normalized per generator-level bin (i.e. horizontally). The panel on the vertical axis shows the selection efficiency per generator-level bin. The panel on the horizontal axis shows the purity of events per detector-level bin.

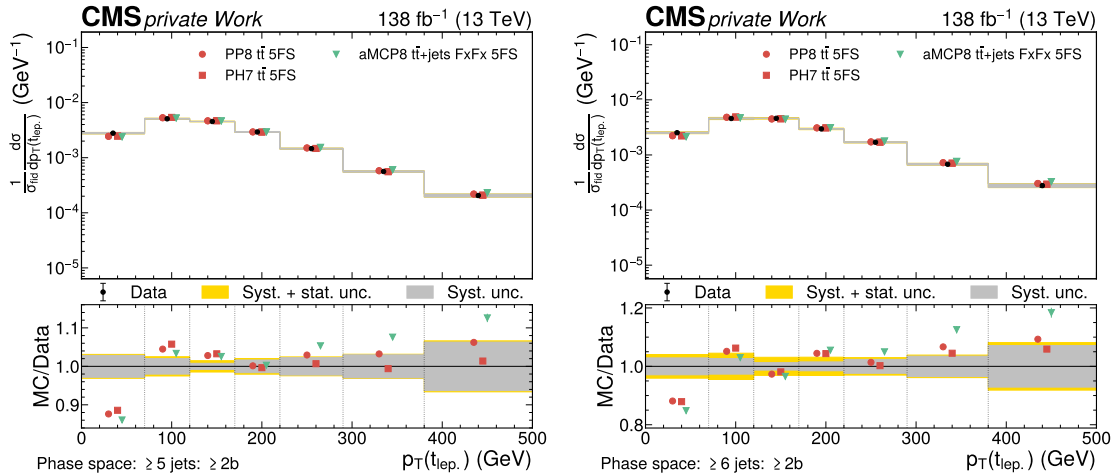


Figure B.43: Predicted and observed normalized differential cross sections of the $p_T(t_{lep})$ observables in the 5j2b (left) and 6j4b (right) phase space regions. The measured cross sections in data are indicated with black dots, with inner (outer) vertical bars indicating the systematic (total) uncertainties, also represented as gray (yellow) bands. The cross section predictions from different $t\bar{t}$ modeling approaches as introduced in Section 8.1 are shown as colored symbols with different shapes. Where the observable can exceed the visible range, the last bin contains the overflow.

B.6 Reconstruction of partonic top quark momentum

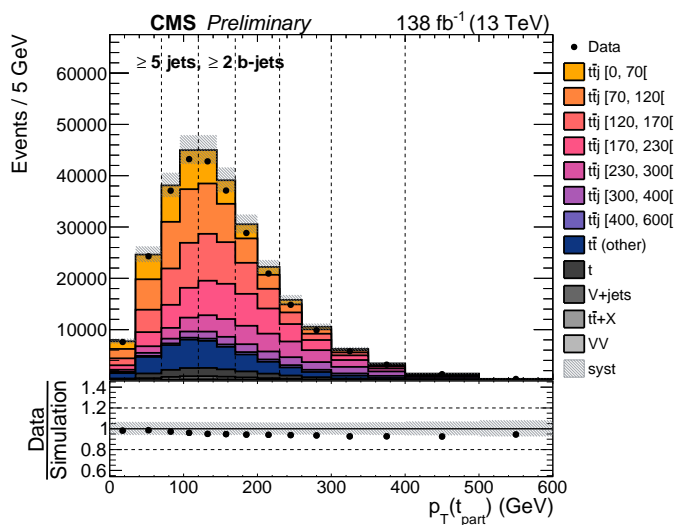


Figure B.44: **The partonic top quark p_T in the 5j2b detector-level phase space region.** The upper plots show the contributions of all processes to the detector-level phase space regions as a stack of histograms. The contributions from the signal model are separated based on the pre-defined generator-level bins indicated by different colors. Data events are shown as black dots. The lower panel shows the ratio of data w.r.t. the simulated events. Uncertainties on the simulated events from systematic uncertainty sources are indicated as grey bands.

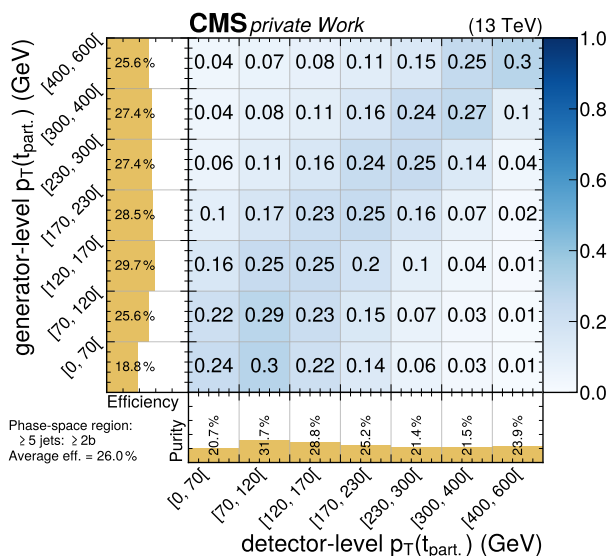


Figure B.45: **Migration matrices of the partonic top quark p_T in the 5j2b phase space region.** The generator-level observable is shown on the vertical axis and the detector-level observable on the horizontal axis. The migration matrix corresponds to the generator-level bins defined for the corresponding observables. Entries in the migration matrix are normalized per generator-level bin (i.e. horizontally). The panel on the vertical axis shows the selection efficiency per generator-level bin. The panel on the horizontal axis shows the purity of events per detector-level bin.

Acronyms

5FS five flavor scheme	59
4FS four flavor scheme	59
BDT boosted decision tree	41
CERN European Organization for Nuclear Research	1
CHS charged hadron subtraction	39
CKM Cabibbo-Kobayashi-Maskawa matrix	10
CMS Compact Muon Solenoid	2
CNN convolutional neural network	43
DGLAP Dokshitzer-Gribov-Lipatov-Altarelli-Parisi	53
DM Dark Matter	1
ECAL electromagnetic calorimeter	30
EM electromagnetic	8
fixedWP fixed working point	65
FS flavor scheme	53
FSR final-state radiation	56
GSF Gaussian sum filter	38
HCAL hadronic calorimeter	30
HLT high-level trigger	32
ISR initial-state radiation	56
L1 Level-1	32
LHC Large Hadron Collider	1
LO leading order	20
LSTM long short term memory	43
MC Monte-Carlo	2
ME matrix element	54

Acronyms

MPI multi-parton interaction	57
NN neural network	43
NNLL next-to-next-to-leading logarithm	86
NNLO next-to-next-to-leading order	23
NLO next-to-leading order	20
OOA out-of-acceptance	83
pdf parton distribution function	23
PF Particle Flow	35
POI parameter of interest	48
pp proton-proton	3
PS parton shower	56
QCD quantum chromodynamics	2
QED quantum electrodynamics	7
SC supercluster	37
SF scale factor	61
SM standard model	1
VEV vacuum expectation value	16
WP working point	44

Bibliography

1. The Particle Data Group. **Review of Particle Physics**. *Progress of Theoretical and Experimental Physics* **2022**, 083C01. <https://doi.org/10.1093/ptep/ptac097> (2022).
2. Ellis, J. **Higgs Physics**. *2013 European School of High-Energy Physics*, 117. <https://doi.org/10.5170/CERN-2015-004.117> (2015).
3. Stirling, W. J. **QCD and collider physics**. <https://cds.cern.ch/record/317239> (1991).
4. Husemann, U. **Top-quark physics: Status and prospects**. *Progress in Particle and Nuclear Physics* **95**, 48. <https://doi.org/10.1016/j.pnpnp.2017.03.002> (2017).
5. Zannoni, A. **On the Quantization of the Monoatomic Ideal Gas**. arXiv: [cond-mat/9912229](https://arxiv.org/abs/cond-mat/9912229) [[cond-mat.stat-mech](https://arxiv.org/abs/cond-mat/9912229)] (1999).
6. Dirac, P. A. M. **On the theory of quantum mechanics**. *Proceedings of the Royal Society London A* **112**, 112661. <https://doi.org/10.1098/rspa.1926.0133> (1926).
7. Pauli, W. **Über den Zusammenhang des Abschlusses der Elektronengruppen im Atom mit der Komplexstruktur der Spektren**. *Zeitschrift für Physik* **31**, 765. <https://doi.org/10.1007/BF02980631> (1925).
8. Einstein, A. **Quantentheorie des einatomigen idealen Gases**. *Sitzungsberichte der Preussischen Akademie der Wissenschaften Phys.-Math. Kl* **1924**, 261. <https://doi.org/10.1002/3527608958.ch27> (1924).
9. Bose, S. **Plancks Gesetz und Lichtquantenhypothese**. *Zeitschrift für Physik* **26**, 178. <https://doi.org/10.1007/BF01327326> (1924).
10. Fermi, E. **Versuch einer Theorie der β -Strahlen. I**. *Zeitschrift für Physik* **88**, 161. <https://doi.org/10.1007/BF01351864> (1934).
11. Feynman, R. & Gell-Mann, M. **Theory of the Fermi Interaction**. *Physical Review* **109**, 193. <https://doi.org/10.1103/PhysRev.109.193> (1958).
12. Lee, T. & Yang, C. **Question of Parity Conservation in Weak Interactions**. *Physical Review* **104**, 254. <https://doi.org/10.1103/PhysRev.104.254> (1956).
13. Glashow, S. **Partial-symmetries of weak interactions**. *Nuclear Physics* **22**, 579. [https://doi.org/10.1016/0029-5582\(61\)90469-2](https://doi.org/10.1016/0029-5582(61)90469-2) (1961).
14. Salam, A. **Weak and electromagnetic interactions**. *Nobel Lectures in Physics 1963-1970*, 547. <https://doi.org/10.1007/BF02726525> (1968).
15. Weinberg, S. **A Model of Leptons**. *Physical Review Letters* **19**, 1264. <https://doi.org/10.1103/PhysRevLett.19.1264> (1967).
16. Nambu, Y. **Dynamical Model of Elementary Particles Based on an Analogy with Superconductivity**. *Physical Review Letters* **4**, 380. <https://doi.org/10.1103/PhysRev.122.345> (1960).

Bibliography

17. Goldstone, J. **Field theories with superconductor solutions.** *Nuovo Cimento* **19**, 154. <https://doi.org/10.1007/BF02812722> (1961).
18. Goldstone, J., Salam, A. & Weinberg, S. **Broken symmetries, massless particles and gauge fields.** *Physical Review* **127**, 965. <https://doi.org/10.1103/PhysRev.127.965> (1962).
19. Nambu, Y. **Quasiparticles and gauge invariance in the theory of superconductivity.** *Physical Review* **117**, 648. <https://doi.org/10.1103/PhysRev.117.648> (1960).
20. Anderson, P. W. **Plasmons, Gauge Invariance, and Mass.** *Physical Review* **130**, 439. <https://doi.org/10.1103/PhysRev.130.439> (1963).
21. Gilbert, W. **Broken Symmetries and Massless Particles.** *Physical Review Letters* **12**, 713. <https://doi.org/10.1103/PhysRevLett.12.713> (1964).
22. Englert, F. & Brout, R. **Broken Symmetry and the Mass of Gauge Vector Mesons.** *Physical Review Letters* **13**, 321. <https://doi.org/10.1103/PhysRevLett.13.321> (1964).
23. Higgs, P. W. **Broken Symmetries, Massless Particles and Gauge Fields.** *Phys. Lett.* **12**, 132. [https://doi.org/10.1016/0031-9163\(64\)91136-9](https://doi.org/10.1016/0031-9163(64)91136-9) (1964).
24. Higgs, P. W. **Broken Symmetries and the Masses of Gauge Bosons.** *Phys. Rev. Lett.* **13**, 508. <https://doi.org/10.1103/PhysRevLett.13.508> (1964).
25. Guralnik, G. S., Hagen, C. R. & Kibble, T. W. B. **Global Conservation Laws and Massless Particles.** *Phys. Rev. Lett.* **13**, 585. <https://doi.org/10.1103/PhysRevLett.13.585> (1964).
26. Migdal, A. A. & Polyakov, A. M. **Spontaneous Breakdown of Strong Interaction Symmetry and Absence of Massless Particles.** *Zh. Eksp. Teor. Fiz.* **51**, 135 (1966).
27. Kibble, T. W. B. **Symmetry Breaking in Non-Abelian Gauge Theories.** *Phys. Rev.* **155**, 1554. <https://doi.org/10.1103/PhysRev.155.1554> (1967).
28. Higgs, P. W. **Spontaneous Symmetry Breakdown without Massless Bosons.** *Phys. Rev.* **145**, 1156. <https://doi.org/10.1103/PhysRev.145.1156> (1966).
29. The ATLAS Collaboration. **Observation of a new particle in the search for the Standard Model Higgs boson with the ATLAS detector at the LHC.** *Physics Letters B* **716**, 1. <https://doi.org/10.1016/j.physletb.2012.08.020> (2012).
30. The CMS Collaboration. **Observation of a new boson at a mass of 125 GeV with the CMS experiment at the LHC.** *Physics Letters B* **716**, 30. <https://doi.org/10.1016/j.physletb.2012.08.021> (2012).
31. Cabibbo, N. **Unitary Symmetry and Leptonic Decays.** *Phys. Rev. Lett.* **10**, 531. <https://doi.org/10.1103/PhysRevLett.10.531> (1963).
32. Kobayashi, M. & Maskawa, T. **CP-Violation in the Renormalizable Theory of Weak Interaction.** *Progress of Theoretical Physics* **49**, 652. <https://doi.org/10.1143/PTP.49.652> (1973).
33. Tomonaga, S. **On a relativistically invariant formulation of the quantum theory of wave fields.** *Prog. Theor. Phys.* **1**, 27. <https://doi.org/10.1143/PTP.1.27> (1946).
34. Schwinger, J. **On Quantum-Electrodynamics and the Magnetic Moment of the Electron.** *Phys. Rev.* **73**, 416. <https://doi.org/10.1103/PhysRev.73.416> (1948).
35. Schwinger, J. **Quantum Electrodynamics. I. A Covariant Formulation.** *Phys. Rev.* **74**, 1439. <https://doi.org/10.1103/PhysRev.74.1439> (1948).

36. Feynman, R. P. **Space-Time Approach to Quantum Electrodynamics.** *Phys. Rev.* **76**, 769. <https://doi.org/10.1103/PhysRev.76.769> (1949).
37. Feynman, R. P. **The Theory of Positrons.** *Phys. Rev.* **76**, 749. <https://doi.org/10.1103/PhysRev.76.749> (1949).
38. Feynman, R. P. **Mathematical Formulation of the Quantum Theory of Electromagnetic Interaction.** *Phys. Rev.* **80**, 440. <https://doi.org/10.1103/PhysRev.80.440> (1950).
39. Dyson, F. J. **The Radiation Theories of Tomonaga, Schwinger, and Feynman.** *Phys. Rev.* **75**, 486. <https://doi.org/10.1103/PhysRev.75.486> (1949).
40. Dyson, F. J. **The S Matrix in Quantum Electrodynamics.** *Phys. Rev.* **75**, 1736. <https://doi.org/10.1103/PhysRev.75.1736> (1949).
41. Dirac, P. A. M. **The Quantum Theory of the Electron.** *Proceedings of the Royal Society of London A* **117**, 610. <https://doi.org/10.1098/rspa.1928.0023> (1928).
42. Noether, E. **Invariante Variationsprobleme.** *Nachrichten von der Gesellschaft der Wissenschaften zu Göttingen, Mathematisch-Physikalische Klasse* **1918**, 235. <https://doi.org/10.1080/00411457108231446> (1918).
43. Weyl, H. **Eine neue Erweiterung der Relativitätstheorie.** *Annalen der Physik* **364**, 101. <https://doi.org/10.1002/andp.19193641002> (1919).
44. Wu, C. S., Ambler, E., Hayward, R. W., Hoppes, D. D. & Hudson, R. P. **Experimental Test of Parity Conservation in Beta Decay.** *Phys. Rev.* **105**, 1413. <https://doi.org/10.1103/PhysRev.105.1413> (1957).
45. LHC Higgs Cross Section Working Group. **Handbook of LHC Higgs Cross Sections: 3. Higgs Properties: Report of the LHC Higgs Cross Section Working Group** <https://doi.org/10.5170/CERN-2013-004> (2013).
46. The CMS Collaboration. **A portrait of the Higgs boson by the CMS experiment ten years after the discovery.** *Nature* **607**, 60 (2022).
47. Yukawa, H. **On the Interaction of Elementary Particles. I.** *Progress of Theoretical Physics Supplement* **1**, 1. <https://doi.org/10.1143/PTPS.1.1> (1955).
48. Gell-Mann, M. **Symmetries of baryons and mesons.** *Physical Review* **125**, 1067. <https://doi.org/10.1103/PhysRev.125.1067> (1962).
49. Gell-Mann, M. **A Schematic Model of Baryons and Mesons.** *Phys. Lett.* **8**, 214. [https://doi.org/10.1016/S0031-9163\(64\)92001-3](https://doi.org/10.1016/S0031-9163(64)92001-3) (1964).
50. Zweig, G. **An SU(3) model for strong interaction symmetry and its breaking. Version 2.** *Developments in the quark theory of hadrons. Vol. 1. 1964 - 1978*, 22. <https://doi.org/10.17181/CERN-TH-412> (1964).
51. Gross, D. J. & Wilczek, F. **Ultraviolet Behavior of Nonabelian Gauge Theories.** *Phys. Rev. Lett.* **30**, 1343. <https://doi.org/10.1103/PhysRevLett.30.1343> (1973).
52. Gross, D. J. & Wilczek, F. **Asymptotically Free Gauge Theories. I.** *Phys. Rev. D* **8**, 3633. <https://doi.org/10.1103/PhysRevD.8.3633> (1973).
53. Gross, D. J. & Wilczek, F. **Asymptotically free gauge theories. II.** *Phys. Rev. D* **9**, 980. <https://doi.org/10.1103/PhysRevD.9.980> (1974).
54. Politzer, H. D. **Reliable Perturbative Results for Strong Interactions?** *Phys. Rev. Lett.* **30**, 1346. <https://doi.org/10.1103/PhysRevLett.30.1346> (1973).

Bibliography

55. The CMS Collaboration. **Measurement and QCD analysis of double-differential inclusive jet cross sections in pp collisions at $\sqrt{s} = 8$ TeV and cross section ratios to 2.76 and 7 TeV.** *JHEP* **03**, 156. [https://doi.org/10.1007/JHEP03\(2017\)156](https://doi.org/10.1007/JHEP03(2017)156) (2017).
56. Dirac, P. A. M. **Quantum theory of emission and absorption of radiation.** *Proceedings of the Royal Society London A* **114**, 243. <https://doi.org/10.1098/rspa.1927.0039> (1927).
57. The CDF Collaboration. **Observation of Top Quark Production in $\bar{p}p$ Collisions with the Collider Detector at Fermilab.** *Phys. Rev. Lett.* **74**, 2626. <https://doi.org/10.1103/PhysRevLett.74.2626> (1995).
58. The D0 Collaboration. **Observation of the Top Quark.** *Phys. Rev. Lett.* **74**, 2632. <https://doi.org/10.1103/PhysRevLett.74.2632> (1995).
59. Czakon, M., Fiedler, P. & Mitov, A. **Total Top-Quark Pair-Production Cross Section at Hadron Colliders Through $\mathcal{O}(\alpha_s^4)$.** *Phys. Rev. Lett.* **110**, 252004. <https://doi.org/10.1103/PhysRevLett.110.252004> (2013).
60. The CMS Collaboration. **First measurement of the top quark pair production cross section in proton-proton collisions at $\sqrt{s} = 13.6$ TeV.** Submitted to JHEP. arXiv: [2303.10680](https://arxiv.org/abs/2303.10680) [hep-ex] (2023).
61. The CMS Collaboration. **Measurement of the ratio $\mathcal{B}(t \rightarrow Wb)/\mathcal{B}(t \rightarrow Wq)$ in pp collisions at $\sqrt{s} = 8$ TeV.** *Phys. Lett. B* **736**, 33. <https://doi.org/10.1016/j.physletb.2014.06.076> (2014).
62. The UA1 Collaboration. **Experimental observation of isolated large transverse energy electrons with associated missing energy at $\sqrt{s} = 540$ GeV.** *Phys. Lett. B* **122**, 103. [https://doi.org/10.1016/0370-2693\(83\)91177-2](https://doi.org/10.1016/0370-2693(83)91177-2) (1983).
63. The UA2 Collaboration. **Observation of single isolated electrons of high transverse momentum in events with missing transverse energy at the CERN anti-p p collider.** *Phys. Lett. B* **122**, 476. [https://doi.org/10.1016/0370-2693\(83\)91638-5](https://doi.org/10.1016/0370-2693(83)91638-5) (1983).
64. The UA1 Collaboration. **Experimental observation of lepton pairs of invariant mass around 95 GeV/c² at the CERN SPS collider.** *Phys. Lett. B* **126**, 398. [https://doi.org/10.1016/0370-2693\(83\)90188-0](https://doi.org/10.1016/0370-2693(83)90188-0) (1983).
65. The UA2 Collaboration. **Evidence for the production of neutral intermediate vector bosons of mass 90 GeV/c² in $\bar{p}p$ collisions.** *Phys. Lett. B* **129**, 130. [https://doi.org/10.1016/0370-2693\(83\)90825-2](https://doi.org/10.1016/0370-2693(83)90825-2) (1983).
66. Lopienska, E. **The CERN accelerator complex, layout in 2022.** General Photo. <https://cds.cern.ch/record/2800984> (2022).
67. The LHCb Collaboration. **The LHCb Detector at the LHC.** *Journal of Instrumentation* **3**, S08005. <https://doi.org/10.1088/1748-0221/3/08/S08005> (2008).
68. The ALICE Collaboration. **The ALICE experiment at the CERN LHC.** *Journal of Instrumentation* **3**, S08002. <https://doi.org/10.1088/1748-0221/3/08/S08002> (2008).
69. The ATLAS Collaboration. **The ATLAS Experiment at the CERN Large Hadron Collider.** *Journal of Instrumentation* **3**, S08003. <https://doi.org/10.1088/1748-0221/3/08/S08003> (2008).
70. The CMS Collaboration. **The CMS experiment at the CERN LHC.** *Journal of Instrumentation* **3**, S08004. <https://doi.org/10.1088/1748-0221/3/08/S08004> (2008).

71. Evans, L. & Bryant, P. **LHC Machine**. *Journal of Instrumentation* **3**, S08001. <https://doi.org/10.1088/1748-0221/3/08/S08001> (2008).
72. Sakuma, T. **Cutaway diagrams of CMS detector**. General Photo. <https://cds.cern.ch/record/2665537> (2019).
73. The CMS Collaboration. **The CMS tracker system project: Technical Design Report** tech. rep. (1997). <https://cds.cern.ch/record/368412>.
74. The CMS Collaboration. **The CMS tracker: addendum to the Technical Design Report** tech. rep. (2000). <https://cds.cern.ch/record/490194>.
75. The CMS Collaboration. **The CMS Phase-1 Pixel Detector Upgrade** tech. rep. (2020). <https://cds.cern.ch/record/2745805>.
76. The CMS Collaboration. **Performance summary of AK4 jet b tagging with data from proton-proton collisions at 13 TeV with the CMS detector** tech. rep. (2023). <https://cds.cern.ch/record/2854609>.
77. The CMS Collaboration. **The CMS electromagnetic calorimeter project: Technical Design Report** tech. rep. (1997). <https://cds.cern.ch/record/349375>.
78. The CMS Collaboration. **Changes to CMS ECAL electronics: addendum to the Technical Design Report** tech. rep. (2002). <https://cds.cern.ch/record/581342>.
79. The CMS Collaboration. **Technical proposal for the upgrade of the CMS detector through 2020** tech. rep. (2011). <https://cds.cern.ch/record/1355706>.
80. The CMS Collaboration. **The CMS hadron calorimeter project: Technical Design Report** tech. rep. (1997). <https://cds.cern.ch/record/357153>.
81. The CMS Collaboration. **CMS Technical Design Report for the Phase 1 Upgrade of the Hadron Calorimeter** tech. rep. (2012). <https://cds.cern.ch/record/1481837>.
82. The CMS Collaboration. **The CMS muon project: Technical Design Report** tech. rep. (1997). <https://cds.cern.ch/record/343814>.
83. The CMS Collaboration. **Performance of the CMS muon detector and muon reconstruction with proton-proton collisions at $\sqrt{s} = 13$ TeV**. *JINST* **13**, P06015. <https://doi.org/10.1088/1748-0221/13/06/P06015> (2018).
84. Sjöstrand, T. *et al.* **An Introduction to PYTHIA 8.2**. *Comput. Phys. Commun.* **191**, 159. <https://doi.org/10.1016/j.cpc.2015.01.024> (2015).
85. The CMS Collaboration. **Performance of the CMS Level-1 trigger in proton-proton collisions at $\sqrt{s} = 13$ TeV**. *JINST* **15**, P10017. <https://doi.org/10.1088/1748-0221/15/10/P10017> (2020).
86. The CMS Collaboration. **The CMS trigger system**. *JINST* **12**, P01020. <https://doi.org/10.1088/1748-0221/12/01/P01020> (2017).
87. The CMS Collaboration. **Simulation of the Silicon Strip Tracker pre-amplifier in early 2016 data** tech. rep. (2020). <https://cds.cern.ch/record/2740688>.
88. The CMS Collaboration. **Description and performance of track and primary-vertex reconstruction with the CMS tracker**. *JINST* **9**, P10009. <https://doi.org/10.1088/1748-0221/9/10/P10009> (2014).
89. Billoir, P. **Progressive track recognition with a Kalman-like fitting procedure**. *Computer Physics Communications* **57**, 390. [https://doi.org/10.1016/0010-4655\(89\)90249-X](https://doi.org/10.1016/0010-4655(89)90249-X) (1989).
90. Billoir, P. & Qian, S. **Simultaneous pattern recognition and track fitting by the Kalman filtering method**. *Nuclear Instruments and Methods in Physics Research A* **294**, 219. [https://doi.org/10.1016/0168-9002\(90\)91835-Y](https://doi.org/10.1016/0168-9002(90)91835-Y) (1990).

Bibliography

91. Rose, K. **Deterministic annealing for clustering, compression, classification, regression, and related optimization problems.** *Proceedings of the IEEE* **86**, 2210. <https://doi.org/10.1109/5.726788> (1998).
92. Waltenberger, W., Frühwirth, R. & Vanlaer, P. **Adaptive vertex fitting.** *Journal of Physics G* **34**, N343. <https://doi.org/10.1088/0954-3899/34/12/N01> (2007).
93. The CMS Collaboration. **Particle-flow reconstruction and global event description with the CMS detector.** *JINST* **12**, P10003. <https://doi.org/10.1088/1748-0221/12/10/P10003> (2017).
94. The CMS Collaboration. **Electron and photon reconstruction and identification with the CMS experiment at the CERN LHC.** *JINST* **16**, P05014. <https://doi.org/10.1088/1748-0221/16/05/P05014> (2021).
95. Frühwirth, R. **Track fitting with non-Gaussian noise.** *Computer Physics Communications* **100**, 1. [https://doi.org/10.1016/S0010-4655\(96\)00155-5](https://doi.org/10.1016/S0010-4655(96)00155-5) (1997).
96. The CMS Collaboration. **Reconstruction of Electrons with the Gaussian-Sum Filter in the CMS Tracker at the LHC** tech. rep. (2005). <https://cds.cern.ch/record/815410>.
97. Cacciari, M., Salam, G. P. & Soyez, G. **The anti- k_T jet clustering algorithm.** *JHEP* **04**, 063. <https://doi.org/10.1088/1126-6708/2008/04/063> (2008).
98. Cacciari, M., Salam, G. P. & Soyez, G. **FastJet user manual.** *Eur. Phys. J. C* **72**, 1896. <https://doi.org/10.1140/epjc/s10052-012-1896-2> (2012).
99. The CMS Collaboration. **Jet energy scale and resolution in the CMS experiment in pp collisions at 8 TeV.** *JINST*, P02014. <https://doi.org/10.1088/1748-0221/12/02/P02014> (2017).
100. The CMS Collaboration. **Identification of heavy-flavour jets with the CMS detector in pp collisions at 13 TeV.** *JINST* **13**, P05011. <https://doi.org/10.1088/1748-0221/13/05/P05011> (2018).
101. Bols, E., Kieseler, J., Verzetti, M., Stoye, M. & Stakia, A. **Jet flavour classification using DeepJet.** *JINST* **15**, P12012. <https://doi.org/10.1088/1748-0221/15/12/p12012> (2020).
102. LeCun, Y. *et al.* **Handwritten digit recognition with a back-propagation network.** *Advances in neural information processing systems* **2**. <https://doi.org/10.5555/109230.109279> (1989).
103. Hochreiter, S. & Schmidhuber, J. **Long short-term memory.** *Neural computation* **9**, 1735. <https://doi.org/10.1162/neco.1997.9.8.1735> (1997).
104. Cowan, G., Cranmer, K., Gross, E. & Vitells, O. **Asymptotic formulae for likelihood-based tests of new physics.** *Eur. Phys. J. C* **71**. [Erratum: *Eur.Phys.J.C* **73**, 2501 (2013)], 1554. <https://doi.org/10.1140/epjc/s10052-011-1554-0> (2011).
105. Neyman, J. & Pearson, E. S. **On the Problem of the Most Efficient Tests of Statistical Hypotheses.** *Philosophical Transactions of the Royal Society of London Series A* **231**, 289 (1933).
106. Wilks, S. S. **The Large-Sample Distribution of the Likelihood Ratio for Testing Composite Hypotheses.** *The Annals of Mathematical Statistics* **9**, 60–62. <https://doi.org/10.1214/aoms/1177732360> (1938).
107. Jansen, M. & Claeskens, G. **Cramér–Rao Inequality.** *International Encyclopedia of Statistical Science*, 322. https://doi.org/10.1007/978-3-642-04898-2_197 (2011).

108. Wertz, S. *Smoofit: a package for smooth binned likelihood fits* Accessed: 2023-05-24. 2022. <https://smoofit.readthedocs.io/en/latest/index.html>.
109. Bradbury, J. *et al.* *JAX: composable transformations of Python+NumPy programs* Accessed: 2023-05-24. 2018. <http://github.com/google/jax>.
110. Iqbal, M. A. *Looking for new physics: Search for anomalous gauge couplings in WW and WZ production at 13 TeV using the CMS experiment* PhD thesis (Karlsruhe Institute of Technology (KIT), 2020). <https://publish.etp.kit.edu/record/21980>.
111. Dokshitzer, Y. L. **Calculation of the Structure Functions for Deep Inelastic Scattering and e^+e^- Annihilation by Perturbation Theory in Quantum Chromodynamics.** *Sov. Phys. JETP* **46**, 641 (1977).
112. Gribov, V. N. & Lipatov, L. N. **Deep inelastic $e p$ scattering in perturbation theory.** *Sov. J. Nucl. Phys.* **15**, 438. [https://doi.org/10.1016/0370-2693\(71\)90576-4](https://doi.org/10.1016/0370-2693(71)90576-4) (1972).
113. Altarelli, G. & Parisi, G. **Asymptotic freedom in parton language.** *Nuclear Physics B* **126**, 298. [https://doi.org/10.1016/0550-3213\(77\)90384-4](https://doi.org/10.1016/0550-3213(77)90384-4) (1977).
114. Politzer, H. D. **Asymptotic freedom: An approach to strong interactions.** *Physics Reports* **14**, 129 (1974).
115. The NNPDF Collaboration. **Parton distributions from high-precision collider data.** *Eur. Phys. J. C* **77**, 663. <https://doi.org/10.1140/epjc/s10052-017-5199-5> (2017).
116. Alioli, S., Nason, P., Oleari, C. & Re, E. **A general framework for implementing NLO calculations in shower Monte Carlo programs: the POWHEG BOX.** *JHEP* **06**, 043. [https://doi.org/10.1007/JHEP06\(2010\)043](https://doi.org/10.1007/JHEP06(2010)043) (2010).
117. Frixione, S., Nason, P. & Oleari, C. **Matching NLO QCD computations with parton shower simulations: the POWHEG method.** *JHEP* **11**, 070. <https://doi.org/10.1088/1126-6708/2007/11/070> (2007).
118. Sudakov, V. V. **Vertex parts at very high-energies in quantum electrodynamics.** *Sov. Phys. JETP* **3**, 65 (1956).
119. Andersson, B., Gustafson, G., Ingelman, G. & Sjostrand, T. **Parton Fragmentation and String Dynamics.** *Phys. Rept.* **97**, 31. [https://doi.org/10.1016/0370-1573\(83\)90080-7](https://doi.org/10.1016/0370-1573(83)90080-7) (1983).
120. Bahr, M. *et al.* **Herwig++ Physics and Manual.** *Eur. Phys. J. C* **58**, 639. <https://doi.org/10.1140/epjc/s10052-008-0798-9> (2008).
121. Bellm, J. *et al.* **Herwig 7.0/Herwig++ 3.0 release note.** *Eur. Phys. J. C* **76**, 196. <https://doi.org/10.1140/epjc/s10052-016-4018-8> (2016).
122. The CMS Collaboration. **Extraction and validation of a new set of CMS PYTHIA8 tunes from underlying-event measurements.** *Eur. Phys. J. C* **80**, 4. <https://doi.org/10.1140/epjc/s10052-019-7499-4> (2020).
123. Agostinelli, S. *et al.* **GEANT4—a simulation toolkit.** *Nucl. Instrum. Meth. A* **506**, 250. [https://doi.org/10.1016/S0168-9002\(03\)01368-8](https://doi.org/10.1016/S0168-9002(03)01368-8) (2003).
124. Alwall, J. *et al.* **The automated computation of tree-level and next-to-leading order differential cross sections, and their matching to parton shower simulations.** *JHEP* **07**, 079. [https://doi.org/10.1007/JHEP07\(2014\)079](https://doi.org/10.1007/JHEP07(2014)079) (2014).
125. Alwall, J., Herquet, M., Maltoni, F., Mattelaer, O. & Stelzer, T. **MadGraph 5 : Going Beyond.** *JHEP* **06**, 128. [https://doi.org/10.1007/JHEP06\(2011\)128](https://doi.org/10.1007/JHEP06(2011)128) (2011).

126. Frixione, S. & Webber, B. R. **Matching NLO QCD computations and parton shower simulations.** *JHEP* **06**, 029. <https://doi.org/10.1088/1126-6708/2002/06/029> (2002).
127. Artoisenet, P., Frederix, R., Mattelaer, O. & Rietkerk, R. **Automatic spin-entangled decays of heavy resonances in Monte Carlo simulations.** *JHEP* **03**, 015. [https://doi.org/10.1007/JHEP03\(2013\)015](https://doi.org/10.1007/JHEP03(2013)015) (2013).
128. Ježo, T. & Nason, P. **On the Treatment of Resonances in Next-to-Leading Order Calculations Matched to a Parton Shower.** *JHEP* **12**, 065. [https://doi.org/10.1007/JHEP12\(2015\)065](https://doi.org/10.1007/JHEP12(2015)065) (2015).
129. Buccioni, F. *et al.* **OpenLoops 2.** *Eur. Phys. J. C* **79**, 866. <https://doi.org/10.1140/epjc/s10052-019-7306-2> (2019).
130. The CMS Collaboration. **Development and validation of HERWIG 7 tunes from CMS underlying-event measurements.** *Eur. Phys. J. C* **81**, 312. <https://doi.org/10.1140/epjc/s10052-021-08949-5> (2021).
131. Bothmann, E. *et al.* **Event Generation with Sherpa 2.2.** *SciPost Phys.* **7**, 034. <https://doi.org/10.21468/SciPostPhys.7.3.034> (2019).
132. Frederix, R. & Frixione, S. **Merging meets matching in MC@NLO.** *JHEP* **12**, 061. [https://doi.org/10.1007/JHEP12\(2012\)061](https://doi.org/10.1007/JHEP12(2012)061) (2012).
133. Alwall, J. *et al.* **Comparative study of various algorithms for the merging of parton showers and matrix elements in hadronic collisions.** *Eur. Phys. J. C* **53**, 473 (2008).
134. Cacciari, M. & Salam, G. P. **Pileup subtraction using jet areas.** *Phys. Lett. B* **659**, 119. <https://doi.org/10.1016/j.physletb.2007.09.077> (2008).
135. The CMS Collaboration. **Measurement of the inelastic proton-proton cross section at $\sqrt{s} = 13$ TeV.** *JHEP* **07**, 161. [https://doi.org/10.1007/JHEP07\(2018\)161](https://doi.org/10.1007/JHEP07(2018)161) (2018).
136. The CMS Collaboration. **Inclusive and differential cross section measurements of $t\bar{t}b\bar{b}$ production in the lepton+jets channel at $\sqrt{s} = 13$ TeV with the CMS detector.** To be submitted to JHEP. <https://cds.cern.ch/record/2852880> (2023).
137. Ježo, T., Lindert, J. M., Moretti, N. & Pozzorini, S. **New NLOPS predictions for $t\bar{t} + b$ -jet production at the LHC.** *Eur. Phys. J. C* **78**, 502. <https://doi.org/10.1140/epjc/s10052-018-5956-0> (2018).
138. Worek, M. **Next-to-Leading Order QCD Corrections to $t\bar{t}b\bar{b}$ Production at the LHC.** *Acta Phys. Polon. B* **40**, 2937. <https://doi.org/10.1088/1126-6708/2008/08/108> (2009).
139. Bevilacqua, G., Czakon, M., Papadopoulos, C. G., Pittau, R. & Worek, M. **Assault on the NLO Wishlist: $pp \rightarrow t\bar{t}b\bar{b}$.** *JHEP* **09**, 109. <https://doi.org/10.1088/1126-6708/2009/09/109> (2009).
140. Bredenstein, A., Denner, A., Dittmaier, S. & Pozzorini, S. **NLO QCD corrections to $pp \rightarrow t\bar{t}b\bar{b} + X$ at the LHC.** *Phys. Rev. Lett.* **103**, 012002. <https://doi.org/10.1103/PhysRevLett.103.012002> (2009).
141. Bredenstein, A., Denner, A., Dittmaier, S. & Pozzorini, S. **NLO QCD corrections to $t\bar{t}b\bar{b}$ production at the LHC: 2. Full hadronic results.** *JHEP* **03**, 021. [https://doi.org/10.1007/JHEP03\(2010\)021](https://doi.org/10.1007/JHEP03(2010)021) (2010).
142. Buccioni, F., Kallweit, S., Pozzorini, S. & Zoller, M. F. **NLO QCD predictions for $t\bar{t}b\bar{b}$ production in association with a light jet at the LHC.** *JHEP* **12**, 015. [https://doi.org/10.1007/JHEP12\(2019\)015](https://doi.org/10.1007/JHEP12(2019)015) (2019).

143. Denner, A., Lang, J.-N. & Pellen, M. **Full NLO QCD corrections to off-shell $t\bar{t}b\bar{b}$ production.** *Phys. Rev. D* **104**, 056018. <https://doi.org/10.1103/PhysRevD.104.056018> (2021).
144. Bevilacqua, G. *et al.* **$t\bar{t}b\bar{b}$ at the LHC: on the size of corrections and b-jet definitions.** *JHEP* **08**, 008. [https://doi.org/10.1007/JHEP08\(2021\)008](https://doi.org/10.1007/JHEP08(2021)008) (2021).
145. The ATLAS Collaboration. **Measurements of inclusive and differential fiducial cross-sections of $t\bar{t}$ production with additional heavy-flavour jets in proton-proton collisions at $\sqrt{s} = 13$ TeV with the ATLAS detector.** *JHEP* **04**, 046. [https://doi.org/10.1007/JHEP04\(2019\)046](https://doi.org/10.1007/JHEP04(2019)046) (2019).
146. The CMS Collaboration. **Measurement of the $t\bar{t}b\bar{b}$ production cross section in the all-jet final state in pp collisions at $\sqrt{s} = 13$ TeV.** *Phys. Lett. B* **803**, 135285. <https://doi.org/10.1016/j.physletb.2020.135285> (2020).
147. The CMS Collaboration. **First measurement of the cross section for top quark pair production with additional charm jets using dileptonic final states in pp collisions at $\sqrt{s} = 13$ TeV.** *Phys. Lett. B* **820**, 136565. <https://doi.org/10.1016/j.physletb.2021.136565> (2021).
148. The CMS Collaboration. **Measurements of $t\bar{t}$ cross sections in association with b jets and inclusive jets and their ratio using dilepton final states in pp collisions at $\sqrt{s} = 13$ TeV.** *Phys. Lett. B* **776**, 355. <https://doi.org/10.1016/j.physletb.2017.11.043> (2018).
149. The ATLAS Collaboration. **Measurement of Higgs boson decay into b-quarks in associated production with a top-quark pair in pp collisions at $\sqrt{s} = 13$ TeV with the ATLAS detector.** *JHEP* **06**, 097. [https://doi.org/10.1007/JHEP06\(2022\)097](https://doi.org/10.1007/JHEP06(2022)097) (2022).
150. The CMS Collaboration. **Measurement of $t\bar{t}H$ production in the $H \rightarrow b\bar{b}$ decay channel in 41.5 fb^{-1} of proton-proton collision data at $\sqrt{s} = 13$ TeV.** <https://cds.cern.ch/record/2675023> (2019).
151. The CMS Collaboration. **Search for $t\bar{t}H$ production in the $H \rightarrow b\bar{b}$ decay channel with leptonic $t\bar{t}$ decays in proton-proton collisions at $\sqrt{s} = 13$ TeV.** *JHEP* **03**, 026. [https://doi.org/10.1007/JHEP03\(2019\)026](https://doi.org/10.1007/JHEP03(2019)026) (2019).
152. The ATLAS Collaboration. **Measurement of the $t\bar{t}t\bar{t}$ production cross section in pp collisions at $\sqrt{s} = 13$ TeV with the ATLAS detector.** *JHEP* **11**, 118. [https://doi.org/10.1007/JHEP11\(2021\)118](https://doi.org/10.1007/JHEP11(2021)118) (2021).
153. **Evidence for four-top quark production in proton-proton collisions at $\sqrt{s} = 13$ TeV.** Submitted to *Phys. Lett. B*. arXiv: 2303.03864 [hep-ex] (2023).
154. Czakon, M. & Mitov, A. **Top++: A program for the calculation of the top-pair cross-section at hadron colliders.** *Comput. Phys. Commun.* **185**, 2930. <https://doi.org/10.1016/j.cpc.2014.06.021> (2014).
155. Hartanto, H. B., Jager, B., Reina, L. & Wackerroth, D. **Higgs boson production in association with top quarks in the POWHEG BOX.** *Phys. Rev. D* **91**, 094003. <https://doi.org/10.1103/PhysRevD.91.094003> (2015).
156. Kidonakis, N. & Yamanaka, N. **Higher-order corrections for tW production at high-energy hadron colliders.** *JHEP* **05**, 278. [https://doi.org/10.1007/JHEP05\(2021\)278](https://doi.org/10.1007/JHEP05(2021)278) (2021).
157. Campbell, J., Neumann, T. & Sullivan, Z. **Single-top-quark production in the t-channel at NNLO.** *JHEP* **02**, 040. [https://doi.org/10.1007/JHEP02\(2021\)040](https://doi.org/10.1007/JHEP02(2021)040) (2021).

Bibliography

158. Li, Y. & Petriello, F. **Combining QCD and electroweak corrections to dilepton production in the framework of the FEWZ simulation code.** *Phys. Rev. D* **86**, 094034. <https://doi.org/10.1103/PhysRevD.86.094034> (2012).
159. The CMS Collaboration. **Precision luminosity measurement in proton-proton collisions at $\sqrt{s} = 13$ TeV in 2015 and 2016 at CMS.** *Eur. Phys. J. C* **81**, 800. <https://doi.org/10.1140/epjc/s10052-021-09538-2> (2021).
160. The CMS Collaboration. **CMS luminosity measurement for the 2017 data-taking period at $\sqrt{s} = 13$ TeV** CMS Physics Analysis Summary CMS-PAS-LUM-17-004 (2018). <https://cds.cern.ch/record/2621960/>.
161. The CMS Collaboration. **CMS luminosity measurement for the 2018 data-taking period at $\sqrt{s} = 13$ TeV** CMS Physics Analysis Summary CMS-PAS-LUM-18-002 (2019). <https://cds.cern.ch/record/2676164/>.
162. Barlow, R. J. & Beeston, C. **Fitting using finite Monte Carlo samples.** *Comput. Phys. Commun.* **77**, 219. [https://doi.org/10.1016/0010-4655\(93\)90005-W](https://doi.org/10.1016/0010-4655(93)90005-W) (1993).
163. Conway, J. S. **Incorporating Nuisance Parameters in Likelihoods for Multisource Spectra.** *PHYSTAT 2011*, 115. <https://doi.org/10.5170/CERN-2011-006.115> (2011).
164. Royston, P. **Lowess Smoothing.** *Stata Technical Bulletin* **3**, 7 (1991).
165. van der Linden, J. *et al.* **Study of $t\bar{t}b\bar{b}$ and $t\bar{t}W$ background modelling for $t\bar{t}H$ analyses.** arXiv: 2301.11670 [hep-ex] (2023).
166. Bierlich, C. *et al.* **Robust Independent Validation of Experiment and Theory: Rivet version 3.** *SciPost Phys.* **8**, 026. <https://doi.org/10.21468/SciPostPhys.8.2.026> (2020).
167. Czakon, M. *et al.* **Top-pair production at the LHC through NNLO QCD and NLO EW.** *JHEP* **10**, 186. [https://doi.org/10.1007/JHEP10\(2017\)186](https://doi.org/10.1007/JHEP10(2017)186) (2017).
168. Bevilacqua, G., Lupattelli, M., Stremmer, D. & Worek, M. **A study of additional jet activity in top quark pair production and decay at the LHC.** arXiv: 2212.04722 [hep-ph] (2022).
169. The CMS Collaboration. **Measurement of differential cross sections for the production of top quark pairs and of additional jets in pp collisions at $\sqrt{s} = 13$ TeV.** <https://cds.cern.ch/record/2803771> (2022).
170. Monni, P. F., Nason, P., Re, E., Wiesemann, M. & Zanderighi, G. **MiNNLO_{PS}: a new method to match NNLO QCD to parton showers.** *JHEP* **05**. [Erratum: *JHEP* **02**, 031 (2022)], 143. [https://doi.org/10.1007/JHEP05\(2020\)143](https://doi.org/10.1007/JHEP05(2020)143) (2020).
171. Monni, P. F., Re, E. & Wiesemann, M. **MiNNLO_{PS}: optimizing $2 \rightarrow 1$ hadronic processes.** *Eur. Phys. J. C* **80**, 1075. <https://doi.org/10.1140/epjc/s10052-020-08658-5> (2020).
172. Mazzitelli, J. *et al.* **Top-pair production at the LHC with MINNLO_{PS}.** *JHEP* **04**, 079. [https://doi.org/10.1007/JHEP04\(2022\)079](https://doi.org/10.1007/JHEP04(2022)079) (2022).
173. Kvita, J. **Study of methods of resolved top quark reconstruction in semileptonic $t\bar{t}$ decay.** *Nucl. Instrum. Meth. A* **900**. [Erratum: *Nucl.Instrum.Meth.A* **1040**, 167172 (2022)], 84. <https://doi.org/10.1016/j.nima.2018.05.059> (2018).

Final words

This thesis would not have been possible without the support, guidance and company of many people.

First and foremost, I would like to thank Ulrich Husemann for all his time and guidance during my time as a Bachelor, Master and PhD student, and for promoting and supporting me wherever possible. I wholeheartedly enjoyed the time in your group. You managed to excite me for the field of experimental particle physics during my Bachelor degree, and I will always be grateful for that! I also want to acknowledge your incredible speed and precision when I was asking for feedback, for example on reports, presentations, or the thesis itself. I have not yet understood how it is possible to proofread 50 pages of text within 24 hours while self-reportedly being busy.

Next, I would like to thank Roger Wolf for being the second referee of my thesis, and also for the really enjoyable particle physics lecture that we organized together.

I would like to acknowledge the financial support of the doctoral school “Karlsruhe School of Elementary and Astroparticle Physics: Science and Technology”, which funded the first three years of my PhD, and the Institute of Experimental Particle Physics which funded the remaining time of my PhD. Thank you for the many opportunities to visit schools, workshops and conferences.

In the early stages of my PhD I relied a lot on Matthias Schröder (cool) and his guidance, I want to thank him for that. It was always a pleasure working together with you and learning from you! You were a big factor in my decision to get a Master and now PhD degree in this field, and I never regretted my choice, thank you!

I want to thank the $t\bar{t}b\bar{b}$ analysis team for the enjoyable collaboration during the last years, and explicitly I want to thank Sébastien Wertz and Kyle Cormier. I learned a lot from both of you, not only about the physics aspects but also about scientific integrity. You were amazing role models and I aspire to follow your good example.

A big thanks also to all my present and past colleagues, I always enjoyed coming to the office, even if that was only possible for around half of my PhD. Thank you Karim, Michael, Philip, Sebastian, Nikita, Emanuel, Rufa and Michele! An explicit shout-out also to R418; Michael, Philip, and Sebastian, it was always fun to share an office with you and I couldn't have wished for better company. In my time as a PhD student, I also had the

Final words

pleasure of supervising some Bachelor and Master students; explicitly I want to thank Emanuel, Lukas and Max for the nice time working together. And finally, I also just want to thank Karim again, because he is a really nice person.

In my time in the CMS Collaboration I have met many people along the way, most of which I enjoyed getting to know and working together, thank you to all of you, and explicitly to the many people of the CMS DESY group, the CMS BTV group, and the CMS TOP group that I got to know during the last years.

Now it is time for friends and family.

Dear DMZ members, while you still think that particle physics is garbage, I would still like to thank you for your valuable friendship and company. Grüße, Tür unten isch auf.

A big shout-out also to the Taldor group, and explicitly Lea, I always enjoyed our time and fun together.

I also am legally required to thank Jin for always being a big support, for many awesome illustrations, and for always being bab.

Finally, a very big thank you to my family! Thanks to my parents, Martina and Dietmar, and my sisters Nina and Maya, for always supporting me. I hereby also acknowledge that you indeed came by for dinner multiple times, as suggested in my Master thesis. In that sense, I also would like to thank the restaurant Mogogo for hosting many of your visits. I will now move a bit further away, but I hope you will still come by sometimes.

And now the final word: Senf.

